DISSERTATION

WIND TUNNEL MODELING AND ANALYSIS OF WIND EFFECTS ON LOW-RISE BUILDINGS

Submitted by

Munehito Endo

Department of Civil and Environmental Engineering

In partial fulfillment of the requirements

For the Degree of Doctor of Philosophy

Colorado State University

Fort Collins, Colorado

Summer 2011

Doctoral Committee:

Advisor: Bogusz Bienkiewicz

Marvin E Criswell
David E Neff
Peter Young

ABSTRACT

WIND TUNNEL MODELING AND ANALYSIS OF WIND EFFECTS ON LOW-RISE BUILDINGS

Wind tunnel modeling is a robust technique which allows determination of wind effects on buildings and other structures. Due to complexity of flows and induced wind loads, other techniques can not be reliably used in practical analyses of such effects. Information deduced from wind tunnel testing has been successfully employed in development of design guidelines and in direct applications in wind-resistant design of variety of structures, including low-rise buildings. Although wind tunnel modeling of wind loading has been generally accepted as a viable tool, over the years a number of questions regarding accuracy and limitations of this technique have been raised. Some of the questions related to modeling of wind loading on low-rise buildings were addressed in the research described in this dissertation.

Investigation of reported discrepancies in the laboratory-field and inter-laboratory comparisons was one of main focuses of this study. To identify the origins of the discrepancies, careful studies of reported wind tunnel set-ups, modeling of field/target approach wind conditions, measurement techniques and quality of obtained data and data analyses were carried out. Series of experiments were performed in boundary-layer wind tunnels at the Wind Engineering and Fluids Laboratory, at Colorado State University, to

aid these analyses. It was found that precise matching of characteristics of approach field wind and flows modeled in wind tunnels was essential to ensure compatibility of the simulated building wind loads.

The issue of the accuracy of predictions of the extreme wind-induced loading based on the results of wind tunnel modeling was addressed. In this investigation, the peak wind-induced pressures on low-rise buildings were analyzed using two advanced techniques: the extreme value distribution (EVD) theory and the peak-over-threshold (POT) approach. The extreme roof suction pressures predicted from these two approaches were compared with field observations. The degree of convergence of the EVD fits was discussed for Type I and Type III EVDs.

The advanced experimental tool, electronically-scanned 1024-channel pressure measurement system (ES1024-PS), was developed and employed in wind tunnel modeling of wind loads on low-rise building. The wind-induced pressures were simultaneously acquired at 990 locations uniformly distributed over the surfaces (walls and roof) of a model of a generic low-rise building. The Proper Orthogonal Decomposition (POD) analysis was performed to capture the spatio-temporal characteristics of the acquired pressure field. It was found from POD analysis that the pressure data sets can be substantially reduced, while preserving the main spatio-temporal features of the building wind loading.

ACKNOWLEDGEMENTS

First and foremost I would like to thank my adviser, Dr. Bogusz Bienkiewicz. I appreciate all his contributions of time, ideas, and funding to make my Ph.D. experience productive and stimulating.

I also would like to record my gratitude to Dr. David E Neff for his advice and guidance from the very early stage of this research and to Mr. David Boyajian for his technical support. I would like to thank my committees, Dr. Marvin E. Criswell and Dr. Peter Young, for their suggestions and help with my dissertation, for their time, interests and interesting questions.

Finally, I take this opportunity to express my profound gratitude to my family for their unconditional love and encouragement. For my parents, Mr. Ikuo Endo and Mrs. Sachiko Endo, and my wife, Mrs. Miao-fang Endo have always supported my endeavors with great enthusiasm.

TABLE OF CONTENTS

LIST OF FIGURES

CHAPTER 2

CHAPTER 3

CHAPTER 4

CHAPTER 5

CHAPTER 6

APPENDIX A

APPENDIX B

LIST OF TABLES

CHAPTER 1

CHAPTER 2

CHAPTER 3

CHAPTER 4

CHAPTER 5

CHAPTER 6

APPENDIX A

CHAPTER 1

INTRODUCTION

1.1 INTRODUCTION

Extreme winds originate mostly from down-slope winds generated in mountain ranges, thunderstorms, tornados, and tropical cyclones known as hurricanes and typhoons. Holms (2001) wrote, “Damage to buildings and others structures by windstorms has been a fact of life for human beings from the time they moved out of cave dwellings to the present day.” All structures standing on the earth’s surface are exposed to one or more types of extreme winds, and they are subjected to potentially catastrophic wind forces during periods of severe wind hazards.

The largest cause of economic and insured losses in natural disasters is wind storms, well ahead of earthquake and floods (Simiu and Scanlan, 1996). According to Simiu and Scanlan (1996), hurricanes and tornadoes caused approximately $41 billion in insured catastrophic losses, compared with $6.18 billion for all other natural hazards in the U.S., between 1986 and 1993. According to Kikugawa and Bienkiewicz (2005), wind-induced losses averaged over 5 years (2000-2004) and 50 years (1955-2004) are 89% and 69%, respectively, of the overall hazard damage participation in the U.S.

Two of the most destructive hurricanes in the U.S. were Andrew in August 1992 and Katrina in August 2005. According to the National Hurricane Center (NHC) of the National Oceanic and Atmospheric Administration (NOAA), Andrew caused $26.5

billion in damage and 23 fatalities and Katrina caused $75 billion in damage and 1200 fatalities. For comparison, Table 1.1 lists property damage and fatalities caused by some of the largest hurricanes in the U.S., over the 10 year span of 2000-2010.

Table 1.1 Property damage and fatalities caused by hurricanes in the U.S.

Year	Hurricane	Property damage ($ billion)	Fatalities
2008	Ike	19.3	20
2005	Wilma	16.8	5
2005	Rita	10	7
2005	Katrina	75	1200
2005	Dennis	2.23	3
2004	Jeanne	6.9	6
2004	Ivan	14.2	25
2004	Frances	8.9	8
2004	Charley	15	10
2003	Isabel	3	17

Tornadoes, which are fiercely swirling columns of air extending between clouds and the earth's surface, also create catastrophic damages along their paths. A comprehensive damage investigation conducted by the American Association for Wind Engineering (AAWE) reported that devastating damages to residential houses, commercial and industrial buildings and public facilities in Missouri and Kansas, were caused by tornadoes traveling across these states in May 2003 (Bienkiewicz, 2003).

Most major windstorms have caused a wide range of damage to non-engineered low-rise buildings such as residential houses, commercial and industrial structures. Such buildings and structures are frequently vulnerable to severe windstorms. Most dominant

failures have occurred in roofs and roof coverings where extremely high suction pressures form; especially near roof corners, leading roof edges and roof ridges (Tieleman, 2003). Understanding how wind-induced loads act on low-rise buildings is an important step in being able to reduce such damages and in providing reliable wind resistant design guidelines in building standards and codes.

According to Holmes (2001), difficulties to assess wind-induced loads for low-rise buildings arise because,

> "They are usually immersed within the layer of aerodynamic roughness on the earth's surface, where the turbulence intensities are high, and interference and shelter effects are important, but difficult to quantify. Roof loadings, with all the variations due to changes in geometry, are of critical importance for low-rise buildings. The highest wind loading on the surface of a low-rise structure are generally the suctions on the roof, and many structural failures are initiated there."

The key to enhance the understanding of wind-induced loads and to improve wind resistant design of low-rise buildings is reliable description of such loads which is typically accomplished via wind tunnel. Since late 1950s, the improvements in wind tunnel modeling techniques to better duplicate physical phenomena such as wind loading on structures have been achieved. Jensen (1958) indicated the necessity of the appropriate simulation of the turbulent boundary layer flow and the adherence to model law requirements for the wind tunnel measurements of wind-induced pressures. Richardson *et al*. (1997) pointed out that more reliable wind tunnel techniques have been developed as a result of improvements in boundary layer simulations and incorporation of findings based on full-scale measurements and practices.

Since the 1970s, a number of field (full-scale) experiments dealing with building pressures on generic low-rise building geometries have been conducted. The Aylesbury

(full-scale) experiment was carried out from 1972 to 1974 on a specially designed low-rise experimental building in Aylesbury, England. The building had planar dimensions of 7 m × 13.3 m and an eave height of 5 m. The pitch of the roof was adjustable from 5^o to 45^o. Surface pressures on walls and roof were measured. In subsequent studies using scaled laboratory tests designed to model conditions of the Aylesbury tests, significant efforts on the improvement of wind tunnel modeling techniques were reported by Apperley *et al*. (1979), Vickery and Surry (1983), Hansen and Sørensen (1986), Vickery *et al*. (1986) and Sill *et al*. (1989).

During the period from 1986 to 1987, a building with a planar dimension of 24 m × 12.9 m and an eave height of 4 m was built in Silsoe, England. The pitch of the roof was 10^o. Seventy pressure taps on the roof and walls, as well as twelve strain gauges on the central portal frame, were installed in order to measure wind-induced pressures on and responses of the building. Comparison of the field and wind tunnel results allowed for improvements in wind tunnel measurement techniques. A good agreement was noted for the compared field and wind tunnel building pressures (Dalley and Richardson (1992), Hoxey and Richards (1992), Richardson and Surry (1991 and 1992), Richardson and Blackmore (1995) and others).

In the early 1990s, a Texas Tech University (TTU) field experiment was carried out in Lubbock, Texas. The TTU test building had planar dimensions of 9.1 m × 13.7 m, an eave height of 4 m and a nearly flat roof. Building pressures were measured on the building roof and walls (Levitan *et al.* (1991), Mehta *et al.* (1992) and Levitan and Mehta (1992)). Many wind tunnel laboratories have addressed issues of wind tunnel testing using existing experimental techniques and have developed new strategies for physical

modeling of the approach wind and wind-induced loading on the TTU test building (Ham and Bienkiewicz (1998), Tieleman *et al*. (1996), Surry (1991) and others).

The field and laboratory experiments involving the TTU test building have contributed significantly to the understanding of the flow past and wind-induced loading on low-rise buildings. This resulted in improvements in wind tunnel modeling techniques for low-rise buildings. However, those accomplishments should be viewed in context of the observation by Surry and Johnson (1986) who pointed out that,

> "there is also the danger that model- and full-scale data may be misused in code application, i.e. there is a tendency to take the worst of the worst cases for application to design without fully exploring the meaningfulness of the underlying data".

Hölscher and Niemann (1998) reported findings from comparative wind tunnel tests initiated by the Windtechnologische Gesellschaft (WTG). Twelve institutes were participated in this program and performed surface pressure measurements on a cubic model. They pointed out issues associated with wind tunnel modeling such as statistical variability of data introduced by measurement instruments, physical variability of simulated flows, imperfections of models and pressure tubing systems, different judgment on the time and geometrical scale imposed by a given wind tunnel flow. Furthermore, another issue associated with wind tunnel modeling is how to represent data acquired from wind tunnel experiments. Kasperski (2003) stated questions about the following issues associated with determination of extreme wind loading: (1) what is the appropriate length of a single run, (2) what is the minimum number of independent runs, and (3) what fractile of the extremes is required for the specification of the design wind load using what target confidence interval.

1.2 PURPOSE OF RESEARCH

The purpose of the research was to address and clarify various issues related to wind tunnel modeling for wind effects on low-rise buildings. Investigation of variability in results drawn from comparisons between field (full-scale) vs. wind tunnel (model-scale) measurements or between wind tunnel laboratories was one of objectives in this study. Additional objectives were to refine the extreme wind loading predictions using extreme value theory and other methods (peak-over-threshold approach and peak non-Gaussian estimate method), and to apply the proper orthogonal decomposition technique to characterize large data sets acquired from the recently-developed 1024-channel pressure measurement system.

1.3 OUTLINE OF DISSERTATION

The four main topics addressed in this dissertation are: (1) Comparisons and investigation of variability in field (full-scale) and wind tunnel measurements, (2) Predictions of extreme wind-induced loadings and evaluation of the statistical convergence issue related to extreme value analysis of such loads, (3) Investigation of the inter-laboratory discrepancy in wind-induced loadings on low-rise buildings, and (4) Development and application of the advanced experimental tool, an electronically scanned 1024-channel pressure acquisition system.

Chapter 2 presents wind tunnel experiments employing 1:50 and 1:12.5 geometrical scale models of the TTU test building. The results of measured wind pressures acquired from the 1:50 scale model were compared with field results, other laboratory results, and numerical data. The roof corner pressures acquired from both the

1:50 and 1:12.5 scale models were employed to investigate the model scale (Reynolds number) effects. The agreement/discrepancy between those results is discussed in detail.

In Chapter 3, extreme value analysis using the generalized extreme value distributions (GEVs) and peak-over-threshold method (POT) was conducted to predict extreme peak roof pressures. Hundreds of peak roof corner pressures acquired from wind tunnel measurements on the 1:12.5 and 1:50 geometrical scale models of the TTU test building were utilized in this analysis. The extreme peaks pressures predicted from GEVs and POT were compared with field observations and the issue of convergence on GEVs was discussed.

In Chapter 4, an investigation of the comparative inter-laboratory study is presented. A broad range of analyses were conducted in order to compare the laboratory approach flows and wind-induced building loadings acquired at six participating laboratories. The variability in the compared data and its origins were addressed.

Chapter 5 describes the comparative inter-wind tunnel investigation involving two boundary-layer wind tunnels at the Wind Engineering and Fluids Laboratory (WEFL), Colorado State University (CSU). Based on findings obtained from Chapter 4, matching approach flows were modeled in two wind tunnels. Subsequently, wind-induced roof pressures on building models were acquired and compared. The limited wind tunnel testing of Reynolds number effects was carried out.

Chapter 6 describes the development of the 1024-channel pressure measurement system. The preliminary wind tunnel experiments for the modeling of wind loads employing this system are also presented. Next, the building pressure data acquired at 990 locations over a generic low-rise building model were used in the Proper Orthogonal

Decomposition (POD) analysis to determine the systematic characteristics hidden in the random nature of fluctuating building pressures.

Chapter 7 provides a summary of the conclusions of this study and offers future research recommendations.

1.4 REFERENCES

Apperley, L., Surry, D., Stathopoulos, T. and Davenport, A.G. (1979), "Comparative measurements of wind pressure on a model of the full-scale experimental house at Aylesbury, England", *J. Wind Eng. Ind. Aerodyn*., Vol. 4, pp. 207-228.

Bienkiewicz, B. (2003), "Lessons learned from damage investigations - a case study of May 2003 Missouri-Kansas tornadoes", *Proceedings of ISWE1 – The First International Symposium on Wind Effects on Buildings and Urban Environment*, 21 pp. March 8-9, Tokyo, Japan.

Dalley, S. and Richardson, G. (1992), "Reference static pressure measurements in wind tunnels", *J. Wind Eng. Ind. Aerodyn.*, Vol. 41-44, pp. 909-920.

Jensen, M. (1958), "The model law for phenomena in the natural wind", *Ingenioren*, Vol. 2, pp. 121-128.

Kikugawa, H. and Bienkiewicz, B. (2005), "Wind damages and prospects for accelerated wind damage reduction in Japan and in the United States", *Proceedings of 37th Joint Meeting Panel on Wind and Seismic Effects*, 14 pp. May 16-21, Tsukuba, Japan.

Ham, H.J. and Bienkiewicz, B. (1998), "Wind tunnel simulation of TTU flow and building roof pressures", *J. Wind Eng. Ind. Aerodyn*., Vol. 77 & 78, pp. 119-133.

Hansen, S.O. and Sørensen, E.G. (1986), "The Aylesbury experiment. Comparison of model and full-scale tests", *J. Wind Eng. Ind. Aerodyn*., Vol. 22, pp. 1-22.

Holmes, J.D. (2001), *Wind loadings of structures*, Spon Press.

Hölscher, N. and Niemann, H.-J. (1998), "Towards quality assurance for wind tunnel tests: A comparative testing program of the Windtechnologische Gesellschaft", *J. Wind Eng. Ind. Aerodyn.*, Vol. 74-76, pp. 599-608.

Hoxey, R.P. and Richards, P.J. (1992), "Structure of the atmospheric boundary layer below 25m and implications to wind loading on low-rise buildings", *J. Wind Eng. Ind. Aerodyn*., Vol. 41-44, pp. 317-327.

Kasperski, M. (2003), "Specification of the design wind load based on wind tunnel experiments", *J. Wind Eng. Ind. Aerodyn*., Vol. 91, pp. 527-541.

Levitan, M.L. and Mehta, K.C. (1992), "Texas Tech field experiments for wind loads part 1: Building and pressure measuring system", *J. Wind Eng. Ind. Aerodyn*., Vol. 41-44, pp. 1565-1576.

Levitan, M.L., Mehta, K.C., Vann, W.P., and Holmes, J.D. (1991), "Field measurements of pressures on the Texas Tech building", *J. Wind Eng. Ind. Aerodyn*., Vol. 38, pp. 227-234.

Mehta, K.C., Levitan, M.L., Iverson, R.E., and McDonald, J.R. (1992), "Roof corner pressures measured in the field on a low building", *J. Wind Eng. Ind. Aerodyn*., Vol. 41-44, pp. 181-192.

NHC: National Hurricane Center (http://www.nhc.noaa.gov/index.shtml).

Richardson, G.M. and Blackmore, P.A. (1995), "The Silsoe structures buildings: Comparisons of 1:100 model-scale data with full-scale data", *J. Wind Eng. Ind. Aerodyn*., Vol. 57, pp. 191-201.

Richardson, G.M., Hoxey, R.P., Robertson, A.P. and Short, J.L. (1997), "The Silsoe structures buildings: Comparisons of pressures measured at full scale and in two wind tunnels", *J. Wind Eng. Ind. Aerodyn*., Vol. 72, pp. 187-197.

Richardson, G.M. and Surry, D. (1992), "The Silsoe building: A comparisons of pressures coefficients and spectra at model and full-scale", *J. Wind Eng. Ind. Aerodyn*., Vol. 41-44, pp. 1653-1664.

Richardson, G.M. and Surry, D. (1991), "Comparisons of wind-tunnel and full-scale surface pressure measurements on low-rise pitched-roof buildings", *J. Wind Eng. Ind. Aerodyn*., Vol. 38, pp. 249-256.

Sill, B.L., Cook, N.J. and Blackmore, P.A. (1989), "IAWE Aylesbury comparative experiment – Preliminary results of wind tunnel comparisons", *J. Wind Eng. Ind. Aerodyn*., Vol. 32, pp. 285-302.

Simiu, E. and Scanlan, R.H. (1996), *Wind effects on structures, third edition*, John Wiley & Sons, Inc.

Surry, D. and Johnson, G.L. (1986), "Comparisons between wind tunnel and full scale estimates of wind loads on a mobile home", *J. Wind Eng. Ind. Aerodyn*., Vol. 23, pp. 165-180.

Surry, D. (1991), "Pressure measurements on the Texas Tech building: Wind tunnel measurements and comparisons with full scale", *J. Wind Eng. Ind. Aerodyn*., Vol. 38, pp. 235-247.

Tieleman, H.W. (2003), "Wind tunnel simulation of wind loading on low-rise structures: a review", *J. Wind Eng. Ind. Aerodyn*., Vol. 91, pp. 1627-1649.

Tieleman, H.W., Surry, D. and Mehta, K.C. (1996), "Full/model scale comparison of surface pressures on the Texas Tech experimental building", *J. Wind Eng. Ind. Aerodyn*., Vol. 61, pp. 1-23.

Vickery, P.J. and Surry, D. (1983), “The Aylesbury experiments revisited – Future wind tunnel tests and comparisons”, *J. Wind Eng. Ind. Aerodyn*., Vol. 11, pp. 39-62.

Vickery, P.J., Surry, D. and Davenport, A.G. (1986), “Aylesbury and ACE: Some interesting findings”, *J. Wind Eng. Ind. Aerodyn*., Vol. 23, pp. 1-17.

CHAPTER 2

INVESTIGATION OF LABORATORY-FIELD DISCREPANCY IN WIND-INDUCED PRESSURE ON LOW-RISE BUILDING

The material in Chapter 2 has been published in the following reference:

Endo, M., Bienkiewicz, B., and Ham, H.J. (2006), "Wind-tunnel investigation of point pressure on TTU test building", Journal of Wind Engineering and Industrial Aerodynamics, Vol. 94, pp. 553-578, and also in Proceedings of the 11th International Conference on Wind Engineering, June 2-5, pp. 949-956, 2003.

2.1 INTRODUCTION

Comparison of field data with simulated physical phenomena - such as wind flow and wind-induced loading on and response of buildings and other structures – constitutes an important element in the validation of tested modeling techniques. Appropriately screened field results are desired to carry out such a check of the laboratory (physical modeling) approach. Laboratory results, in turn, can be used to validate numerical, analytical and hybrid modeling techniques.

The wind engineering research at the Texas Tech University (TTU) field site (Levitan *et al.* (1991), Mehta *et al.* (1992) and Levitan and Mehta (1992a)) has stimulated many investigations focused on the modeling of wind conditions at this site and wind-induced loading on the TTU test building and low-rise buildings in general. Most of the related efforts were of experimental nature and they were carried out in various laboratories. They addressed issues of wind tunnel testing using existing

experimental techniques and development of new strategies for physical modeling of approach wind and wind-induced effects at geometrical scales appropriate for testing of low-rise buildings, Bienkiewicz and Ham (2003), Ham and Bienkiewicz (1998), Tieleman *et al*. (1996), Surry (1991) and others. The TTU field data were also employed in validation of numerical simulations resulting from application of in-house developed and commercial software packages configured to model wind-induced loading on low-rise buildings (Bekele and Hangan (2002) and Selvam (1997)).

Overall, researchers reported a good agreement between the laboratory and field wind pressures induced on the envelope of the TTU test building. For the cornering approach wind, however, it was found that laboratory external point peak suctions in roof corner/edge areas were lower than those measured during field observations. Most of the comparisons of numerical results with laboratory and/or field data were focused on the mean external pressures. Overall, good agreement was noted in these comparisons. In the limited number of numerical studies including transient simulations of the pressures, a varying degree of agreement between these results and field/laboratory data was reported.

There have been limited investigations reported on the comparisons of full-scale data with laboratory testing at larger geometrical scales. Cheung *et al.* (1997) considered a 1:10 scale model and Jamieson and Carpenter (1993) used a 1:25 scale model of the TTU test building. They investigated the model scale (Reynolds number) effects, in order to resolve the laboratory-field mismatch of the roof corner pressures.

Meaningful comparisons of laboratory/field/numerical results require careful screening of the compared data. Issues of inherent variability of field wind need to be

appropriately addressed in selection of field data representative of wind flow conditions modeled during laboratory and/or numerical testing. In addition, analysis of time-dependent data requires careful assessment of instrumentation capabilities (dynamic range, frequency response), data acquisition (sampling rate, signal filtering), signal-to-noise ratio and other pertinent conditions.

Some of the above issues are addressed in this chapter in the context of comparisons of laboratory, field and numerical wind pressures on the TTU test building. Wind tunnel investigations were carried out using the 1:50 and 1:12.5 geometrical scale models of the TTU test building. External point pressures induced at wall and roof locations in the building mid-plane and in the roof corner region were measured and these data are discussed in this chapter. First, the mid-plane laboratory pressures are compared with field and numerical results. Next, the roof corner pressures are addressed. Representative results of recent measurements of the pressures, acquired for a wider than previously reported range of the wind directions (Bienkiewicz and Ham, 2003), are presented and compared with the available field results. The laboratory roof corner pressures are subsequently employed to investigate the model scale (Reynolds number) effects.

2.2 EXPERIMENTAL CONFIGURATION

The laboratory data were acquired during an experimental study performed at the Wind Engineering and Fluids Laboratory (WEFL) at Colorado State University (CSU). Testing was carried out in two boundary-layer wind tunnels: Meteorological Wind Tunnel (MWT) and Environmental Wind Tunnel (EWT). The details of WEFL and

boundary-layer wind tunnel facilities are described in Appendix A. As mentioned above, two geometrical scales (1:50 and 1:12.5) were employed in this testing.

The overall view of a 1:50 geometrical scale model of the TTU test building is shown in Figure 2.1. The building geometry and the pressure measurement locations are depicted in Figure 2.2. These locations were determined from the field building information provided by Levitan and Mehta (1992a). The modeled pressure taps had a 0.8-mm diameter. Figure 2.3 shows the labeling of the pressure taps and defines the wind directions considered in the testing.

A 1:12.5 geometrical scale model of the TTU test building was furnished with pressure taps of 0.8 mm in diameter. A schematic view of the model and the locations of pressure taps considered in this testing employing this model are shown in Figure 2.4.

The mean velocity and turbulence intensity profiles of the approach flow were measured using hot-film probes in conjunction with constant temperature hot-wire anemometers. The reference velocity and the static pressure were monitored using a pitot-static tube mounted at the roof height, upstream of the model. Hot-film data were sampled at a rate of 1,000 samples/second. Typical flow data records were 30 second in length. The analog signals were low-pass filtered with a cut-off frequency of 500 Hz.

The pressure was measured using Honeywell Micro Switch pressure transducers connected to pressure taps via short tubing with restrictors for the 1:50 scale model, and with very short-length tubing for the 1:12.5 model. The frequency response of the pressure measurement system had a constant magnitude, within $\pm$ 3% error for the 1:50 scale model and within $\pm$ 5% error for the 1:12.5 scale model. It had a linear phase in the frequency range spanning from DC through approximately 220 Hz for the 1:50 scale

model and 340 Hz for the 1:12.5 scale model. The magnitude of the frequency response of the pressure measurement systems used for the two models is shown in Figure 2.5.

In the wind tunnel testing of the 1:50 scale model, most of the pressure time series were low-pass filtered with a frequency cut-off of 200 Hz and they were acquired at a sampling rate of 1000 samples/second. For each pressure tap, ten records of pressure data, each consisting of 18,000 data points, were acquired. Additional data sets were acquired at a sampling rate of 250 samples/second and they were low-pass filtered with a cut-off frequency of 50 Hz. The length of the laboratory data records employed in the present study corresponded to field record of 15-min duration.

In the wind tunnel testing of the 1:12.5 scale model the pressure time series were acquired with various sampling conditions. The data obtained using a sample rate of 200 samples/second were low-pass filtered with the frequency cut-off of 40 Hz. For this case, the corresponding prototype values of the sampling conditions were: sampling rate 20 samples/sec, cut-off frequency 4 Hz, and 15- minute record length. A total of 10 records of the time series were acquired for wind directions ranging from 180^o through 270^o, with an increment of 5^o.

2.3 RESULTS AND DISCUSSION

2.3.1 Results from Testing 1:50 Scale Model

Approach Flow

The modeled nominal flow conditions - flow prevailing at the TTU field – are presented in Figures 2.6 through 2.8. The flow was simulated using the experimental technique described by Bienkiewicz and Ham (2003). The laboratory profile of the mean

velocity (denoted CSU) in Figure 2.6 is compared with the field data reported by Chock (1988). The mean wind velocity is expressed by means of the power-law representation, which is commonly used in wind engineering applications, and specified in reference documents, such as ASCE 7 (2005) and AIJ (1985). The power law of the mean wind velocity can be written as

$$U(z_{g1}) = U(z_{g2})\left(\frac{z_{g1}}{z_{g2}}\right)^{\alpha} \qquad [2.1]$$

where α is an exponent dependent on roughness of terrain and z_{g1} and z_{g2} denote heights above ground. A very good agreement between the laboratory mean velocity profile and the TTU nominal (prevailing) field data implied by the average power law exponent α = 0.14 (for the approach wind zone A, in Chock (1988)) can be seen in Figure 2.6. The mean velocity profile implied by the maximum deviation from the average value of the power-law exponent (in zone A discussed by Chock (1988)) is also marked in the figure, using a dash-dot line. The along-wind turbulence intensity of the modeled flow is compared in Figure 2.7 with the field turbulence intensity (denoted TTU) reported by Chok (1988) and Tieleman *et al*. (1996).

The measured power spectra of the along-wind velocity fluctuations (denoted CSU) are depicted in Figure 2.8, for two reference elevations. These are compared with the empirical turbulence spectrum model proposed by Kaimal (1972) and with the TTU field data reported by Tieleman *et al*. (1996). The Kaimal spectrum for along-wind (longitudinal) velocity component can be written as

$$\frac{nS(z,n)}{\bar{u}^2} = \frac{33.3f}{(1+50f)^{5/3}} \qquad [2.2]$$

where n is frequency, $\overline{u}^2$ is the variance of the longitudinal velocity component, $f = nz/\overline{U}(z)$ is the reduced frequency, and $\overline{U}(z)$ is the mean longitudinal velocity. It is apparent that the field spectrum is attenuated for the reduced frequency $nz/\overline{U}$ >0.3, due to the drop-off in the frequency response of the field instrumentation used to acquire time series of the wind velocity.

Roof mid-plane pressure

The obtained pressure p on the surface of the building model is expressed in the form of a non-dimensional pressure coefficient C_p:

$$C_p = \frac{p - p_0}{\frac{1}{2}\rho \overline{U}_r^2} \qquad [2.3]$$

where p is the pressure, p_0 is the reference static pressure, ρ is air mass density and $\overline{U}_r$ is the reference mean velocity.

The wall and roof pressures in the mid-plane of the TTU test building are shown in Figures 2.9 through 2.11, for two wind directions θ = 270^o and 240^o. The depicted laboratory results include two data sets, corresponding to two data sampling rates: high sampling rate of 1000 Hz (denoted CSU) and low sampling rate of 250 Hz (denoted CSU-LSR). These data are compared with laboratory results obtained at the University of Western Ontario (denoted UWO) reported by Surry (1991) and with field data (denoted TTU) reported by Levitan *et al*. (1991). A good agreement between compared mean pressures can be observed in Figure 2.9. Further examination of these data reveals a better agreement for the wind direction of 270^o.

As depicted in Figure 2.10, the standard deviation of the field pressure is in better agreement with the laboratory data for the wind direction of 270^{o}, see Figure 2.10a. However, as shown in Figure 2.10b the field values are significantly higher than the laboratory data for the wind direction of 240^{o}. A comparison of the corresponding peak pressures in Figure 2.11 shows a similar trend.

Three sets of peak pressures obtained during the present study are included in Figure 2.11: high-sampling-frequency maxima (denoted CSU), low-sampling-frequency maxima (denoted CSU-LSR) and the average peaks (denoted CSU-ave), obtained using ten peaks extracted from ten data records. Figure 2.11a shows a very good agreement between the average laboratory (CSU-ave) and field (TTU) peaks. Except for one roof tap, the maximum peaks obtained at CSU are within the scatter of the field data. Figure 2.11b shows that for the wind direction of 240^{o}, the average peaks obtained at CSU (CSU-ave) are lower than their field counterparts and that the CSU maximum peaks are close in magnitude to the average field peaks.

Bekele and Hangan (2002) compared a number of experimental and numerical data with the results of their numerical simulations. These results are included in Figure 2.11 (denoted UWO-CWE). They noted that for wind direction of 270^{o}, most of the compared (experimental and numerical) peak pressures appeared to be in a good agreement with the field data, while the laboratory peaks obtained at CSU significantly exceeded the field peaks. For the wind direction of 240^{o}, their comparison indicated a very good agreement between the CSU and field pressures and an under-prediction of the field peaks by the remaining data used in their comparison.

The above variability in the agreement between the laboratory and field peak pressures was discussed by Bienkiewicz and Ham (2003), where the laboratory roof peaks obtained by Ham (1998) were compared with the full-scale data. It was concluded that the field-laboratory agreement/disagreement could be attributed to differences in wind conditions associated with the field pressures used in the comparison.

The laboratory data obtained during the present study at CSU and presented herein allow for a better quantification of the above effects. A comparison of the average field (TTU) and laboratory (CSU) peak pressures in Figure 2.11 can be related to the approach wind conditions presented in Table 2.1. It can be seen (in the table) that for the wind direction $\theta = 270^o$, the overall field turbulence intensity was lower than that modeled at CSU. For $\theta = 240^o$, the field turbulence intensity was higher than the laboratory turbulence intensity. Figures 2.10 and 2.11 show that for $\theta = 270^o$ the standard deviation and the peak laboratory pressures were overall larger than the field pressure, while the reverse was true for $\theta = 240^o$. These discrepancies in the laboratory-field comparison of pressure are attributed to the departure of the field turbulence from the turbulence level modeled at CSU. It is also postulated that the high scatter in the field pressure fluctuations is the result of the variability in the approach field flow manifested by the range of the flow turbulence intensity indicated in the table.

The two laboratory sets of the maximum pressure obtained at CSU and included in Figures 2.10 and 2.11 illustrate the effects of the sampling rate (and low-pass filtering) on the standard deviation and peaks of the acquired pressures. These effects are significant and they should be taken into account in comparisons of field and laboratory pressure data.

Table 2.1 Laboratory and field flow at roof height

	CSU	TTU (Levitan *et al*., 1991)	
		$\theta = 270^o$	$\theta = 240^o$
$U_{z = 4\ m}$ (m/s)	10.2	6.6 – 10	5.8 – 8.2
$I_{u,z = 4m}$ (%)	21	16 – 22	19 – 27

Flow variability (Table 2.1) and scatter in fluctuating pressures (Figures 2.10 and 2.11) bring into attention the importance of careful matching of the laboratory and field flows, data sampling conditions, and frequency response of instrumentation employed in comparative studies.

Roof Corner Pressure

The roof corner pressures acquired during the present study are presented in Figure 2.12, for taps 50101, 50205, 50209, 50501, 50505, 50509, 50901, 50905 and 50909 (see Figures 2.3 and 2.4), and the wind direction ranging from 0^o through 360^o, with an increment of 5^o. The laboratory results are compared with the field data for the wind directions of 90^o through 270^o. The format of this comparison is similar to that presented by Bienkiewicz and Ham (2003), where the laboratory roof corner pressures acquired by Ham (1998) were compared with their field counterparts. As discussed by Bienkiewicz and Ham (2003), the field data originated from two sources. The pressures at taps 50101 and 50501 were taken from Tieleman *et al*. (1996) and were restricted to roof pressure records associated with the approach flow of the lateral turbulence intensity not exceeding 20%. The field data for the remaining taps were taken from Mehta *et al*. (1992), where no restriction was placed on the level of turbulence in the approach flow.

Figure 2.12 depicts the highest and lowest peaks for each wind direction out of the ten largest suctions and the average peaks determined from ten segments of the pressure time series.

The laboratory-field comparison of the roof corner pressures (wind direction of 90^{o} through 270^{o}) was discussed by Bienkiewicz and Ham (2003). An overall very good agreement was found for most of the compared roof locations and wind directions. However, a measurable discrepancy between the laboratory and field peak pressures was noted at taps near the roof edges for the cornering wind direction range. The results presented in Figure 2.12 exhibit similar trends.

2.3.2 Results from Testing 1:12.5 Scale Model

Comparison of approach flow characteristics

Profiles of the modeled approach flow are shown in Figures 2.13 and 2.14. The laboratory mean velocity and the along-wind turbulence intensity modeled for the 1:12.5 scale model are compared with the 1:50, 1:25 (Jamieson and Carpenter, 1993) and 1:10 (Cheung *et al*., 1997) geometrical scale wind data.

As depicted in Figure 2.13, except for the 1:10 scale model, overall good agreement among the compared mean velocity profiles can be observed. The profile reported for the 1:10 scale model exhibits localized significant departure from the boundary-layer flow. Such perturbations indicate steep changes in wind velocity and generation of severe wind shear. The effects of such flow features on the measured wind loading are uncertain. The power law exponent of the mean velocity generated for the (CSU) 1:12.5 scale model was 0.148.

The vertical profiles of the along-wind turbulence intensity modeled for four geometrical scales are compared in Figure 2.14. As can be seen, the turbulence intensity at the building height modeled for the 1:12.5 geometrical scale is slightly lower than that obtained for the remaining scales. Namely, at the building height of 4 m, the turbulence intensity was 19.5% for the 1:12.5 scale, while it was 21% for the 1:50 and 1:25 scale, and 22% for the 1:10 scale model.

Figure 2.15 compares the along-wind velocity spectra for the 1:50, 1:25 and 1:12.5 geometrical scale flows. The spectra data for 1:10 scale model was not included because no spectral information for this scale was reported by Cheung et al. (1997). In the figure, the empirical spectral model proposed by Kaimal (1972) (see Equation [2.2]) is included. The integral length scales of the longitudinal (along-wind) flow turbulence, for the 1:50, 1:25 and 1:12.5 scale flow models, are listed in Table 2.2. The value obtained from the TTU field site (Levitan and Mehta, 1992b) is also included in the table. The integral length scale denoted L_u^x is defined (Simiu and Scanlan, 1996) as follows:

$$L_u^x = \frac{U}{\overline{u^2}} \int_0^\infty R_u(\tau) d\tau \qquad [2.4]$$

where $R_u(\tau)$ = autocovariance function of fluctuation $u(x_1, t)$,
U = mean wind speed and
$\overline{u^2}$ = mean square value of $u(x_1, t)$.

Table 2.2 Longitudinal (along-wind) length scale

Prototype Height	1:12.5 model	1:25 model	1:50 model	TTU field site
4 m	9.4 m	28 m	43.2 m	107 m

As can be seen in Figure 2.15, the overall agreement of the spectra obtained for flows modeled at the 1:25 and 1:12.5 scales with the Kaimal empirical spectrum is not satisfactory. However, at the 1:50 scale, the experimental and Kaimal spectra are in a very good agreement. At large scales (1:12.5 and 1:25) the spectra exhibit a significant shift towards the high frequencies, by approximately a factor of two for the 1:12.5 scale model and a factor of four for the 1:25 scale model. As a result the flows generated at these scales do not ensure sufficient low-frequency turbulence content. This fact is reflected in the relatively short integral length scales listed in Table 2.2. In the high-frequency range (small-scale turbulence), the spectral levels for these two scale models distinctively exceed the spectral Kaimal model. Tieleman (1992) postulates that the small-scale turbulence plays an important role in the reproduction of physical phenomena such as wind-induced surface pressures on a bluff body such as low-rise buildings, and it is critical that the small scale turbulence be sufficiently simulated during wind tunnel testing.

Effects of model scale on roof corner pressure

The roof pressures for pressure taps 50101, 50501, 50205 and 50505 (see Figure 2.4) on the 1:12.5 scale model of the TTU test building are shown in Figures 2.16 and 2.17. These are compared with data obtained from measurements carried out for the 1:50 scale model. The prototype sampling conditions for the 1:12.5 and 1:50 models were identical, as described in Section 2.2. The data for taps 50101 and 50501 for 1:10 scale model reported by Cheung *et al*. (1997) and the 1:25 scale model reported by Jamieson and Carpenter (1993) are also included in the figures.

Figure 2.16 compares the mean and peak negative pressures (suctions). The average peak suction (denoted Peak-ave) and the maximum peak suction (denoted Peak-max) were determined using ten peaks extracted from ten data records for the 1:12.5 and 1:50 scale models, while the maximum peak suction for the 1:10 and 1:25 scale models was determined from one record. A very good agreement is observed between the mean pressures for the four considered taps. The average peak suctions for the 1:50 scale model are higher than those for the 1:12.5 scale model, except for tap 50101 for the wind direction ranging from 225^{o} through 265^{o}. In the comparison of the maximum peak suctions for tap 50501, the magnitude of those peaks is very similar among the 1:10, 1:25 and 1:50 scale models. These peaks are predominantly larger than those obtained from the 1:12.5 scale model, for the compared wind directions. For tap 50101, the maximum peak suctions are highly variable among the four scale models. However, a comparison of the maximum and average peak suctions for the 1:50 scale model indicates that they are consistently larger than those of the 1:12.5 scale model, for taps 50501, 50205, and 50505. Larger peak suctions on the 1:50 scale model are attributed to a higher level of turbulence intensity of the modeled flow employed for this scale. Thus the effects of turbulence are more pronounced.

A comparison of the standard deviations of roof pressures among these four scale models is depicted in Figure 2.17. It can be seen that the 1:12.5 and 1:50 models the compared data are in a good agreement, for all of the compared pressure taps. Furthermore, standard deviations for the 1:10 and 1:25 scale models are in a better agreement at tap 50501. In contrast, the agreement for these two scales models is less satisfactory at tap 50101.

Overall, geometrical scale effects on roof pressures could not be identified from the limited comparisons obtained during the present study and extracted from references published by other researchers. Differences in characteristics of the approach flows, such as the level of turbulence and characteristics of wind velocity spectra, employed in the measurement of the compared data, difficulties in modeling of large-scale turbulent flows in small and medium size wind tunnels are considered to be contributing factors to the observed scatter in the obtained results on model scale effects. Further investigations are needed to clarify the issue of the geometrical scale effects on wind-induced loading on buildings and structures.

2.4 CONCLUSIONS

The findings of this chapter can be summarized as follows:

1. The degree of the disagreement between the field and laboratory mid-plane pressures was attributed to the variability in the approach and modeled winds. A comparison of the average peaks and standard deviations of the CSU data with the field pressures showed that a closer laboratory-field matching of the approach wind led to a better laboratory-field agreement between the compared pressures.
2. The roof corner pressures were presented for a broader range of wind directions than those discussed in past studies. The laboratory-field comparison of the roof corner pressures indicated trends similar to those observed in previous investigations.

3. Meaningful comparisons of laboratory/field/numerical wind-induced pressures require careful selection of field data records representative of wind flow conditions modeled during laboratory and/or numerical testing.
4. The maximum and average peaks of roof pressure suctions on the 1:12.5 scale model did not exceed those acquired for the small (1:50 scale) model. The maximum peak suctions compared for the 1:10, 1:12.5, 1:25 and 1:50 scale models did not show a consistent dependence on the model scale, taps 50101 and 50501.
5. Differences in characteristics of the modeled approach flows employed in measurements of roof pressures on small and large models did not allow for definite quantification of the geometrical scale effects on fluctuating pressures.

2.5 REFERENCES

AIJ (1985), *Recommendations for loads on buildings*, Architectural Institute of Japan, Tokyo, Japan.

ASCE 7 Standard (2005), *Minimum design loads for buildings and other structures*, American Society of Civil Engineers, New York, USA.

Bekele, S.A. and Hangan, H. (2002), "A comparative investigation of the TTU pressure envelope. Numerical versus laboratory and full scale results", *Wind and Structures*, Vol. 5, pp. 337-346.

Bienkiewicz, B. and Ham, H.J. (2003), "Wind tunnel modeling of roof pressure and turbulence effects on the TTU test building", *Wind and Structures*, Vol. 6, pp. 91-106.

Cheung, J.C.K., Holmes, J.D., Melbourne, W.H., Lakshmanan, N., and Bowditch, P. (1997), "Pressures on a 1/10 scale model of the Texas Tech building," *J. Wind Eng. Ind. Aerodyn*., Vol. 69-71, pp. 529-538.

Cochran, L.S. and Cermak, J.E. (1992), "Full- and model-scale cladding pressures on the Texas Tech University experimental building," *J. Wind Eng. Ind. Aerodyn*, Vol. 41-44, pp. 1589-1600.

Chok, C.V. (1988), *Wind parameters of Texas Tech University field site*, M.S. thesis, Department of Civil Engineering, Texas Tech University, Lubbock, Texas.

Ham, H.J. (1998), *Turbulence effects on wind-induced building pressure*, Ph.D. dissertation, Department of Civil Engineering, Colorado State University, Fort Collins, Colorado.

Ham, H.J., and Bienkiewicz, B. (1998), "Wind tunnel simulation of TTU flow and building roof pressure," *J. Wind Eng. Ind. Aerodyn*., Vol. 77 & 78, pp. 119-133.

Jamieson, N.J. and Carpenter, P. (1993), "Wind tunnel pressure measurements on the Texas Tech building at a scale of 1:25 and comparison with full scale," The Seventh U.S. National Conference on Wind Engineering, pp. 303-312.

Kaimal, J.E. (1972), "Spectral Characteristics of Surface-Layer Turbulence", Journal of Royal Meteorological Society, Vol. 98, pp. 563-589.

Levitan, M.L. and Mehta, K.C. (1992a), "Texas Tech field experiments for wind load part I: Building and pressure measuring system," *J. Wind Eng. Ind. Aerodyn*., Vol. 41-44, pp. 1565-1576.

Levitan, M.L. and Mehta, K.C. (1992b), "Texas Tech field experiments for wind load part II: Meteorological instrumentation and terrain parameters," *J. Wind Eng. Ind. Aerodyn*., Vol. 41-44, pp. 1577-1588.

Levitan, M.L., Mehta, K.C., Vann, W.P., and Holmes, J.D. (1991), "Field measurements of pressures on the Texas Tech building", *J. Wind Eng. Ind. Aerodyn*., Vol. 38, pp. 227-234.

Mehta, K.C., Levitan, M.L., Iverson, R.E., and McDonald, J.R. (1992), "Roof corner pressures measured in the field on a low building", *J. Wind Eng. Ind. Aerodyn*., Vol. 41-44, pp. 181-192.

Okada, H. and Ha, Y.C. (1992), "Comparison of wind tunnel and full-scale pressure measurement tests on the Texas Tech building," *J. Wind Eng. Ind. Aerodyn*, Vol. 41-44, pp. 1601-1612.

Rofail, A.W. (1995), "Full-scale/model-scale comparisons of wind pressures on the TTU building," *The Ninth International Conference on Wind Engineering*, New Delhi, India, pp. 1055-1066.

Simiu, E. and Scanlan, R.H. (1996), *Wind effects on structures, third edition*, John Wiley & Sons, Inc.

Surry, D. (1991), "Pressure measurements on the Texas Tech building: Wind tunnel measurements and comparisons with full scale", *J. Wind Eng. Ind. Aerodyn*., Vol. 38, pp. 235-247.

Selvam, P.R. (1997), "Computation of pressures on Texas Tech University building using large eddy simulation", *J. Wind Eng. Ind. Aerodyn*., Vol. 67 & 68, pp. 647-657.

Tieleman, H.W., Surry, D. and Mehta, K.C. (1996), "Full/model scale comparison of surface pressures on the Texas Tech experimental building", *J. Wind Eng. Ind. Aerodyn*., Vol. 61, pp. 1-23.

Tieleman, H.W. (1992), "Problems associated with flow modeling procedures for low-rise structures", *J. Wind Eng. Ind. Aerodyn*., Vol. 41-44, pp. 923-934.

Figure 2.1 1:50 geometrical scale model of TTU test building inside MWT

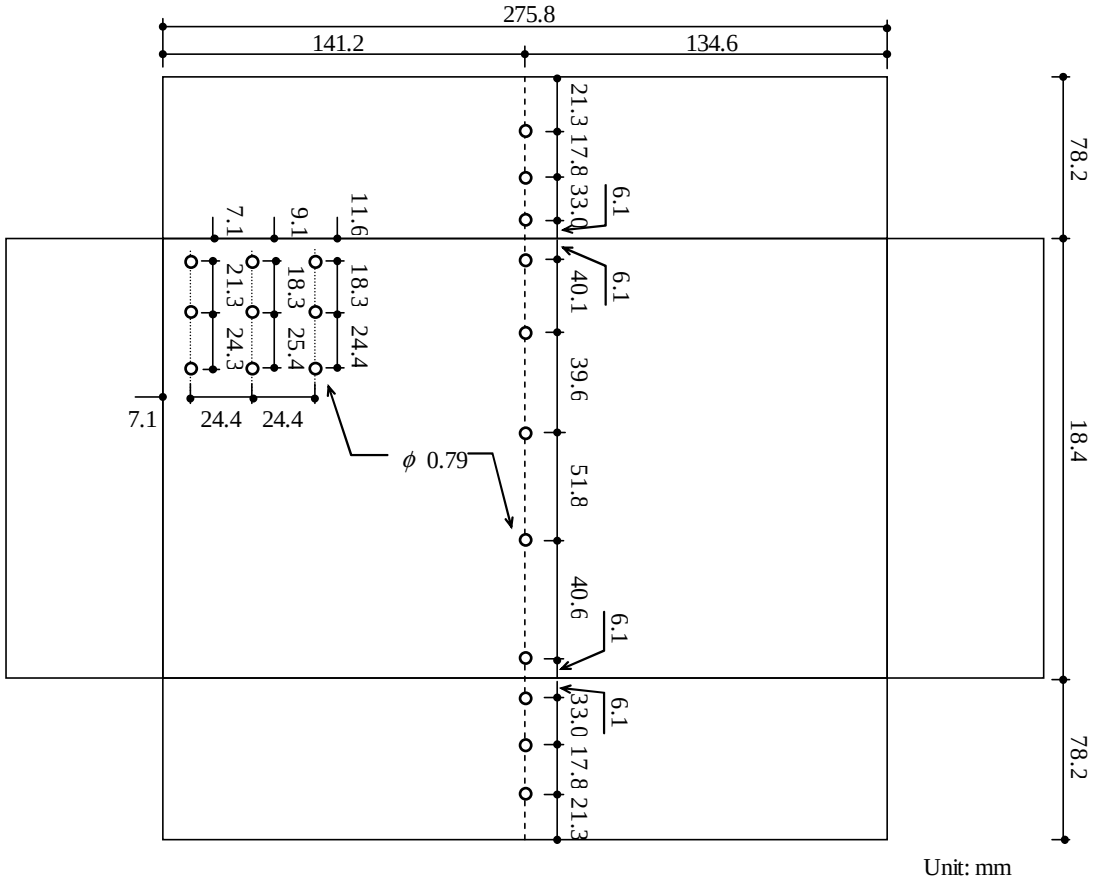

Figure 2.2 Geometry of 1:50 scale model of TTU test building and pressure tap locations

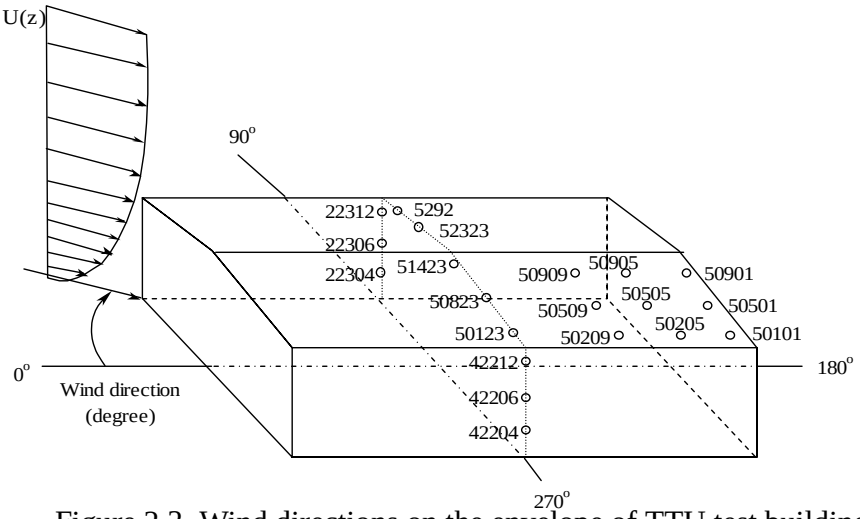

Figure 2.3 Wind directions on the envelope of TTU test building

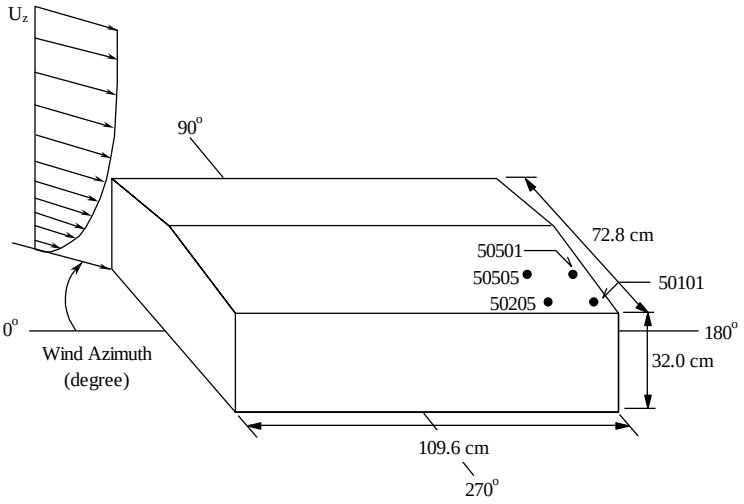

(a) Dimensions of model

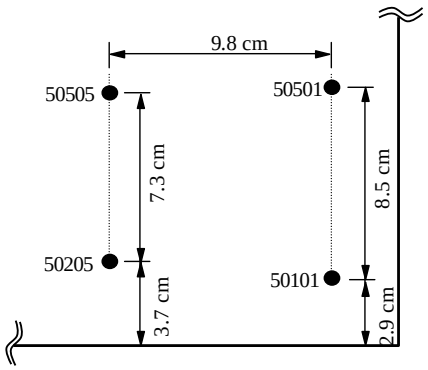

(b) Pressure tap locations

Figure 2.4 Geometry of 1:12.5 scale model of TTU test building and pressure tap locations

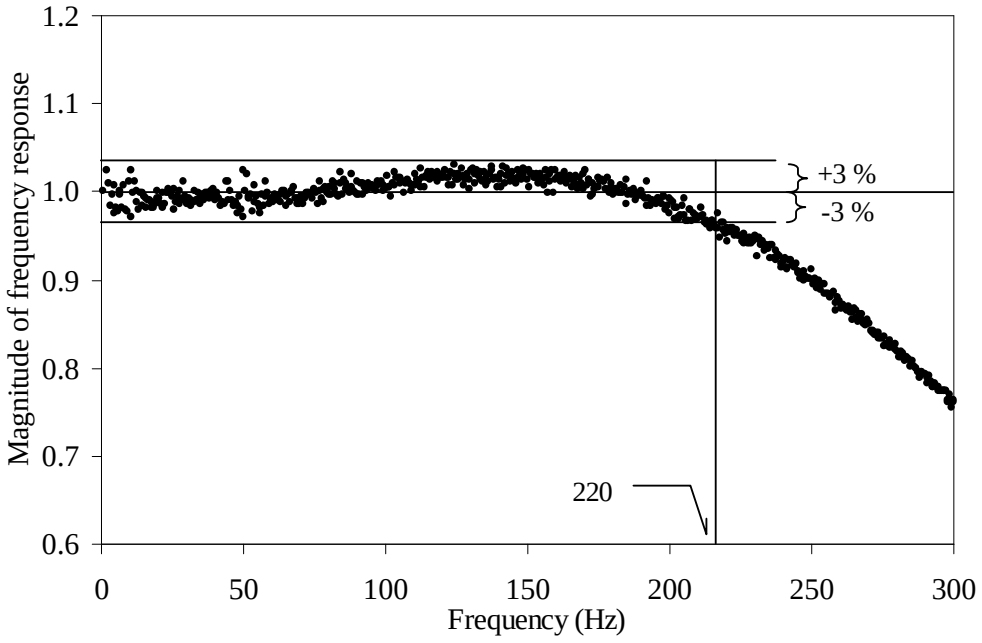

(a) 1:50 scale model of the TTU test building

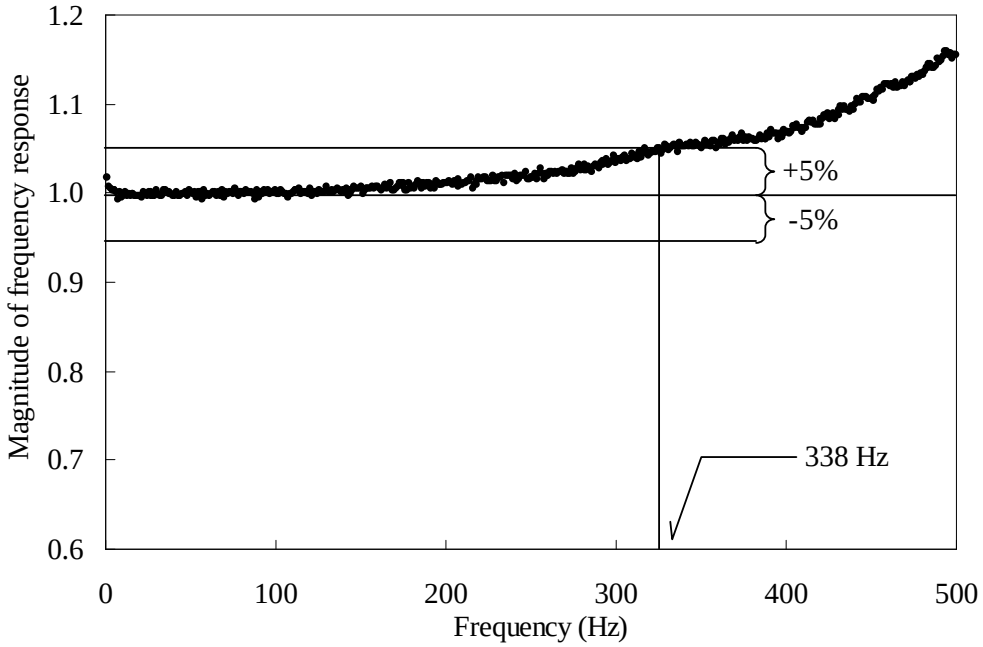

(b) 1:12.5 scale model of the TTU test building

Figure 2.5 Frequency response of pressure measurement tubing system

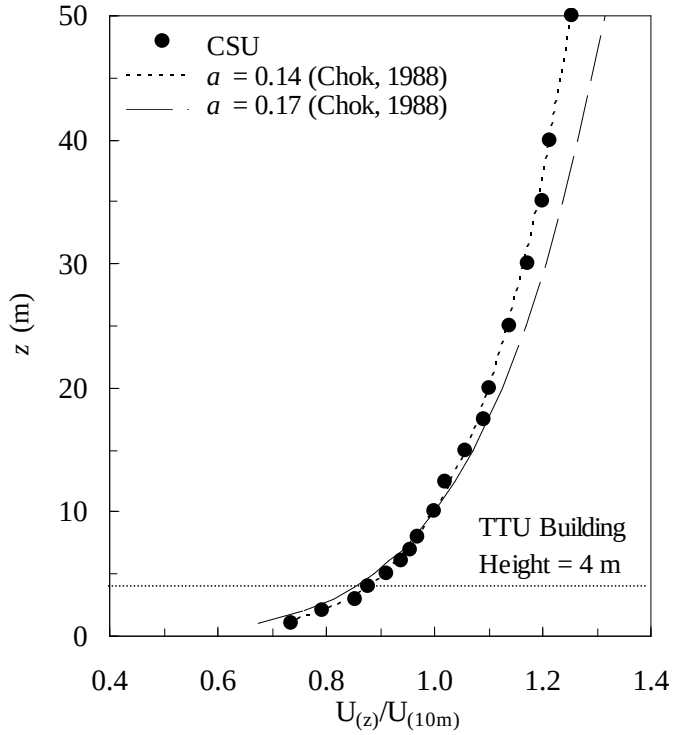

Figure 2.6 Mean velocity profiles

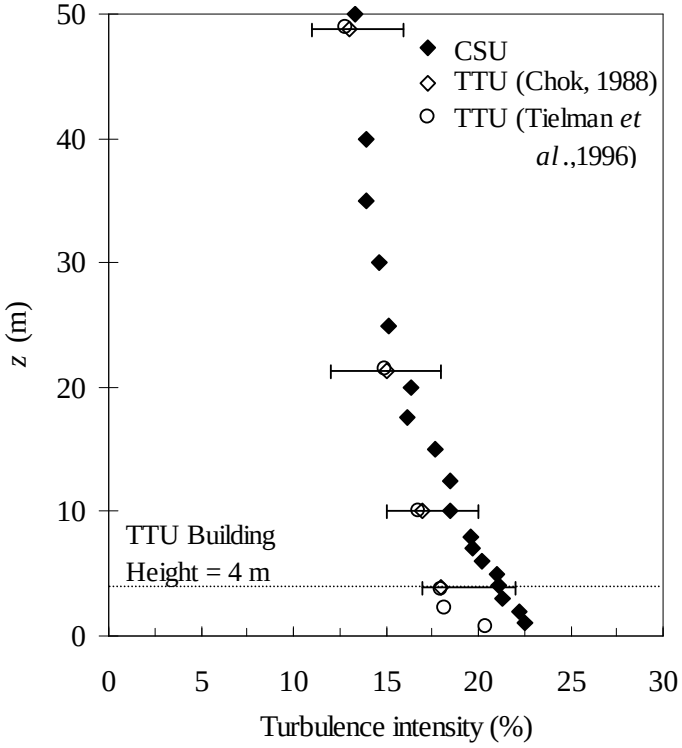

Figure 2.7 Along-wind turbulence intensity profiles

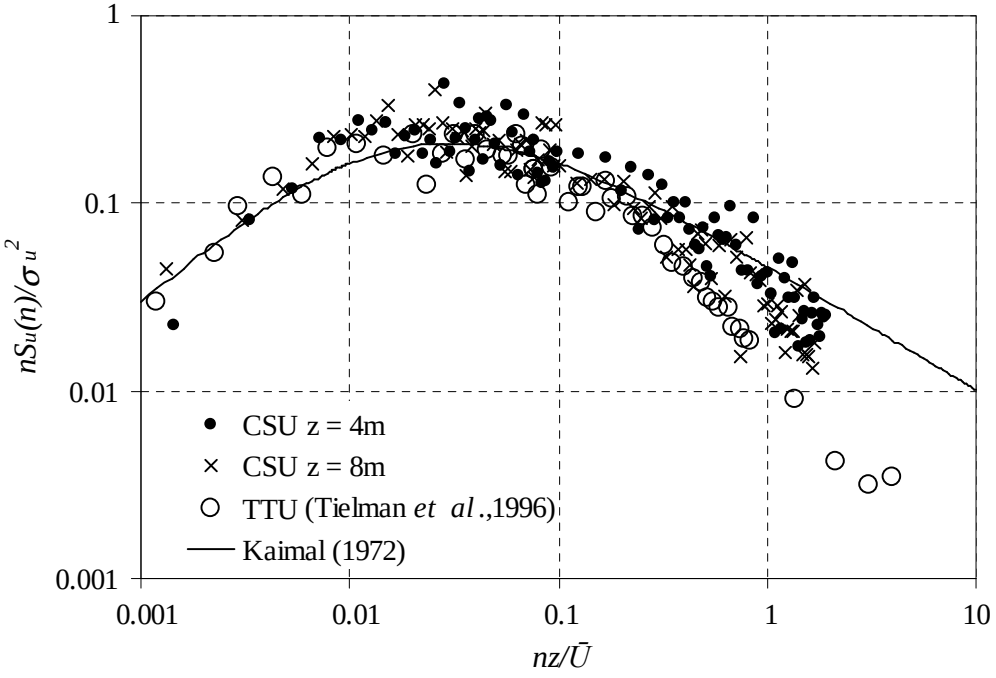

Figure 2.8 Along-wind velocity spectra

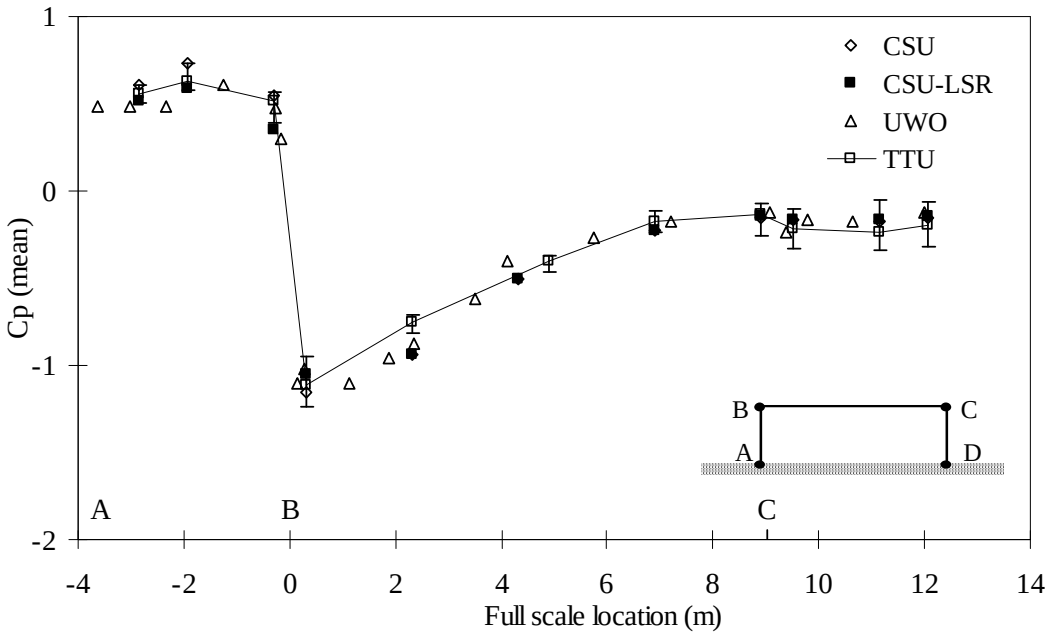

(a) Wind direction θ = 270°

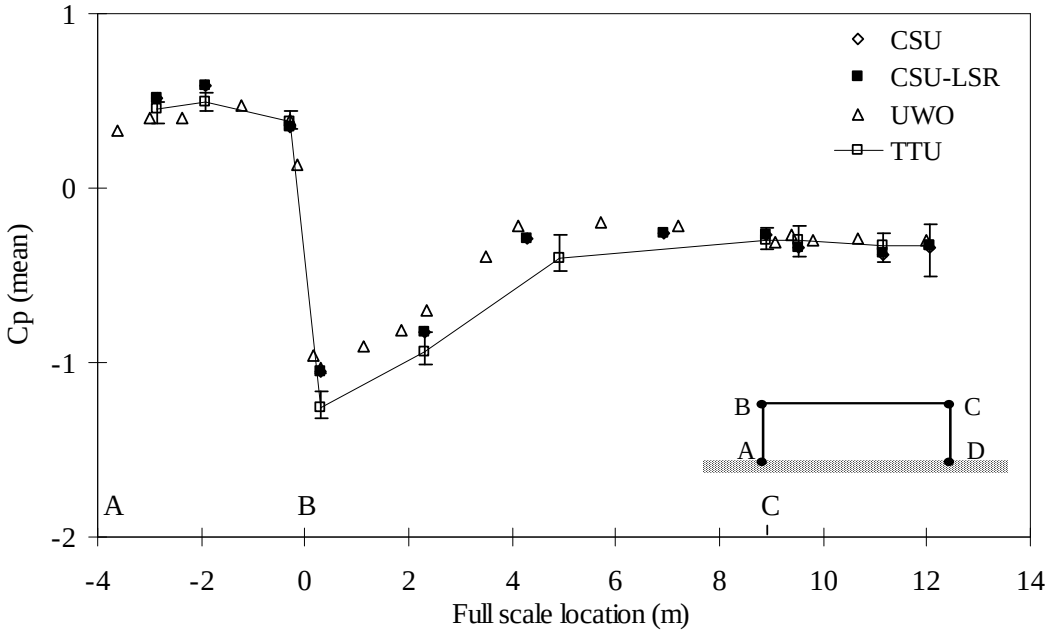

(b) Wind direction θ = 240°

Figure 2.9 Mean pressure at mid-plane locations

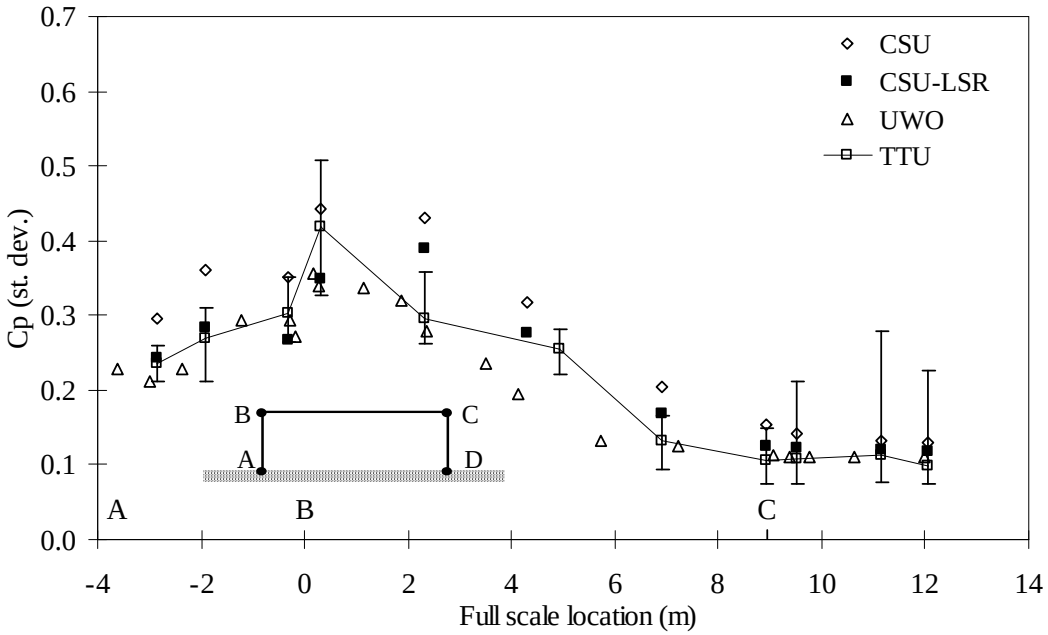

(a) Wind direction $\theta = 270^{o}$

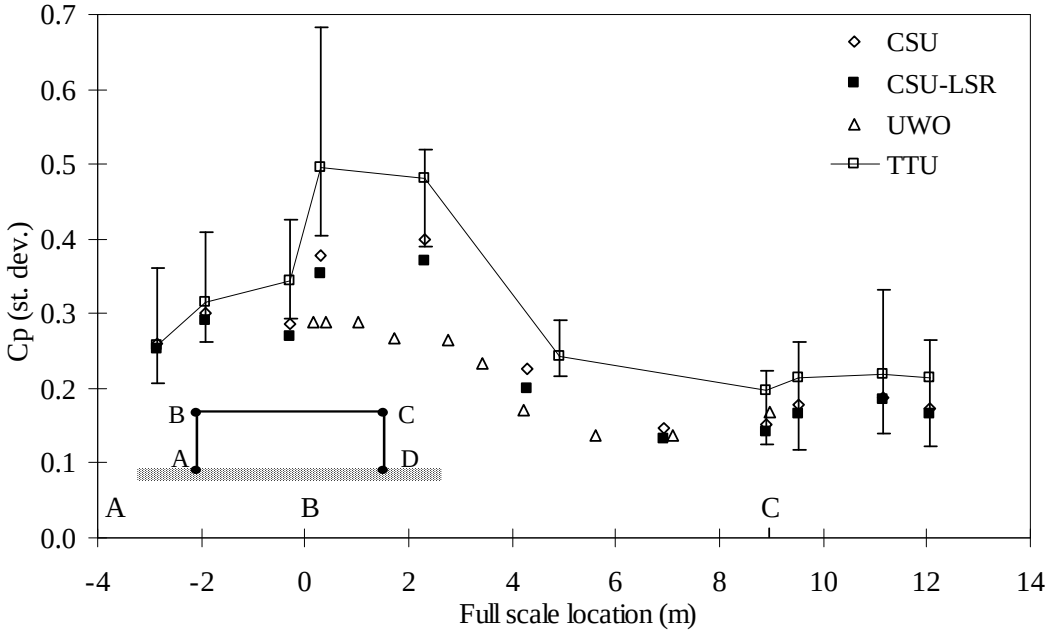

(b) Wind direction $\theta = 240^{o}$

Figure 2.10 Standard deviation of pressure at mid-plane locations

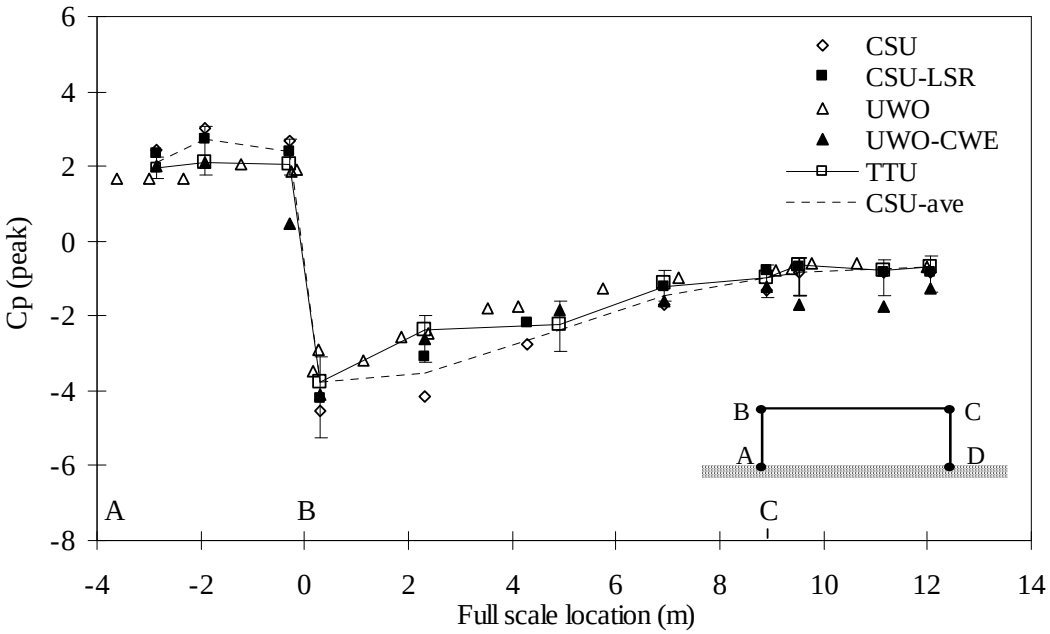

(a) Wind direction θ = 270°

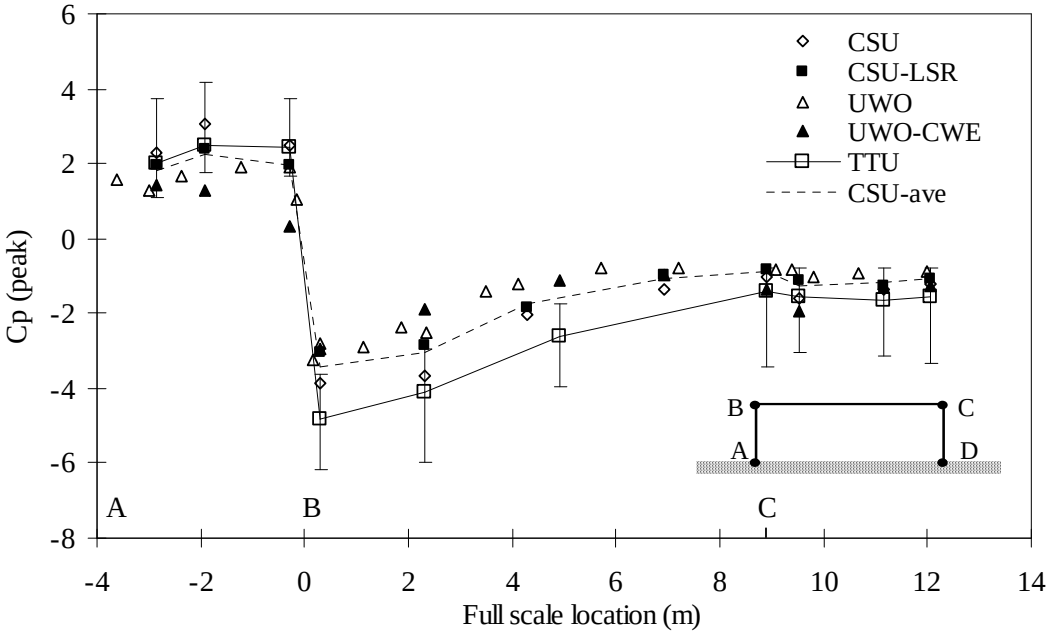

(b) Wind direction θ = 240°

Figure 2.11 Peak pressure at mid-plane locations

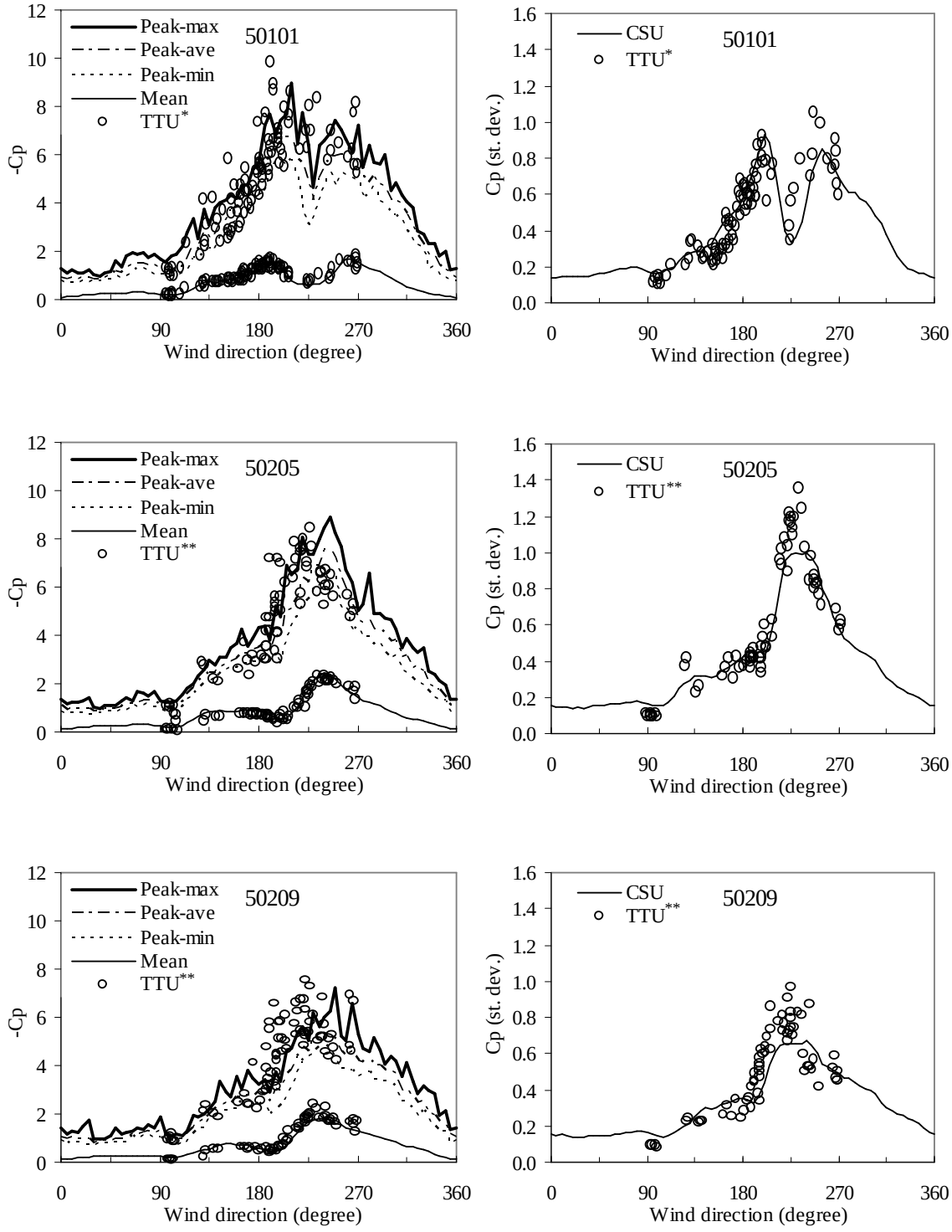

* Data taken from Tieleman *et al*. (1996)
** Data take from Mehta *et al*. (1992)

Figure 2.12 Roof corner pressure

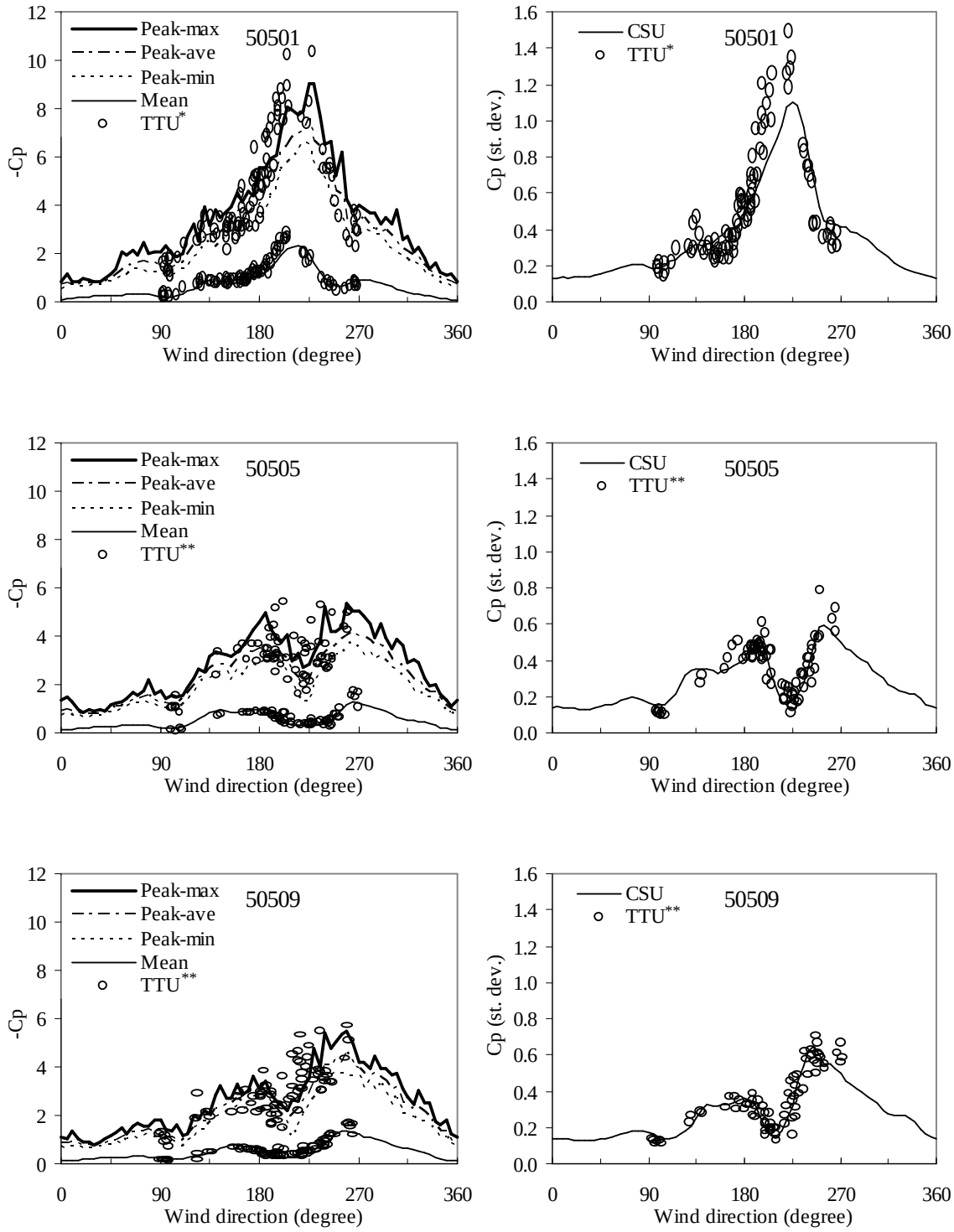

* Data taken from Tieleman *et al*. (1996)
** Data take from Mehta *et al*. (1992)

Figure 2.12 Continued

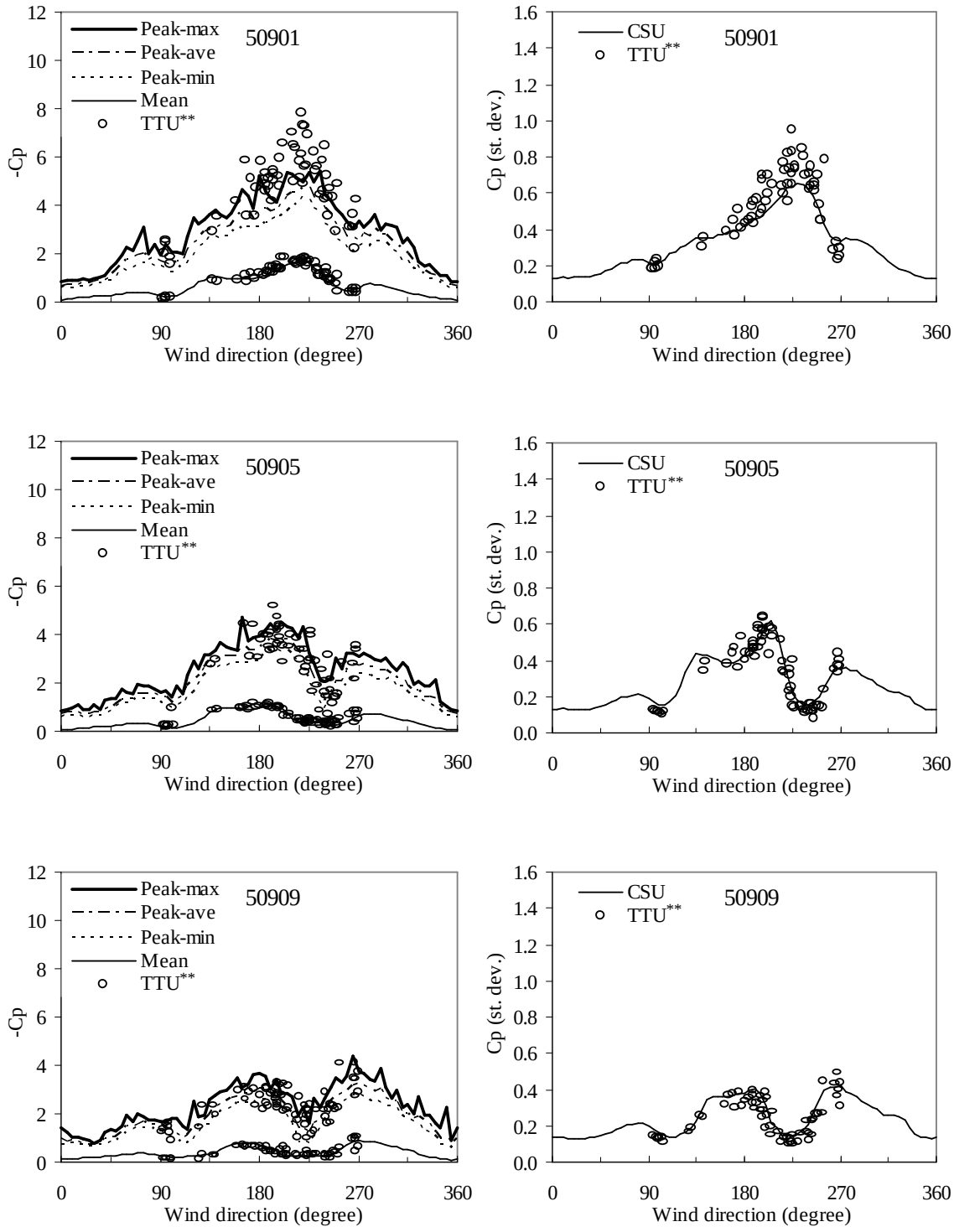

* Data taken from Tieleman *et al*. (1996)
** Data taken from Mehta *et al*. (1992)

Figure 2.12 Continued

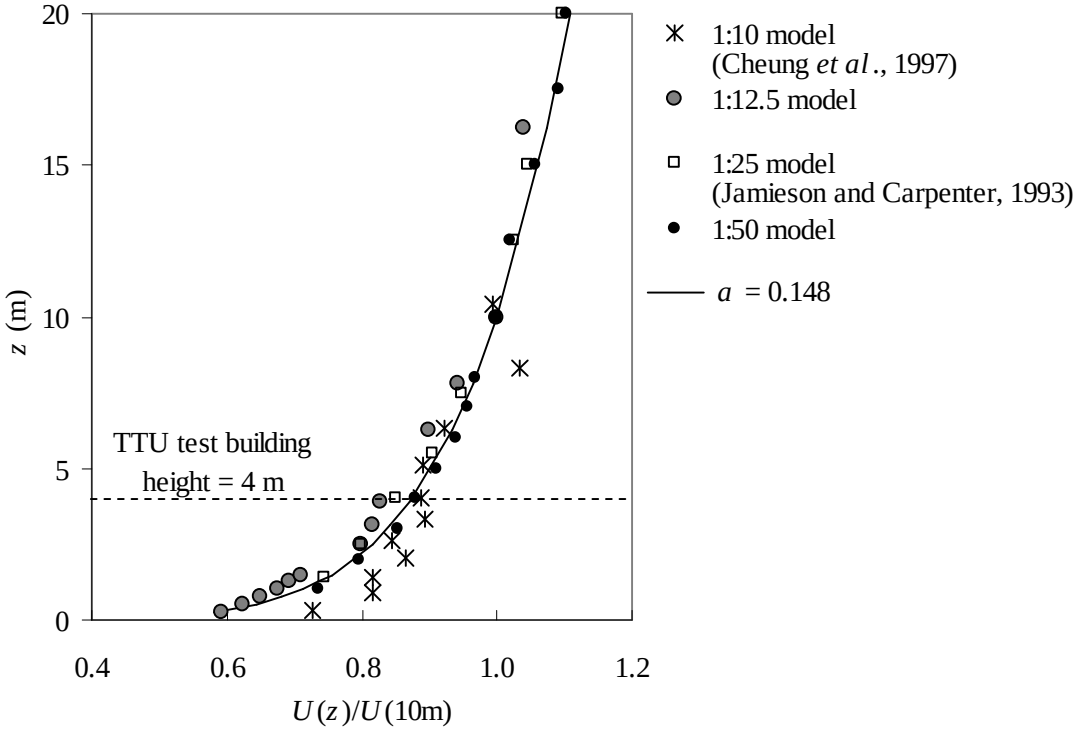

Figure 2.13 Mean velocity profiles

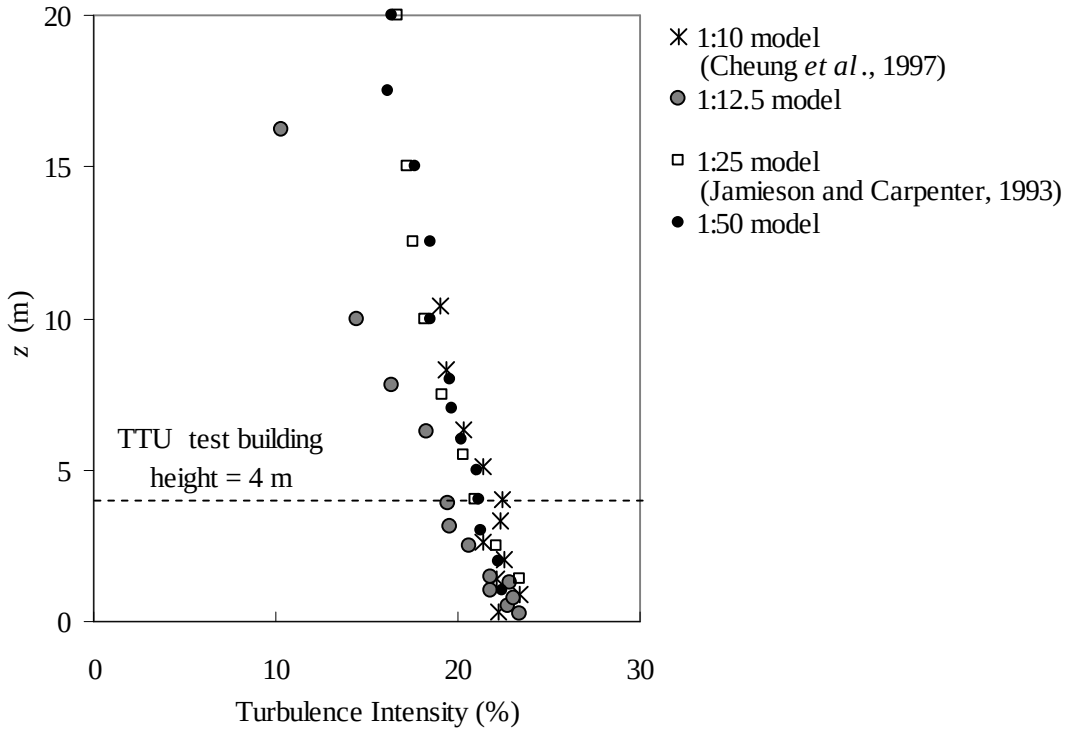

Figure 2.14 Along-wind turbulence intensity profiles

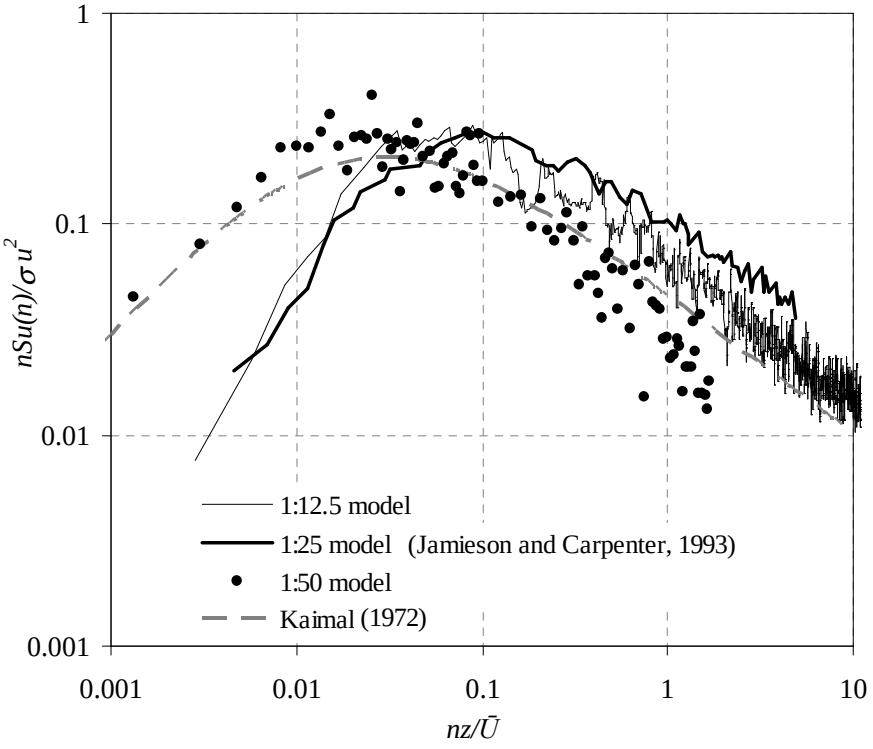

Figure 2.15 Along-wind velocity spectra

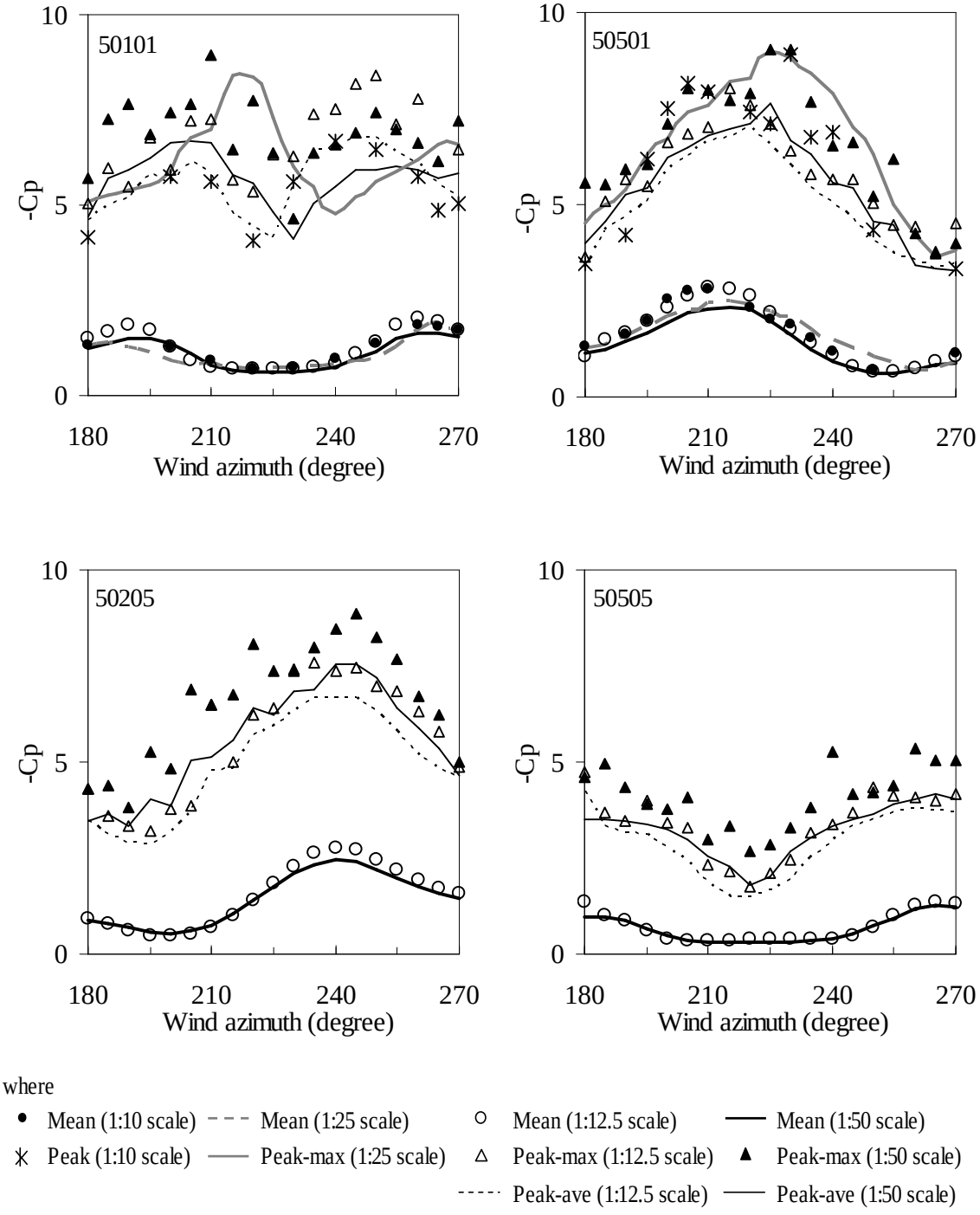

Figure 2.16 Mean and peak suction pressures

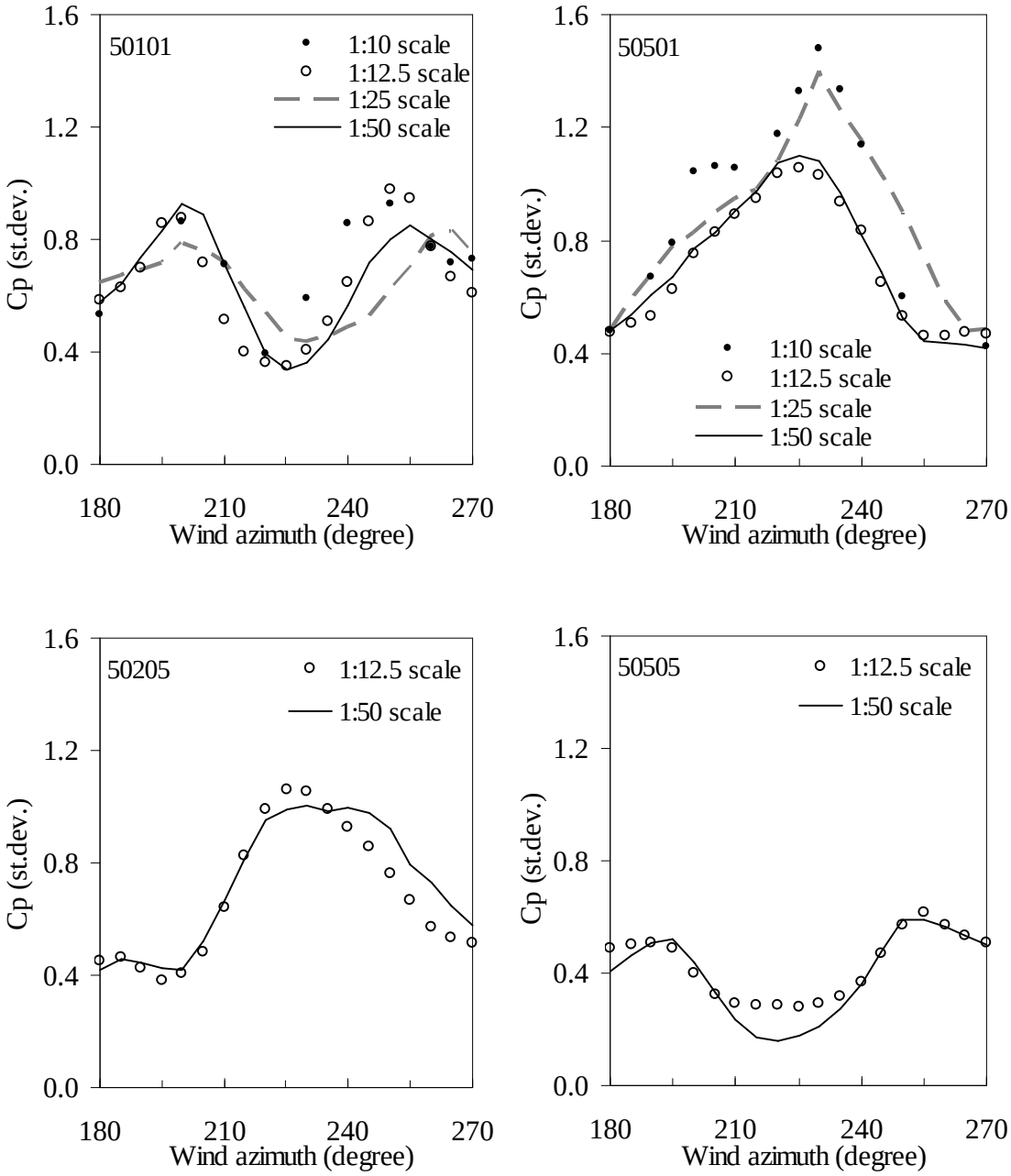

Figure 2.17 Standard deviation of pressures

CHAPTER 3

PREDICTION AND VALIDATION OF EXTREME WIND-INDUCED PEAK PRESSURE

Some of the material presented in this chapter has been extracted from the following reference

Endo, M., Bienkiewicz, B. and Ham, H.J. (2006), "Wind-tunnel investigation of point pressure on TTU test building", Journal of Wind Engineering and Industrial Aerodynamics, Vol. 94, pp. 553-578.

3.1 INTRODUCTION

Extremes of environmental loads such as wind-induced pressures and loads corresponding to small probability of exceedance are commonly required in order to provide reliable structural designs. Two estimation methods that have been used in such applications for prediction of extremes, are discussed in this chapter: (1) generalized extreme value distributions (GEV) and (2) peaks-over-threshold (POT) based on the generalized Pareto distributions (GPD).

The difference between these two approaches is schematically presented in Figure 3.1. A sample of time records of the pressure coefficients (C_p) is displayed in the figure. The first method (GEV) considers the maxima of C_p extracted from successive time records. In Figure 3a, the pressure coefficients C_{p2}, C_{p9}, C_{p16} and C_{p19} are the peak values extracted from the four records. They represent the extreme events, also called block maxima. The second method (POT) focuses on the observations which exceed a given

threshold. For instance, the observations C_{p1}, C_{p2}, $C_{p9,}$ $C_{p10,}$ C_{p18} and C_{p19} in Figure 3.1b exceed the threshold *u* and they represent a set of the extreme events.

The GEV method is based on analysis of the largest (or smallest) values identified in each of the considered data records. In wind engineering practice, this technique has been applied for prediction of extreme wind speeds, using the observations of annual maximum wind speeds, Gomes and Vickery (1978), Harris (2001), Cook *et al*. (2003) and others. The POT method has also been used in such analyses, Holmes and Moriarty (1999), Lechner *et al*. (1992), and Simiu and Heckert (1996), and others. Its advantage over the GEV method is that it allows for analysis of an entire time series. Thus the size of the subset data suitable for this analysis is typically larger than the population of the peak values extracted for GEV analysis.

Rigorous extreme value analysis of local pressures on buildings has been reported by a limited number of researchers, Cook and Mayne (1979), Peterka (1983), Holmes (1984), Holmes and Cochran (2003). For predictions of extreme wind speeds, wind speed records of past observations can be obtained from meteorological stations, airports, national climate centers, etc. In the case of extreme wind loading on buildings, the field data records of sufficient length, available in public domain, are limited. Examples of such data (acquired in the U.S.) are field observations of peak pressures reported for the Texas Tech University (TTU) test building (Mehta *et al.*, 1992).

This chapter presents the extreme value analysis of roof corner peak pressures acquired during wind tunnel testing at WEFL at five locations on the models of the TTU test building. The extreme peak pressures were predicted by fitting Type I and III

extreme value distributions. The POT method was also employed in prediction of the extreme peak pressures.

3.2 OVERVIEW OF GENERALIZED EXTREME VALUE APPROACH

The largest of n independent samples, each drawn from the same parent distribution $F(x)$, have a probability distribution $[F(x)]^n$, Harris (2004b). However, the parent distribution is typically unknown or the parent distribution is not well defined in the tail region associated with the extreme values of interest. Various remedies have been developed to overcome these limitations. One of such techniques used in the classical extreme value theory is the method employing the generalized extreme value (GEV) distribution, first proposed by von Mises (1936).

The extreme value distributions of roof corner peak pressures are typically estimated using Type I and III distributions, which are special cases of GEV (Jenkinson, 1955):

$$F(x) = \exp\left\{ -\left[1 - k\left(\frac{x - u}{a} \right) \right]^{\frac{1}{k}} \right\} \qquad [3.1]$$

When shape factor k is positive, the GEV represents the Type III distribution. It becomes the Type I distribution when $k = 0$. As k is reduced to zero, the following asymptotic limit of the GEV, the Type I distribution, is obtained

$$F(x) = \exp\left\{ -\exp\left[-\left(\frac{x - u}{a} \right) \right] \right\} \qquad [3.2]$$

In the above formulas, u and a are location and scale parameters, respectively. The asymptotic limit of x in the Type III fit can be determined from Equation [3.1]

$$x_{\text{limit}} = u + \frac{a}{k} \qquad [3.3]$$

Based on the Type III fit of peak pressures in the roof corner region reported by Holmes and Cochran (2003), the anticipated value of the shape factor is -0.5 < k < 0.5. For such a case, Hosking and Wallis (1997) proposed the following estimations for the Type III fit:

$$k \approx 7.8590c + 2.9554c^2 \qquad [3.4]$$

$$a = \frac{\tilde{\lambda}_2 k}{(1-2^{-k})\ \ \Gamma(1+k)} \qquad [3.5]$$

$$u = \tilde{\lambda}_1 - \frac{a\{1-\Gamma(1+k)\}}{k} \qquad [3.6]$$

$$\text{where} \quad c = \frac{2}{3+\tilde{\tau}_3} - \frac{\log 2}{\log 3} \qquad [3.7]$$

$$\tilde{\tau}_3 = \frac{\tilde{\lambda}_3}{\tilde{\lambda}_2}, \qquad [3.8]$$

$$\tilde{\lambda}_1 = \tilde{\beta}_0, \qquad \tilde{\lambda}_2 = 2\tilde{\beta}_1 - \tilde{\beta}_0, \qquad \tilde{\lambda}_3 = 6\beta_2 - 6\tilde{\beta}_1 + \tilde{\beta}_0, \qquad [3.9]$$

$$\tilde{\beta}_r\left[p_{i,n}\right] = \frac{1}{n}\sum_{i=1}^{n} p_{i,n}^r X_i \qquad [3.10]$$

$$p_{i,n} = \frac{i - a}{n} \quad \text{for } 0 < a < 1 \qquad [3.11]$$

The accuracy of the shape factor k calculated using the above approach is better than 10^{-3} if -0.5 < τ_3 < 0.5. This accuracy can be improved if an alternative, iterative algorithm is employed. In such a case no limit is placed on the value of k. For the Type I fit, the following formulas were employed (Hosking and Wallis, 1997):

$$a = \frac{\tilde{\lambda}_2}{\log 2} \qquad [3.12]$$

$$u = \tilde{\lambda}_1 - a\gamma \quad \text{where } \gamma \text{ is Euler's constant, 0.5772…. .} \qquad [3.13]$$

3.3 OVERVIEW OF PEAK-OVER-THRESHOLD APPROACH

The peaks-over-threshold (POT) method is based on utilizing all peak events in a given time series exceeding a specified threshold. The POT method, which is based on the generalized Pareto distribution (GPD), was first shown by Pickands (1975). The expression for the GPD is:

$$F(x) = 1 - \left(1 + \frac{k(x-u)}{a}\right)^{-1/k} \qquad [3.14]$$

In the above formula, *k*, *u* and *a* are shape, location and scale parameters, respectively. The prediction of the R year return period value X_R can be calculated from:

$$X_R = u + \frac{a[1-(\lambda R)^{-k}]}{k} \qquad [3.15]$$

In Equation [3.15], λ is the number of data points crossing the set of threshold level per year. For the solutions of parameters *k* and *a*, Hosking and Wallis (1997) proposed the following estimations:

$$k = \frac{(\lambda_1 - u)}{\lambda_2} - 2 \qquad [3.16]$$

$$a = (1+k)(\lambda_1 - u) \qquad [3.17]$$

$$\text{where } \tilde{\lambda}_1 = \tilde{\beta}_0, \quad \tilde{\lambda}_2 = 2\tilde{\beta}_1 - \tilde{\beta}_0, \qquad [3.18]$$

$$\tilde{\beta}_r\left[p_{i,n}\right] = \frac{1}{n}\sum_{i=1}^{n} p_{i,n}^{r} X_i \qquad [3.19]$$

$$p_{i,n} = \frac{i - a}{n} \quad \text{for } 0 < a < 1 \qquad [3.20]$$

3.4 ANALYSES AND RESULTS

3.4.1 GEV Analysis

The GEV analysis was performed using roof corner peak pressures acquired from two geometrical scale models of the TTU test building, for a wind direction of 215 ^{o}. Two data sets were used in analysis: (1) 150 peak pressures (from taps 50101, 50501, 50505 and 50901, see Figure 2.2) extracted from 150 records of the data acquired for the 1:50 scale model; and (2) 555 peak pressures (from taps 50101, 50205 and 50501, see Figure 2.5) extracted from 555 records of the data acquired for the 1:12.5 scale model. The sampling conditions of these data were described in Section 2.2.

The extracted peak pressures were used to fit Type I and III extreme value distributions (EVDs). For the estimation of parameters for the EVDs, a computer program, based on the approach described in Section 3.2, was developed using LabView programming software. The user interface of this software is shown in Figure 3.2. To minimize the statistical bias, the reduced variate was based on the plotting position estimator $p_{i:n} = (i - 0.35)/n$ suggested by Hosking *et al*. (1985).

The results of the EVD fits are presented in Figure 3.3 for both cases: 1:50 scale model (taps 50101, 50501, 50505 and 50901) and 1:12.5 scale model (taps 50101, 50205 and 50501). The calculated values of shape *k*, scale *a* and location *u* parameters of the

EVDs are presented in Table 3.1. The asymptotic values of the peak pressures implied by Type III EVD fit, obtained using Equation [3.3], are included in the table.

It can be seen in Figures 3.3a and 3.3b that the peak pressure data for taps 50101 and 50501 are not aligned along a straight line and their trend indicates a good agreement with the Type III fitting, except for a limited number of the peaks. On the other hand, peak pressure data for taps 50205, 50505 and 50901 indicate a nearly perfect (straight-line) matching with the Type I fittings, as seen in Figures 3.3c through 3.3e. As anticipated, values of *k* for taps 50205, 50505 and 50901 are approximately two times smaller than those of taps 50101 and 50101 (except for tap 50501 at the 1:12.5 scale) as seen in Table 3.1. Consequently, the estimated fits for taps 50201, 50505 and 50901 indicate a linear-line distribution since values of *k* are close to zero.

Table 3.1 Parameters of extreme value distributions

Tap	Model scale	Type I		Type III			
		a	*u*	*k*	*a*	*u*	Asymptotic limit of Cp_{peak}
50101	1:50	-0.692	-5.728	0.094	-0.750	-5.759	-13.73
	1:12.5	-0.590	-4.936	0.114	-0.649	-4.968	-10.64
50501	1:50	-0.606	-6.708	0.109	-0.664	-6.740	-12.86
	1:12.5	-0.319	-6.550	0.055	-0.335	-6.558	-12.66
50205	1:12.5	-0.295	-4.776	0.036	-0.305	-4.781	-13.18
50505	1:50	-0.339	-2.106	0.059	-0.357	-2.115	-8.11
50901	1:50	-0.381	-4.330	0.053	-0.400	-4.340	-11.94

Table 3.2 lists the along-wind turbulence intensities at the TTU test building roof height for modeled at CSU laboratory and TTU field site flows. Since the level of along-wind turbulence intensities modeled at CSU was in a range of the TTU field observations, it is reasonable to compare the laboratory and field peak pressures. In this context, the asymptotic limits listed in Table 3.1 are compared in Table 3.3 with the largest (in magnitude) laboratory peak pressures acquired during the studies described in Chapter 2 (CSU laboratory) and with the largest field peak pressures (TTU field site) reported by Mehta *et al*. (1992). It can be seen in Table 3.3 that the TTU field site peaks are bounded by the measured at CSU laboratory peaks and the Type III EVD asymptotic limits of peak pressures determined from the laboratory peak pressures.

Table 3.2 Laboratory and TTU field along-wind turbulence intensity at roof height

CSU laboratory		TTU field site (Mehta *et al*., 1992)	
1:12.5 scale	1:50 scale	Average	Range
19.4 %	21 %	20 %	15 % - 21 %

Table 3.3 Comparison of laboratory (CSU), field (TTU) and Type III EVD asymptotic limits of peak roof corner pressures

	Model scale	50101	50501	50505	50901
Asymptotic limit	1:50 scale	-13.72	-12.86	-8.11	-11.94
	1:12.5 scale	-10.64	-12.66		
TTU field site (Mehta *et al*., 1992)		-9.82	-11.82	-4.09	-7.84
CSU laboratory	1:50 scale	-6.46	-7.74	-3.32	-5.10
	1:12.5 scale	-5.67	-8.02	-2.13	

Next, the validity of the Type III EVD fit was examined. The value of shape parameter k was compared with the minimum value acceptable for such fit, discussed by Harris (2004b):

$$k_{\min} = 1.2346/\sqrt{N} \qquad [3.21]$$

where N is the size of a sample of peak pressures. Equation [3.21] leads to the required $k_{\min}$ = 0.101 for N = 150 peaks and $k_{\min}$ = 0.052 for N = 555 peaks. Based on this condition and the values of k listed in Table 3.1, the Type III EVD fits for taps 50505 and 50901 for the 1:50 scale and tap 50205 for the 1:12.5 scale were rejected, and Type I EVDs were assigned for these locations. The Type III EVD fit was tentatively retained for the remaining two taps, 50101 and 50501.

The convergences of the Type I EVD fits, as well as the corresponding parameters (scale a and location u), were then examined for samples of an increasing size, ranging from 10 through 150 peaks (1:50 scale model) and through 555 peaks (1:12.5 scale model). Figure 3.4 presents the variations of estimated values of a and u with as functions of the sample size. As seen in the figure, the estimated values of a and u become stable as the sample reaches moderate size – approximately 30 to 50 peaks – for most of the considered five taps. The convergences of the Type I EVD fits are evaluated in Figure 3.5. Except for 1:12.5 scale of tap 50501, fast convergence to the Type I EVD is reached when a sample of moderate size – 20 peaks – is used for all considered taps. The use of a small sample size, 10 peaks for example, to fit to the Type I EVD shows very poor convergence for all the taps.

Similarly the convergences of parameters for Type III EVD fits were examined for taps 50101 and 50501, where the constraint condition imposed by Eq, [3.21] was

satisfied. Figure 3.6 compares the estimated shape *k*, scale *a* and location *u* parameters with an increase in the sample size. In the figure, overall estimated parameters *a* and *u* of the Type III EVDs also indicate fast convergence of those two parameters observed for the Type I EVDs (see Figure 3.4). However, the estimated values of *k* show noticeably unstable behavior for a wide range of the sample sizes. An approximate sample size of 400 peaks is required to ensure stability of the estimated *k*, for the 1:12.5 scale model. In the case of the maximum sample size of 150 peaks (1:50 scale model), estimated parameter *k* has not yet become fully stable.

In Figures 3.7 and 3.8, convergences of the Type III EVD fits are examined for two types of plotting: reduced variate vs. peak pressure (left graphs) and peak pressure vs. probability of exceedance (right graphs), with different sample sizes, for taps 50101 and 50501, respectively. Very good predictions can be made for peaks up to the reduced variate of 2 in the left graphs, or probability of exceedance (POE) of 0.1 for the graphs on the right, for sample sizes equal to/exceeding 50, for both the 1:50 and 1:12.5 scale models at these two taps. This was the result of the fast convergence of parameters *a* and *u*, as seen in Figure 3.6. On the other hand, the overall tail behavior (reduced variate larger than 2 in left graphs or POE lower than 0.1 in right graphs) of predicted Type III EVDs are variable over the different sample sizes at these taps. The shape parameter *k* generally governs the tail behavior of Type III EVD, especially in a range of very small POE. The results for tap 50501 (1:12.5 scale), shown in Figure 3.8 seem to suggest approximate convergence when the sample exceeds 200 peaks. In the case of tap 50101 (1:12.5 scale) approximate convergence is reached when the sample size is greater than 400 peaks. Relatively faster convergence observed in tap 50501 can be attributed, in part,

to a very small (close to zero) value of *k*. As described in Section 3.2, when the shape factor *k* is equal to zero, GEV distribution becomes the Type I distribution. Additionally, slower convergence observed in tap 50101 may be due to the close proximity of this tap to the vertex. The considered sample (of peak pressures) is of a mixed-population type, resulting from various physical phenomena occurring at this location.

In contrast, a lack of convergence is exhibited at those two taps for the 1:50 scale model due to lack of stability in estimated *k* using the limited number of sample size (150 peaks) as observed in Figure 3.7. It should be pointed out that the sample size of 150 is relatively small (Harris (2004a and 2004b), Kasperski (2003 and 2004), and others) and its use in fitting Type III EVD is expected to lead to a certain level of approximation. Further studies are desired to investigate these issues, in the context of tolerance levels acceptable for specific wind engineering applications.

In view of the above limitations, Type I EVD has been ultimately selected as a conservative predictor of the extreme peak pressures investigated in the present study. The values of the mode and parameters of the Type I EVD, listed in Table 3.1, were used to calculate the average largest 15-min (full-scale) peak pressure, $\overline{C}_{p(peak)} = u + \gamma a$, where $\gamma = 0.5772\ldots$ is the Euler's constant. The POE, $P(>\overline{C}_{p(peak)})$, implied by the Type I EVD fit, is included in Table 3.4. In addition, the average $\overline{C}_{p(peak)10seg}$ and largest $C_{p(peak)10seg}$ peak pressures extracted from 10 segments of the pressure time series (presented in Figure 2.12 for the 1:50 scale model and Figure 2.16 for the 1:12.5 scale model) and the associated POE $P(>\overline{C}_{p(peak)10seg})$ and $P(>C_{p(peak)10seg})$ are listed in the table.

Table 3.4 Extreme predicted and laboratory peak pressures and exceedence probabilities

Tap	50101		50501		50205	50505	50901
Model scale	1:50	1:12.5	1:50	1:12.5	1:12.5	1:50	1:50
$\overline{C}_{p(peak)}$	-6.13	-5.28	-7.06	-6.73	-4.95	-2.30	-4.55
$P(> \overline{C}_{p(peak)})$				0.43			
$\overline{C}_{p(peak)\ 10seg}$	-5.78	-4.80	-6.99	-6.77	-4.91	-2.27	-4.50
$P(> \overline{C}_{p(peak)\ 10seg})$	0.607	0.717	0.466	0.394	0.476	0.456	0.475
$C_{p(peak)\ 10seg}$	-6.46	-5.67	-7.74	-8.02	-5.01	-3.32	-5.10
$P(> C_{p(peak)\ 10seg})$	0.295	0.250	0.168	0.010	0.367	0.028	0.124

It can be seen that for four pressure taps (50501, 50205, 50505 and 50901), the POE $P(> \overline{C}_{p(peak)10seg})$ is approximately equal and differs by less than 11% from the POE $P(> \overline{C}_{p(peak)})$ determined from the Type I EVD fit. For the location in the roof vertex zone (tap 50101), this discrepancy is significantly higher – approximately 40% and 65% for the 1:50 and 1:12.5 scale models, respectively. Also provided in this table is information on the range of the POE $P(> C_{p(peak)10seg})$ for the largest peak $C_{p(peak)10seg}$ extracted from 10 segments of the pressure time series. As expected, variation of these probabilities is relatively large. Overall, although the POE of the average of the 10 largest peaks appears to have a consistent POE, the need for consistent (with respect to the exceedence probability) largest peaks mandates the use of EVD fit. The above findings provide quantitative evidence in support of the reported wind engineering practice, e.g. Koop *et al*. (2005), in which a limited number of peaks is used to fit Type I EVD.

3.4.2 POT Analysis

The peaks-over-threshold approach using the generalized Pareto distribution (GPD) was applied for the prediction of the extreme roof corner pressures acquired from the 1:12.5 geometrical scale models of the TTU test building for a wind direction of 215°. A total of 555 records of pressure time series acquired at taps 50101 and 50501 (see Figure 2.5) was employed in this analysis. Sampling conditions of these pressure data are described in Section 2.2. For the estimation of parameters for the GPDs and predictions of extreme peaks, a computer program based on the approach described in Section 3.3 was developed using LabView programming software (see Figure 3.9).

The characteristics of probability distributions by means of the 3rd- and 4th-order L-moment variables, L-skewness τ_3 and L-kurtosis τ_4, for time series of pressure coefficient Cp were computed for decreasing values of the threshold u_0 and a decrement of 0.05. To reduce computational time, the calculation was performed starting from u_0 = -1 for tap 50101 and u_0 = -2 for tap 50501. Values of τ_3 and τ_4 were calculated using the following equation (Hosking and Wallis, 1997):

$$\tilde{\tau}_r = \frac{\tilde{\lambda}_r}{\tilde{\lambda}_2} \qquad r = 3,4,..... \qquad [3.22]$$

$$\text{where } \tilde{\lambda}_r = \sum_{k=0}^{r} p^*_{r.k} \beta_k$$

The results - the τ_3-τ_4 relationship - are shown in Figure 3.10, as determined from the Cp time series (denoted Data) and the generalized Pareto distribution (GPD) fitted to the Cp time series (denoted Fit) for taps 50101 and 50501. In the figure, traces of τ_3-τ_4 relationships of GPD (denoted GPD) and the exponential distribution are included.

Those traces were computed using polynomial approximations proposed by Hosking and Wallis (1997) as follows:

$$\tau_4 = \frac{\tau_3(1+5\tau_3)}{5+\tau_3} \qquad [3.23]$$

In the figure, τ_3-τ_4 scatter of Data is gradually approaching the GPD trace line with decrease in u_0 and a good agreement is seen with the GPD trace line between τ_3 = 0.28 and 0.38 for tap 50101 and τ_3 = 0.25 and 0.32 for tap 50501.

Next, shape parameter *k* was determined using Equations [3.16] through [3.20]. The extreme roof corner pressure $C_{p,R}$ for 100-, 1000-, 10000- and 100000-record (segment) return periods was also predicted using Equation [3.15]. In Figure 3.11, the estimated value of *k* and extreme pressures are plotted with a decrease in u_0 in Figure 3.11 for taps 50101 and 50501. Plots of estimated *k* values show a strong variation in higher thresholds (less than Cp = -7) for both pressure taps. A similar trend was observed in the predicted values of $C_{p,R}$ for the specified return periods, as seen in the figure. This strong variation was affected by the decreasing values of u_0 and consequently decreasing number of samples used for the GPD fit.

Due to the sensitivity of parameter *k* to the threshold value u_0, it is important to select the appropriate threshold for the estimation of parameter *k*. Using the established τ_3-τ_4 relationship shown in Figure 3.10, fit errors of τ_3 and τ_4 were computed for Fit with respect to Data. In this analysis, those errors were limited to less than 2% for the determination of parameter *k*. Figures 3.12 and 3.13 show the τ_3-τ_4 scatter of restricted Fit data having less than 2% errors (denoted Data-2% error) and those associated parameter *k* and extreme peaks $C_{p,R}$ for taps 50101 and 50501, respectively.

As expected, values of τ_3 and τ_4 restricted with such small error provide an appropriate range of the threshold values where the parent distribution of data indicates the close convergence to a GPD model for both taps 50101 and 50501. The estimated values of parameter *k* indicate stable behavior in the restricted range. A similar trend was exhibited for predicted values of $Cp,_R$ for the specified return periods in those figures. The estimated values of parameter *k* and predicted values of $Cp,_R$ for the specified return periods for the selected highest threshold in magnitude are presented in Table 3.5.

The results of predicted $Cp,_R$, as listed in Table 3.5, are next compared with Type I and Type III EVD approaches. The prediction of the R-year return period value $Cp,_R$ for EVDs can be obtained from

$$Cp,_R = u - a\log\left[-\log\left(1-\frac{1}{R}\right)\right] \qquad \text{for Type I EVD} \qquad [3.24]$$

$$Cp,_R = u - \frac{a}{k}\left\{1-\left[-\log\left(1-\frac{1}{R}\right)\right]^{-k}\right\} \qquad \text{for Type III EVD} \qquad [3.25]$$

Table 3.5 Parameter *k* for generalized Pareto distributions and predicted $Cp,_R$

Tap	Highest threshold u_0	*k*	$Cp,_R$			
			10^2 segments	10^3 segments	10^4 segments	10^5 segments
50101	-4.25	0.082	-7.35	-8.11	-8.74	-9.26
50501	-6.35	0.033	-8.01	-8.55	-9.05	-9.51

Table 3.6 lists the extreme roof corner pressures $Cp,_R$ of 1000-, 10000- and 100000-record (segment) return periods for POT (GPD) and GEVs (type I and type III) for taps

50101 and 50501. In the table, the level of discrepancy with respect to $Cp,_R$ for GPD is also included.

It is interesting to note that $Cp,_R$ estimated from GPD indicates a good agreement with Type III EVD for tap 50101, while tap 50501 shows a relatively close agreement between GPD and Type I EVD. Predictions of $Cp,_R$ are strongly influenced by shape parameters *k* for type III EVD/GPD, which determine the characteristics of the upper tail of those distributions (in a range of small POE). As expected, comparing values of *k* between GPD and Type III EVD for tap 50101, the estimated values were very similar (0.082 for GPD and 0.094 for Type III EVD). In contrast, for tap 50501, the estimated value of parameter *k* for GPD is very close to zero (k = 0.033), as seen in Table 3.5. When k = 0, the GPD becomes an exponential distribution which has an exponential tail similar to the tail of Type I EVD. This is also implied that values of τ_3 and τ_4 for Data-2% error were very close to those of the exponential distribution, as seen in Figure 3.13.

Table 3.6 Predicted extreme roof corner pressure $Cp,_R$ from GPD and GEV analyses

Number of segments	Tap 50101			Tap 50501		
	GPD	GEV Type I	GEV Type III	GPD	GEV Type I	GEV Type III
1000	-8.11	-9.01 (-11.2 %)	-7.21 (11.1 %)	-8.55	-8.75 (-2.4 %)	-5.62 (34.2 %)
10000	-8.74	-10.37 (-18.7 %)	-8.21 (6.0 %)	-9.05	-9.49 (-4.9 %)	-7.02 (22.4 %)
100000	-9.26	-11.73 (-26.7 %)	-8.87 (4.2 %)	-9.51	-10.22 (-7.5 %)	-8.03 (15.5 %)

where ( ) indicate the discrepancy between GPD and GEVs with respect to Cp,R for GPD.

3.5 CONCLUSIONS

The findings of this study can be summarized as follows:

1. In the GEV analysis, the field largest (in magnitude) roof peak pressures were found to be bounded by the laboratory peak pressures (lower bound) and by the asymptotic limits of the peak pressures implied by the Type III extreme value fit (upper bound).
2. Rapid convergence and other attributes make the Type I EVD the fit of choice for extreme roof corner pressures. It was found that the convergence to the Type I EVD was reached when a sample of a moderate size -20 peaks- was used, for the taps considered.
3. The Type III EVD fit indicated a much slower convergence than the Type I EVD fit. The degree of convergence depended on tap locations.
4. In the POT analysis, estimated values of parameter *k* and predicted values of extreme pressures for specified return periods showed a strong variation in the region of higher thresholds.
5. Restrictions placed on characteristic parameters led to the stable estimation of parameter *k* and extreme roof corner pressures predictions for specified return periods.
6. It was found that the predictions of extreme roof corner pressure resulting from use of GEV Type I/Type III and GPD fits were very close.

3.6 REFERENCES

Cook, N.J., Harris, R.I., and Whiting, R. (2003), "Extreme wind speeds in mixed climates revisited," *J. Wind Eng. Ind. Aerodyn*., Vol. 91, pp. 403-422.

Cook, N.J. and Mayne, J.R. (1979), "A novel working approach to the assessment of wind loads for equivalent static design," *J. Wind Eng. Ind. Aerodyn.*, Vol. 4, pp. 149-164.

Gomes, L., Vickery, B.J. (1978), "Extreme wind speeds in mixed climates," *J. Wind Eng. Ind. Aerodyn*., Vol. 2, pp. 331-344.

Harris, R.I. (2004a), Discussion of "Specification of the design wind load based on wind tunnel experiments," [*J. Wind Eng. Ind. Aerodyn*. 91 (2003) 527-541], *J. Wind Eng. Ind. Aerodyn*., Vol. 92, pp. 71-76.

Harris, R.I. (2004b), "Extreme value analysis of epoch maxima – convergence, and choice of asymptote," *J. Wind Eng. Ind. Aerodyn*., Vol. 92, pp. 897-918.

Harris, R.I. (2001), "The accuracy of design values predicted from extreme value analysis," *J. Wind Eng. Ind. Aerodyn*., Vol. 89, pp. 153-164.

Holmes, J.D. (1984), "Effect of frequency response on peak pressure measurements," *J. Wind Eng. Ind. Aerodyn*., Vol. 17, pp. 1-9.

Holmes, J.D. and Cochran, L.S. (2003), "Probability distribution of extreme pressure coefficients," *J. Wind Eng. Ind. Aerodyn*., Vol. 91, pp. 893-901.

Holmes, J.D. and Moriarty, W.W. (1999), "Application of the generalized Pareto distribution to extreme value analysis in wind engineering," J. *Wind Eng. Ind. Aerodyn*., Vol. 83, pp. 1-10.

Hosking, J.R.M. (1990), "L-moments: analysis and estimation of distributions using linear combinations of order statistics," *Journal of the Royal Statistical Society*, Series B, Vol. 52, No. 1, pp. 105-124.

Hosking, J.R.M. and Wallis, J.R. (1997), *Regional frequency analysis*, Cambridge University Press.

Hosking, J.R.M., Wallis, J.R., and Wood, E.F. (1985), "Estimation of the generalized extreme-value distribution by the method of probability-weighted moments," *Technometrics*, Vol. 27, pp. 251-261.

Jenkinson, A.F. (1955), "The frequency distribution of the annual maximum (or Minimum) of meteorological elements," *Quarterly Journal of the Royal Meteorological Society*, Vol. 81, pp. 158-171.

Kopp, G.A., Surry, D. and Mans, C. (2005), "Wind effects of parapets on low buildings: Part1. Basic aerodynamics and local loads," *J. Wind Eng. Ind. Aerodyn*., Vol. 93, pp. 817-841.

Kasperski, M. (2003), "Specification of the design wind load based on wind tunnel experiments," *J. Wind Eng. Ind. Aerodyn*., Vol. 91, pp. 527-541.

Kasperski, M. (2004), Reply to discussion of "Specification of the design wind load based on wind tunnel experiments," [*J. Wind Eng. Ind. Aerodyn*., Vol. 91 (2003) pp. 527-541], *J. Wind Eng. Ind. Aerodyn*., Vol. 92, pp. 781-785.

Lechner, J.A., Leigh, S.D., and Simiu, E. (1992), "Recent approaches to extreme value estimation with application to wind speeds. Part 1: the Pickands method," *J. Wind Eng. Ind. Aerodyn*., Vol. 41, pp. 509-519.

Mehta, K.C., Levitan, M.L., Iverson, R.E., and McDonald, J.R. (1992), "Roof corner pressures measured in the field on a low building," *J. Wind Eng. Ind. Aerodyn*., Vol. 41-44, pp. 181-192.

Peterka, J.A. (1983), "Slelction of local peak pressure coefficients for wind tunnel studies of buildings," *J. Wind Eng. Ind. Aerodyn*., Vol. 13, pp. 477-488.

Pickands, J. (1975), "Statistical inference using extreme order statistics," *Ann. Statist*., Vol. 3, pp. 119-131.

Simiu, E. and Heckert, N.A. (1996), "Extreme wind distribution tails: a peaks over threshold approach," *J. Struct. Eng*., Vol. 122, pp. 539-547.

von Mises, R. (1936), "La distribution de la plus grande de n valeurs." Reprinted in *Selected Papers Volumen II, American Mathematical Society,* Providence, R.I., 1954, pp. 271-294.

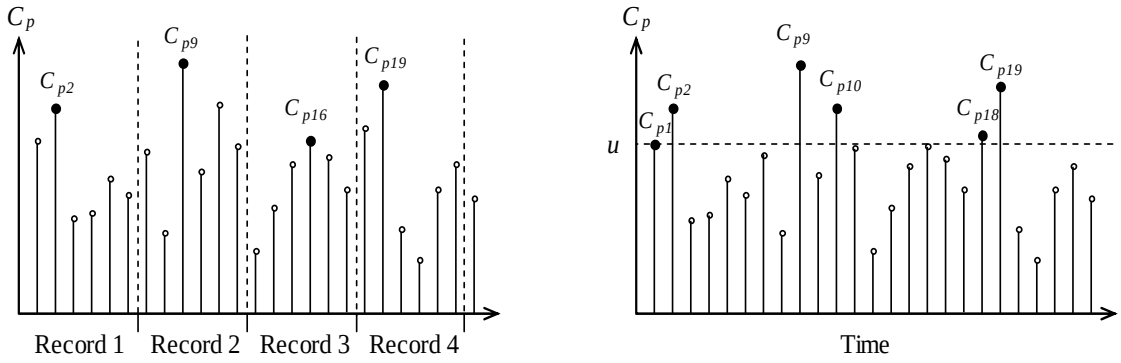

(a) Extreme value analysis (b) Peak-over-threshold method

Figure 3.1 Type of extreme event analysis

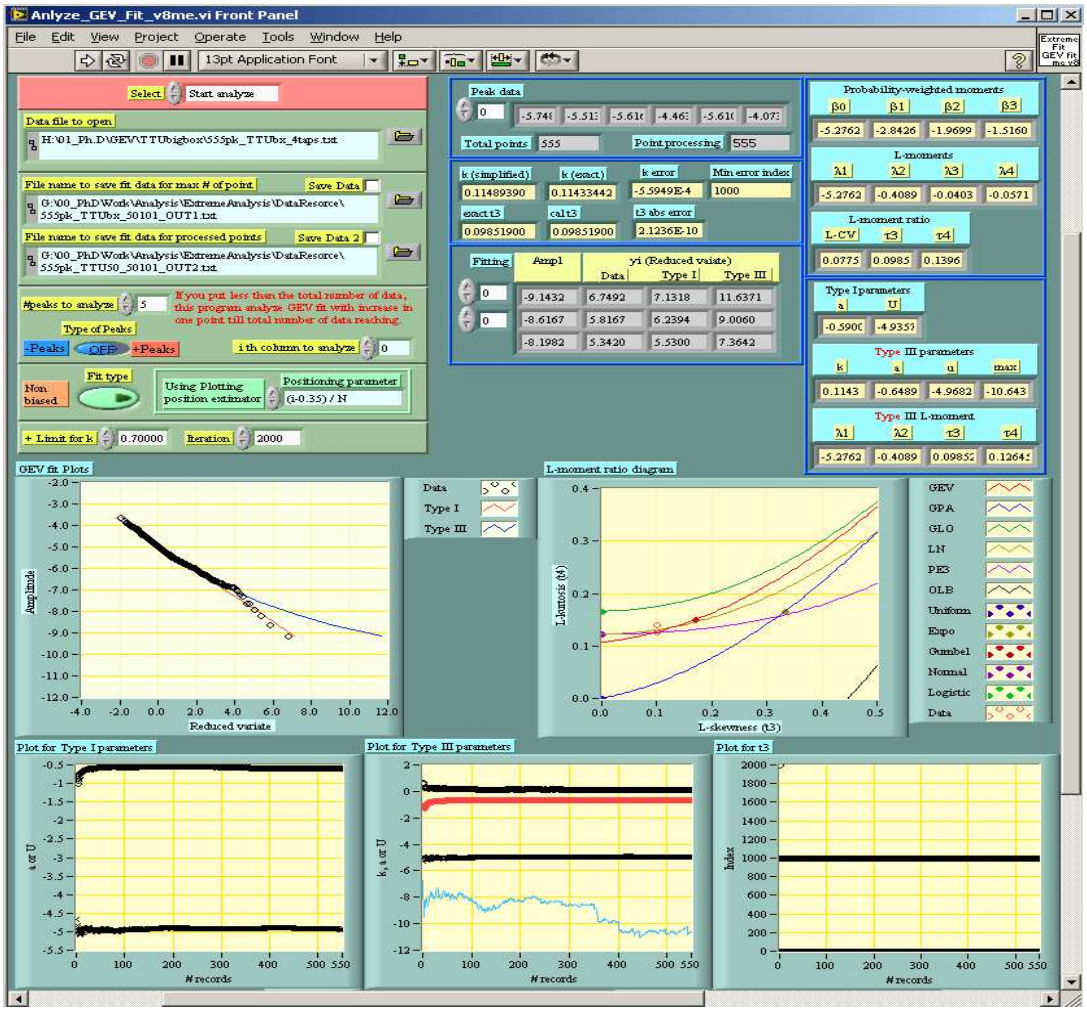

Figure 3.2 GEV fit analysis programmed in LabView software

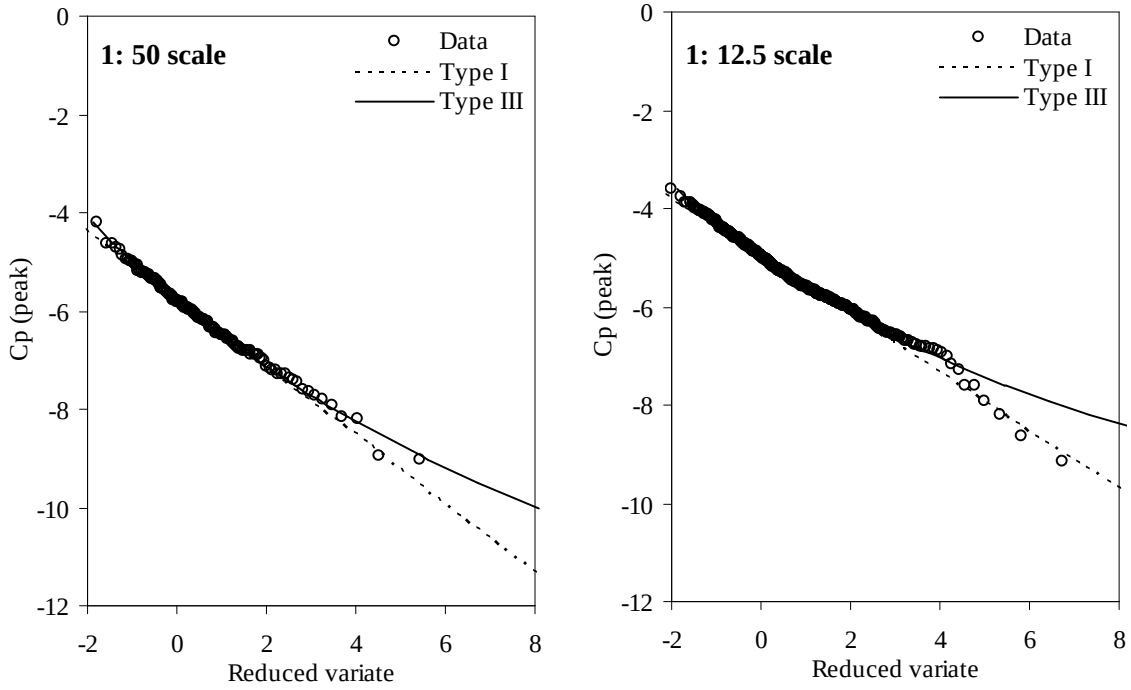

(a) Tap 50101

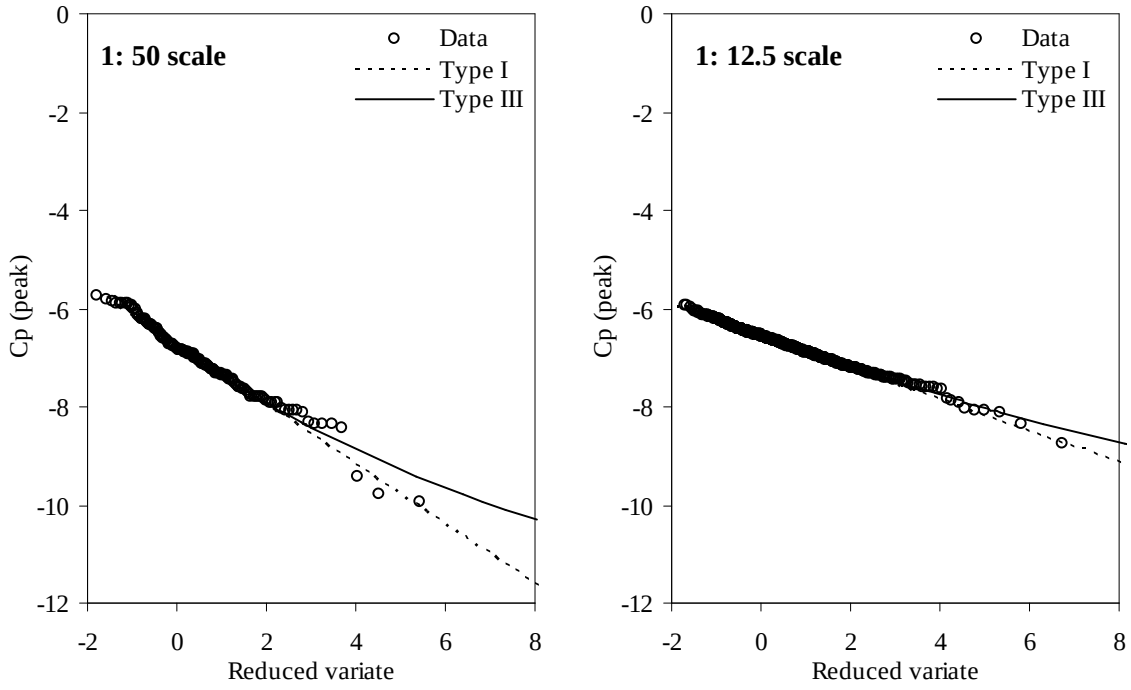

(b) Tap 50501

Figure 3.3 Extreme value distribution fitted to peak roof corner, 1:50 and 1: 12.5 geometrical scales of TTU test building

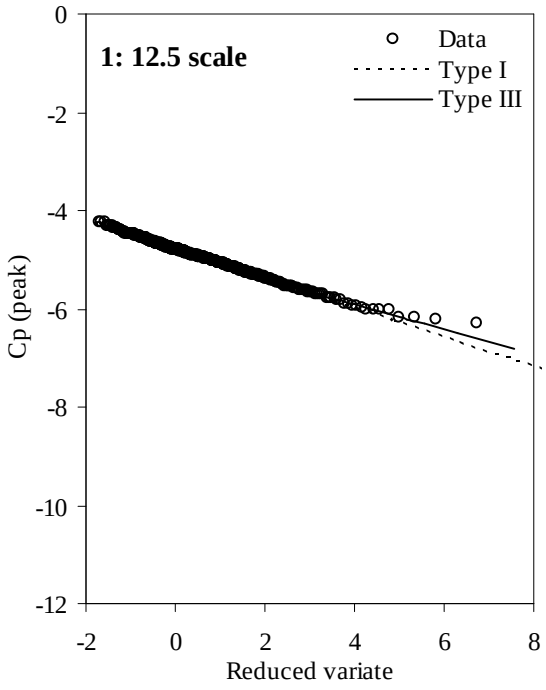

(c) Tap 50205

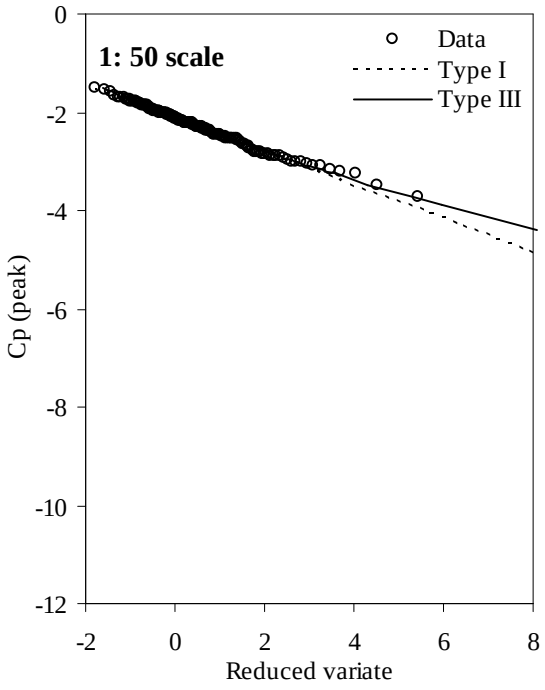

(d) Tap 50505

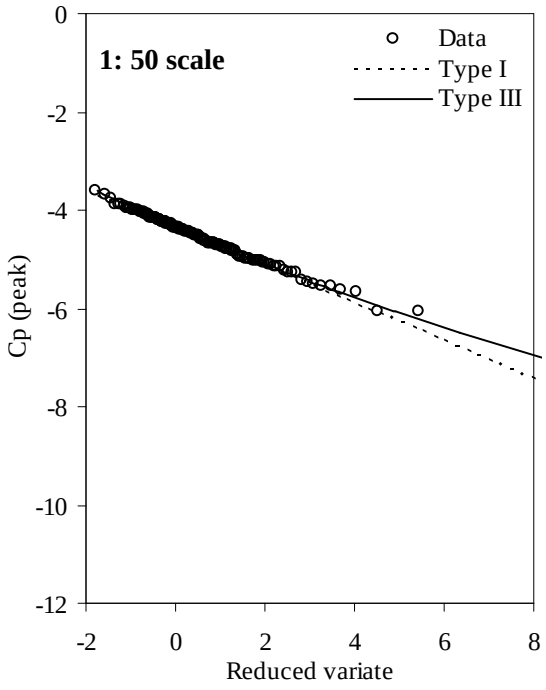

(e) Tap 50901

Figure 3.3 Continued

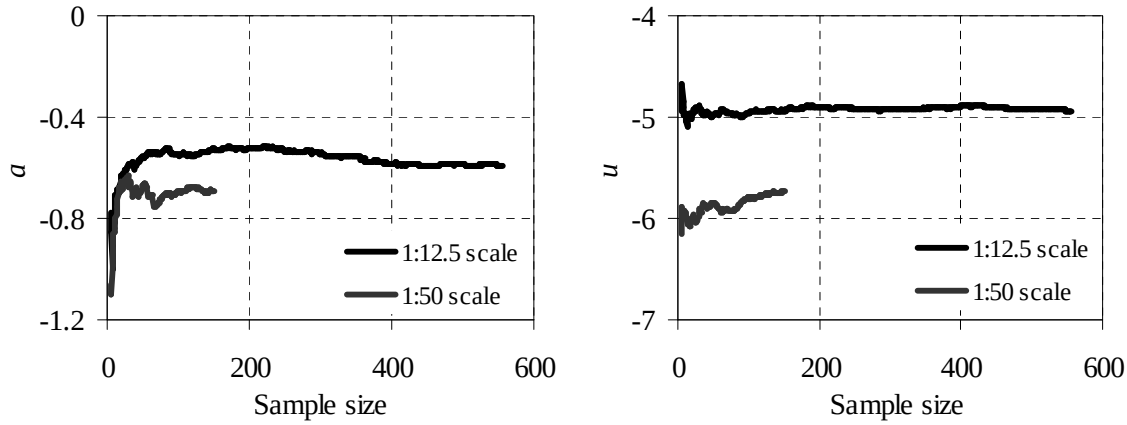

(a) 50101

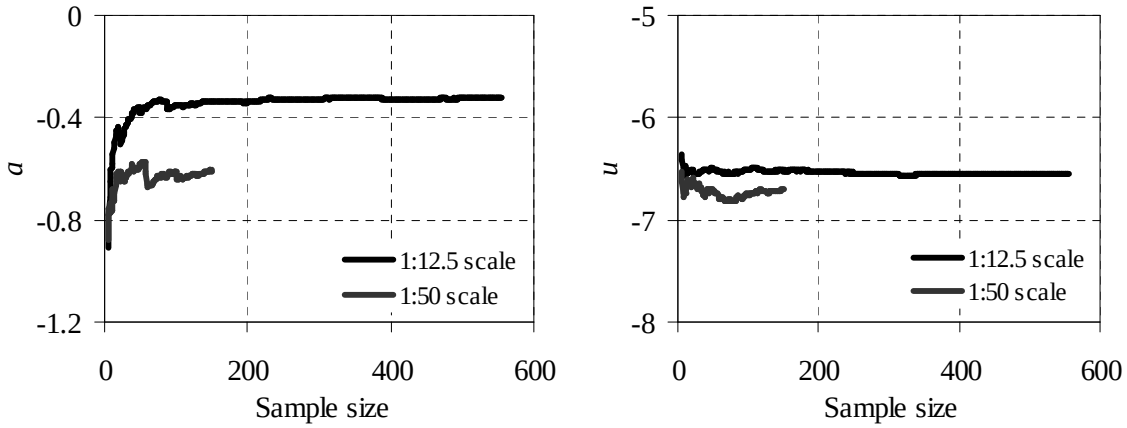

(b) 50501

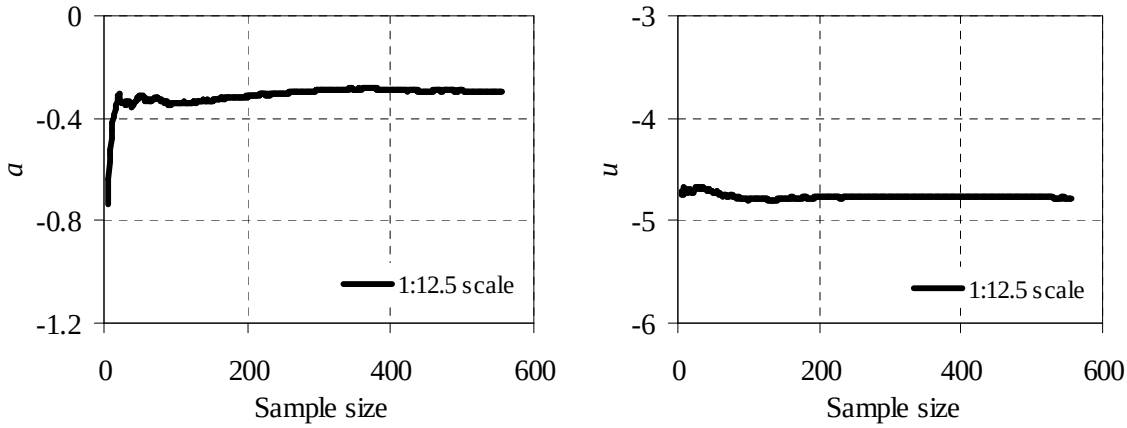

(c) 50205

Figure 3.4 Convergence of Type I EVD fit on parameters *a* and *u*

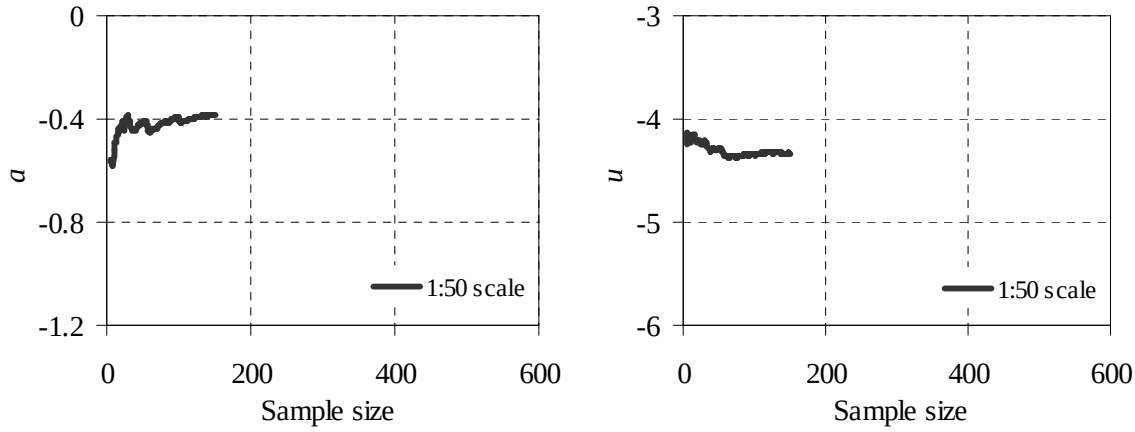

(d) 50901

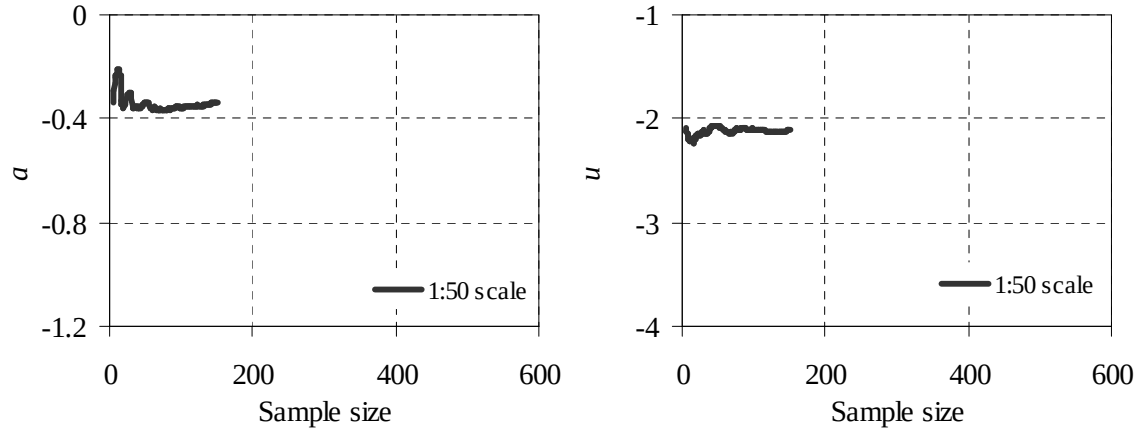

(e) 50501

Figure 3.4 Continued

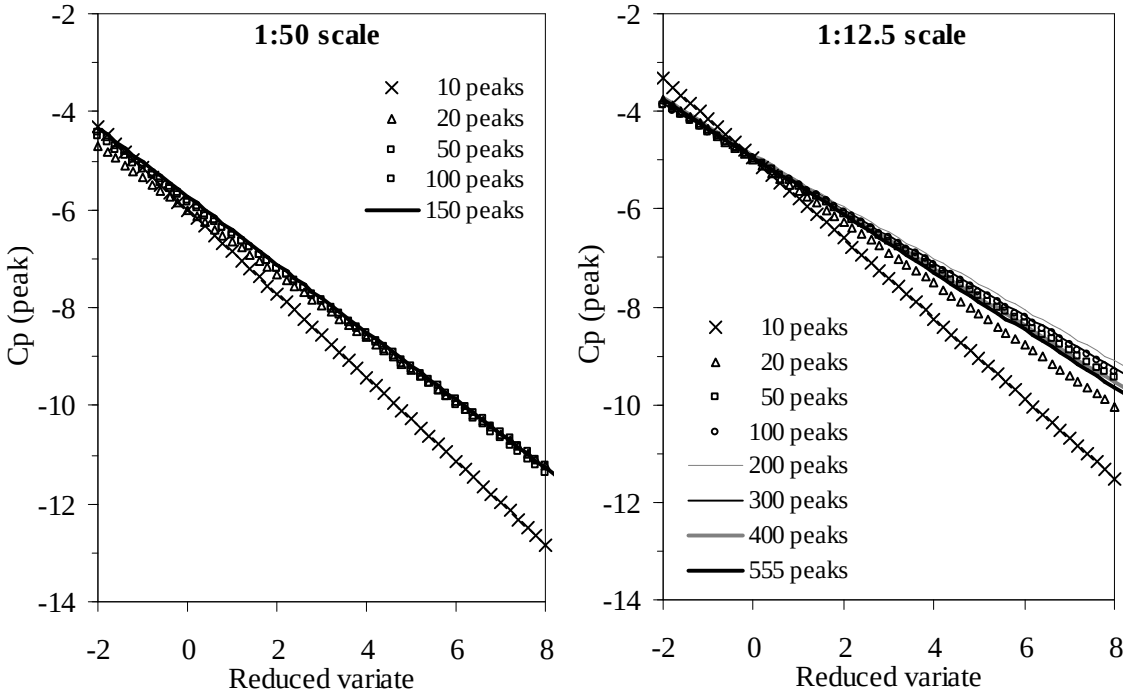

(a) 50101

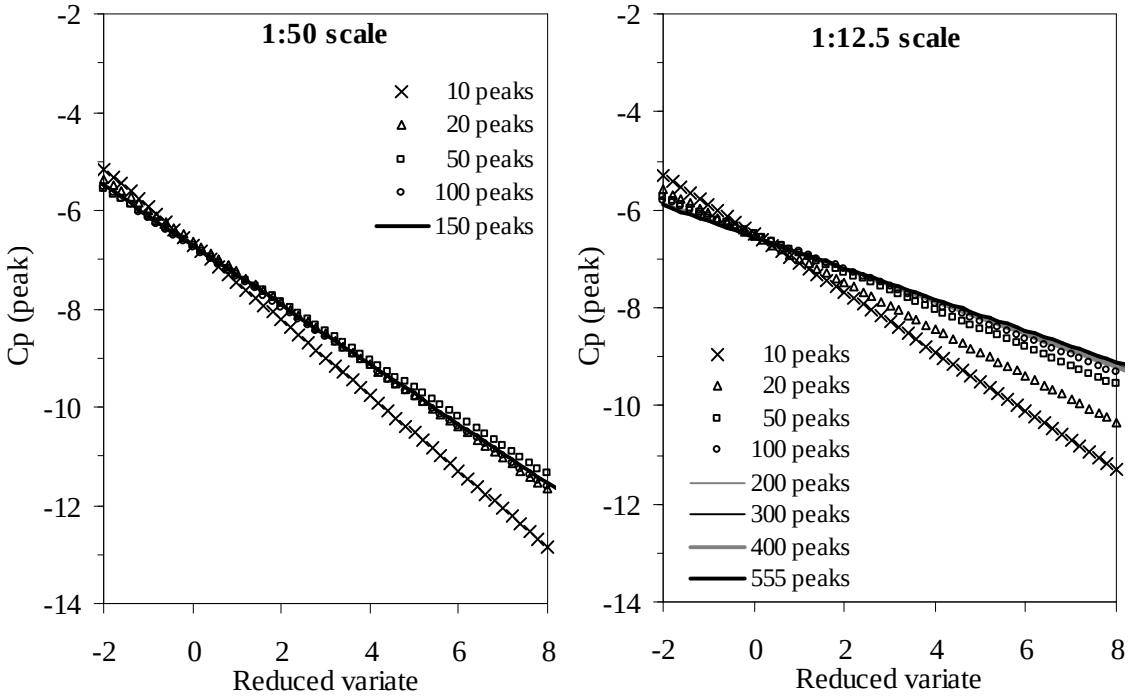

(b) 50501

Figure 3.5 Convergence of Type I EVD fit

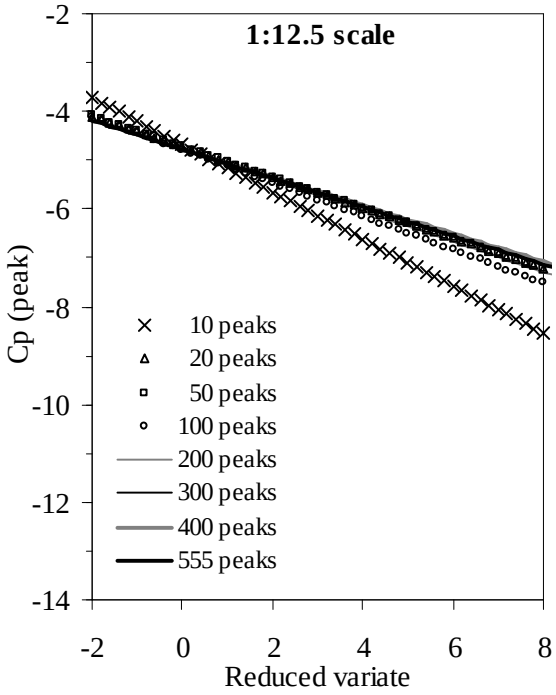

(c) 50205

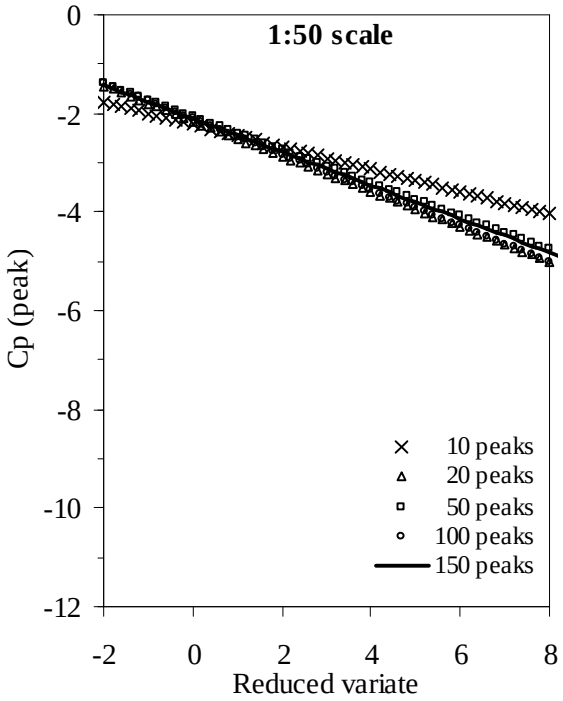

(d) 50505

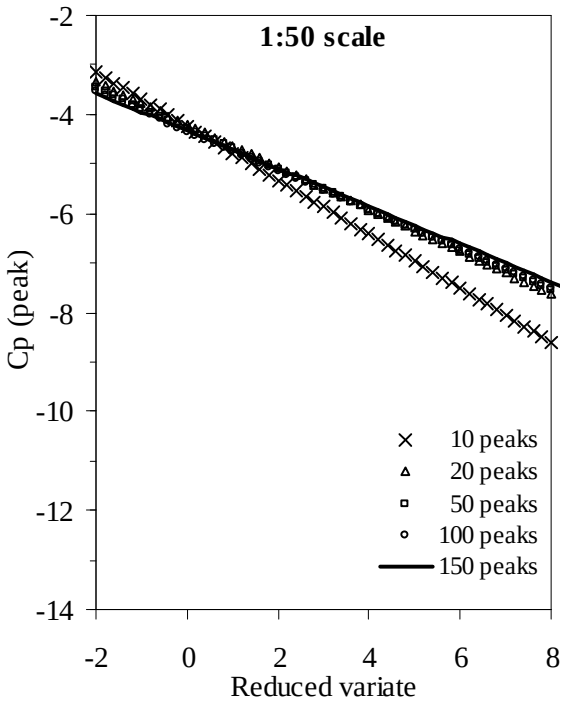

(e) 50901

Figure 3.5 Continued.

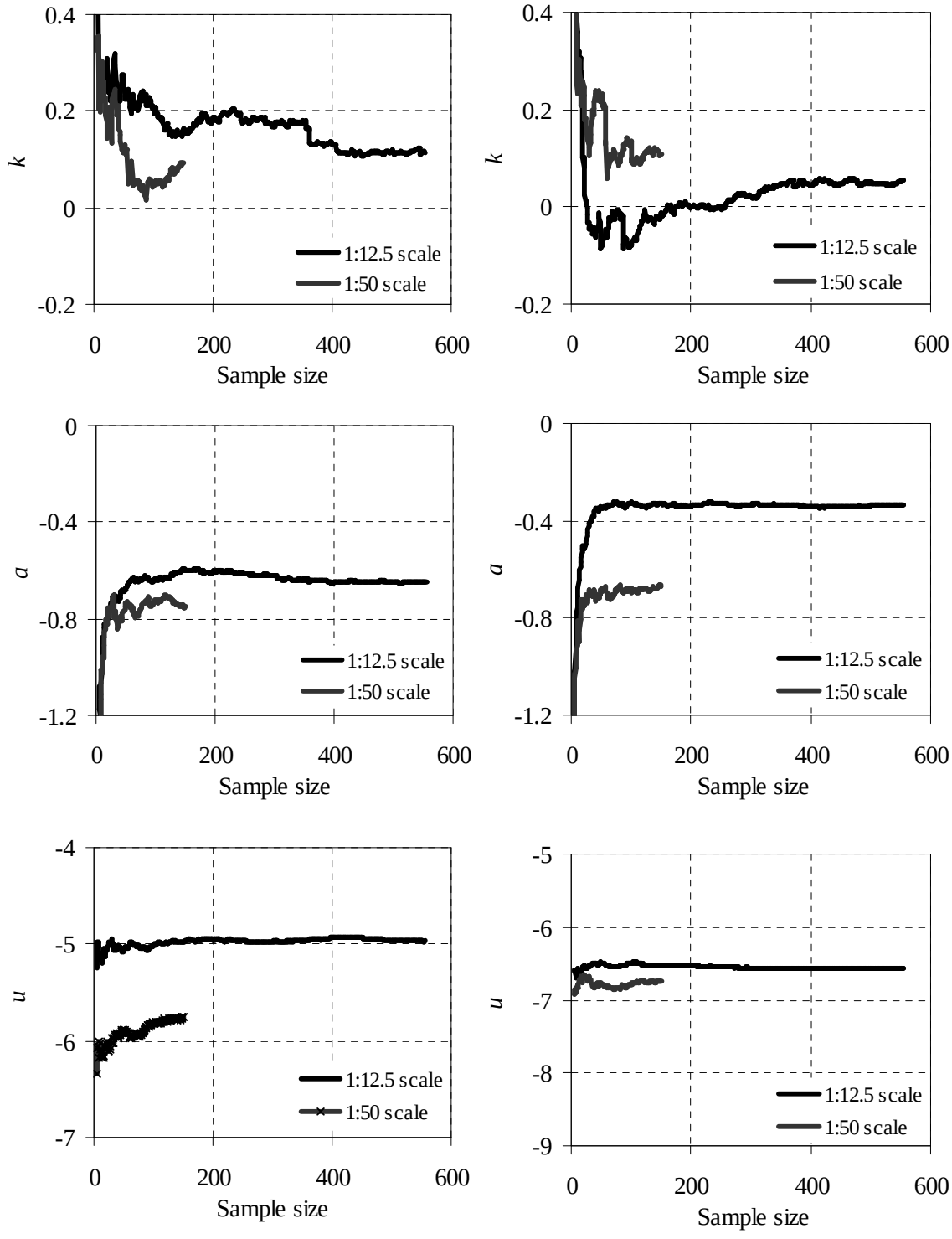

(a) Tap 50101 (b) Tap 50501

Figure 3.6 Convergence of Type III EVD fit on parameters *k*, *a* and *u* for taps 50101 and 50501

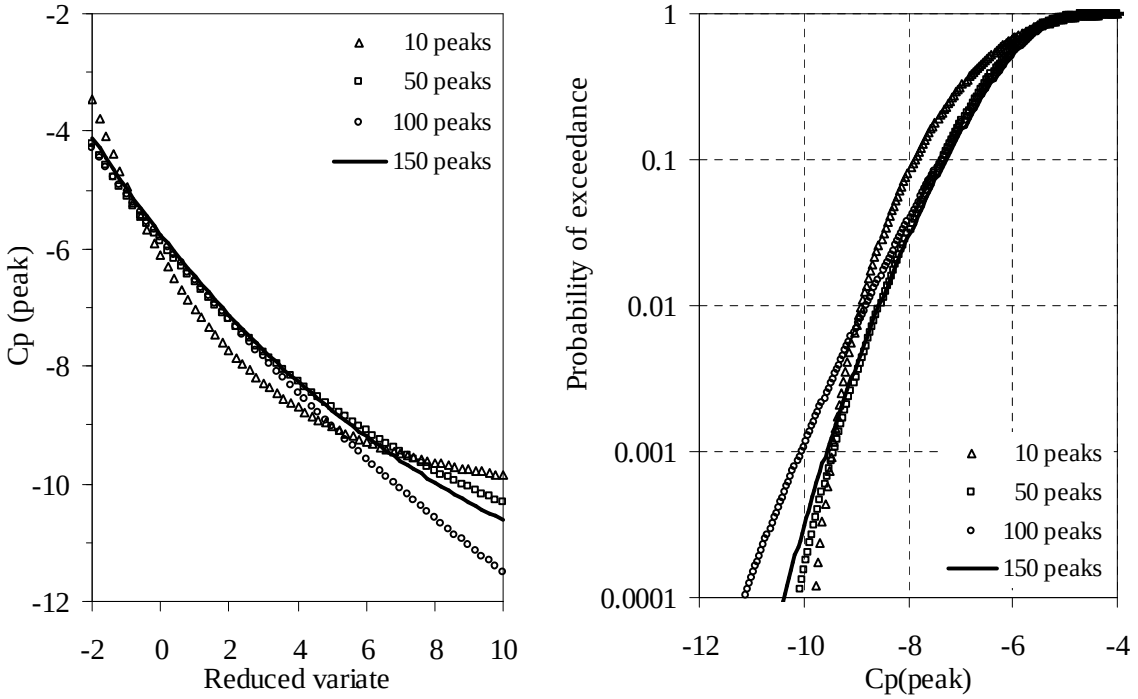

(a) 1:50 scale

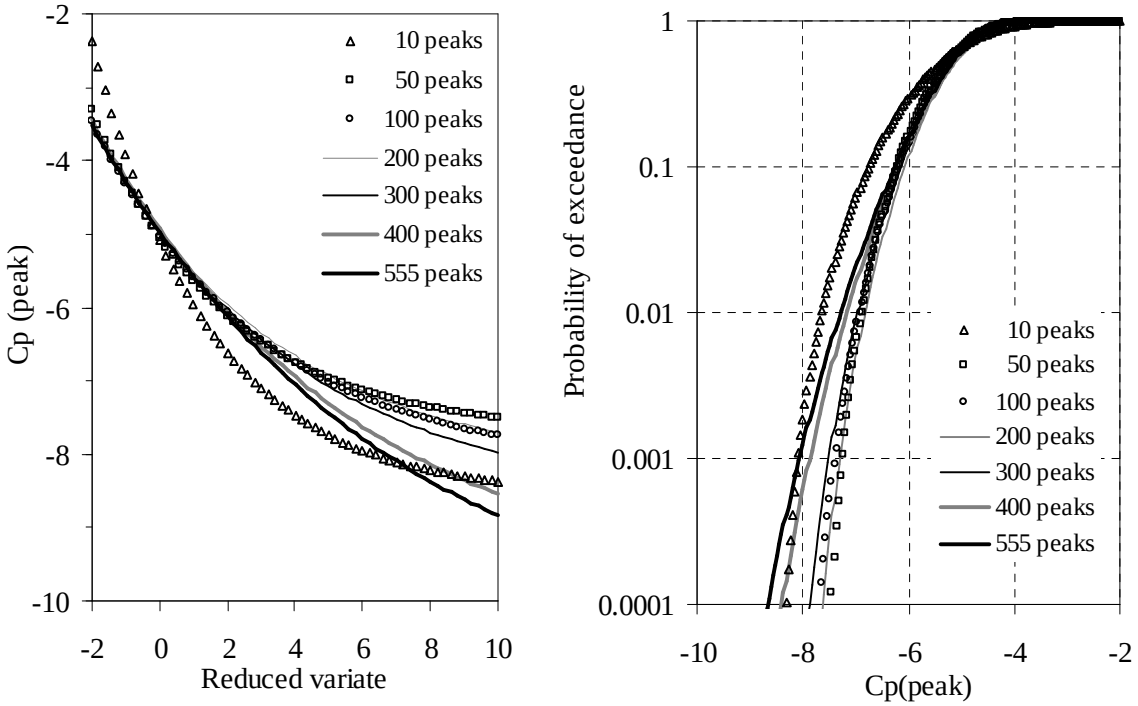

(b) 1:12.5 scale

Figure 3.7 Convergence of Type III EVD fit for tap 50101

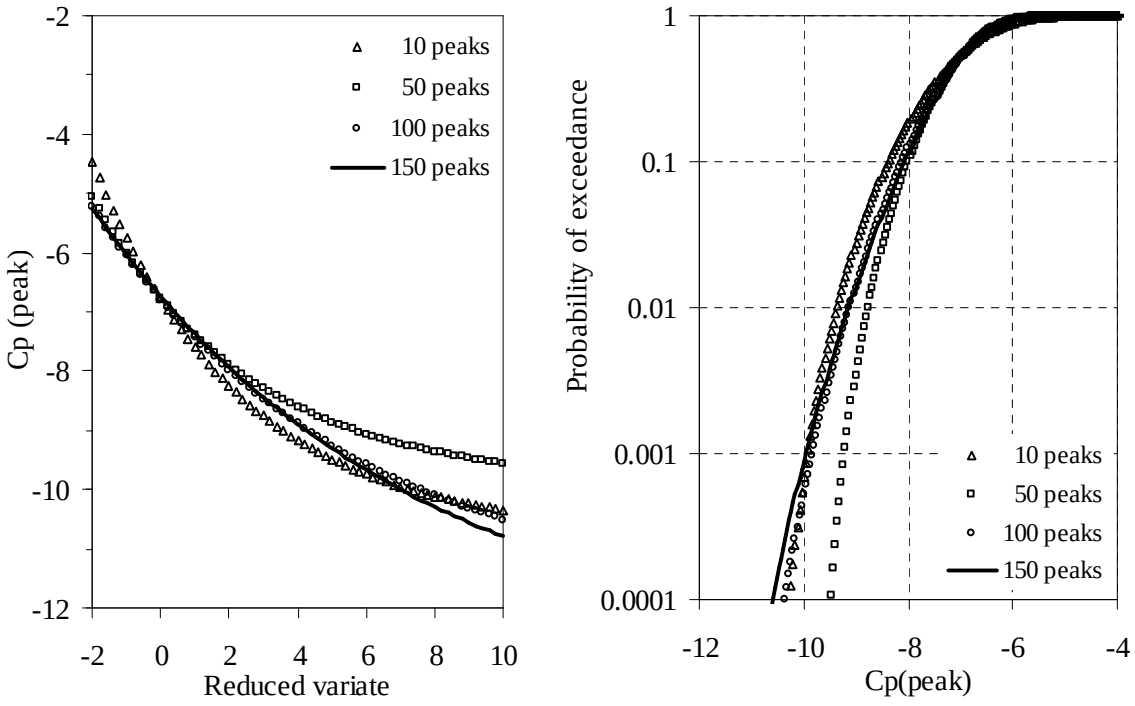

(a) 1:50 scale

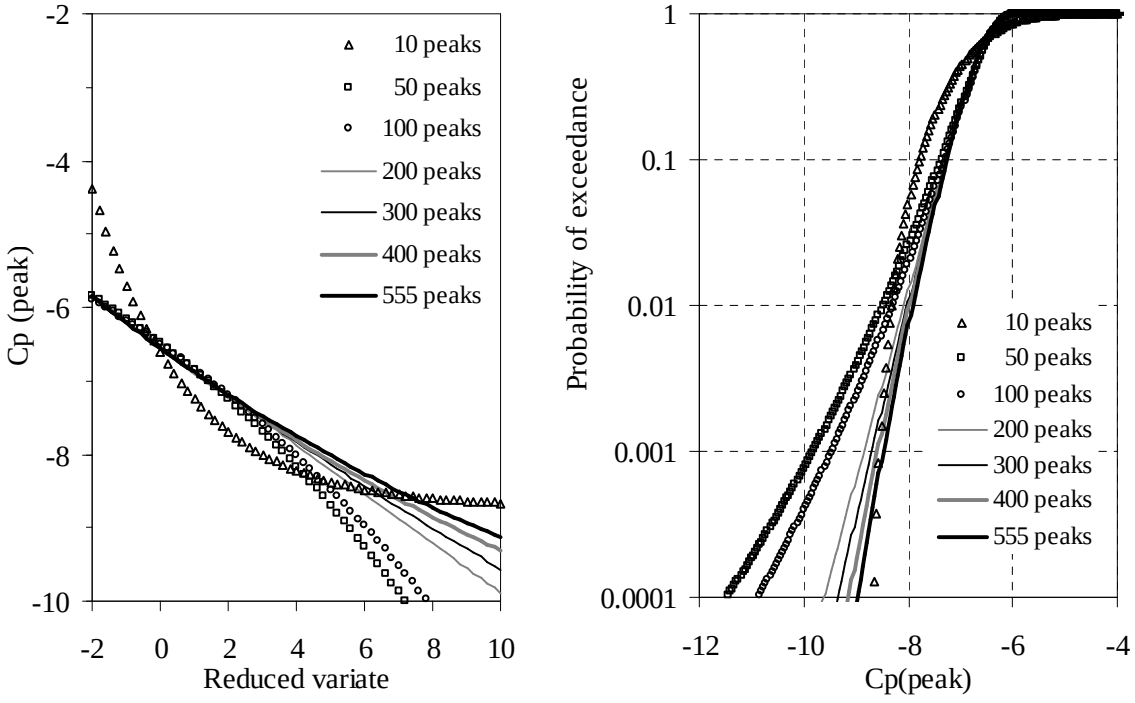

(b) 1:12.5 scale

Figure 3.8 Convergence of Type III EVD fit for tap 50501

Figure 3.9 POT analysis programmed in LabView software

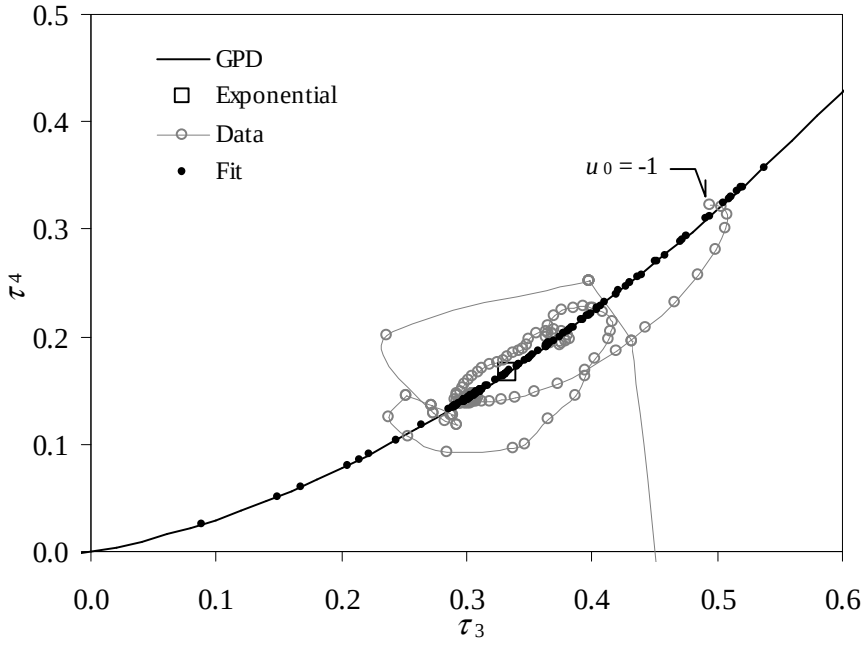

(a) Tap 50101

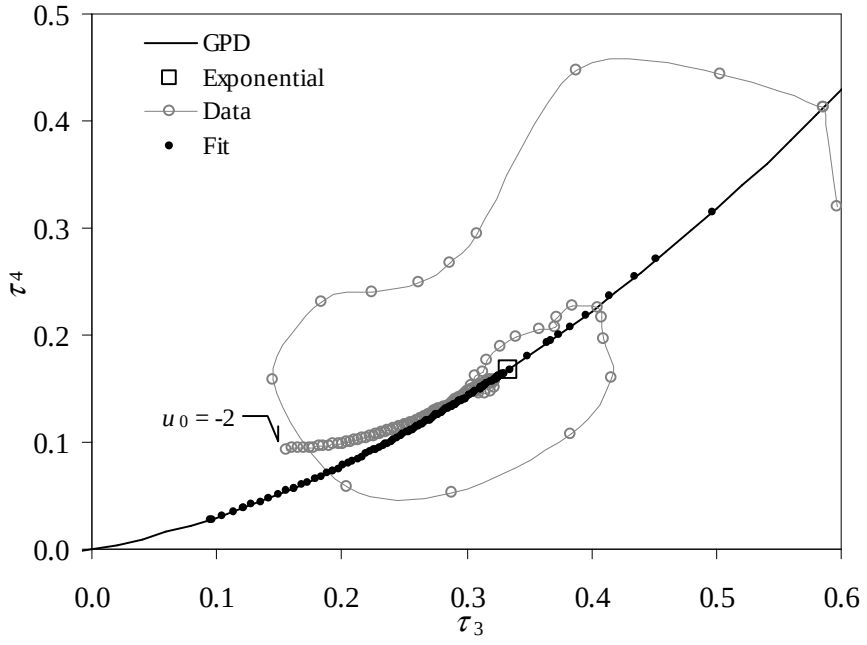

(b) Tap 50501

Figure 3.10 τ_3-τ_4 relationship for Cp data

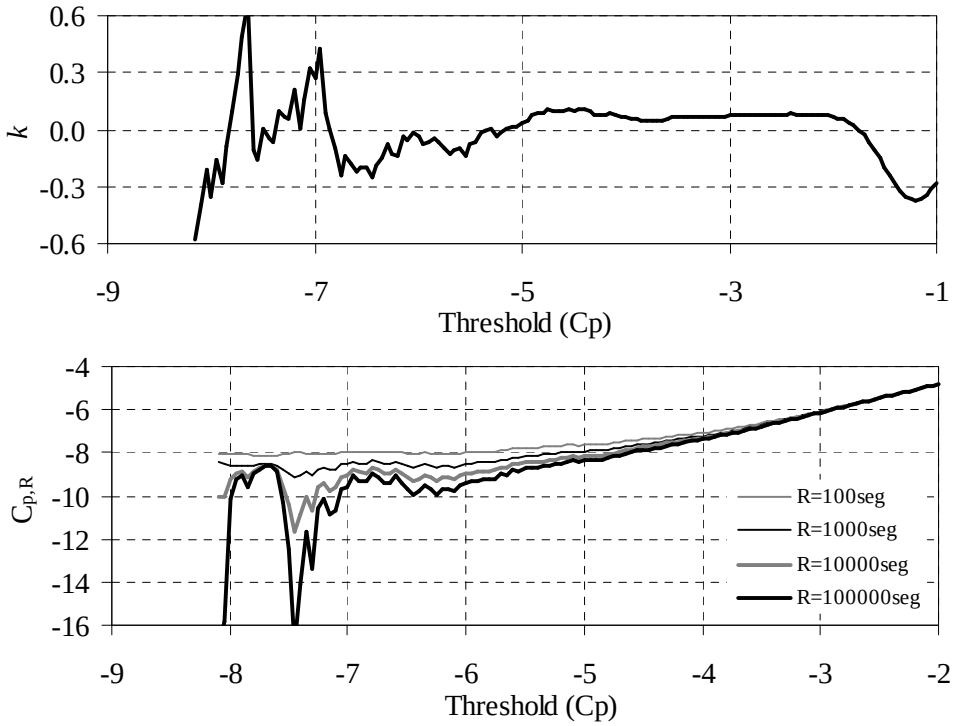

(a) Tap 50101

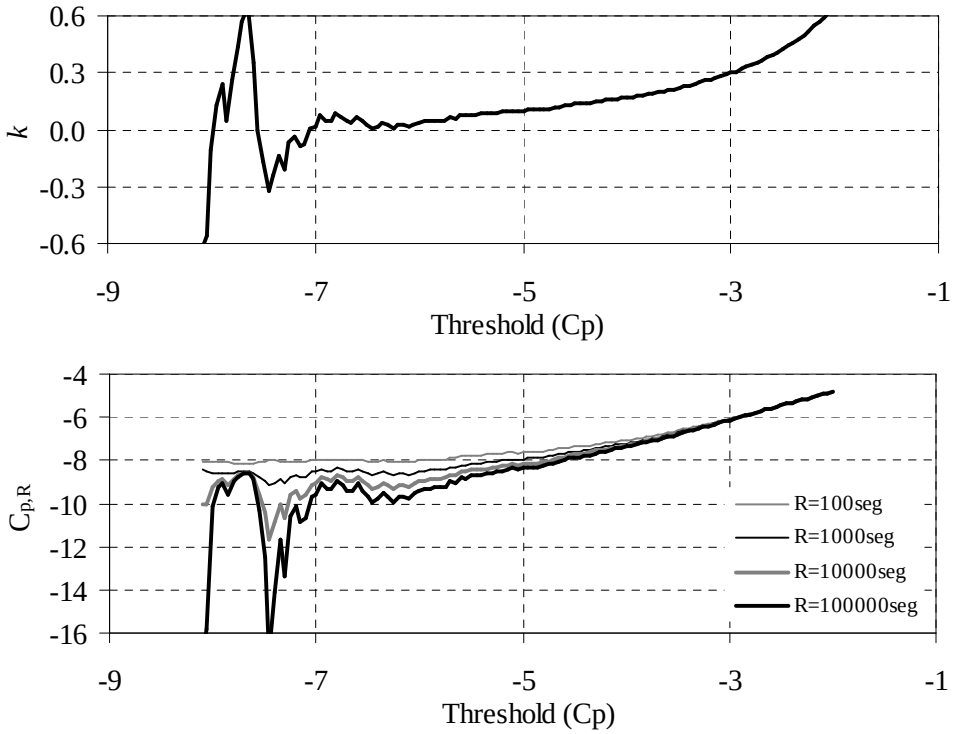

(b) Tap 50501

Figure 3.11 Estimated values of parameters *k* and extreme roof corner pressures

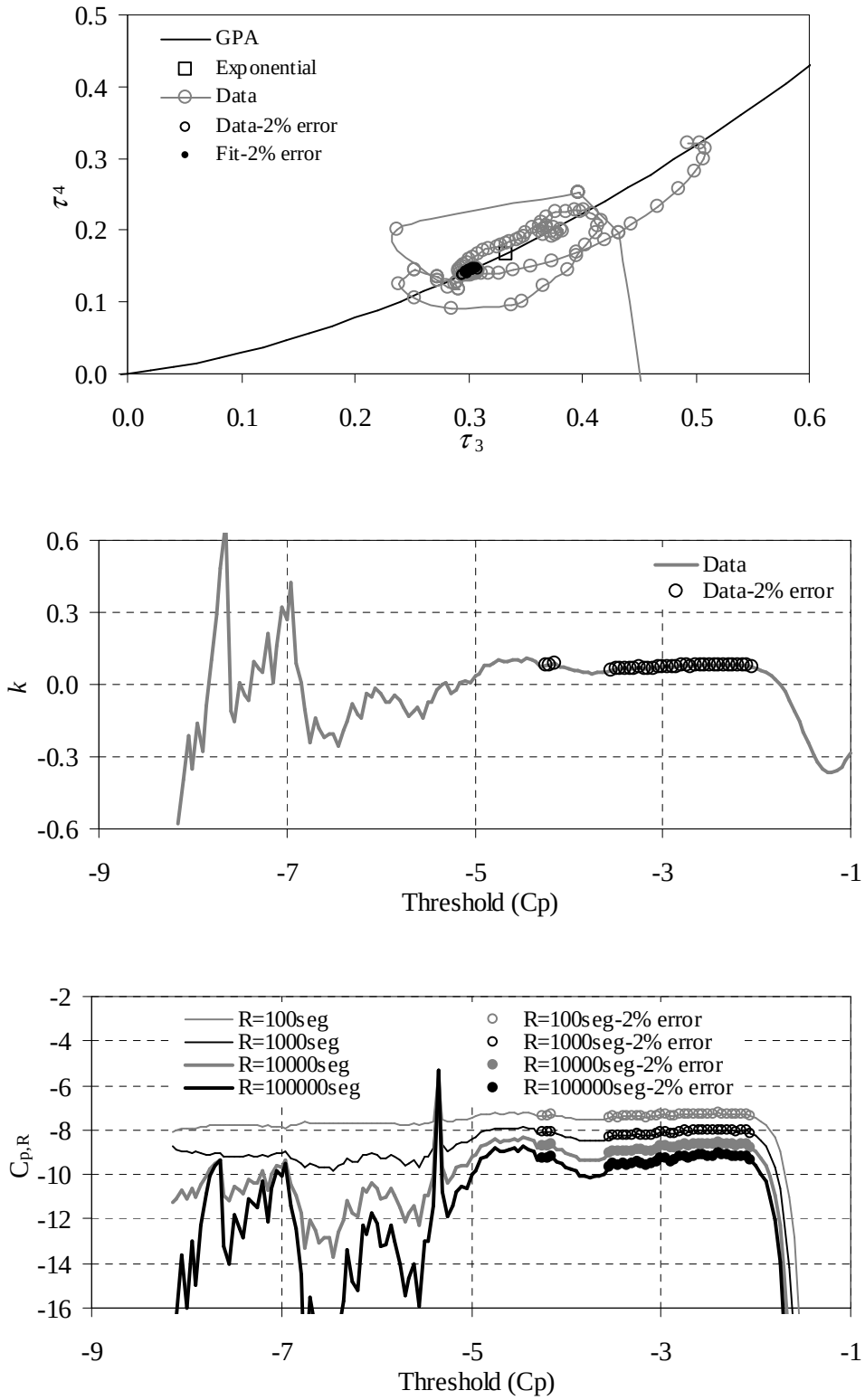

Figure 3.12 τ_3-τ_4 relationship, estimated values of k and extreme roof corner pressures for fitted data within 2 % errors at tap 50101

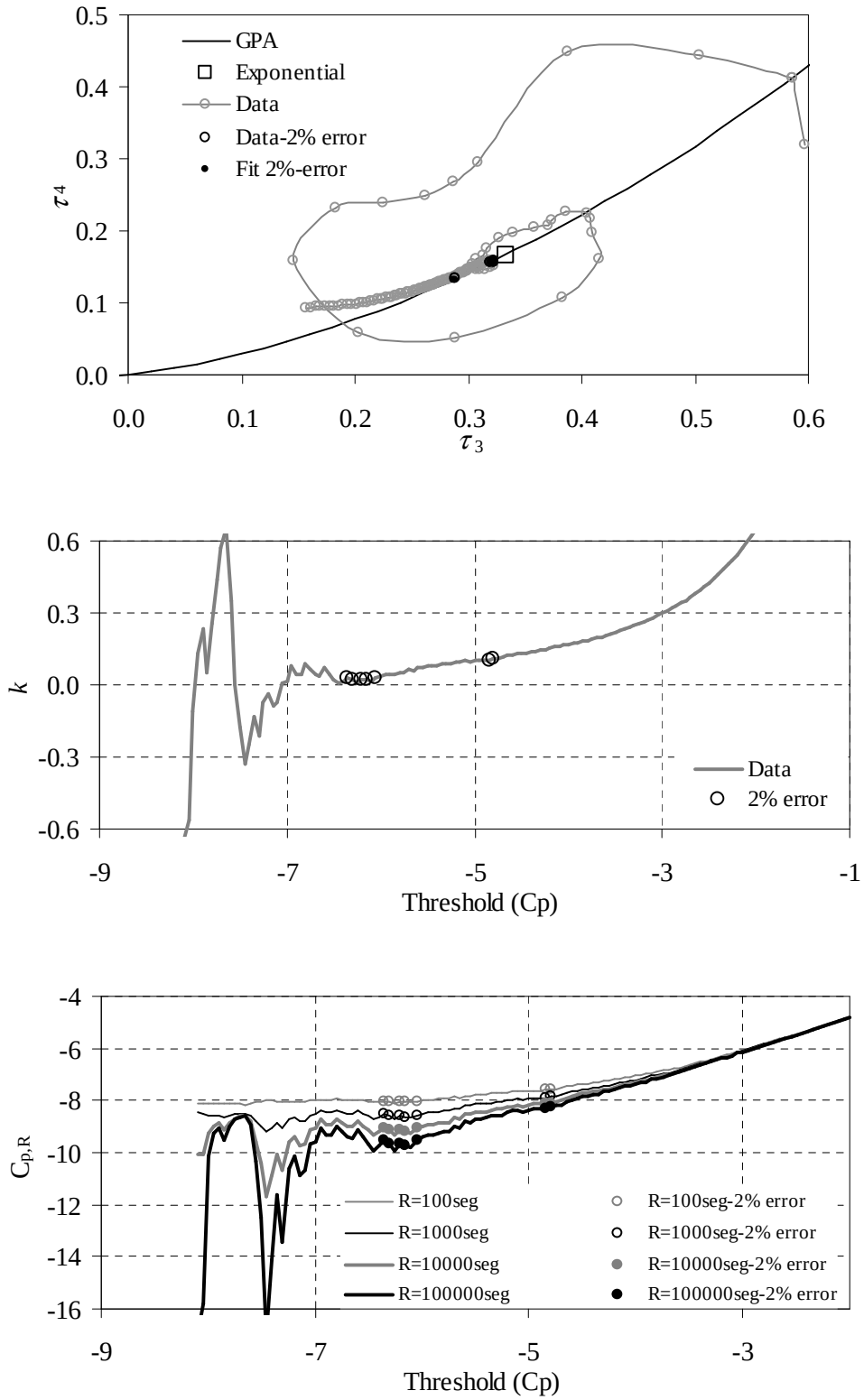

Figure 3.13 τ_3-τ_4 relationship, estimated values of k and extreme roof corner pressures for fitted data within 2 % errors at tap 50501

CHAPTER 4

COMPARATIVE STUDY OF WIND-INDUCED LOADING ON LOW-RISE BUILDINGS MODELED IN BOUNDARY-LAYER WIND TUNNELS

This chapter presents an expanded version of material contained in the following reference:

Bienkiewicz, B., Endo, M. and Main, J. (2009), "Impact of empirical models for approach wind exposures on wind loading on low buildings – A comparative study." Proceedings of the 2009 SEI/ASCE Structures Congress, Austin, Texas, April 29 – May 2, pp. 2439-2448.

4.1 INTRODUCTION

The consistency of wind loading on low-rise buildings inferred from wind tunnel testing has been of concern to wind engineering researchers and practitioners, structural engineers and code writers. The National Institute of Standards and Technology (NIST) has initiated and coordinated a pilot project addressing this issue. Two representative low-rise buildings of rectangular plan and two wind exposures were selected for the study, and a number of wind engineering laboratories were invited to carry out wind tunnel testing to determine wind loading on the buildings.

To ensure consistency in laboratory settings, most of the experimental conditions were specified by the coordinating team at the NIST. They included: geometrical scale, data sampling rate and record length, number of data records and locations of pressure taps. Ultimately, six laboratories including Colorado State University (CSU) (four from

North America, one from Japan and one from Europe) provided datasets, of which a total of seven have been deposited at and analyzed by NIST. These sets consisted of time series and statistical summaries of coefficients of external pressure acquired at specified taps on the low-rise building models. Information on modeling and statistical properties of approach wind was also provided.

The above data were employed in calculations of internal forces (bending moment, shear force, etc.) in representative frames of metal buildings of geometry modeled in the wind tunnel tests (Fritz *et al.*, 2006). The results of this analysis indicated large differences in the forces calculated using the datasets generated at different laboratories. The largest variability was found for building of a relatively low height (a prototype eave height of 6.1 m), placed in the suburban terrain (Fritz *et al*., 2006). These discrepancies were tentatively attributed to a number of experimental factors and assumptions made during wind tunnel testing. However, it has been recognized that a systematic investigation would be required to provide a definite explanation of the origins of this variability and to develop means to reduce/eliminate these discrepancies.

The present chapter describes the investigation of the inter-laboratory comparative study. In order to address the above variability, its origins and related issues, a broad range of investigations were conducted for the comparison of laboratory approach flows and wind-induced pressures and forces on the low-rise buildings among the six participating laboratories. The empirical turbulence models defined by the design guidelines, codes and others sources were also taken into account in this comparative study. The time series of roof pressures were employed for the statistical analysis and the computation of the internal forces (bending moments) using a numerical tool developed

in this study. The peak loadings were estimated by employing the non-Gaussian procedure proposed by Sadek and Simiu (2002).

4.2 OVERVIEW OF EMPIRICAL TURBULENCE MODELS

There are many building standards and design guidelines specifying the turbulence models developed to take into account the gustiness of wind. Representative turbulence models specified in such building standards and design guidelines are presented in this section.

Minimum Design Loads for Buildings and Other Structures (ASCE 7, 2005)

$$I_{\bar{z}} = c\left\{\frac{33}{\bar{z}}\right\}^{1/6} \qquad [4.1]$$

where $I_{\bar{z}}$ = intensity of turbulence at height $\bar{z}$,
c = turbulence intensity factor,
$\bar{z}$ = equivalent height of the structure defined as 0.6h but not less than $z_{\min}$ for all building heights h, and
$z_{\min\ (\mathrm{ASCE})}$ = exposure constant.

The recommended values of the parameters $I_{\bar{z}}$, c, $\bar{z}$ and $z_{\min\ (\mathrm{ASCE})}$ in Equation [4.1] are listed in Table 4.1.

Table 4.1 Parameters c and $z_{\min}$ specified in ASCE 7

Exposure category	c	$z_{\min\ (\mathrm{ASCE})}$ *
B	0.3	9.14 m (30 ft)
C	0.2	4.57 m (15 ft)
D	0.15	2.13 m (7 ft)

* z_{min} = minimum height used to ensure that the equivalent height $\bar{z}$ is greater of 0.6h or z_{min}. For building with h < z_{min}, $\bar{z}$ shall be taken as z_{min}.

Eurocode (1995)

$$I_v(z) = \frac{k_T}{c_r(z)\ \ c_t(z)} \qquad [4.2]$$

where $I_v(z)$ = turbulence intensity at height z
$c_r(z)$ = roughness coefficient
$= k_T \ln(z/z_0)$ for $z_{min} \leq z \leq 200$ m
$= c_r(z_{min\ (Eurocode)})$ for $z < z_{min}$,
$c_t(z)$ = topography coefficient = 1 for non-topographic effect,
k_T = terrain factor,
z_0 = roughness length, and
$z_{min\ (Eurocode)}$ = minimum height.

The recommended values of the parameters k_T, z_0 and $z_{min\ (Eurocode)}$ in Equation [4.2] are listed in Table 4.2.

Table 4.2 Parameters k_T, z_0 and $z_{min\ (Eurocode)}$ specified in Eurocode

Exposure category	k_T	z_0	$z_{min\ (Eurocode)}$
A	0.24	1 m	16 m
B	0.22	0.3 m	8 m
C	0.19	0.05 m	4 m
D	0.17	0.01 m	2 m

Recommendations for loads on buildings (AIJ, 1996)

$$I = 0.1\left(\frac{Z}{Z_G}\right)^{-\alpha-0.05} \text{ for } Z_b < Z \leq Z_G \qquad [4.3]$$

where I = turbulence intensity at height Z,
α = power-law exponent, and
Z_b and Z_G = terrain factors.

The recommended values of the parameters α, Z_b and Z_G in Equation [4.3] are listed in Table 4.3.

Table 4.3 Values of α, Z_b and Z_G specified in AIJ

Exposure category	I	II	III	IV	V
α	0.35	0.27	0.20	0.15	0.10
Z_b	20 m	10 m	5 m	5 m	5 m
Z_G	650 m	550 m	450 m	350 m	250 m

Australian Standards (AS1170.2, 1989) *and Canadian Standards* (NRCC, 1996)

The turbulence intensity models of the Australian and Canadian standards are employed herein from Zhou and Kareem (2002). The turbulence intensity profile can be expressed in terms of a power law,

$$I(z) = c\left\{\frac{z}{10}\right\}^{-d} \qquad [4.4]$$

where $I(z)$ = turbulence intensity at height z

c and d = terrain dependent coefficients.

The recommended values of the coefficients c and d in Equation [4.4] are listed in Table 4.4.

Table 4.4 Parameters c and d (Zhou and Kareem, 2002)

Exposure category	AS1170.2		NBCC	
	c	d	c	d
A	0.42	0.28	0.62	0.36
B	0.24	0.20	0.34	0.25
C	0.18	0.16	0.20	0.14
D	0.16	0.13		

Engineering Science Data Unit (ESDU, 1993)

The turbulence model proposed by ESDU is widely used in the wind engineering practice. The ESDU turbulence model is defined as follows:

$$I_u = \frac{\sigma_u}{V_z} = \frac{\sigma_u}{u_*} \bullet \frac{u_*}{V_z} \qquad [4.5]$$

$$\text{where } \frac{\sigma_u}{u_*} = \frac{7.5\eta\left[0.538 + 0.09\ln\left(\frac{z}{z_0}\right)\right]^{\eta^{16}}}{1 + 0.156\ln\left(\frac{u_*}{fz_0}\right)},$$

$$\eta = 1 - \frac{6fz}{u_*}, \text{ and } z_g = \frac{u_*}{6f},$$

$$\frac{V_z}{u_*} = 2.5\ln\left[\left(\frac{z}{z_0}\right) + \frac{23}{4}\frac{z}{z_g} - \frac{15}{8}\left(\frac{z}{z_g}\right)^2 - \frac{4}{3}\left(\frac{z}{z_g}\right)^3 + \frac{1}{3}\left(\frac{z}{z_g}\right)^{-4}\right]. \qquad [4.6]$$

Equation [4.6] can be even simplified for the limited range of elevations as follows:

$$\frac{V_z}{u_*} = 2.5\left[\ln\left(\frac{z}{z_0}\right) + 3.45\frac{3}{4}\frac{fz}{z_g}\right] \qquad \text{up to 300 m} \qquad [4.7]$$

$$\frac{V_z}{u_*} = 2.5\ln\left(\frac{z}{z_0}\right) \qquad \text{up to 30 m} \qquad [4.8]$$

4.3 BACKGROUND INFORMATION ON PEAK NON-GAUSSIAN ESTIMATE

The time series of roof suction pressures and wind-induced internal forces (bending moments) were employed to predict peak pressures and forces. The peak non-Gaussian procedure proposed by Sadek and Simiu (2002) was employed. There are two main steps involved in this procedure:

Step 1. Selection of probability distribution model for parent distribution of time series data.

Step 2. After the selection of most optimal distribution model, estimation of peak statistics based on the standard translation procedure.

In Step 1, nine candidate probability distribution models were considered in this study: normal distribution, gamma (Pearson Type III) distribution, extreme value Type I (Gumbel) and Type III distributions, generalized Pareto distribution, exponential distribution, generalized logistic distribution, logistic distribution, and lognormal distribution. The normal distribution is written in the general form available in any fundamental statistics textbooks. The other eight distribution models are expressed herein after Hosking and Wallis (1997). These nine probability distribution models are defined below.

Normal distribution

$$F(x) = \frac{1}{2}\left[1 + \mathrm{erf}\left(\frac{x-\mu}{\sigma\sqrt{2}}\right)\right] \qquad \text{for } -\infty < x < \infty \qquad [4.9]$$

where $\sigma =$ scale parameter and $\mu =$ location parameter

$$\mathrm{erf}(z) = \frac{2}{\sqrt{\pi}}\int_0^z \mathrm{e}^{-t^2}\,dt$$

Gamma distribution (Pearson Type III distribution)

If $k > 0$, the range of x is $\xi \le x < \infty$.

$$F(x) = \frac{G\left(\alpha, \frac{x-\xi}{\beta}\right)}{\Gamma(\alpha)} \qquad [4.10]$$

where $\alpha = 4/k^2$, $\beta = \sigma|k|/2$, $\xi = \mu - 2\sigma$

k = shape parameter, σ = scale parameter and μ = location parameter

$G(\alpha, x) = \int_0^x t^{\alpha-1} e^{-t} dt$

If $k < 0$, the range of x is $-\infty < x \le \xi$.

$$F(x) = 1 - \frac{G\left(\alpha, \frac{\xi - x}{\beta}\right)}{\Gamma(\alpha)} \qquad [4.11]$$

Extreme value Type I (Gumbel) distribution (Type I EVD)

The range of x is $-\infty < x < \infty$.

$$F(x) = \exp\left[-\exp\left(-\frac{x-\mu}{\alpha}\right)\right] \qquad [4.12]$$

where α = scale parameter and μ = location parameter

Extreme value Type III distribution (Type III EVD)

If $k > 0$, the range of x is $-\infty < x \le \mu + \alpha/k$. If $k < 0$, the range of x is $\mu + \alpha/k \le x < \infty$.

$$F(x) = \exp\left\{-\left[1 - k\left(\frac{x-\mu}{\alpha}\right)\right]^{\frac{1}{k}}\right\} \qquad \text{where } k \neq 0 \qquad [4.13]$$

where k = shape parameter, α = scale parameter and μ = location parameter

Generalized Pareto distribution (GPD)

If $k > 0$, the range of x is $\mu \le x \le \mu + \alpha/k$. If $k < 0$, the range of x is $\mu + \alpha/k \le x < \infty$.

$$F(x) = 1 - \left(1 - \frac{k(x-\mu)}{\alpha}\right)^{1/k} \qquad \text{where } k \neq 0 \qquad [4.14]$$

where k = shape parameter, α = scale parameter and μ = location parameter

Exponential distribution

The exponential distribution is the special case of the generalized Pareto distribution defined in Equation [4.14] when $k = 0$. The range of x is $\mu \le x < \infty$.

$$F(x) = 1 - \exp\left[-\frac{x-\mu}{\alpha}\right] \qquad [4.15]$$

where α = scale parameter and μ = location parameter

Generalized logistic distribution

If $k > 0$, the range of x is $-\infty < x \le \mu + \alpha/k$. If $k < 0$, the range of x is $\mu + \alpha/k \le x < \infty$.

$$F(x) = \frac{1}{1 + \left(1 - \frac{k(x-\mu)}{\alpha}\right)^{1/k}} \qquad [4.16]$$

where k = shape parameter, α = scale parameter and μ = location parameter

Logistic distribution

The logistic distribution is the special case of the generalized logistic distribution defined in Equation [4.16] when $k = 0$. The range of x is $-\infty < x < \infty$.

$$F(x) = \frac{1}{1 + e^{-\frac{(x-\mu)}{\alpha}}} \qquad [4.17]$$

where α = scale parameter and μ = location parameter

Lognormal distribution

If $k > 0$, the range of x is $-\infty < x \le \mu + \alpha/k$. If $k < 0$, the range of x is $\mu + \alpha/k \le x < \infty$.

$$F(x) = \Phi\left[-\frac{1}{k}\log\left(1 - \frac{k(x-\mu)}{\alpha}\right)\right] \qquad [4.18]$$

where k = shape parameter, α = scale parameter and μ = location parameter

$$\Phi(x) = \frac{1}{\sqrt{2\pi}} \int_{-\infty}^{x} \mathrm{e}^{-\frac{1}{2}t^2} dt$$

These nine probability distribution models were employed to fit a parent distribution obtained from time series data. For the solutions of parameters associated with the probability distribution models, the estimation procedure proposed by Hosking and Wallis (1997) was employed. The solutions of parameters for Type I and Type III EVDs and GPD were described in Sections 3.2 and 3.3, respectively. For other models, parameter fitting details can be found in Hosking and Wallis (1997).

The selection of the best fit probability distribution model (among the nine candidate models) was made by using the probability plot correlation coefficient (PPCC) test proposed by Filliben (1975). The PPCC test was also employed by Sadek and Simiu (2002). The PPCC test statistic is defined as the product moment correlation coefficient between the ordered observations X_i and the order statistic medians M_i from a probability distribution model:

$$r = Corr(X, M) = \frac{\sum\left\{\left(X_i - \overline{X}\right)\left(M_i - \overline{M}\right)\right\}}{\sqrt{\left[\sum\left(X_i - \overline{X}\right)^2\right]\left[\sum\left(M_i - \overline{M}\right)^2\right]}} \qquad [4.19]$$

The value of $r = 1$ indicates perfect correlation, whereas the value close to $r = 0$ indicates weaker correlation from this equation. Therefore, selecting the probability distribution model with the largest value produced by the PPCC test implies the best probability distribution model representing the parent distribution of time series data.

In Step 2, peaks can be estimated based on the standard translation process approach described by Sadek and Simiu (2002) using the probability distribution model obtained in Step 1. This procedure is as follows:

Assume a stationary non-Gaussian time series $x(t)$ with probability distribution $F_x[x(t)]$ and duration T. This process is mapped onto a time series $y(t)$ with standardized normal distribution $\Phi[y(t)]$. For the process of $y(t)$, the cumulative distribution function of the largest peak $y_{pk,T}$ during time interval T can be obtained by using classical results (Rice, 1954).

$$F_{Y_{pk,T}}(y_{pk,T}) = \exp\left[-\nu_{0,y} T \exp\left(-y_{pk,T}^2/2\right)\right] \qquad [4.20]$$

where $\nu_{0,y}$ = mean zero upcrossing rate of the Gaussian process $y(t)$

$$\nu_{0,y} = \sqrt{\frac{\int_0^\infty n^2 S_y(n)dn}{\int_0^\infty S_y(n)dn}} \text{ (Rice, 1954)}$$

n = frequency and $S_y(n)$ = spectral density function of $y(t)$

After the determination of the largest peaks $F_{Y_{pk,T}}(y_{pk,T})$ from Equation [4.20], the largest peaks of $x(t)$ can be obtained by mapping the peaks of the normal distribution space onto the non-Gaussian distribution space. Figure 4.1 schematically describes this procedure. For a given cumulative probability distribution of the peaks $F_{Y_{pk,T}}(y_{pk,T})$, the Gaussian peak $y_{pk,T}$ and its cumulative probability in the Gaussian space $\phi(y_{pk,T})$ are first determined. Then, the corresponding peak in the non-Gaussian space $x_{pk,T}$ is estimated corresponding to a cumulative probability with $F_X(x_{pk,T}) = \Phi(y_{pk,T})$.

4.4 INTER-LABORATORY DATA RESOURCE

Two buildings selected for the inter-laboratory study initiated by the NIST, (see Figure 4.2), had the same planar dimensions, 30.5 m by 61 m, and the same slope of the gable roof, 2.39^{o}. The main difference between the buildings was the eave height: 6.1 m and 9.8 m.

Each participating laboratory (six laboratories total) selected the number of pressure tap locations on building models depending on capabilities of their pressure measurement systems. Selection of the pressure tap locations was based on a layout developed by the Boundary Layer Wind Tunnel Laboratory at the University of Western Ontario, for wind tunnel testing carried out as part of the NIST/Texas Tech University Windstorm Mitigation Initiative (Ho *et al.*, 2003). The number of pressure taps ranged from 115 taps to 625 taps among the six laboratories.

The wind-induced pressures on the low-rise building models were acquired for two wind exposures: open and suburban terrains. The measurements of the pressures were performed for wind directions between 0^{o} and 180^{o} with increments of 5^{o} or 10^{o}. The sampling rate ranged from 300 Hz through 1000 Hz. Table 4.5 summarizes the wind tunnel testing conditions employed by the six participating laboratories. Letter labeling - A through F - is used to denote the source (participating laboratory) of the compared external point pressure, computed internal forces, approach wind and other referenced information provided by the laboratories.

In view of varying capabilities – the number of data channels of pressure measurement systems available at different laboratories (see Table 4.5) - a subset of that layout (comprising of a smaller number of taps) was chosen for comparison of inter-

laboratory data, in this investigation. The selected taps were arranged in rows 1 through 5, as schematically depicted in Figure 4.2.

Table 4.5 Summary of wind tunnel testing conditions for six laboratories

Laboratory		A	B	C	D	E	F
Geometric scale		1:150	1:200	1:200	1:200	1:200	1:200
Eave height		6.1 m 9.8 m	6.1 m 9.8 m	6.1 m 9.8 m	6.1 m 9.8 m	6.1 m 9.8 m	6.1 m
Number of taps	H_{eave} = 6.1 m	336	115	625	207	437	442
	H_{eave} = 9.8 m	364	125	557	225	475	
Wind exposure		open suburban	open suburban	open suburban	open suburban	open suburban	open
Wind directions	Range	0^o-185^o	0^o-180^o	0^o-180^o	0^o-180^o	0^o-180^o	10^o-360^o
	Increment	5^o	5^o	5^o	10^o	5^o	10^o

4.5 DEVELOPMENT OF NUMERICAL TOOL FOR WIND-INDUCED INTERNAL FORCE ANALYSIS

The main wind force resisting system (MWFRS) of the prototype building, employed in the analysis of wind-induced internal forces, comprised of two end frames and seven interior frames, as shown in Figure 4.3. This structural system was also used by Whalen *et al*. (1998) and Endo *et al*. (2004).

Simplified geometry of frames, displayed in Figure 4.4, was assumed in determination of influence lines for vertical and horizontal reaction forces at two supports, A and E of a representative frame. Parameters α and β, indicated in Figure 4.4, were introduced to allow for modification of the relative flexural rigidity of the frame and its effects on the calculated reaction forces. The coefficient α is the ratio of the flexural

rigidity (EI) of the frame roof part to the rigidity of the column. The frame span-to-height ratio is controlled by the parameter β.

The influence lines for the vertical and horizontal reactions at various frame locations, see Figure 4.4, were first calculated. The equations of the influence lines for those reactions were expressed as functions of α, β, h, P, x_1, x_2 and x_3, defined in Figure 4.5.

For $0 \leq x_1 < h$ in left column,

$$H_A = P\left[\frac{3}{2}\left(\frac{\alpha}{2\alpha+3\beta}\right)\left\{\left(\frac{x_1}{h}\right)\left(1+\frac{\beta}{\alpha}\right)-\frac{1}{3}\left(\frac{x_1}{h}\right)^3\right\}-1\right] \quad [4.21]$$

$$V_A = -\frac{P}{\beta}\left(\frac{x_1}{h}\right) \quad [4.22]$$

$$H_E = \frac{3}{2}P\left(\frac{\alpha}{2\alpha+3\beta}\right)\left\{\left(1+\frac{\beta}{\alpha}\right)\left(\frac{x_1}{h}\right)-\frac{1}{3}\left(\frac{x_1}{h}\right)^3\right\} \quad [4.23]$$

$$V_E = \frac{P}{\beta}\left(\frac{x_1}{h}\right) \quad [4.24]$$

For $0 \leq x_2 \leq \beta h$ in roof beam,

$$H_A = \frac{3}{2}P\left(\frac{1}{2\alpha+3\beta}\right)\beta^2\left\{\left(\frac{x_2}{\beta h}\right)^2-\left(\frac{x_2}{\beta h}\right)\right\} \quad [4.25]$$

$$V_A = P\left\{1-\left(\frac{x_2}{\beta h}\right)\right\} \quad [4.26]$$

$$H_E = \frac{3}{2}P\left(\frac{1}{2\alpha+3\beta}\right)\beta^2\left\{\left(\frac{x_2}{\beta h}\right)^2-\left(\frac{x_2}{\beta h}\right)\right\} \quad [4.27]$$

$$V_E = P\left(\frac{x_2}{\beta h}\right) \qquad [4.28]$$

For $0 \leq x_3 \leq h$ in right column,

$$H_A = \frac{3}{2}P\left(\frac{\alpha}{2\alpha+3\beta}\right)\left\{\left(1+\frac{\beta}{\alpha}\right)\left(\frac{x_3}{h}\right)-\frac{1}{3}\left(\frac{x_3}{h}\right)^3\right\} \qquad [4.29]$$

$$V_A = \frac{P}{\beta}\left(\frac{x_3}{h}\right) \qquad [4.30]$$

$$H_E = P\left[\frac{3}{2}\left(\frac{\alpha}{2\alpha+3\beta}\right)\left\{\left(\frac{x_3}{h}\right)\left(1+\frac{\beta}{\alpha}\right)-\frac{1}{3}\left(\frac{x_3}{h}\right)^3\right\}-1\right] \qquad [4.31]$$

$$V_E = -\frac{P}{\beta}\left(\frac{x_3}{h}\right) \qquad [4.32]$$

The derivations of these equations are presented in Appendix B. Representative results - influence lines for reactions at the two supports (A and E) of the frame (see Figure 4.4) are shown in Figure 4.6, for $\alpha = \beta = 1$ and P = 1. The obtained influence lines were subsequently used to calculate the time series of the reaction forces, via weighted summation involving (for each time step) instantaneous values of the wind-induced pressures pre-multiplied by appropriate tributary areas indicated in Figure 4.7. The bending moments at selected sections of the frame were calculated in a similar manner. For the computation of the wind-induced internal forces on a structural frame, a computer program, based on the influence line functions for the support reactions defined in Equations [4.21] through [4.32], was developed using LabView programming software, with a user interface shown in Figure 4.8. For a selected number of simplified wind

loadings, the computed internal forces were validated by hand calculations and by commercial structural analysis software.

For the calculation of the internal forces in structural frames of the MWFRS, it was assumed that the building was located in open terrain, within Miami, FL. Similar wind conditions were selected by Whalen *et al*. (1998) and Jang *et al*. (2002). According to the ASCE7 Standard (2005), the basic wind speed at this location – 3 second gust wind speed at an elevation of 10 m – is 66.7 m/sec. The corresponding mean hourly wind speed at the roof height $\overline{V}_{\bar{z}}$ was determined using the relationship defined in the ASCE7 Standard (2005)

$$\overline{V}_{\bar{z}} = \bar{b}\left(\frac{\bar{z}}{33}\right)^{\bar{\alpha}} V\left(\frac{88}{60}\right) \qquad [4.33]$$

where $\bar{b}$ = mean hourly wind speed factor ($\bar{b}$ = 0.65 for Exposure C),
V = basic wind speed (mph),
$\bar{z}$ = equivalent height of structure (ft), and
$\bar{\alpha}$ = power law exposure for mean hourly wind speed ($\bar{\alpha}$ = 1/6.5 for Exposure C)

The calculated hourly mean wind speed obtained from Equation [4.33] was 43.4 m/sec.

The representative time snapshots of the computed wind-induced internal forces - bending moments M_x in frame F2 (see Figure 4.3), for wind directions of 0^o, 45^o and 90^o, are presented in Figure 4.9. The bending moments were computed using the building pressure data in tap rows 2 to 4 acquired for a building model with an eave height of 9.8 m (prototype) in laboratory B. Each graph in the figure shows the representative 200 instantaneous (consecutive) distributions of M_x.

4.6 RESULTS AND DISCUSSION

The primary focus of this study was to investigate the inter-laboratory discrepancy in wind-induced loadings among the participated laboratories. Results of this effort are presented herein. While wind loading uncertainty estimates were not provided by each laboratory, estimates based on repeated tests from one particular laboratory indicated a coefficient of variation (COV) of approximately 2% in the mean wind speed and a COV of approximately 3% in the mean and standard deviation of pressure coefficients.

Representative wind-induced mean and standard deviation of roof pressures at tap rows 1 through 5 (tap locations are defined in Figure 4.2), acquired at five laboratories are depicted in Figures 4.10 through 4.15. In this comparison, three wind directions (0^o, 40^o and 90^o), two wind exposures (open and suburban terrains) and two eave heights (6.1 m and 9.8 m) were considered. Similarly, the resulting wind-induced mean bending moments in frames F1 and F2 (frames are defined in Figure 4.3), normalized by the square of the rooftop mean velocity, are shown in Figures 4.16 through 4.19.

As can be seen, the mean and standard deviations of the roof pressures (provided by the participating laboratories) exhibit measurable discrepancies. Larger discrepancies are observed in regions of windward corner and edges, where relatively larger suction pressures occur, especially in suburban wind exposure. Similar trends are exhibited by the mean bending moments, especially at the windward corner(s) and around the middle portion of the roof beam, in suburban exposure.

The time series of roof pressures and bending moments were subsequently employed to predict peak pressures and peak bending moments. The peak estimation

procedure described in Section 4.3 was employed. A computational tool was developed for this procedure using LabView programming software, see Figure 4.20. Representative results of the predicted peaks are presented in Figures 4.21 through 4.24, for open and suburban wind exposures, and two eave heights (6.1 m and 9.8 m). The 90th percentile peak roof pressures at taps P1 and P2 (see Figure 4.2) in a roof corner region are displayed in Figures 4.21 and 4.22, respectively. The 90th percentile peak bending moments at location B in frames F1 and F2 (see Figures 4.3 and 4.4) are shown in Figures 4.23 and 4.24, respectively.

As observed in the above comparisons of the mean and standard deviation, the predicted peak pressures and bending moments also exhibit significant scatter, especially in suburban wind exposure. Next, the observed variability is quantified using the coefficient of variation (COV). Figure 4.25 compares the COVs of mean and peak roof pressures at taps P1 and P2, for the open and suburban exposures, and two eave heights. It can be seen that the COVs for suburban exposure is significantly larger than for open exposure, for both the peak and mean roof pressures. Similarly, comparisons of COVs for the peak and mean bending moments at location B in frames F1 and F2 are shown in Figure 4.26. Larger COVs were also observed for suburban terrain, especially in the mean bending moments.

Next, the modeled laboratory approach flows were compared. It was found that significantly different experimental set-ups were used by the laboratories to simulate target wind exposures. Figure 4.27 compares the wind tunnel configurations employed to generate open and suburban wind exposures at three representative laboratories (denoted A, B and C). The impact of the differences in the setups depicted in Figure 4.27 can be

inferred from Figures 4.28 and 4.29, where the available vertical profiles of the along-wind mean velocity and turbulence intensity are displayed for the two wind exposures (open and suburban).

As can be seen in Figure 4.28, the inter-laboratory discrepancy in the mean velocity profiles is moderate. The power-law exponent *a* ranged from 0.134 to 0.191 (target value of 0.143) and from 0.201 to 0.234 (target value of 0.22) for the open and suburban terrain wind exposures, respectively. The roughness length z_0 ranged from 0.014 to 0.121 (target value of 0.03 m) and from 0.176 to 0.279 (target value of 0.3) for open and suburban terrains, respectively. Table 4.6 lists characteristics *a* and z_0 of the approach flows generated by the participating laboratories.

Table 4.6 Characteristics of approach flows generated by participating laboratories

Wind exposure	Parameter	Target	Laboratory					
			A	B	C	D	E	F
Open	*a*	0.143	0.139	0.147	0.134		0.191	0.183
	z_0 (m)	0.03	0.014	0.021	0.016		0.109	0.121
Suburban	*a*	0.22	0.212	0.234	0.201		0.225	
	z_0 (m)	0.03	0.176	0.279	0.260		0.249	

In Figure 4.29, along-wind turbulence intensity profiles are compared for two ranges of elevations (up to 100 m in the left graphs and up to 30 m in the right graphs). The graphs on the right show that the spread among the compared turbulence intensity profiles is significantly larger. The larger discrepancy is observed for the (modeled) suburban terrain. It should be pointed out that the participating laboratories used different empirical models to define the target profiles for the approach flows modeled in

their (boundary-layer) wind tunnels. Representative comparisons of these turbulence models (described in Section 4.2) are depicted in Figure 4.30. The compared models include: ASCE (2005), Eurocode (1995), AIJ (1996), AS1170.2 (1989, from Zhou and Kareem (2002)), NBCC (1996, from Zhou and Kareem (2002)), and two variants of ESDU models (from Ho *et al*. (2003) and Flamand (2003)). The spread in these profiles is overall similar to that exhibited by the profiles of the simulated (laboratory) approach flows, shown in Figure 4.29.

The comparison of the results for roof pressures and bending moments originating from different laboratories revealed a scatter among these data. This scatter has been primarily attributed to the level of turbulence modeled in laboratory approach flows. The highest level of the inter-laboratory discrepancy in the compared wind pressures and internal forces occurred in suburban terrain, which exhibited the largest discrepancy in the turbulence intensity of the modeled approach flow, as seen in Figure 4.29.

The overall COV of roof pressures and bending moments are compared in Table 4.7 with the COV of turbulence intensity. For each of the four cases displayed in the table (see left-most column), the right-most column is the average of COV of the peak and mean roof pressure (Cp) and bending moment at location B (M_B). In open exposure, the inter-laboratory variability in the roof pressure and the frame bending moment was moderate with the average COV of approximately 14% for the eave height of 6.1 m and 11% for the eave height of 9.8 m. In contrast, the variability was approximately twice as large in suburban terrain. This increase can be attributed to an increased variability in the turbulence level (turbulence intensity), as displayed in Table 4.7. It is postulated that the inter-laboratory variability in the internal loading reported by Fritz *et al*. (2006), in large

measure was caused by the variability in the approach flow turbulence employed in physical modeling of wind-induced pressures on the tested buildings, by the participating laboratories.

Table 4.7 Overall inter-laboratory variability of approach flows, point pressures and frame bending moments

Eave height (m)	Exposure	Turbulence intensity (%)				COV (%) for Cp(peak) [Cp(mean)]		COV (%) for M_B(peak) [M_B(mean)]		Average COV (%)
		Max	Mean	Min	COV	Tap P1	Tap P2	Frame F1	Frame F2	
6.1	Open	21.1	19.6	18.2	6.2	16.6 [11.7]	11.6 [9.0]	14.7 [8.8]	21.3 [13.1]	13.4
6.1	Suburban	31.2	27.4	24.9	9.9	26.9 [32.3]	22.9 [21.3]	21.9 [31.0]	21.7 [45.5]	27.9
9.8	Open	20.7	19.3	16.8	9.1	20.4 [8.8]	10.4 [8.4]	13.7 [6.6]	13.1 [8.4]	11.2
9.8	Suburban	32.4	27.0	23.8	13.8	26.9 [31.3]	24.3 [19.7]	24.6 [26.2]	22.2 [33.0]	26.0

For the measurement of time-varying surface pressures on a building model, it is common that pressures are measured through long or short tubes connecting from pressure taps on the surface of the model with pressure transducer(s). However, longer tubing system creates more distortion of pressure fluctuations, over a frequency range of interest. Figure 4.31 shows the frequency response of tubing systems employed by representative three participating laboratories. As can be seen, the levels of error associated with distortions in the magnitude of the system transfer function depended on a particular laboratory and they varied from approximately 6 % through 18 %.

The representative comparisons of power spectra for roof pressure fluctuations at locations (pressure taps) P1 and P2 (see Figure 4.2) are shown in Figures 4.32 and 4.33, respectively, for three wind directions (0^o, 40^o and 90^o) and two wind exposures (open and suburban). In these two figures, there are some variations in the power spectra in lower frequency range, frequencies lower than n = 1 Hz.

4.7 CONCLUSIONS

The main findings resulting from the study described in this chapter can be summarized as follows:

1. The largest variability in the laboratory wind-induced pressures and the associated bending moments on the generic low-rise building models was found in suburban wind exposure.
2. The variability in the laboratory wind-induced loading was primarily attributed to differences in the approach flows employed in physical modeling of wind pressures on tested building models, carried out by the participated laboratories.
3. The variability in the modeled approach flows was a result of the differences in the along-wind turbulence intensity implied by different empirical models defining the target wind exposures and used by the laboratories.
4. Comparison of power spectra for roof pressure provided by the participating laboratories showed discrepancies in low and high frequency ranges. Some of these departures might have been caused by the resonance effects the employed tubing-pressure measurement systems, aliasing effects or other experimental variability.

4.8 REFERENCES

AIJ. (1996). *Recommendations for loads on buildings*, Architectural Institute of Japan, Tokyo, Japan.

AS1170.2. (1989). *Australian standards: SAA loading code, Part2 – Wind loads*, AS1170.2-89, Australia.

ASCE. (2005). *Minimum design loads for buildings and other structures*, ASCE Standard, ASCE/SEI 7-05, American Society of Civil Engineers, New York, USA.

Bienkiewicz, B. and Endo, "Recent efforts on investigation of discrepancies in laboratory modeling of wind loading and development of standardized wind tunnel testing protocols for low buildings", *Proceedings of 2011 NSF Engineering Research and Innovation Conference*, Atlanta, Georgia, January 4-7, 2011, 10 pp.

Endo, M., Bienkiewicz, B., and Lim, J. (2004), *Wind engineering study in support of development of aerodynamic database – Part 2. Wind-induced pressures and internal forces in a generic low-rise building*, Technical Report, Wind Engineering and Fluids Laboratory, Colorado State University, 33 pp.

ESDU (1993), *Characteristics of atmospheric turbulence near the ground, Part II: Single point data for strong winds (neutral atmosphere)*, Engineering Science Data Unit.

Eurocode. (1995). *Eurocode 1:Basis of design and actions on structures. Part 2-4: Actions on structures–wind actions*, European Prestandard, ENV-1991-2-4, Brussels, Belgium.

Filliben, J.J. (1975), "The probability plot correlation coefficient test for normality", *Technometrics*, Vol. 17, No. 1, pp. 111-117.

Flamand, O. (2003). *Measurement of time series of pressures on a low-rise building for the NIST*, Tech. Rep. EN-CAPE 03.146 C-V0, CSTB, Nantes, France, 12 pp.

Fritz, W.P., Bienkiewicz, B., Flamand, O., Ho, E., Kikitsu, H., Letchford, C. W., and Bo, C. (2006). "International comparison of wind tunnel estimates of wind effects on an industrial building model: test-related uncertainties." *Proceedings of the 4th U.S.-Japan Workshop on Wind Engineering*, UJNR, Tsukuba, Japan, 51-62.

Ho, T.C.E., Surry, D., and Morrish, D. (2003). *NIST/TTU Cooperative agreement – Windstorm Mitigation Initiative: Wind tunnel experiments on generic low buildings*, Tech. Rep. BLWT-SS20-2003, The Boundary Layer Wind Tunnel Laboratory, The University of Western Ontario, London, Ontario, Canada, 105 pp.

Hosking, J.R.M. and Wallis, J.R. (1997), *Regional frequency analysis*, Cambridge University Press.

Jang, S., Lu, L.-W., Sadek, F., and Simiu, E. (2002), "Database-assisted wind load capacity estimates for low-rise steel frames," *Journal of Structural Engineering*, 128, 1594-1603.

NBCC. (1996). *Commentary B–Wind loads, User's guide-NBC 1995 structural commentaries*, Canadian Commission on Building and Fire Codes, National Research Council of Canada, Ottawa, Canada, Part 4, 9-42.

Sadek, F., and Simiu, E. (2002). "Peak non-Gaussian wind effects for database-assisted low-rise building design." *J. Eng. Mech*. 128 (5), 530-539.

Whalen, T., Simiu, E., Harris, G., Lin, J., and Surry, D. (1998). "The use of aerodynamic database for the effective estimation of wind effects in main wind-force resisting systems: application to low buildings." *J. Wind Eng. Ind. Aerodyn.* 77&78, 685-693.

Zhou, Y., and Kareem, A. (2002). "Definition of wind profiles in ASCE 7,"*J. Struct. Eng.*, 128 (8), 1082-1086.

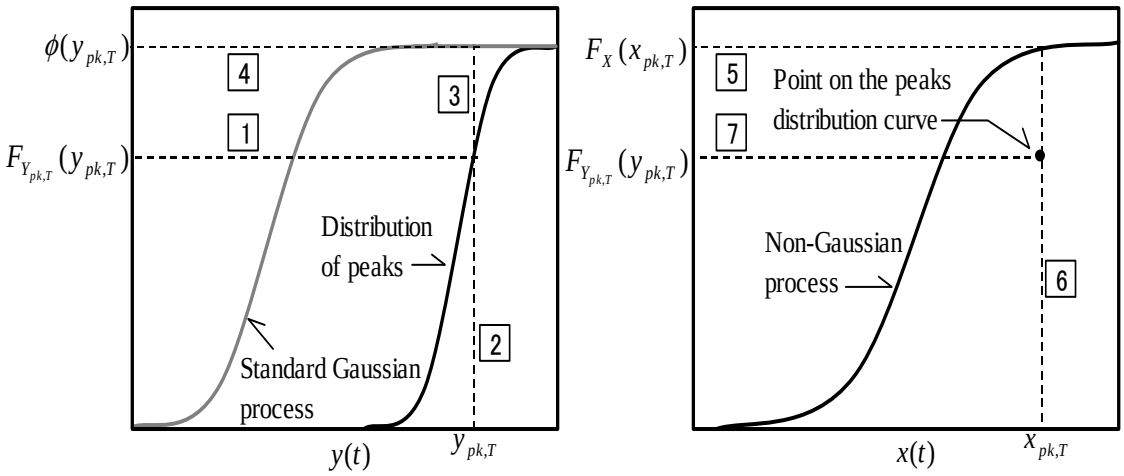

Figure 4.1 Mapping between non-Gaussian process $x(t)$ and Gaussian process $y(t)$ (Sadek and Simiu, 2002)

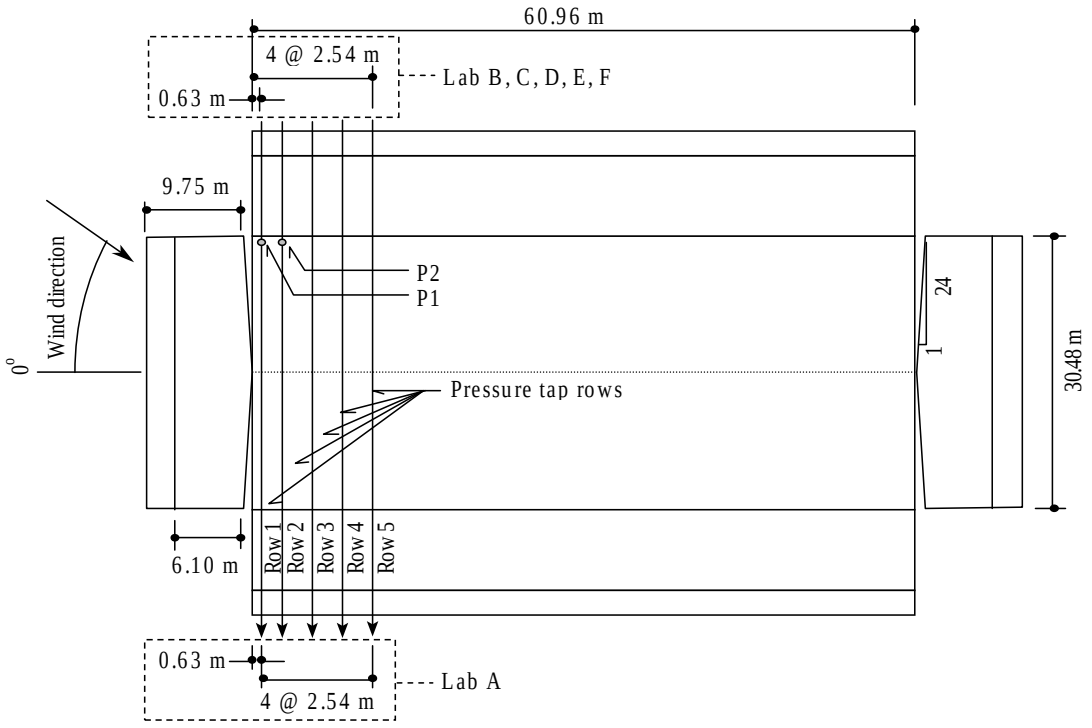

Figure 4.2 Geometry of prototype low-rise buildings and pressure tap locations

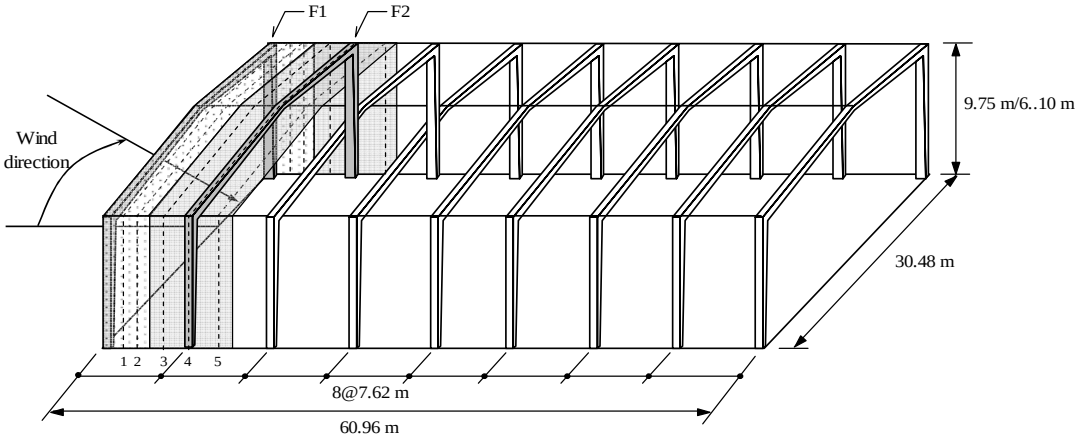

Figure 4.3 Geometry and MWFRS of low-rise building

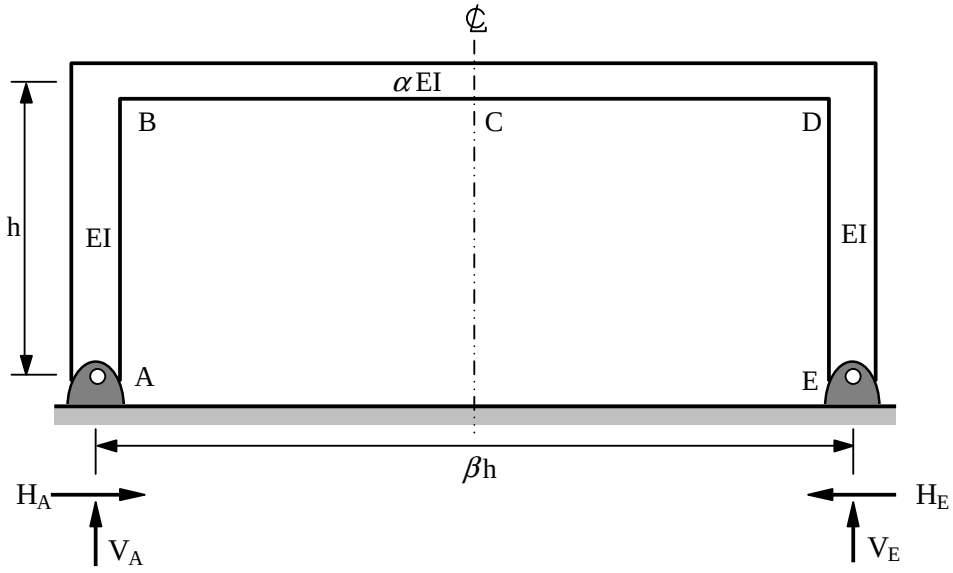

Figure 4.4 Idealized structural frame

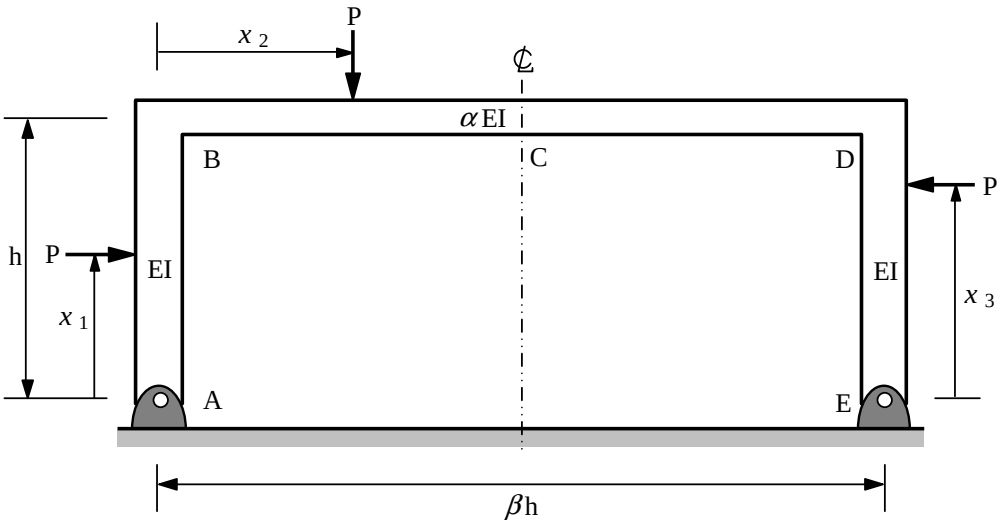

Figure 4.5 Definition of coordinate system for influence lines of structural frame

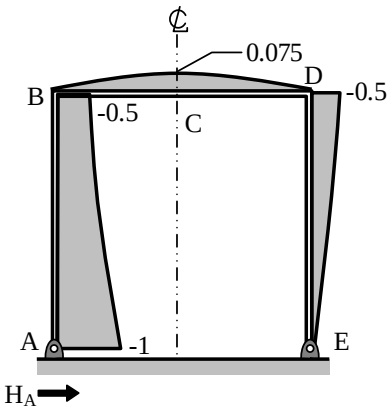

(a) Horizontal reaction at support A

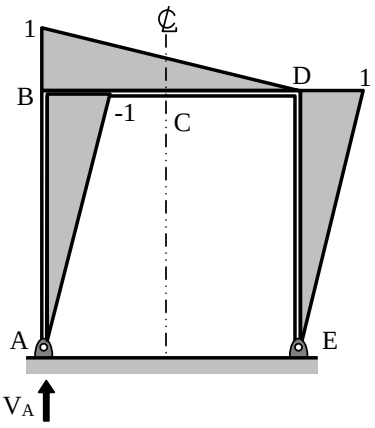

(b) Vertical reaction at support A

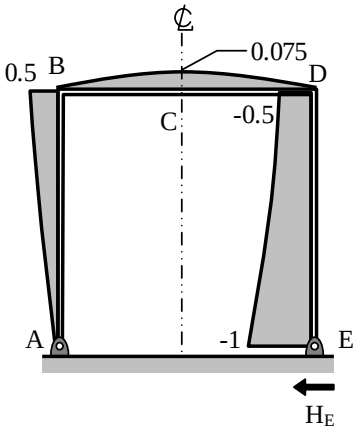

(c) Horizontal reaction at support E

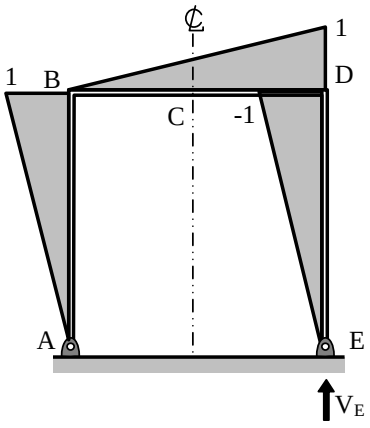

(d) Vertical reaction at support E

Figure 4.6 Influence lines of reactions at supports A and E

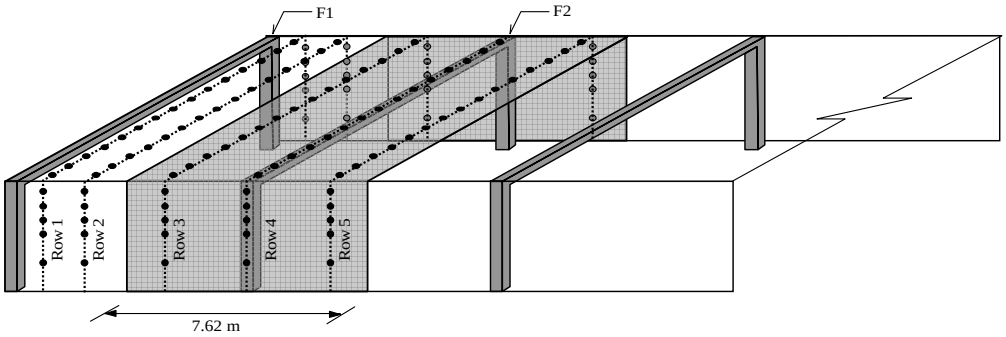

Figure 4.7 Description of tributary area

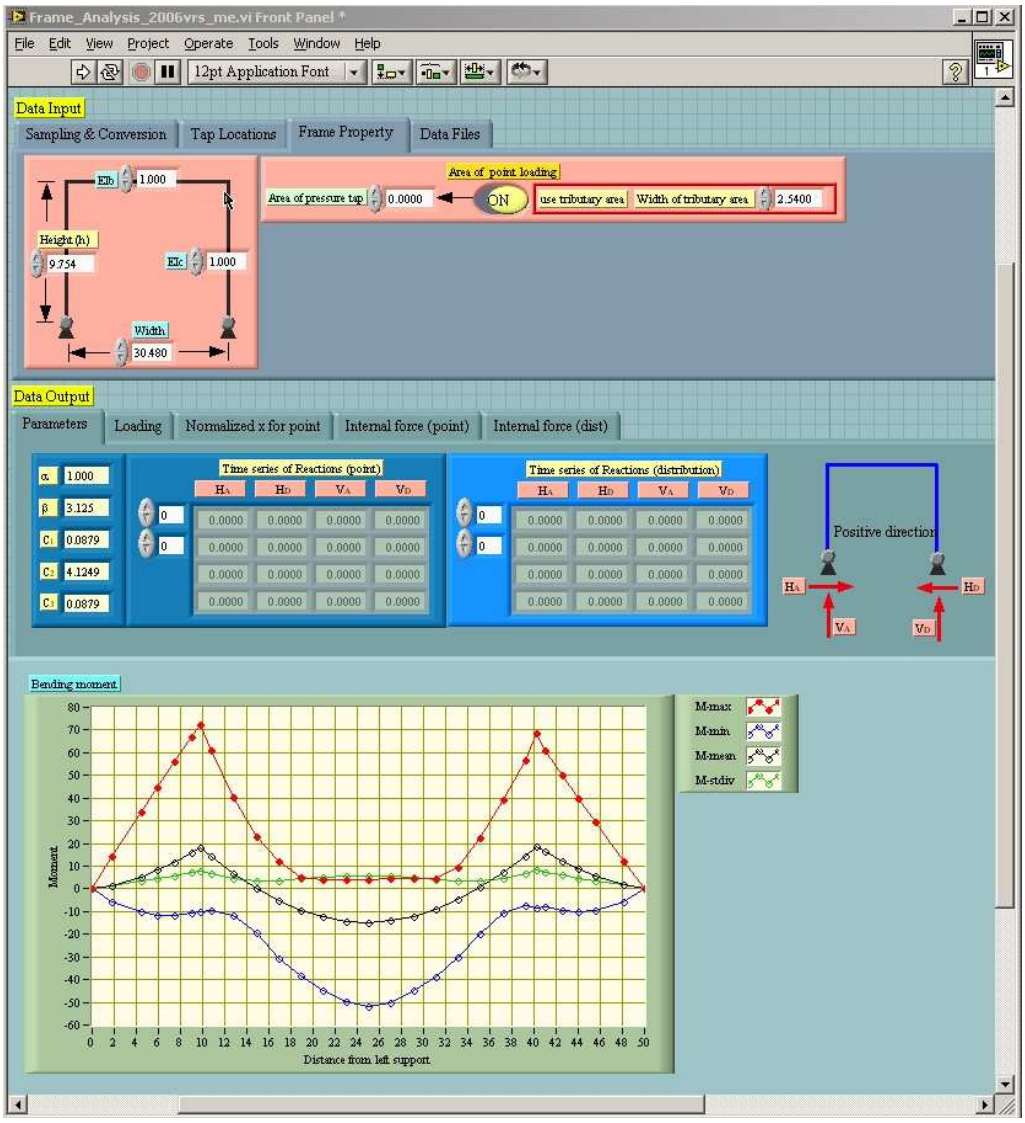

Figure 4.8 Wind-induced internal force analysis programmed in LabView software

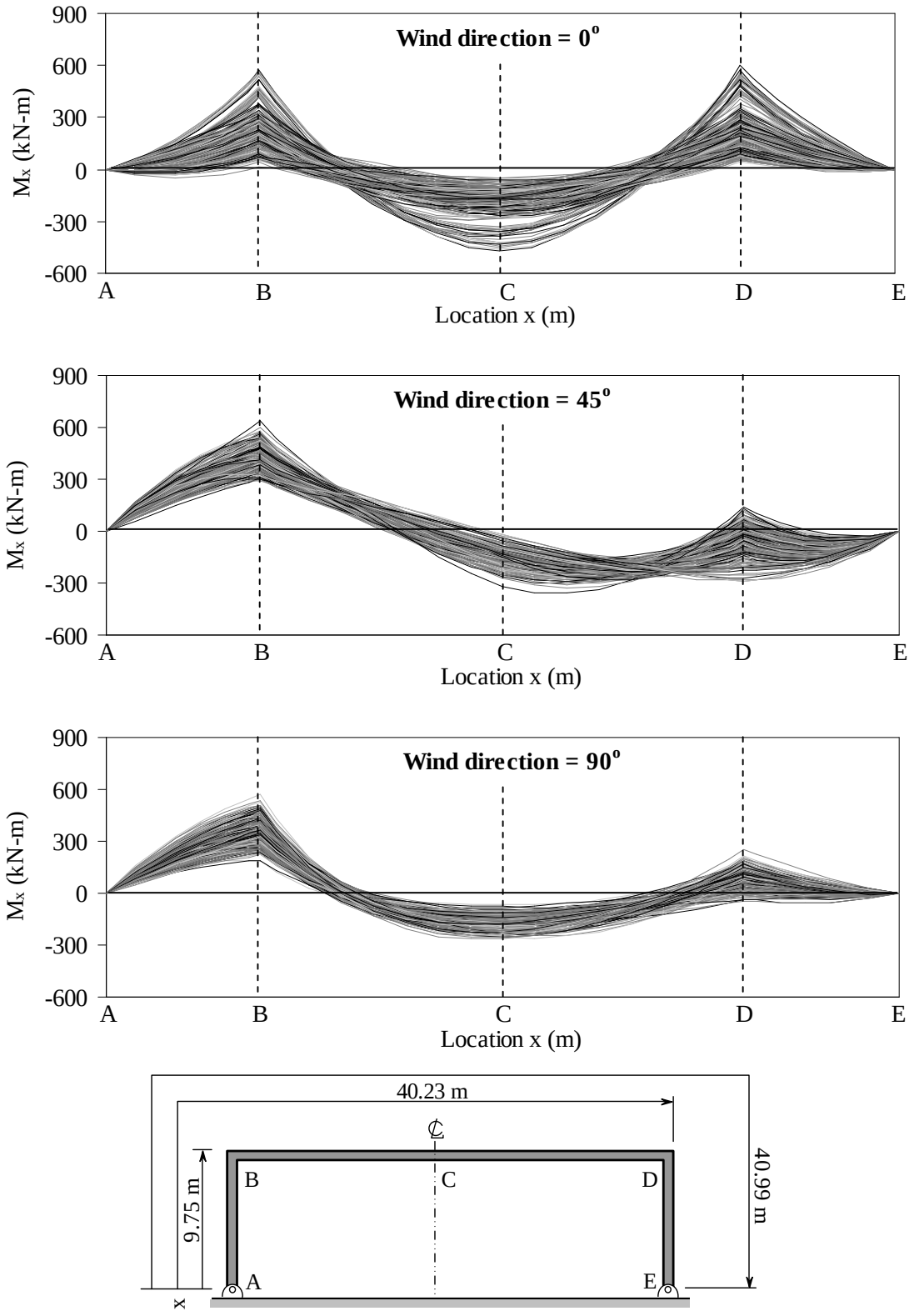

Figure 4.9 Trace of time series of bending moments

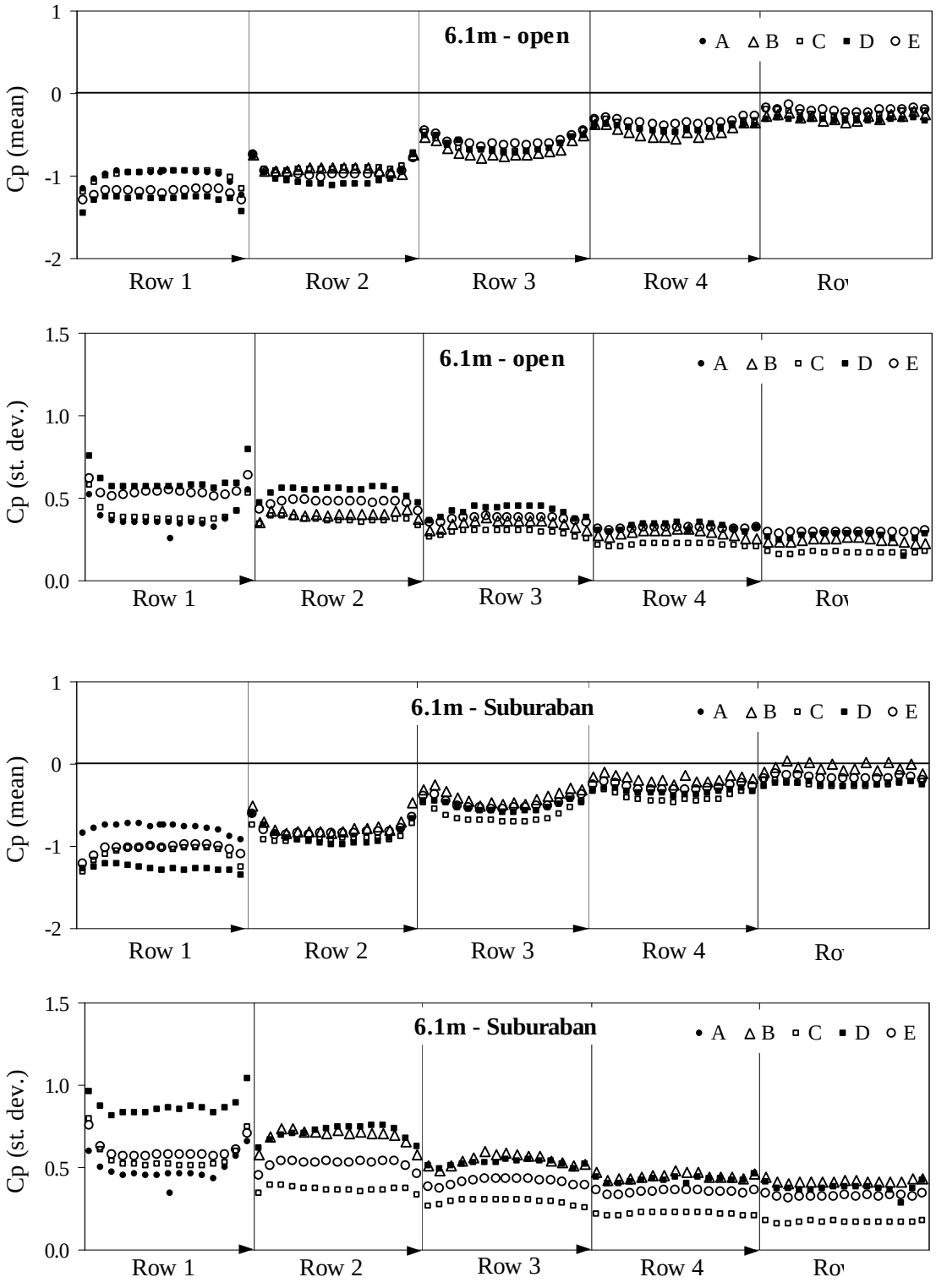

Figure 4.10 Mean and standard deviation of roof pressure coefficient, wind direction of 0^{o}, eave height = 6.1 m

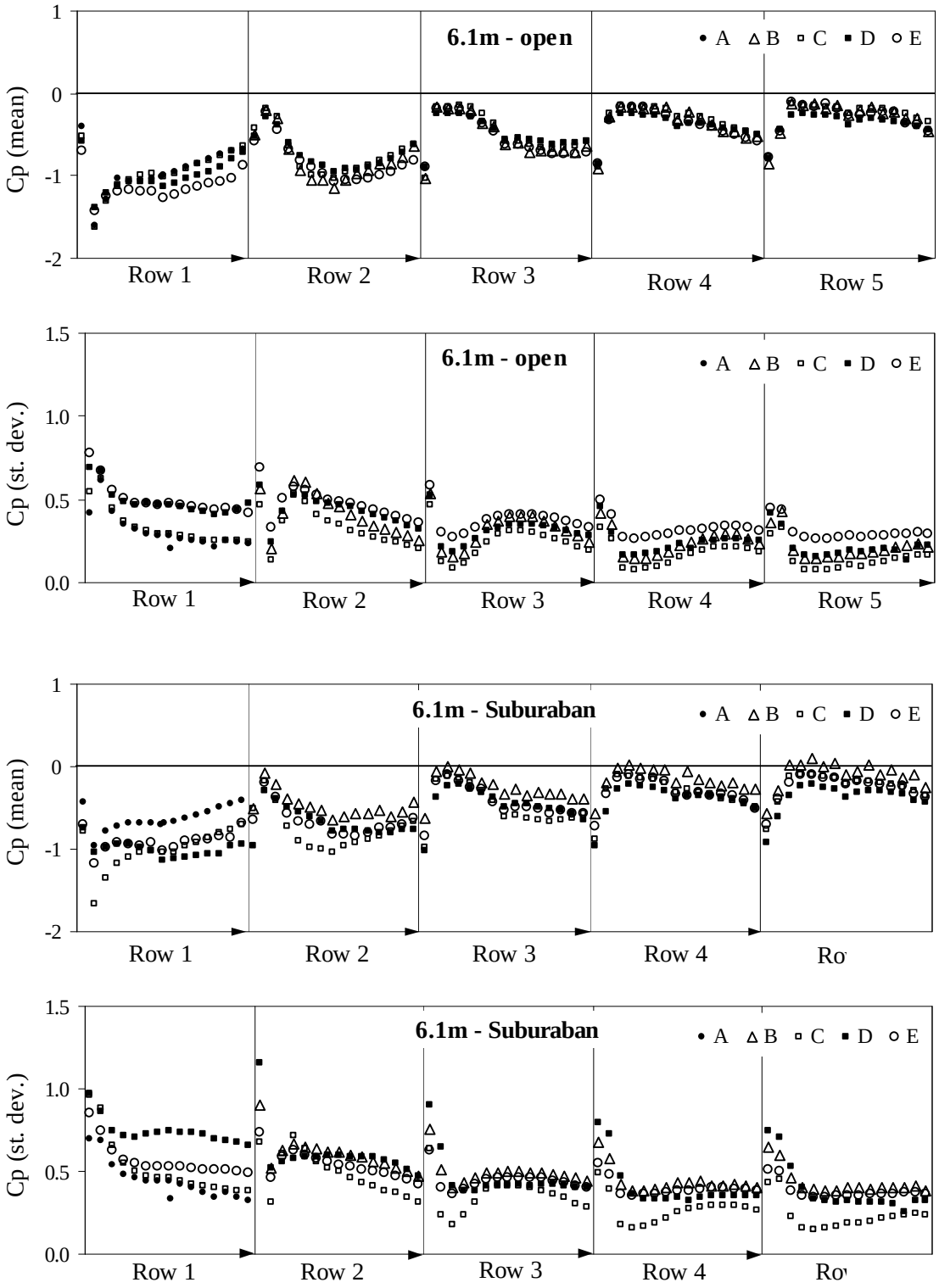

Figure 4.11 Mean and standard deviation of roof pressure coefficient, wind direction of 40°, eave height = 6.1 m

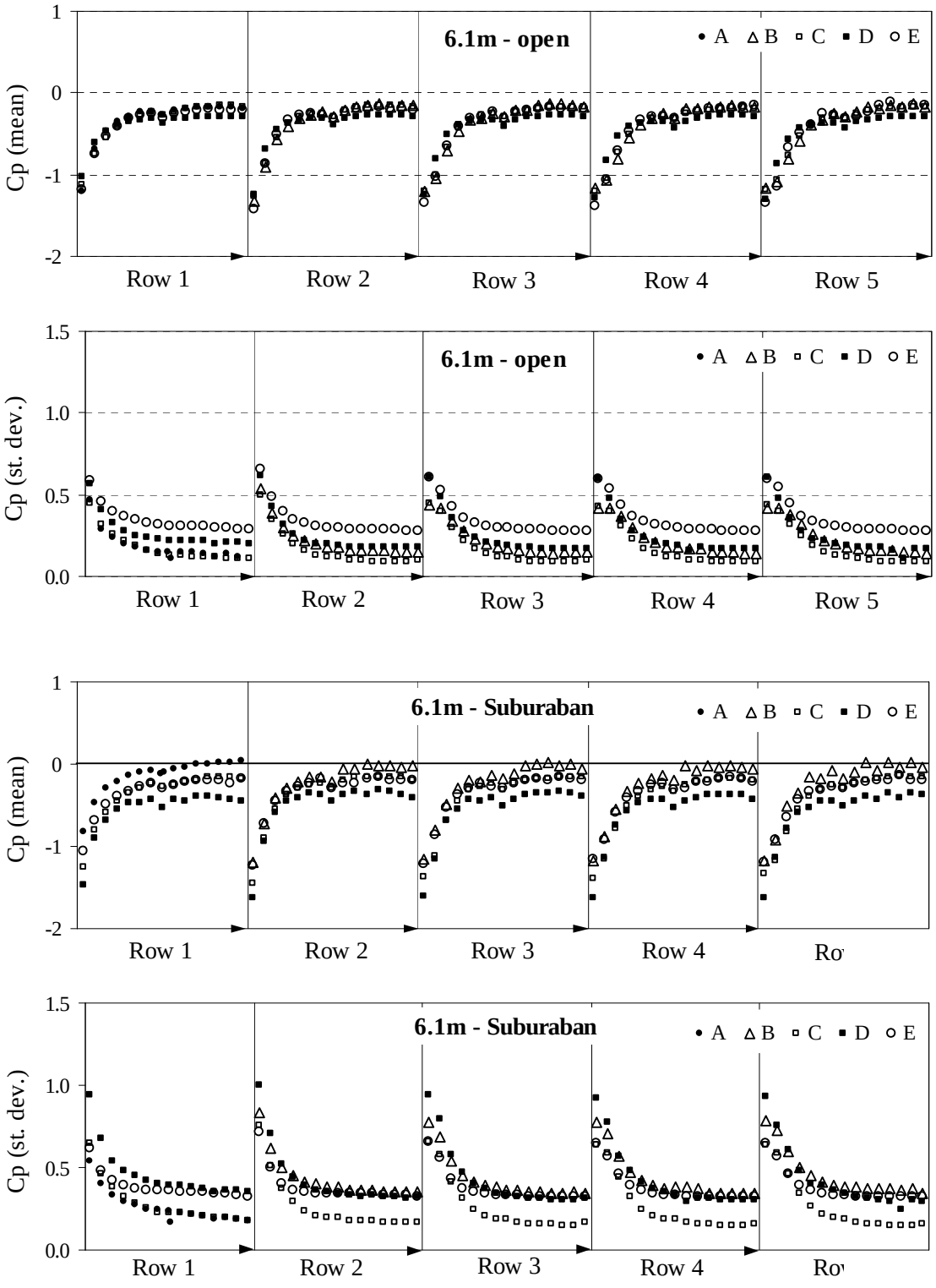

Figure 4.12 Mean and standard deviation of roof pressure coefficient, wind direction of 90^{o}, eave height = 6.1 m

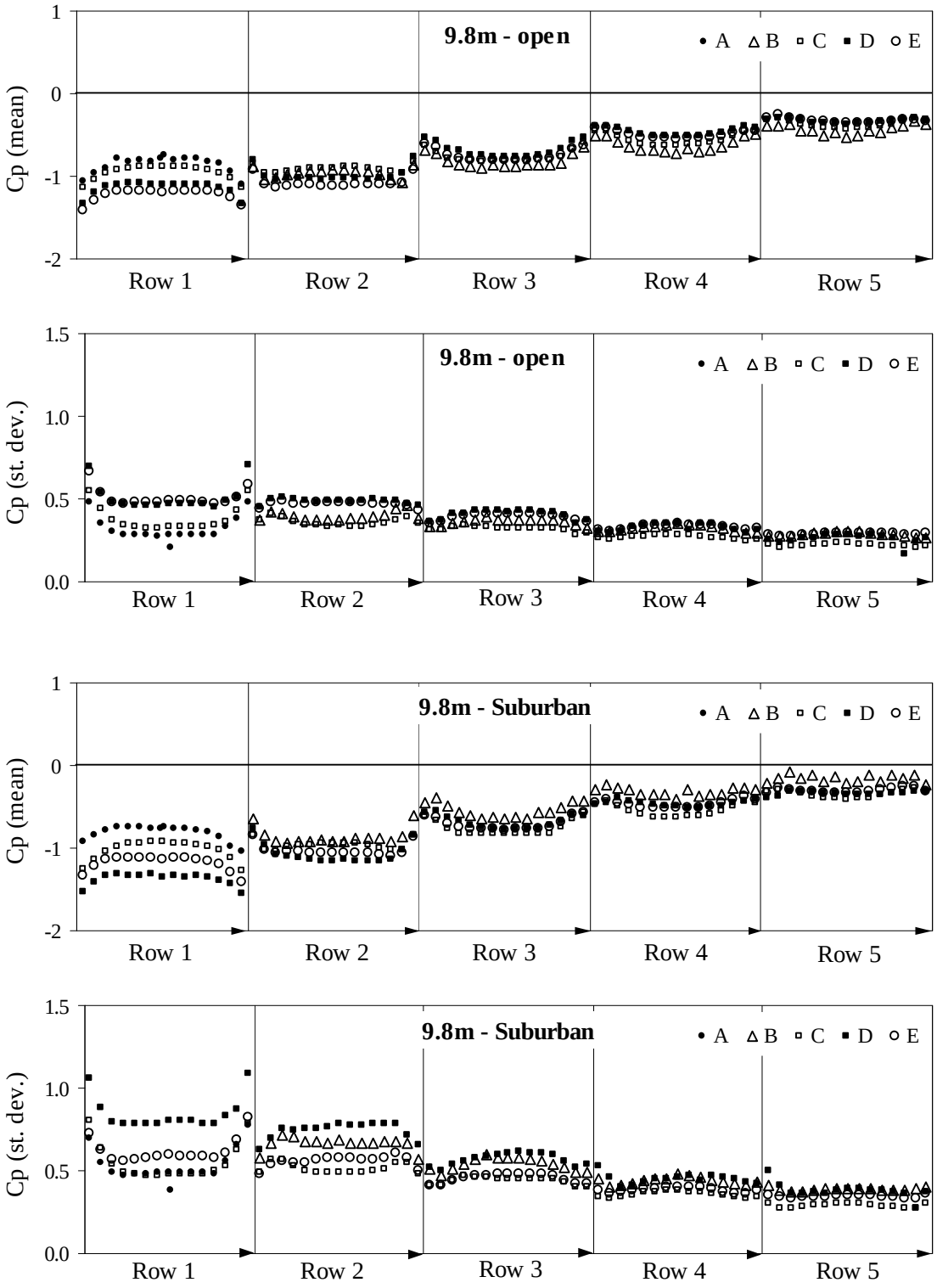

Figure 4.13 Mean and standard deviation of roof pressure coefficient, wind direction of 0^{o}, eave height = 9.8 m

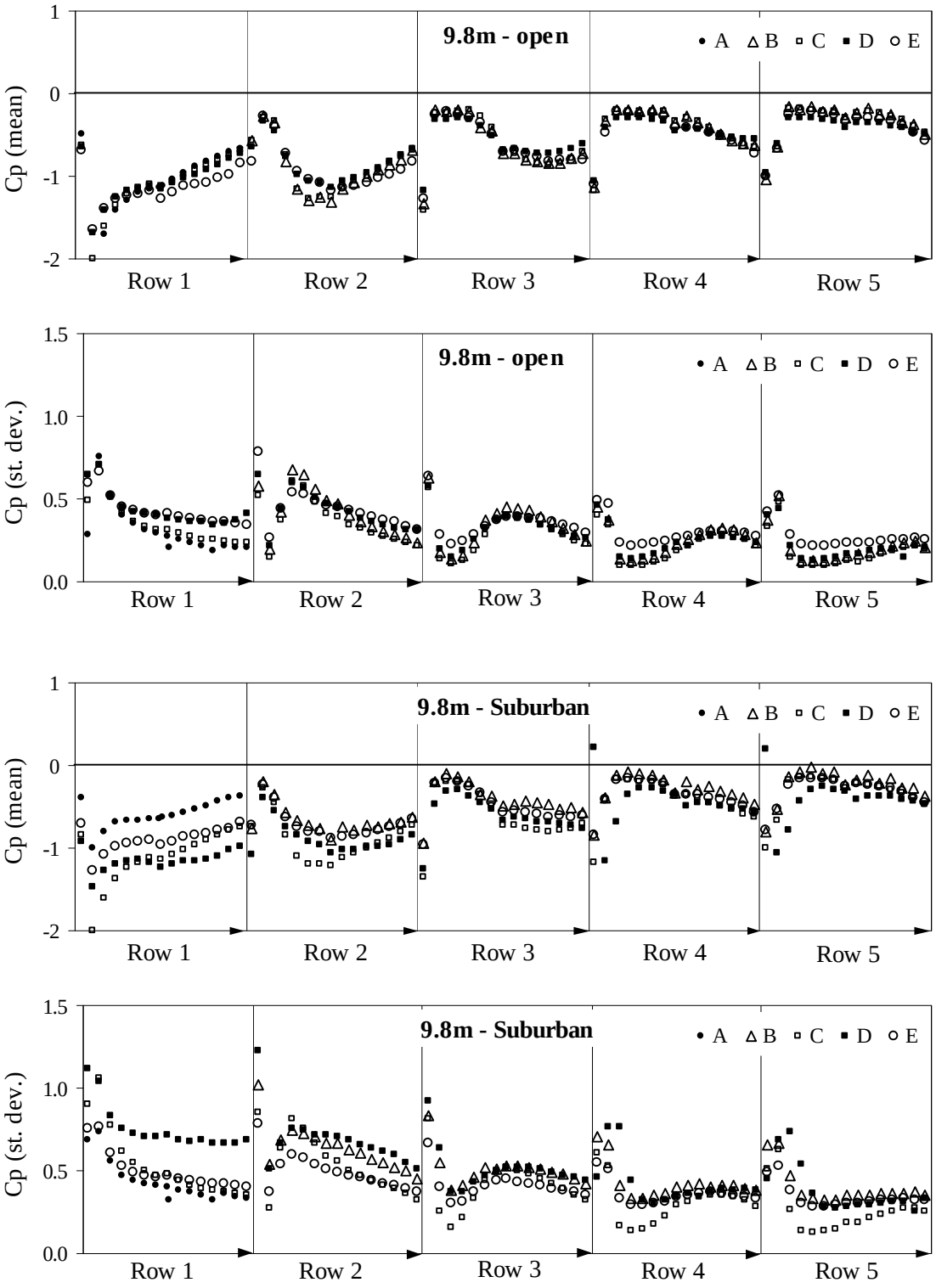

Figure 4.14 Mean and standard deviation of roof pressure coefficient, wind direction of 40^{o}, eave height = 9.8 m

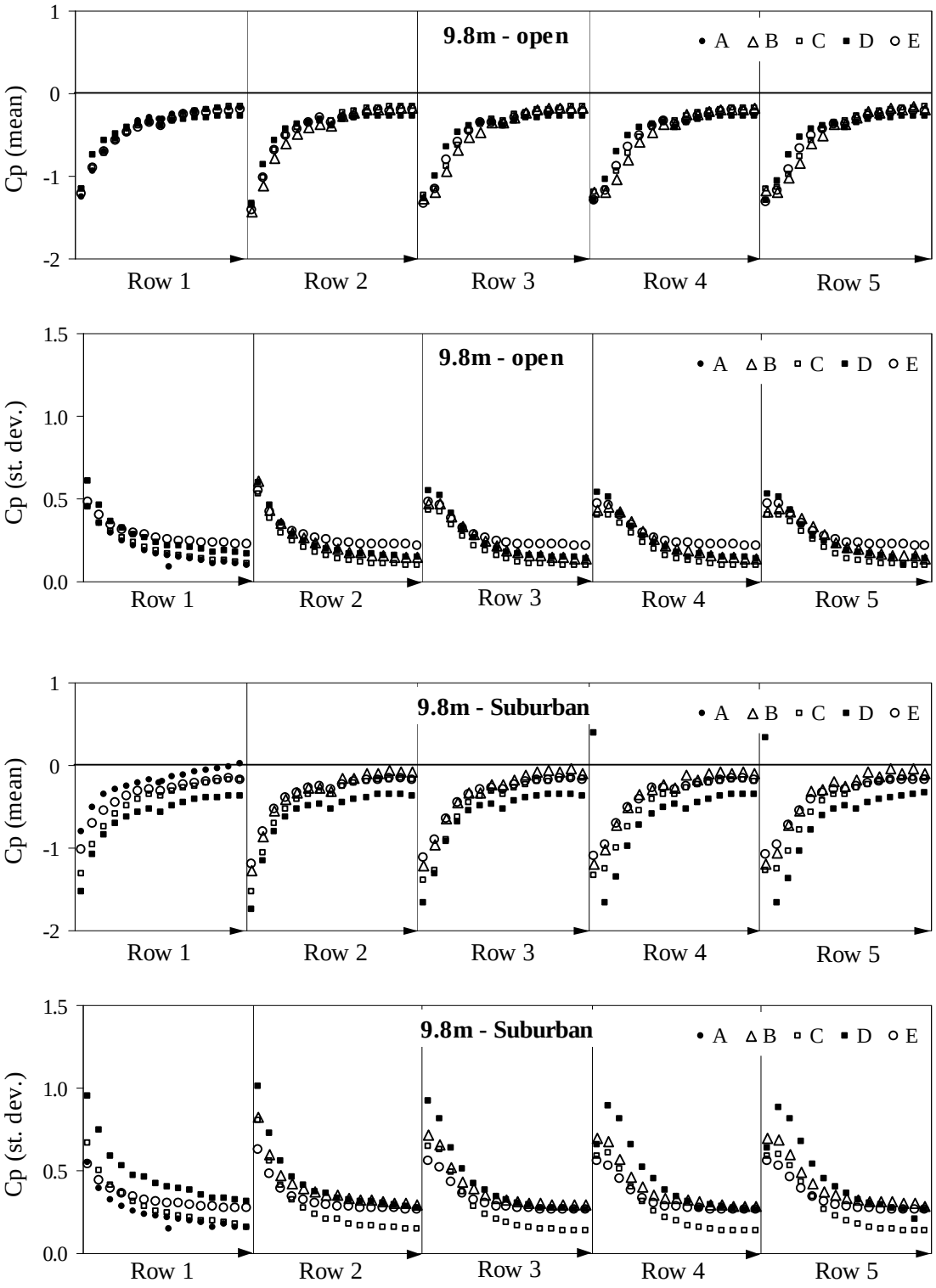

Figure 4.15 Mean and standard deviation of roof pressure coefficient, wind direction of 90^{o}, eave height = 9.8 m

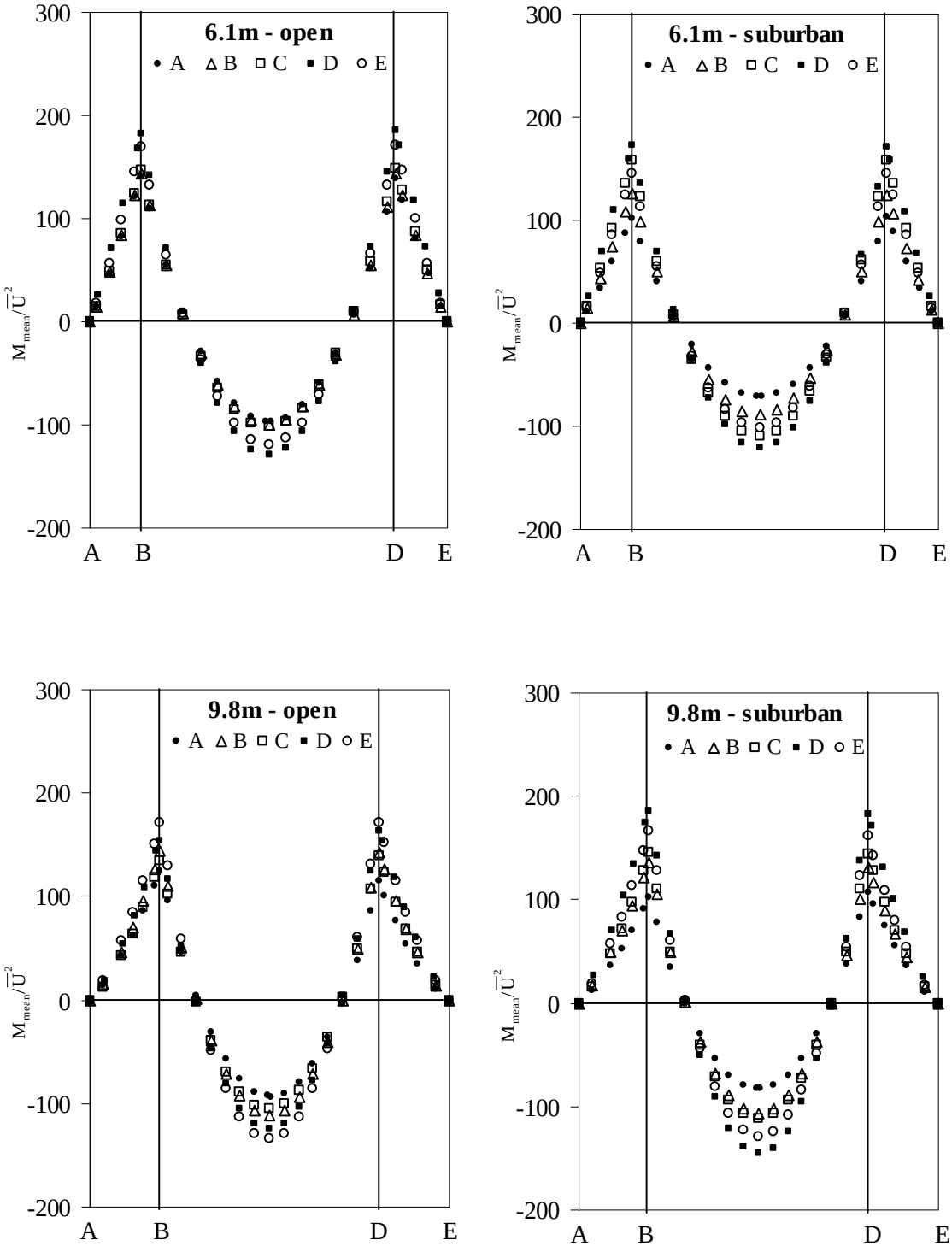

Figure 4.16 Mean bending moment, frame F1, wind direction of 0^o

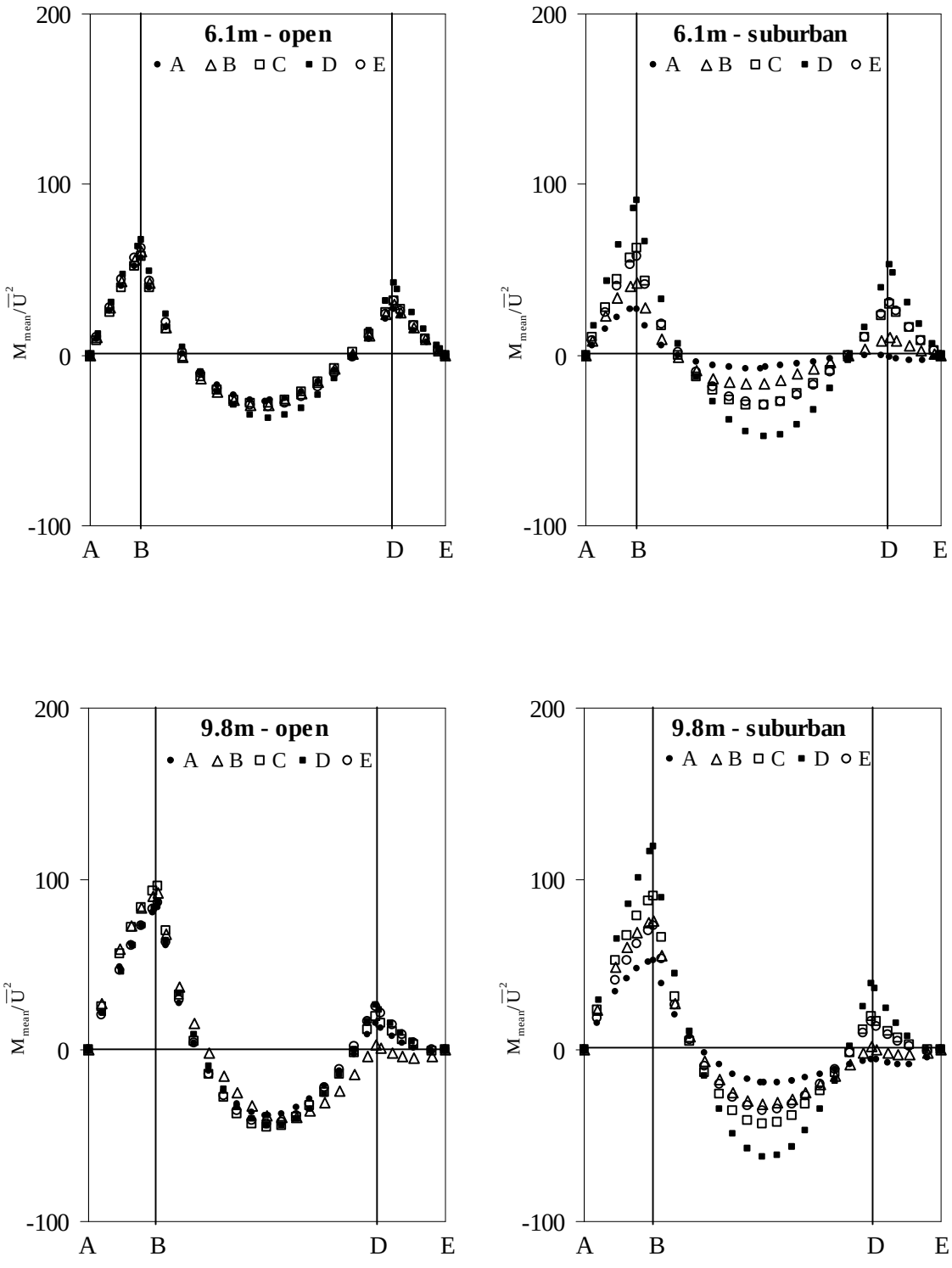

Figure 4.17 Mean bending moment, frame F1, wind direction of 90^o

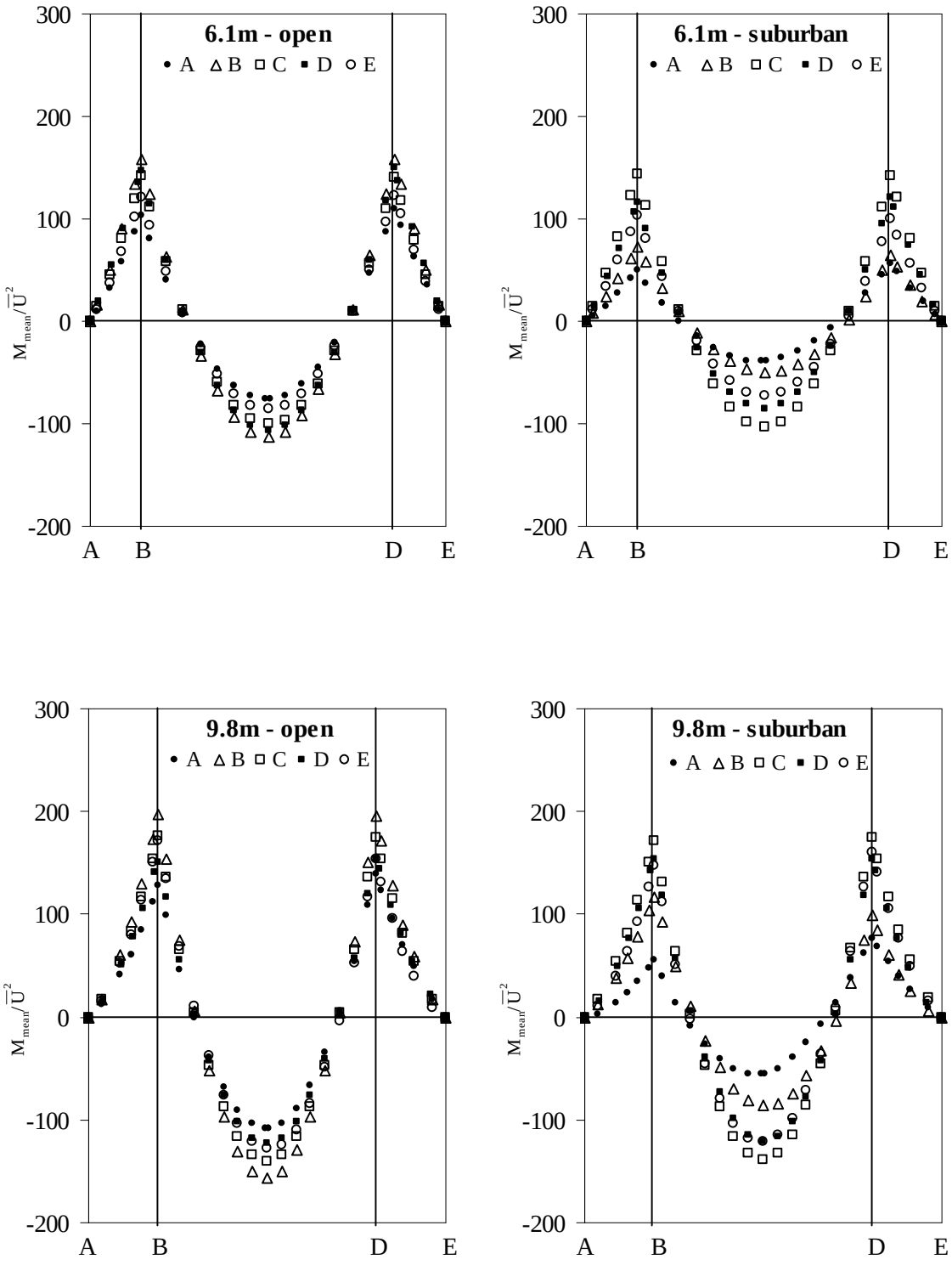

Figure 4.18 Mean bending moment, frame F2, wind direction of 0^o

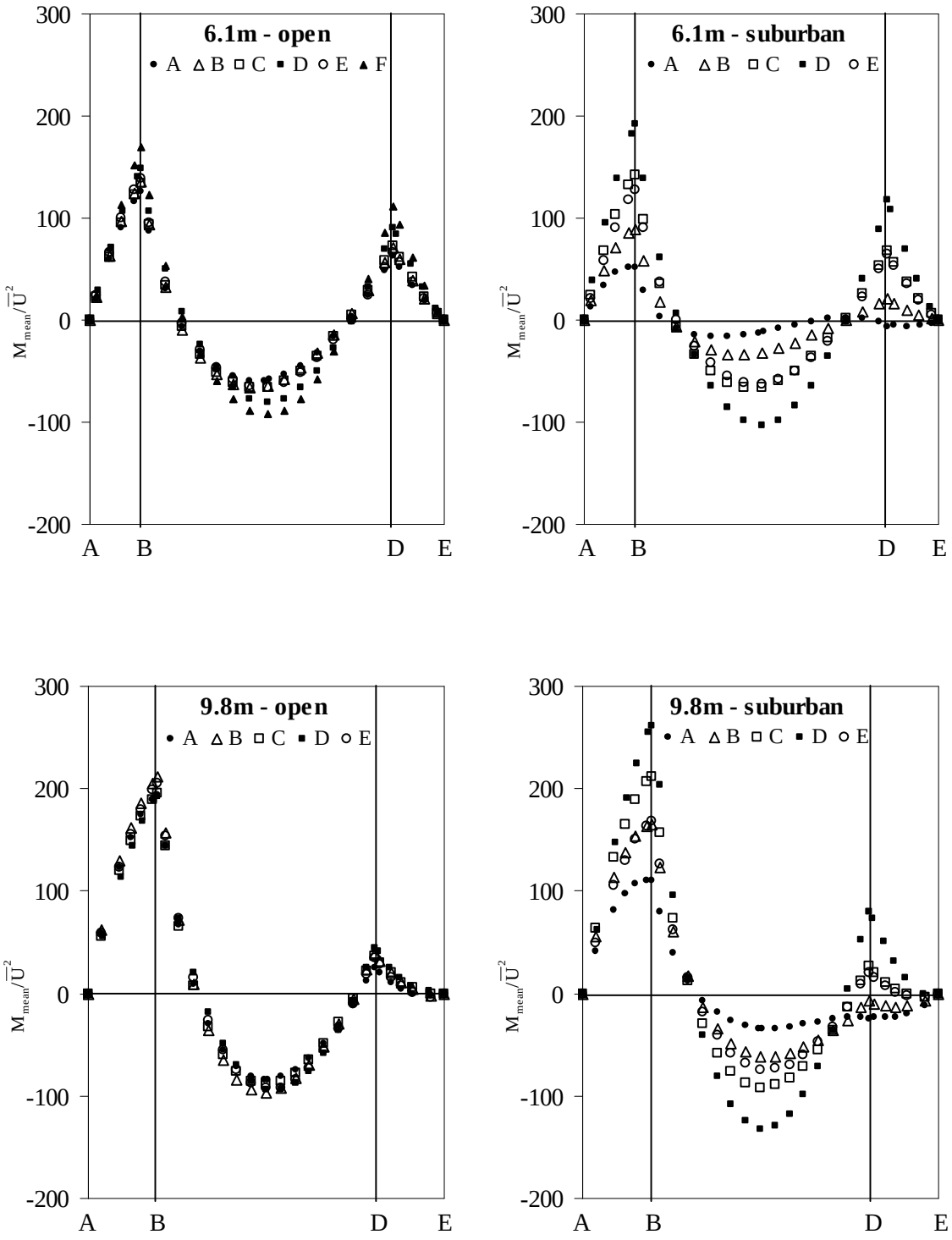

Figure 4.19 Mean bending moment, frame F2, wind direction of 90^o

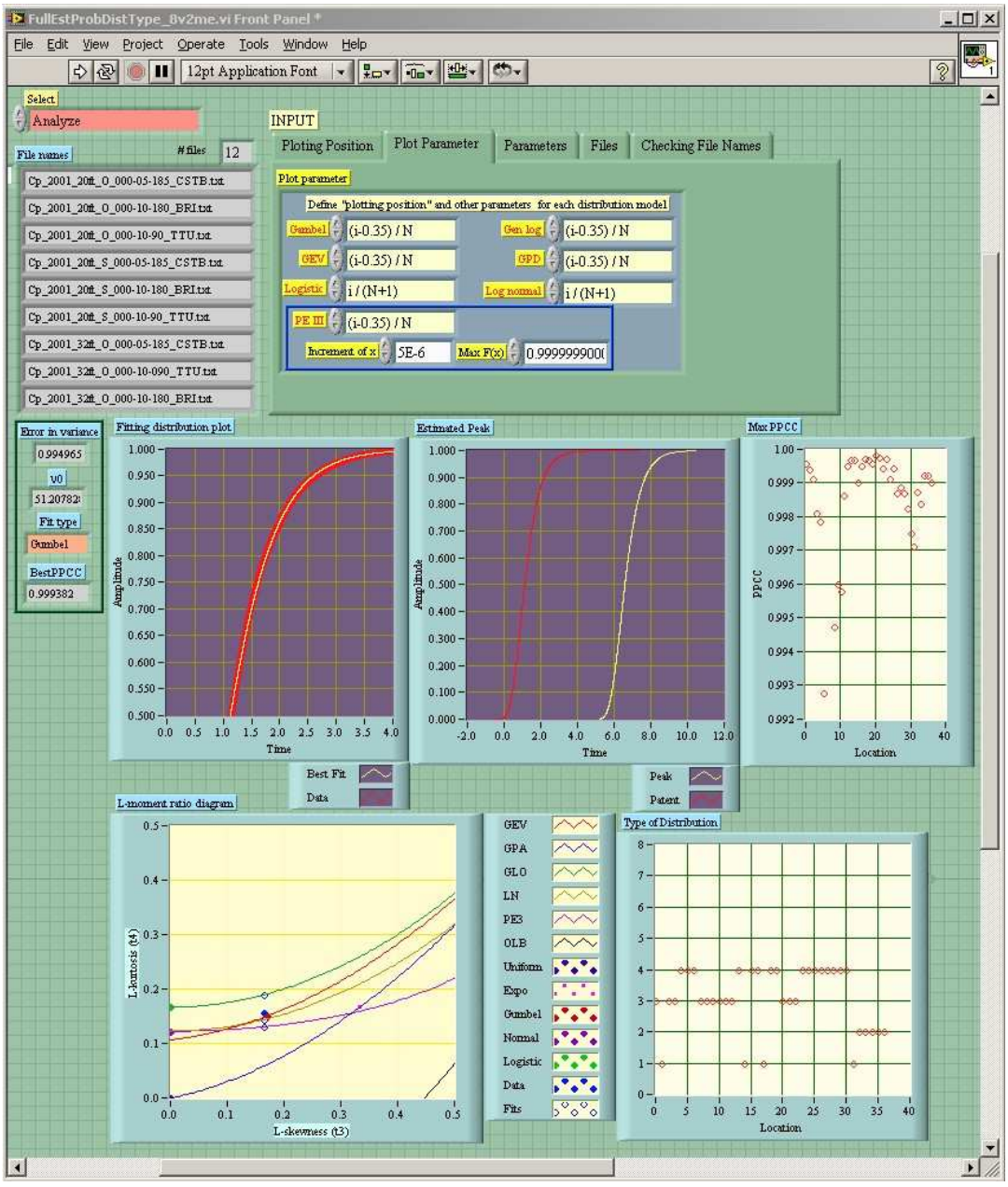

Figure 4.20 Peak non-Gaussian estimation programmed in LabView software

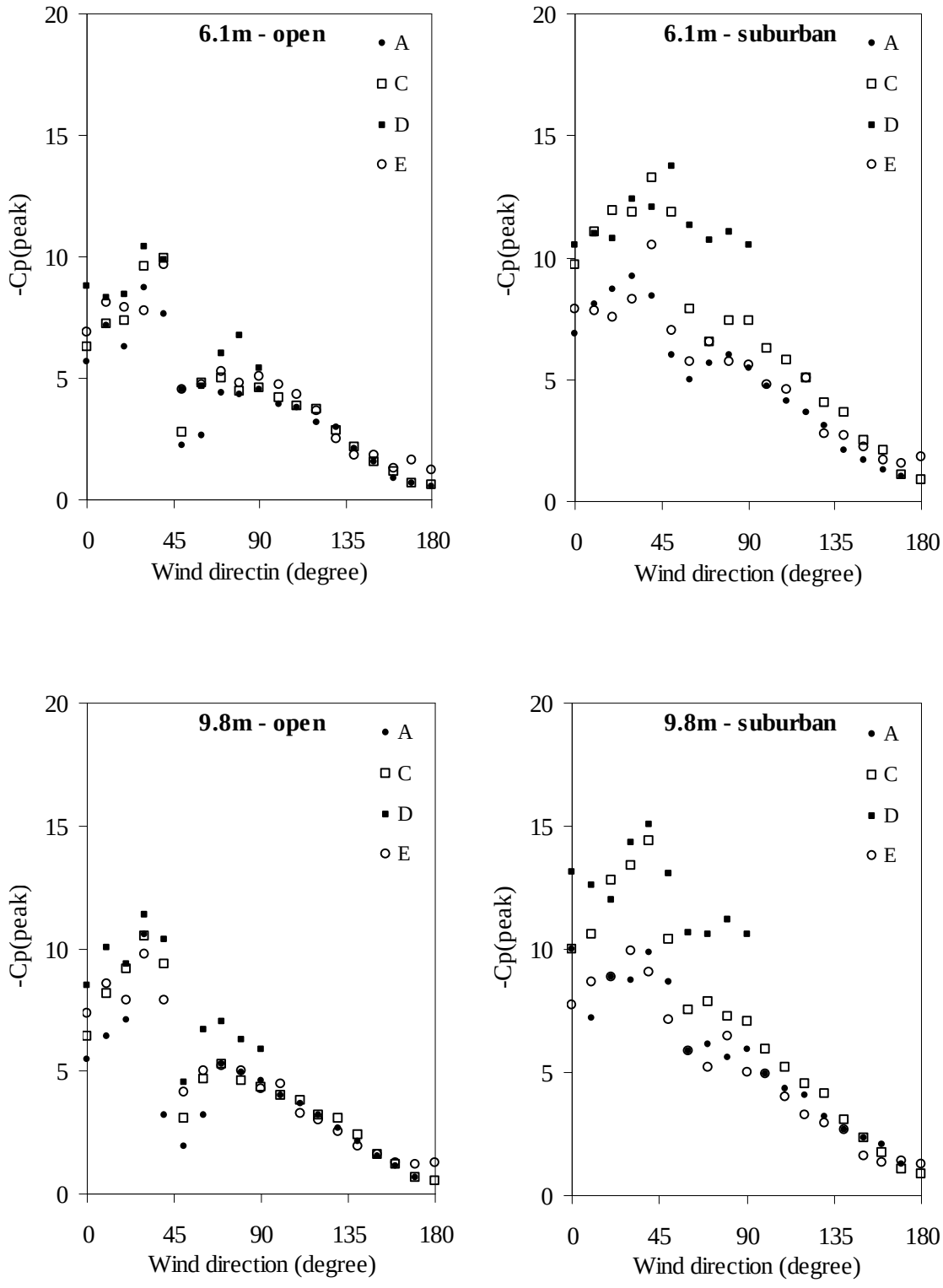

Figure 4.21 90th percentile estimated roof peak pressures, tap P1

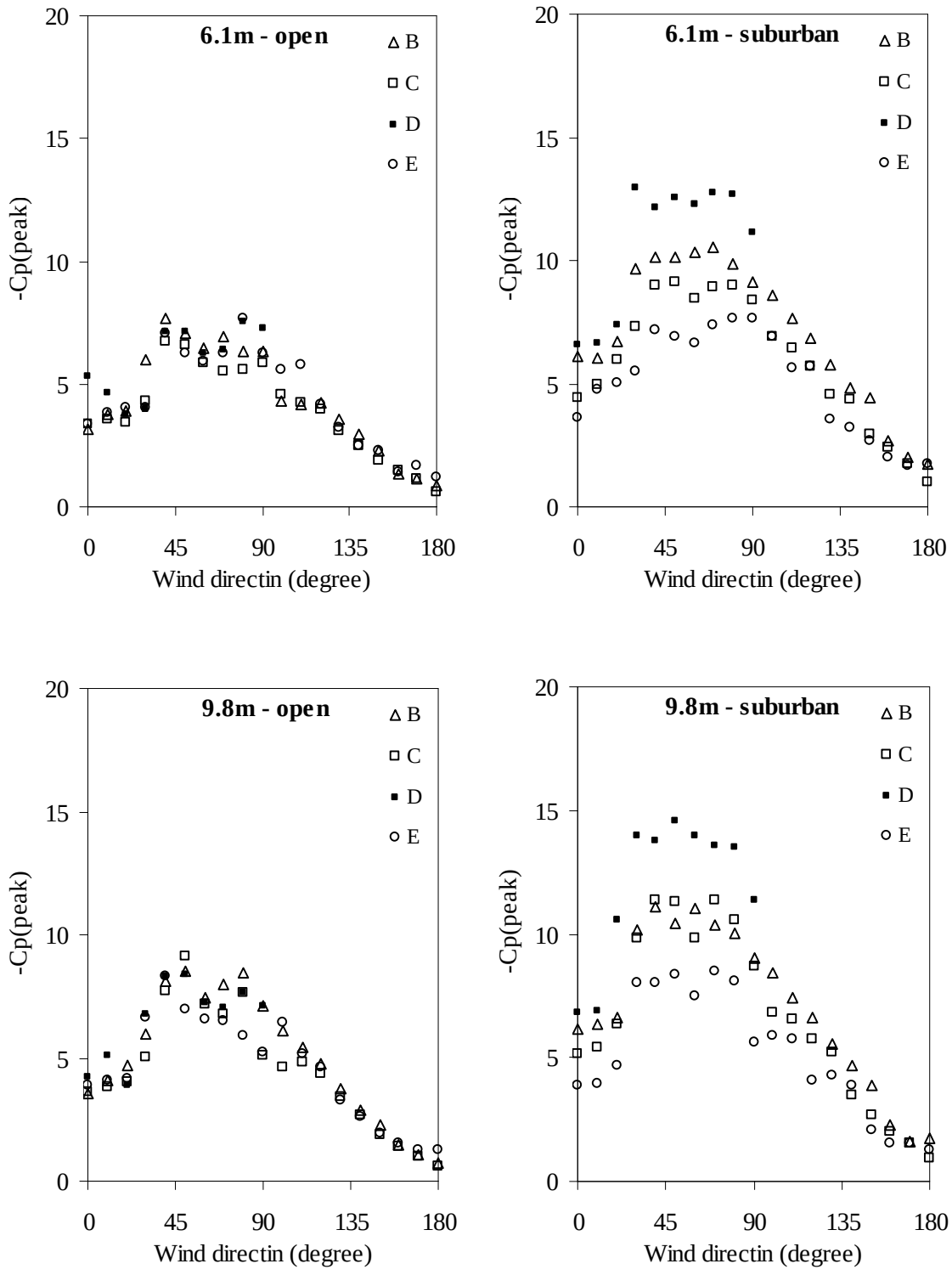

Figure 4.22 90th percentile estimated roof peak pressures, tap P2

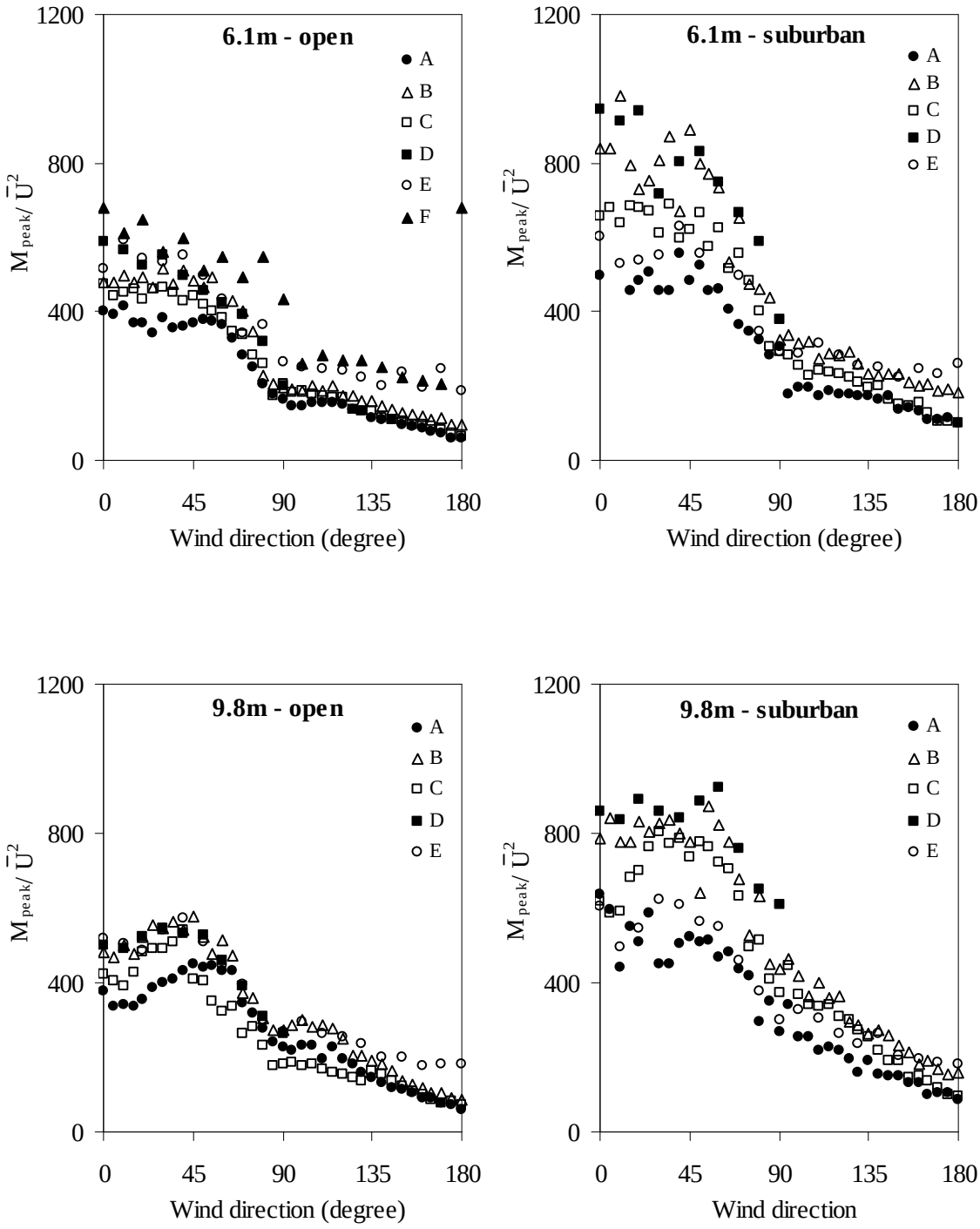

Figure 4.23 90th percentile peak bending moment, location B, frame F1

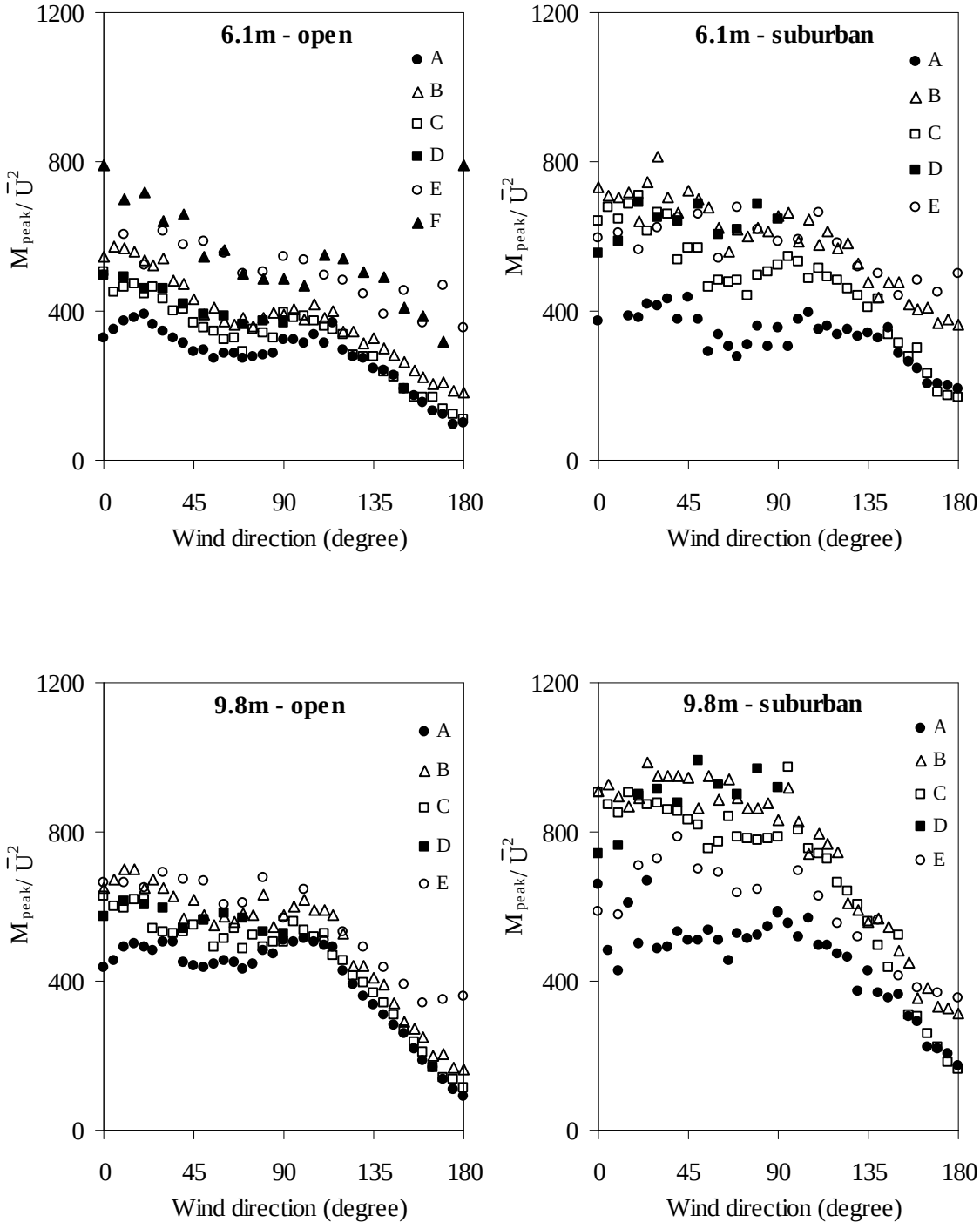

Figure 4.24 90th percentile peak bending moment, location B, frame F2

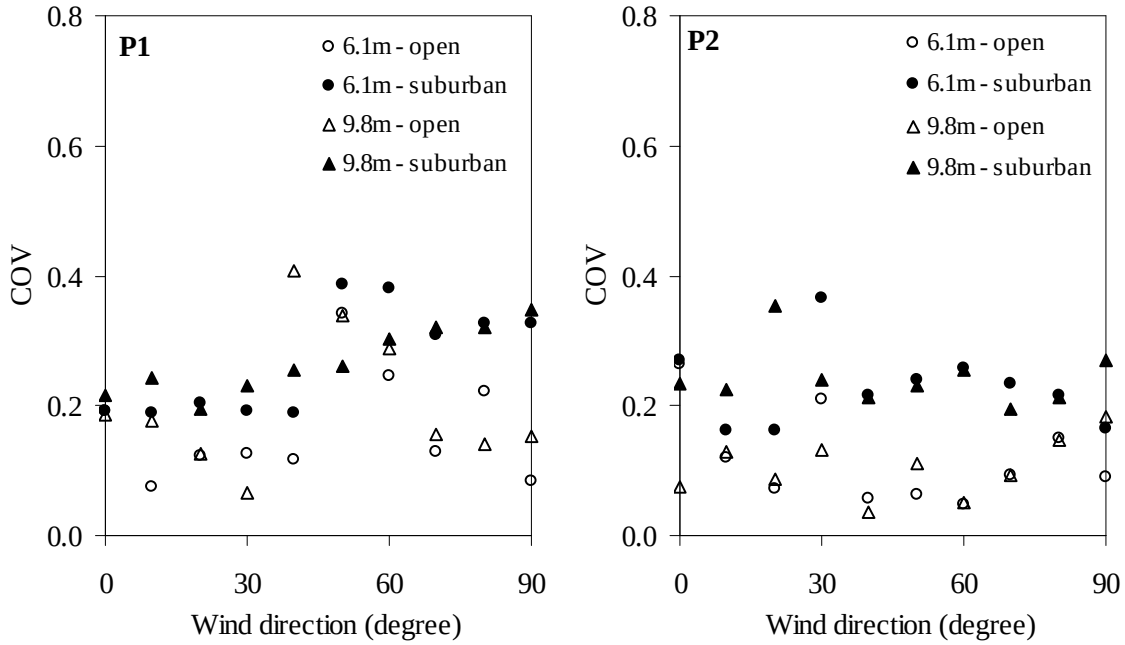

(a) COV for the 90th percentile peak

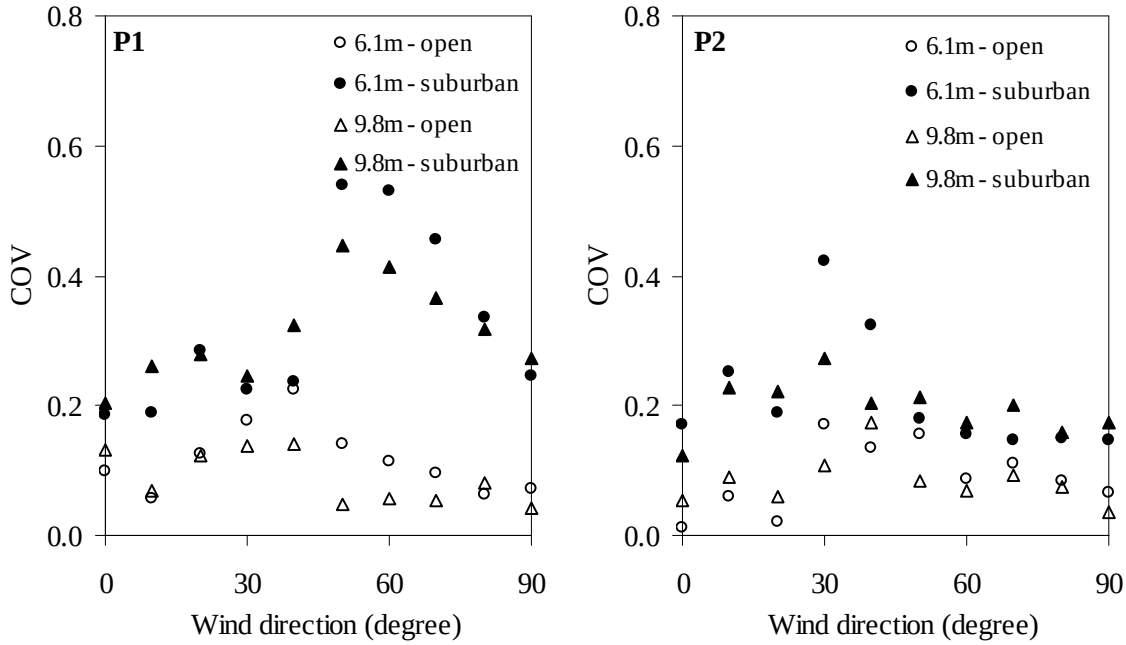

(b) COV for mean

Figure 4.25 Comparison of COV for peak pressure, taps P1 and P2

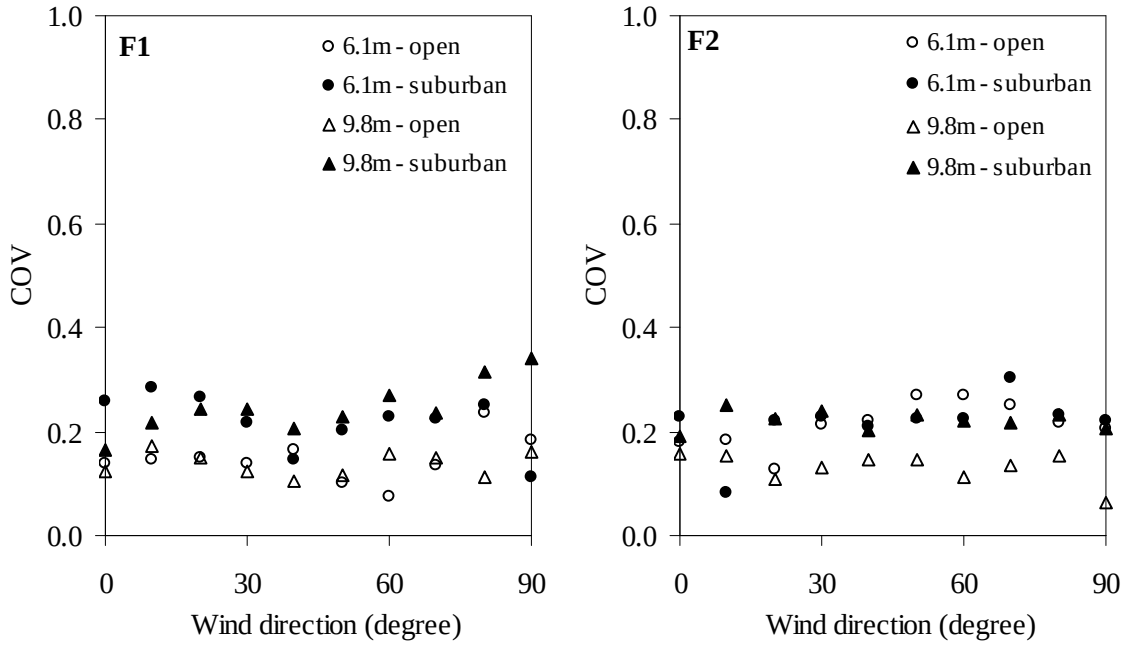

(a) COV for the 90th percentile peak

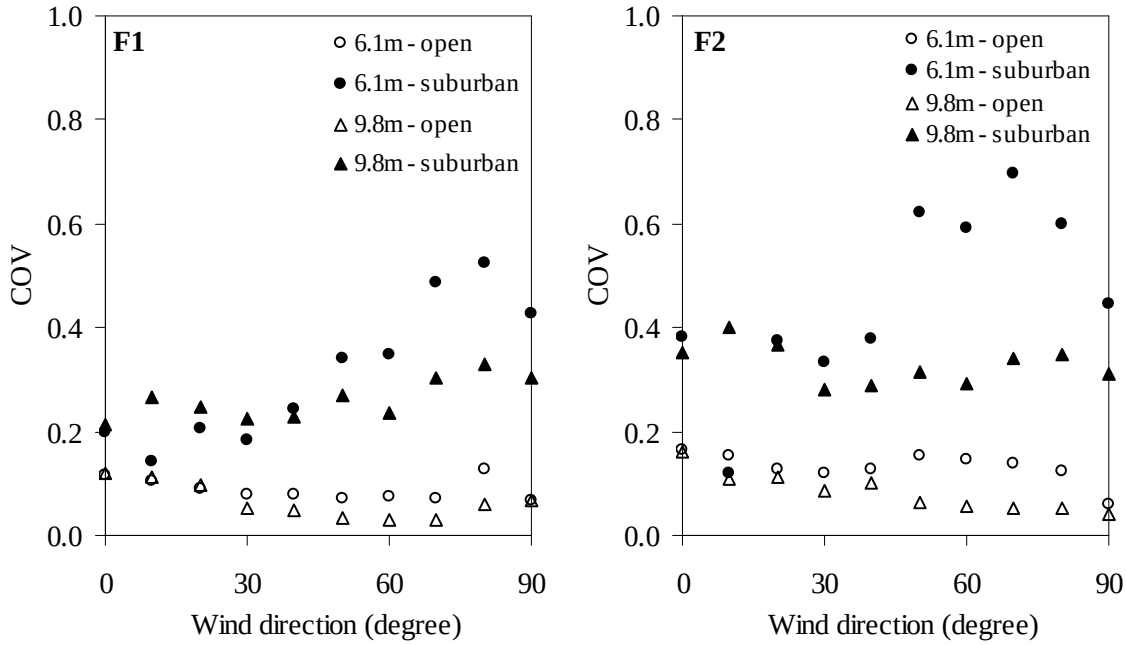

(b) COV for mean

Figure 4.26 Comparison of COV for peak and mean bending moments, location B, frames F1 and F2

A B C

(a) Open terrain

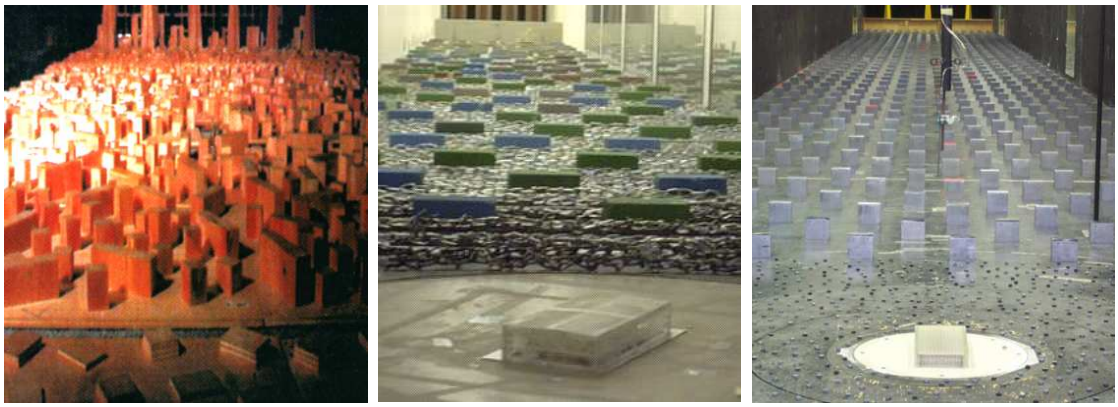

A B C

(b) Suburban terrain

Figure 4.27 Wind tunnel setups to generate open and suburban terrain wind exposures in three representative laboratories

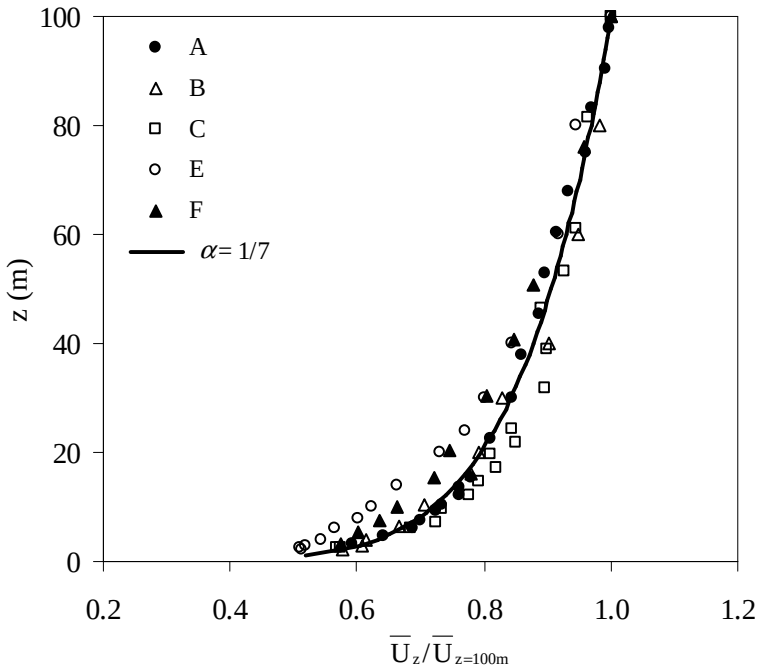

(a) Open terrain

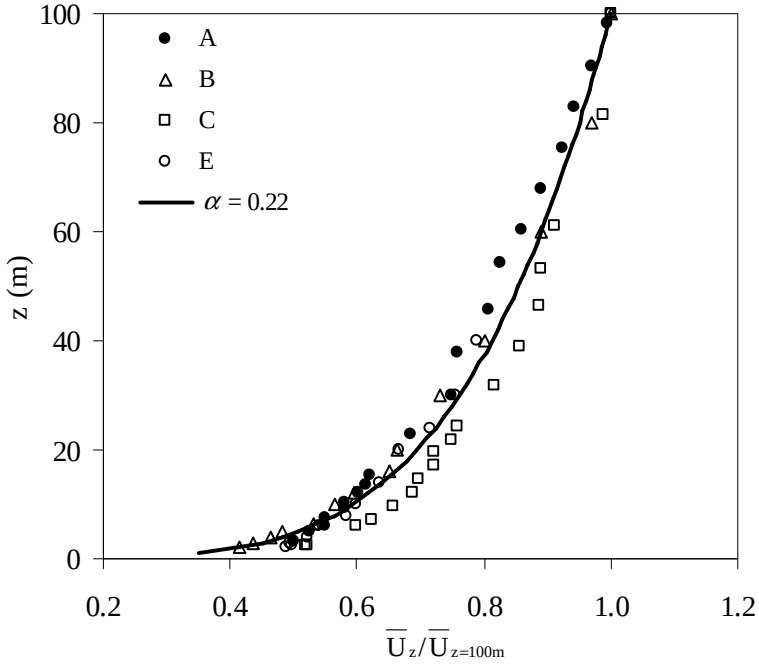

(b) Suburban terrain

Figure 4.28 Comparison of laboratory and target along-wind mean wind speed profiles

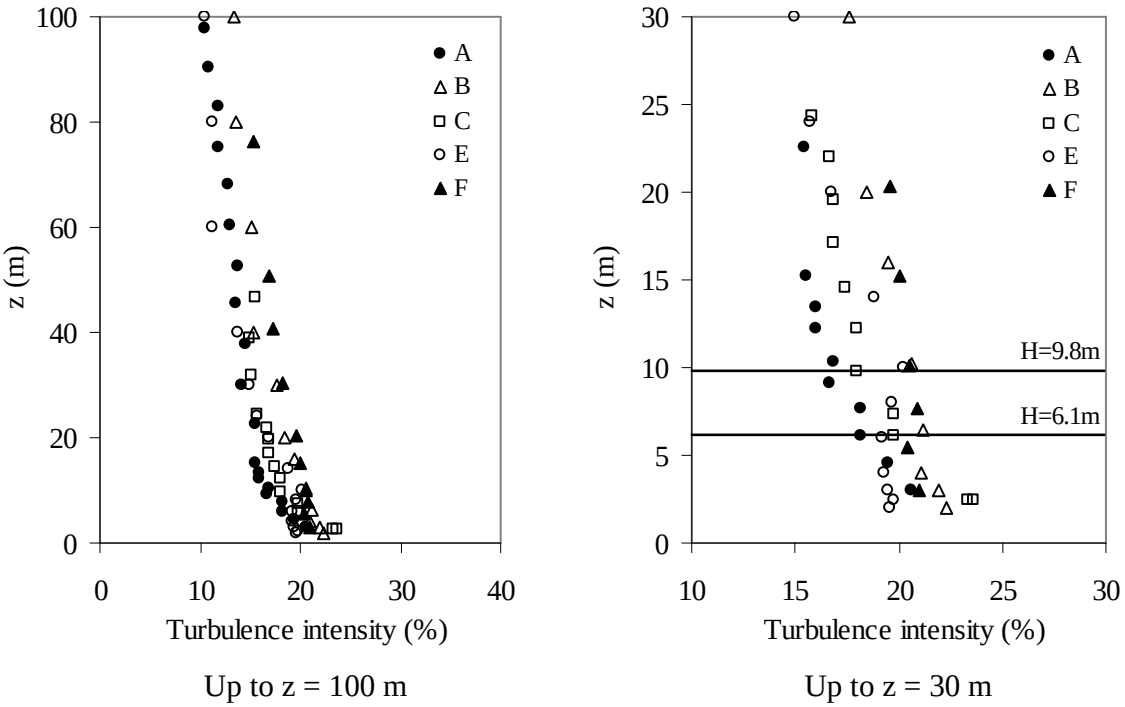

(a) Open terrain

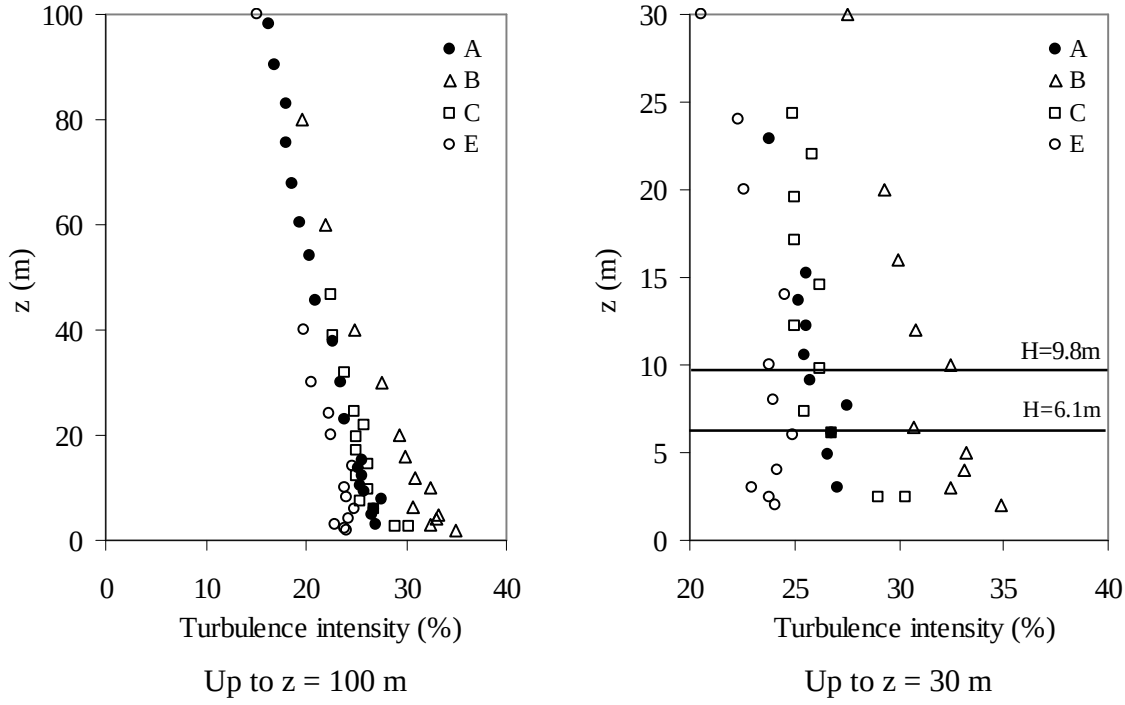

(b) Suburban terrain

Figure 4.29 Comparison of laboratory along-wind turbulence intensity profiles

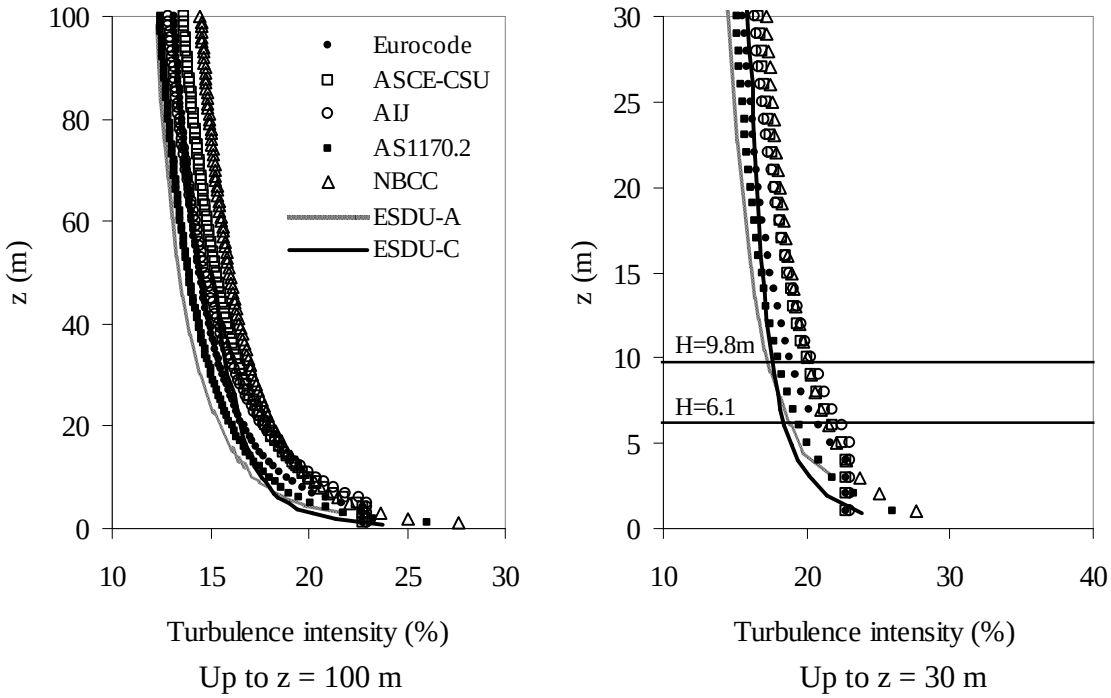

(a) Open terrain

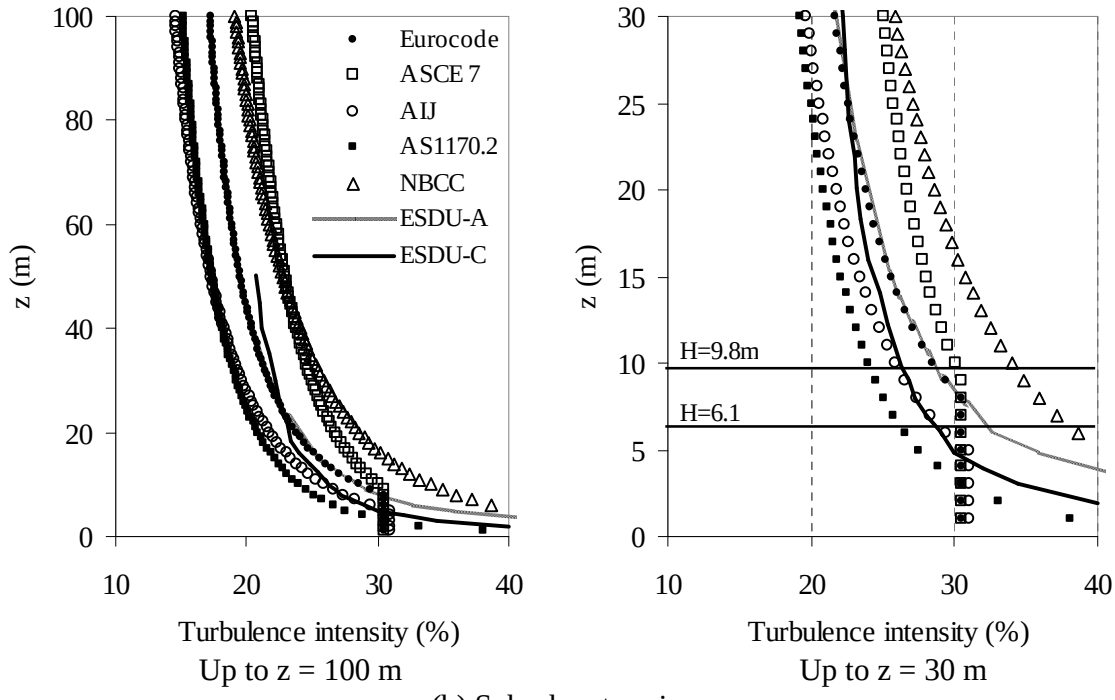

(b) Suburban terrain

Figure 4.30 Comparison of empirical models for along-wind turbulence intensity profiles

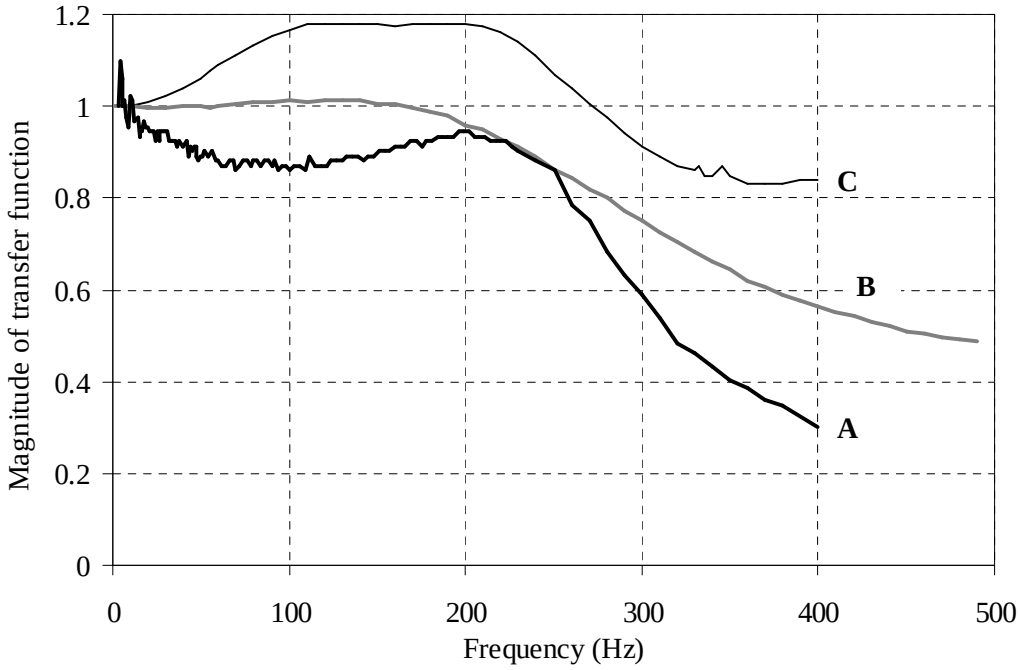

Figure 4.31 Comparison of frequency response of tube system

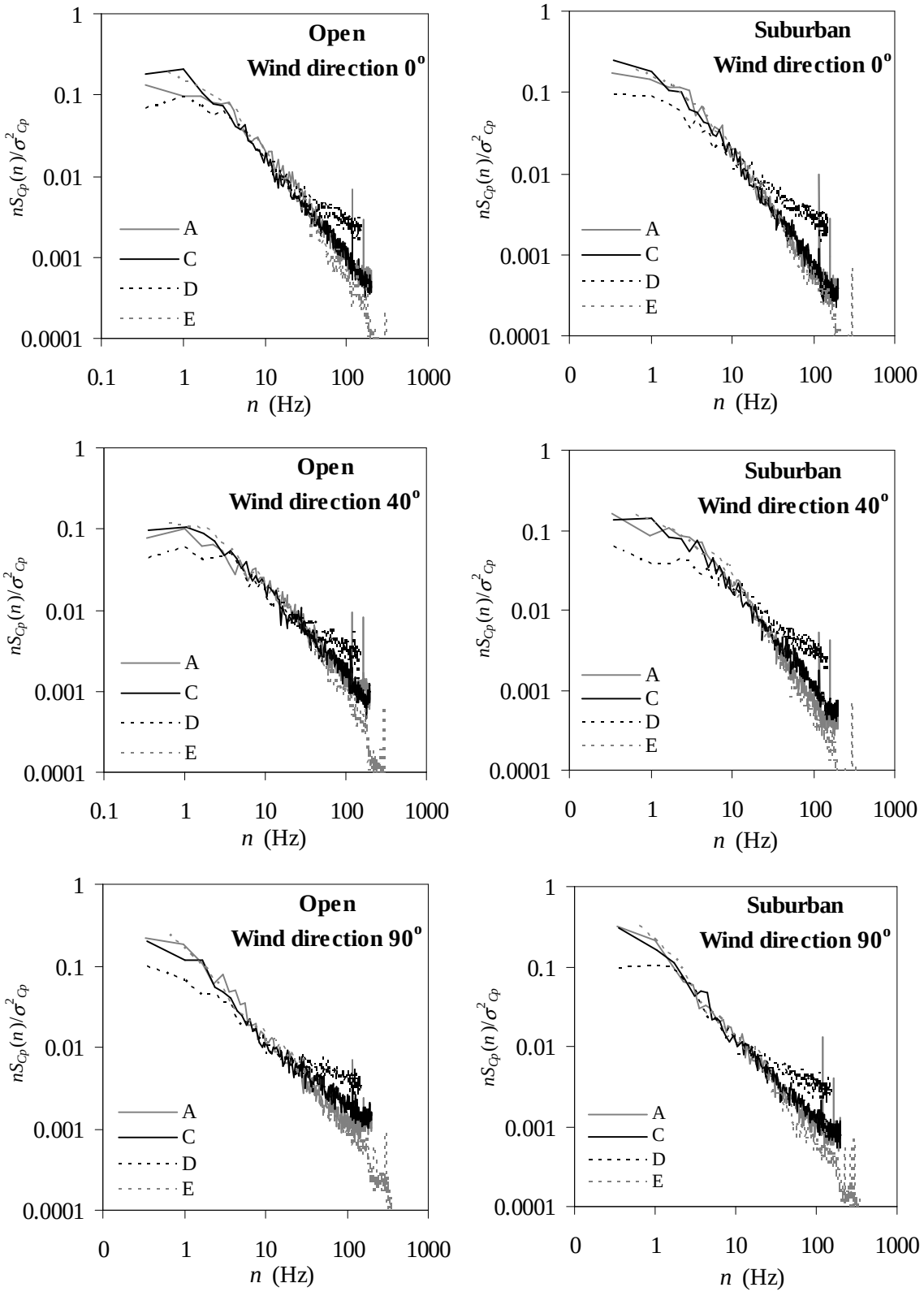

Figure 4.32 Power spectra of roof pressure fluctuation for tap P1, eave height = 9.8 m

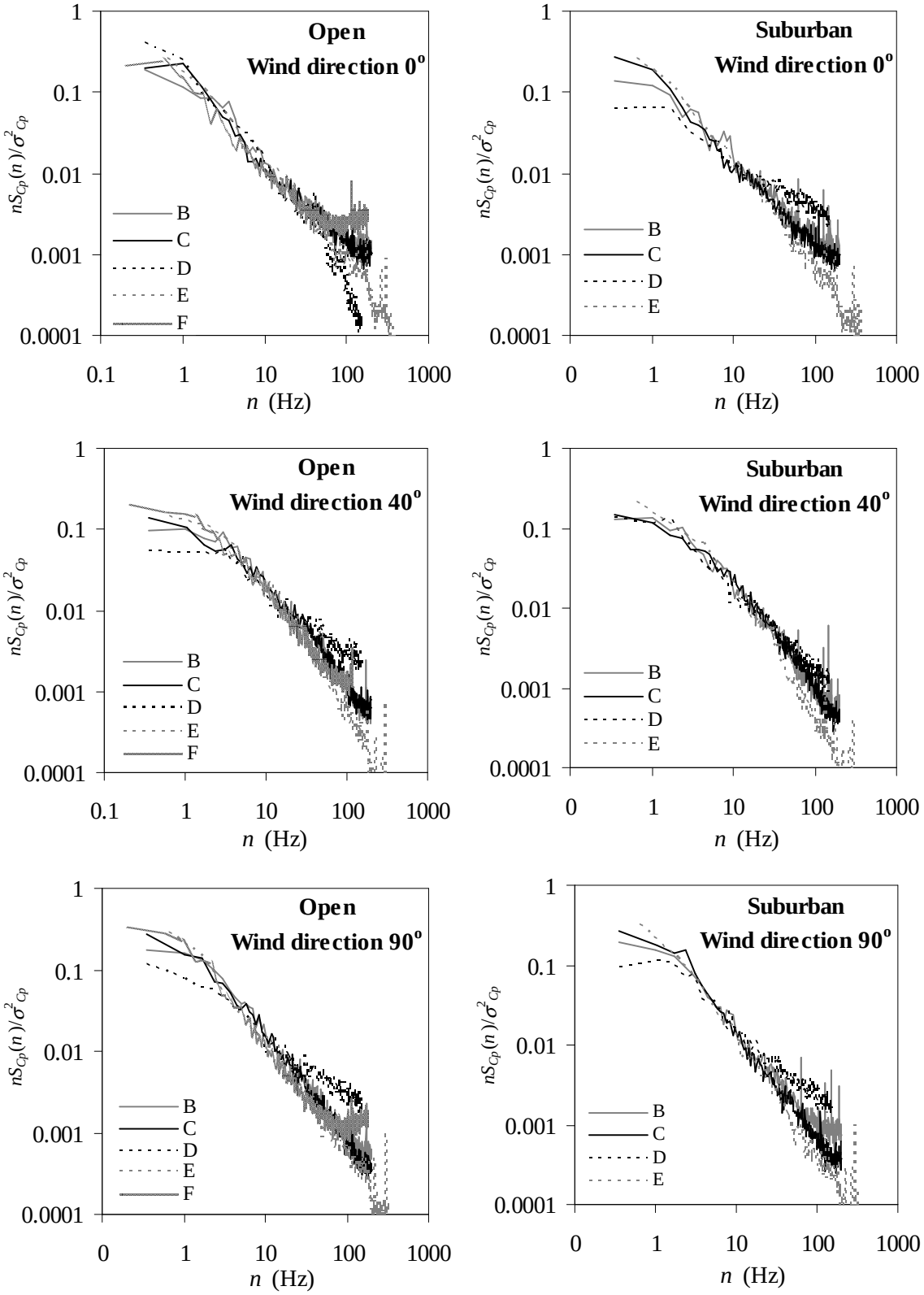

Figure 4.33 Power spectra of roof pressure fluctuation for tap P2, eave height = 6.1 m

CHAPTER 5

PHYSICAL MODELING OF MATCHING APPRAOCH FLOWS AND WIND-INDUCED LOADING IN BOUNDARY-LAYER WIND TUNNELS

The material presented in this chapter has been presented in the following reference

Endo, M., Bienkiewicz, B. and Bae, S., "Investigation of Discrepancies in Laboratory Modeling of Wind Loading on Low Buildings", Proceedings of the 11th Americas Conference on Wind Engineering (11ACWE), San Juan, Puerto Rico, June 22-26, 2009, 10 pp. (CD ROM).

5.1 INTRODUCTION

The comparative inter-laboratory study presented in Chapter 4 revealed large scatter in the modeled building pressures and wind-induced forces. It was postulated that ambiguity in the definition of the wind exposures (the empirical (target) models for these exposures were not specified) led to significant spread in the approach flow conditions (developed by the participating laboratories) and this resulted in significant variability in the measured wind loadings reported by these laboratories (Bienkiewicz *et al*., 2009). This hypothesis has been subsequently tested at the Wind Engineering and Fluids Laboratory (WEFL), Colorado State University (CSU).

This chapter describes the inter-wind tunnel investigation carried out at WEFL. This study was focused on the comparative study of wind loading on low-rise buildings determined from wind tunnel experiments performed in two boundary-layer wind tunnels

at WEFL. Matching approach flows were modeled in these wind tunnels. Subsequently, wind-induced roof pressures on generic low-rise building models were acquired in these flows. A limited wind tunnel testing of the Reynolds number effects on wind-induced roof pressures was also conducted.

5.2 EXPERIMENTAL CONFIGURATION

5.2.1 Building Model

The inter-wind tunnel investigation was carried out in two closed-circuit boundary-layer wind tunnels at WEFL: Meteorological Wind Tunnel (MWT) and Industrial Aerodynamics Wind Tunnel (IWT). Details of these wind tunnels are described in Appendix A.

Models of two low-rise buildings – having the same planar dimensions and two different building heights – were employed in the wind tunnel experiments. The prototype planar dimensions of the buildings were 30.5 m × 61 m and the building heights were 6.1 m and 9.8 m. The building roof slope was 1:24. These buildings were also considered in Chapter 4. They were modeled at the geometrical scale of 1:200. The models were made of 6.0-mm thick plexiglass. The prototype roof slope was preserved in both the models. The models were furnished with a total of 60 pressure taps located on the building roofs. The pressure taps were arranged in four rows, rows 1 through 4, as indicated in Figure 5.1. Pressure taps manufactured by Scanivalve Corporation, 0.79-mm in diameter and 10.67-mm in length, were installed flush with the external building surface. The dimensions of the models, pressure tap locations and the definition of the wind direction are schematically shown in Figure 5.1.

5.2.2 Flow Measurement

Overall views of the wind-tunnel set-ups used to model the atmospheric boundary layer flows for open and suburban terrains are shown in Figure 5.2. Measurements of the simulated approach flows were carried out using hot-film probes in conjunction with constant temperature hot-wire anemometers. The reference velocity and the static pressure were monitored using a pitot-static probe mounted at an elevation of 110 cm above the wind tunnel floor, in a plane of the windward wall of the building model.

The hot-film data were acquired at a sampling rate of 1,000 samples/second. The analog signal was low-pass filtered with a cut-off frequency of 500 Hz. Wind speed data records consisted of 30,000 data points. Thus, the data record length was 30 seconds. Up to five segments (data records) were employed in calculation of the power spectra of the along-wind velocity fluctuations.

5.2.3 Pressure Measurement

The wind-induced roof pressures were measured using Electronically Scanned Pressure Measurement System (ESP) manufactured by Pressure Systems, Inc. (PSI). ESP developed in WEFL has a total of 128 channels configured to (nearly) instantaneously scan pressures. The pressure taps on the building model were connected with ESP ports (of the pressure measurement system) via 19.5-cm long Tygon tubing with an inner diameter of 0.51-mm. The reference pressure was provided to the ESP's by connecting the reference sides of the ESPs (using Tygon tubing) with the static side of a pitot-static probe mounted at the elevation of 110 cm above the turntable.

The frequency response (the magnitude of the system transfer function) of the employed tubing system is shown in Figure 5.3. It can be seen that for the frequency

range up to 210 Hz, the departure of the magnitude of the transfer function from the ideal gain of unity did not exceed $\pm$ 5%. For this frequency range, the phase of the system transfer function was approximately linear. The pressure time series were acquired at a sampling rate of 400 samples per second. For each configuration tested, 60-second long data records (24,000 data points) per pressure tap were acquired for wind directions ranging from 0^o through 180^o, with an increment of 5^o. In addition, a total of 250 data records of the pressure at 60 pressure taps, on a 9.8-m building model, were acquired for three wind directions (0^o, 45^o and 90^o), in open terrain.

5.3 RESULTS

5.3.1 Approach Wind

Modeling of approach winds for open and suburban terrains (wind exposures) was performed in the MWT and IWT. Figure 5.4 compares the mean velocity profiles of the two wind exposures modeled in these wind tunnels. Similarly, Figure 5.5 compares the along-wind turbulence intensity profiles, while representative along-wind power spectra are presented in Figure 5.6. The characteristics of modeled approach winds: power-law exponent *a*, roughness height z_0, turbulence intensity TI and integral length scale L_u^x, are presented in Table 5.1. Overall, a very good agreement among the simulated profiles and spectra was obtained for both exposures. Also the values of *a*, z_0 and L_u^x were in a very good agreement, as can be seen in Table 5.1. The discrepancy in turbulence intensity at the eave heights did not exceed 1.8%.

Table 5.1 Characteristics of approach wind modeled in MWT and IWT

		Wind exposure			
		Open		Suburban	
		MWT	IWT	MWT	IWT
a		0.145	0.145	0.235	0.240
z_0 (m)		0.02	0.03	0.31	0.29
TI (%)	H_{eave}=6.1m	21.1	21.8	30.7	32.1
	H_{eave}=9.8m	20.6	20.5	32.5	30.3
L_u^x (m)	H_{eave}=6.1m	115	111	101	140
	H_{eave}=9.8m	121	136	132	135

5.3.2 Wind Loading

The representative power spectra of roof pressure fluctuations in pressure tap A (see Figure 5.1) are presented in Figure 5.7, for the building of the eave height of 6.1 m. They are displayed for three wind directions (0^o, 40^o and 90^o) and two wind exposures (open and suburban terrains). Overall, a good agreement among the compared spectra can be seen in the figure. However there are some differences in the magnitude of power spectra at frequencies lower that 1 Hz, for all considered cases.

Representative wind-induced roof pressures - the mean and standard deviation of the pressure coefficients defined using the eave mean dynamic pressure - are depicted (for the two buildings and the two wind exposures) in Figures 5.8 through 5.11. The pressure coefficients at the roof locations in rows 1 through 4 (see Figure 5.1) are displayed in Figure 5.8 for the wind direction of 0^o. Similar results for a cornering wind (wind direction of 40^o) and for the wind direction of 90^o, are shown in Figures 5.9 and 5.10, respectively. The effects of the wind direction on the mean pressure and the pressure standard deviation, at a representative location in a roof corner region - tap A

identified in Figure 5.1 - are depicted in Figure 5.11. Overall, a very good agreement among the pressures simulated in the two wind tunnels can be observed for most of the compared cases.

The time series of roof pressures were subsequently employed to predict peak roof pressures, estimated using the numerical tool developed in Chapter 4 (Section 4.3), based on the peak non-Gaussian estimate procedure. Representative results of these calculations – pressure peaks – are presented in Figure 5.12, for the two wind exposures and two eave heights. The displayed values are the 90th percentile peak pressures, at tap A in the roof corner region. The comparison of peak pressures obtained in the two wind tunnels indicates overall smaller discrepancies than those observed in inter-laboratory comparisons, presented in Figures 4.21 and 4.22. However, in the present case large scatter is also observed for cornering wind directions, ranging from approximately 30^o through 60^o. It must be pointed out that the displayed pressure peaks were estimated from one record of time series of (pressure coefficient) Cp data.

Next, 250 records of Cp time series were acquired for the 9.8 m-eave height building, in open terrain modeled in MWT. Figure 5.13 shows scatter of the 90th percentile peaks estimated from each record of the 250 records (one peak/record) for wind directions of 0^o, 45^o and 90^o. Significant scatter in peak/record values was found for wind directions of 45^o and 90^o. This fact implies that peak pressures extracted from small number of records of the data would lead to insufficient representation of peak characteristics. Figure 5.14 depicts plots of the probability of exceedance (POE) using 250 records for wind directions of 0^o, 45^o and 90^o. The peaks shown in Figure 5.13 were estimated from values of the pressure coefficient Cp, for the POE = 0.1. Examination of

Figure 5.13 reveals a scatter in the peaks. The largest scatter is noted for the wind direction of 45^o. For the remaining directions it is smaller.

The large scatter in the estimated peaks observed for a cornering wind (wind direction of 45^o) can be explained using Figure 5.15. In the figure, the average of POE, shown for 250 records in Fig. 5.14, is plotted for the three wind directions. It can be seen that for the wind directions of 0^o and 90^o, the slope of the left tail is very consistent (straight-line). In contrast, for the wind direction of 45^o there is a change in the slope around the POE = 0.4, see the right graph of Figure 5.15. This implies that the probability distribution of the pressures at this wind direction may not be precisely represented by using a single probability distribution model employed in the estimation of peaks.

In Figure 5.16, the average values of the estimated 250 peaks presented in Figure 5.13 (for the wind directions of 0^o, 45^o and 90^o) are compared with those determined using one record of the MWT data shown in Figure 5.12 (the eave height of 9.8 m and open terrain). In the figure, the range of scatter of the 250 records and peaks predicted from the Type I extreme value distribution (EVD) fit are also included. The largest scatter of peaks is 31% (with respect to the average peak) and it occurs for the wind direction of 45^o. The values of the peak scatter at the remaining wind directions are 17 % and 20 %, respectively for the wind directions of 0^o and 90^o. The average peaks and the peaks predicted from the Type I EVD fit are in a very good agreement for the wind directions of 0^o and 90^o. However for the wind direction of 45^o, the average peak is 23 % larger than the peak obtained using the Type I EVD fit.

The above difference is attributed to the selection of the probability distribution model used to determine peak from the peak non-Gaussian estimate procedure. Figure 5.17 displays the τ_3-τ_4 relationship for 250 records of the Cp data, for the three wind directions. As described in Section 4.3, in the peak non-Gaussian estimate procedure, the mapping process from the parent distribution of Cp data to the distribution of peaks uses the same probability distribution model. For example, if the lognormal distribution is selected for the parent distribution of Cp data, its associating distribution of peak is in the lognormal distribution domain. For the wind directions of 0^o and 90^o, the data lies close to the generalized extreme value distribution (denoted GEV) line, as seen in Figure 5.17. Since the parent distributions of Cp data for these two wind directions are in the GEV domain, the peaks estimated using the peak non-Gaussian procedure are also in the GEV domain. It is obvious that the average peaks are very close to the peaks predicted from Type I EVD fit. On the other hand, the data for wind direction of 45^o lie close to the generalized Pareto distribution (denoted GPA). It can be said that the observed discrepancy between the average peak and peak predicted from the Type I EVD fit are resulted from different probability distributions used to predict peaks, in the employed estimate methods (peak non-Gaussian procedure and Type I EVD fit).

5.3.3 Investigation of Effects of Reynolds Number on Modeled Approach Flow and Wind-induced Building Loading

One of concerns in wind tunnel modeling of wind-induced loading on buildings and structures is the Reynolds number issue. Based on the study reported by Djilali and Gartshore (1991), if the Reynolds number is larger than 10^4, the Reynolds number effect

can be considered to be negligible. However recent investigation reported by Lim *et al*. (2007) showed significant Reynolds number effects on the surface pressure on bluff bodies. As shown in Figure 5.18, fluctuating surface pressures measured in the filed indicates larger magnitude than those obtained in wind tunnel testing.

A series of experiments were conducted in the MWT to investigate the effects of Reynolds number on the modeled approach flows and wind-induced building loadings. The Reynolds number is the ratio of inertia to viscous forces and it is written as follows:

$$R_e = \frac{\rho UL}{\mu} = \frac{UL}{\nu} \qquad [5.1]$$

where ρ is fluid density, U is velocity, L is length, μ is (dynamic) viscosity and $\nu = \mu/\rho$ is the kinematic viscosity. Typical value of kinematic viscosity for air is 0.15 cm^2/s at 20^oC and standard atmospheric pressure (Simiu and Scanlan, 1996).

A wind tunnel experiment was carried out in the modeled open terrain wind exposure. The approach flow and wind loading were acquired for a range of the reference wind speed - the mean wind speed at the building eave height. The obtained mean velocity and turbulence intensity profiles of the approach flows are presented in Figure 5.19, for four representative Reynolds numbers, defined in Equation [5.1]. The roof pressures (mean, standard deviation and peak pressures) acquired at tap rows 1 to 3 (see Figure 5.1) are displayed, for the four cases of the Reynolds number, in Figures 5.20 and 5.21, respectively for the wind directions of 45^o and 90^o. The data shown in these figures are average values obtained from two records of Cp time series.

Overall, the results show that the Reynolds number effects on the approach flow profiles and roof pressures are not significant for the considered range of the Reynolds numbers. It should be noted that the range of the Reynolds number considered in this

study was very limited, with R_e ranging from 1.8×10^4 through 3.1×10^4, which is a typical range used in wind tunnel simulations. Testing for a significantly broader range of R_e would be needed to formulate a definite statement regarding the Reynolds number effects on the investigated flow and wind loading.

5.4 CONCLUSIONS

The findings of the investigation of the inter-wind tunnel study, focused on wind tunnel modeling of wind loading on low-rise building, can be summarized as follows:

1. The comparison of wind-induced loading on low-rise building models measured in two boundary-layer wind tunnels at WEFL showed a good agreement in the roof pressures when the characteristics of the approach flow (the mean velocity and turbulence intensity profiles, and the along-wind power spectra) were closely matched in these tunnels.
2. The agreement of the peak roof pressures estimated from the peak non-Gaussian procedure was satisfactory. The peak values determined in the two tunnels exhibited a small discrepancy. However, it should be pointed out that the peaks were extracted/predicted from small number of records. Thus a measurable statistical variability is expected.
3. The peak pressure coefficients obtained using the non-Gaussian procedure and the extreme value distribution method were in a good agreement when the parent distribution of the coefficients was in the GEV domain, in the non-Gaussian procedure.

4. The effects of the Reynolds number on the measured mean, standard deviation and peak of the roof pressures were found to be insignificant for the wind speed range investigated. Testing for a significantly broader range of R_e is desired to formulate a definite statement regarding the Reynolds number effects on the investigated flow and wind loading.

5.5 REFERENCES

Cook, N.J., Harris, R.I., and Whiting, R. (2003), "Extreme wind speeds in mixed climates revisited," *J. Wind Eng. Ind. Aerodyn*., Vol. 91, pp. 403-422.

Bienkiewicz, B., Endo, M. and Main, J. (2009), "Impact of empirical models for approach wind exposures on wind loading on low buildings – A comparative study", Proceedings of the 2009 SEI/ASCE Structures Congress, Austin, Texas, April 29 – May 2, pp. 2439-2448 (CD ROM).

Djilali, N. and Gartshore, I.S. (1991), "Turbulent flow around a bluff rectangular plate. Part I: Experimental investigation", *J. Fluids Eng*., Vol. 113, pp. 51-59.

Lim, H.C., Castro, I. and Hoxey, R.P. (2007), "Bluff bodies in deep turbulent boundary layers: Reynolds-number issues", *J. Fluid Mech*., Vol. 571, pp. 97-118.

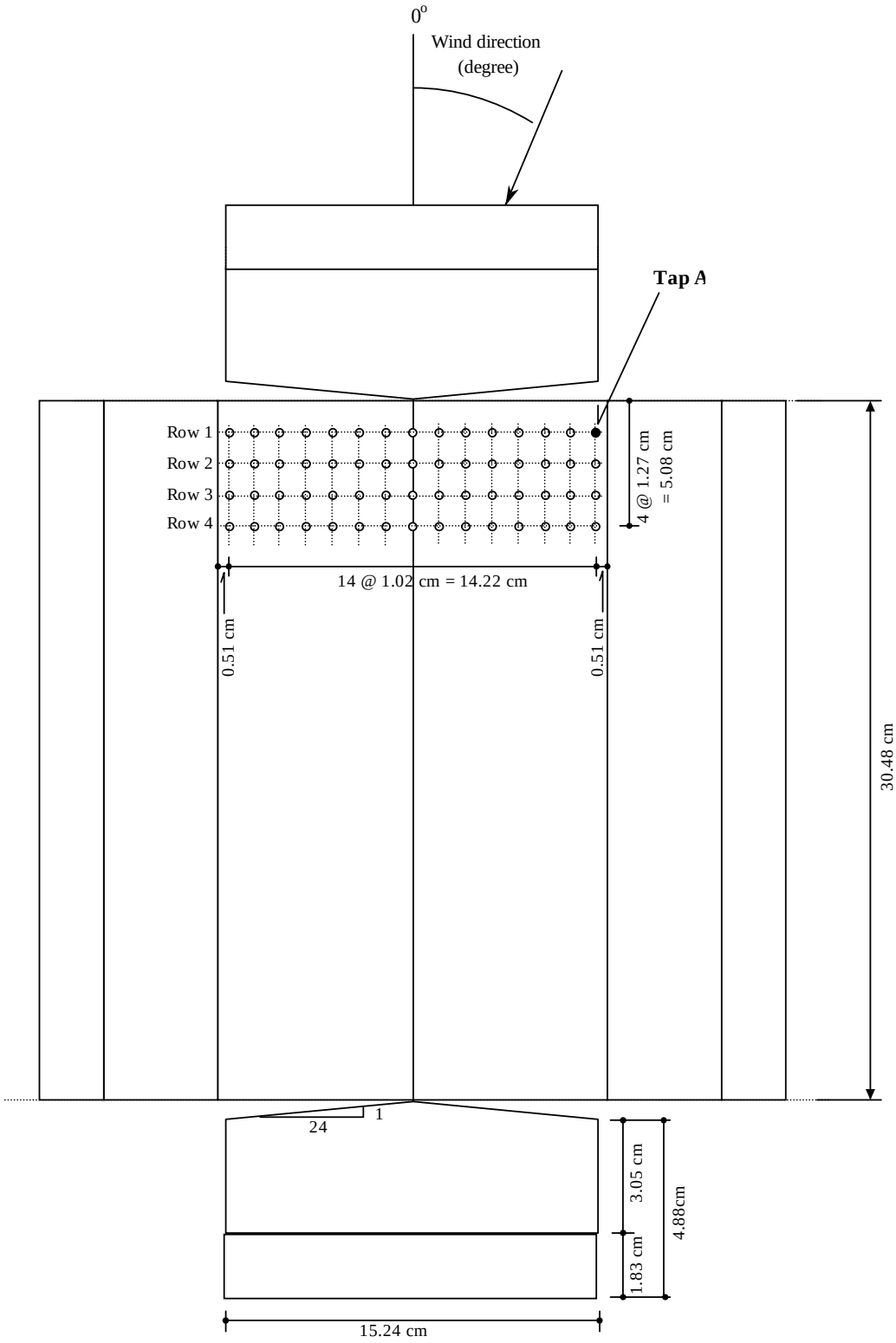

Figure 5.1 Geometry of prototype buildings and pressure tap locations

MWT

IWT

(a) Open wind exposure

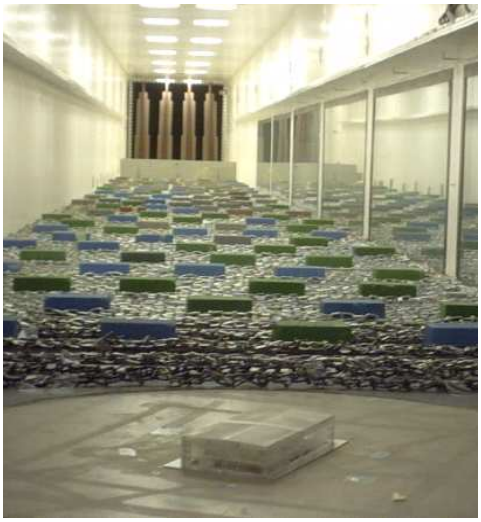

MWT

IWT

(b) Suburban wind exposure

Figure 5.2 Wind tunnel setups to generate open and suburban wind exposures

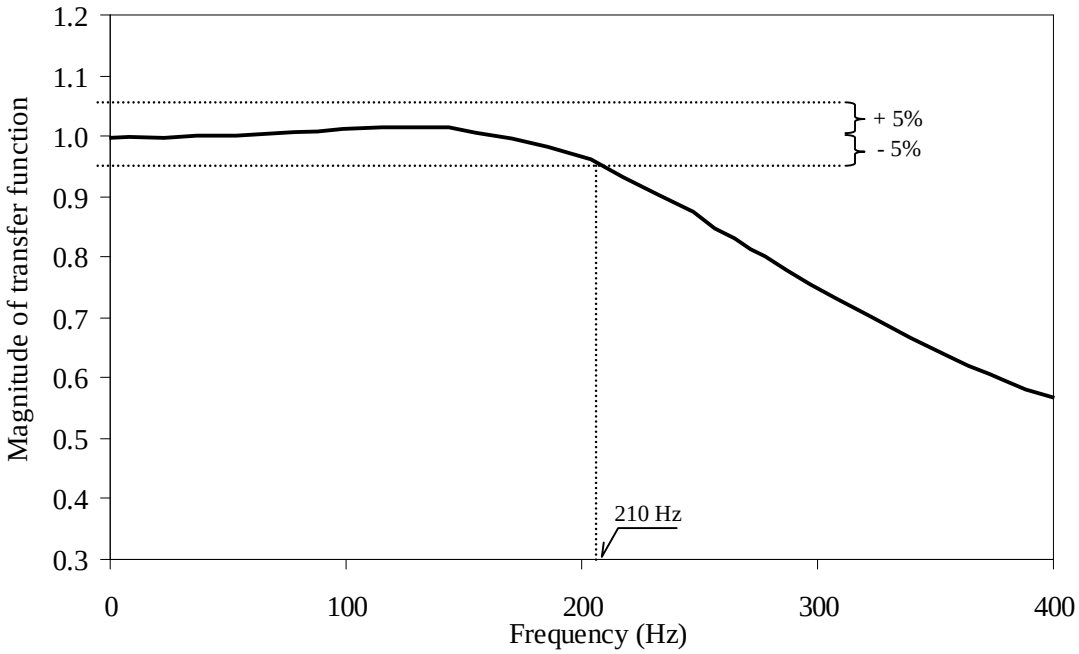

Figure 5.3 Frequency response of pressure measurement system

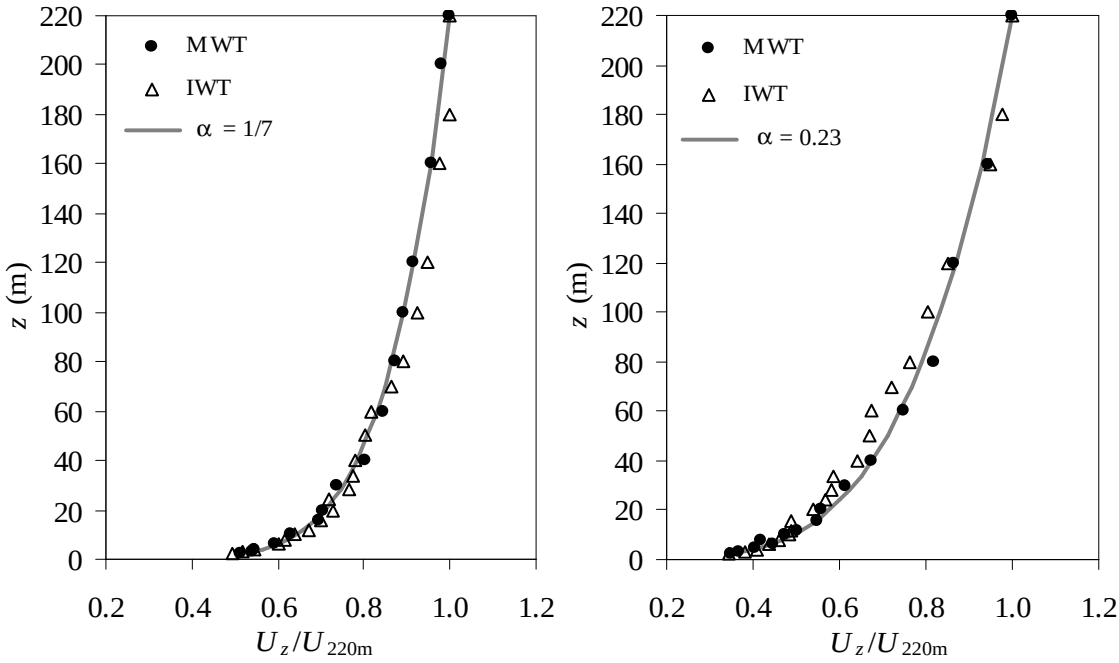

(a) Open wind exposure (b) Suburban wind exposure

Figure 5.4 Comparison of wind tunnel and target mean wind speed profiles

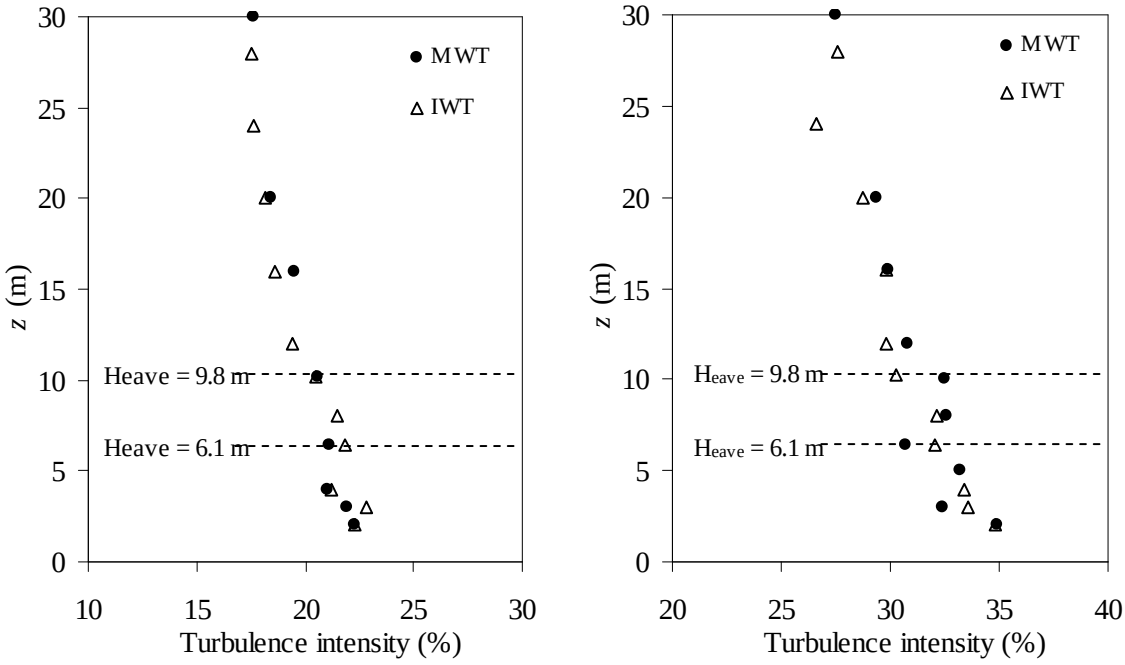

(a) Open exposure (b) Suburban exposure

Figure 5.5 Comparison of turbulence intensity profiles

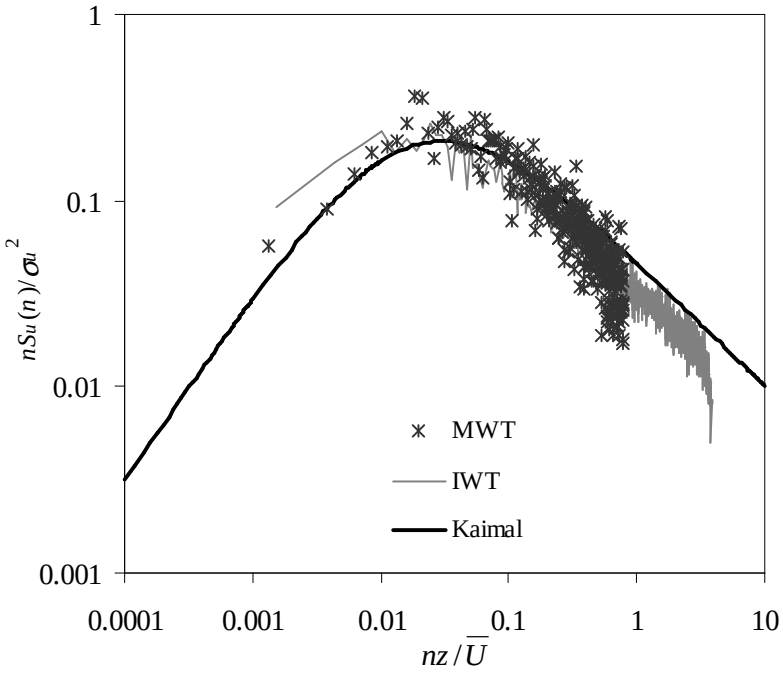

(a) Open exposure

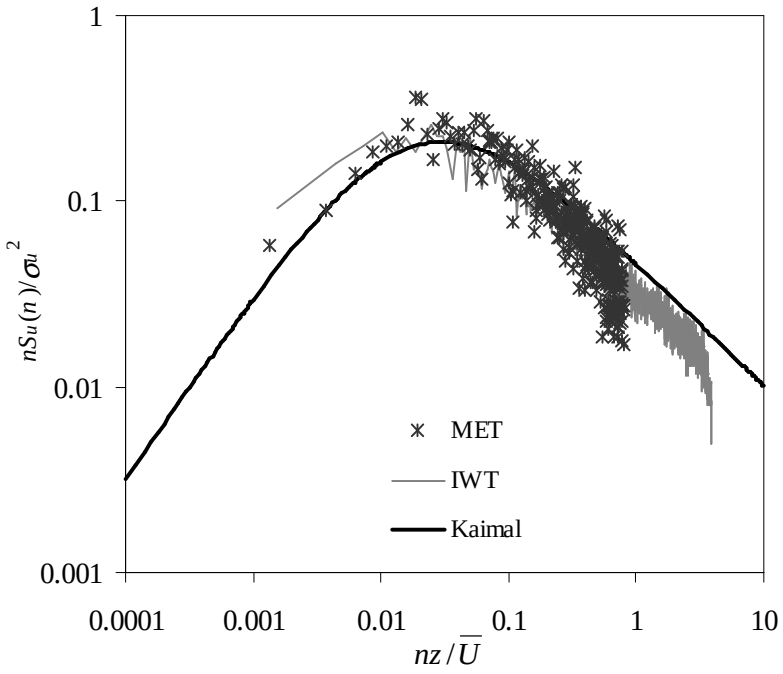

(b) Suburban exposure

Figure 5.6 Comparison of wind tunnel and target velocity spectra

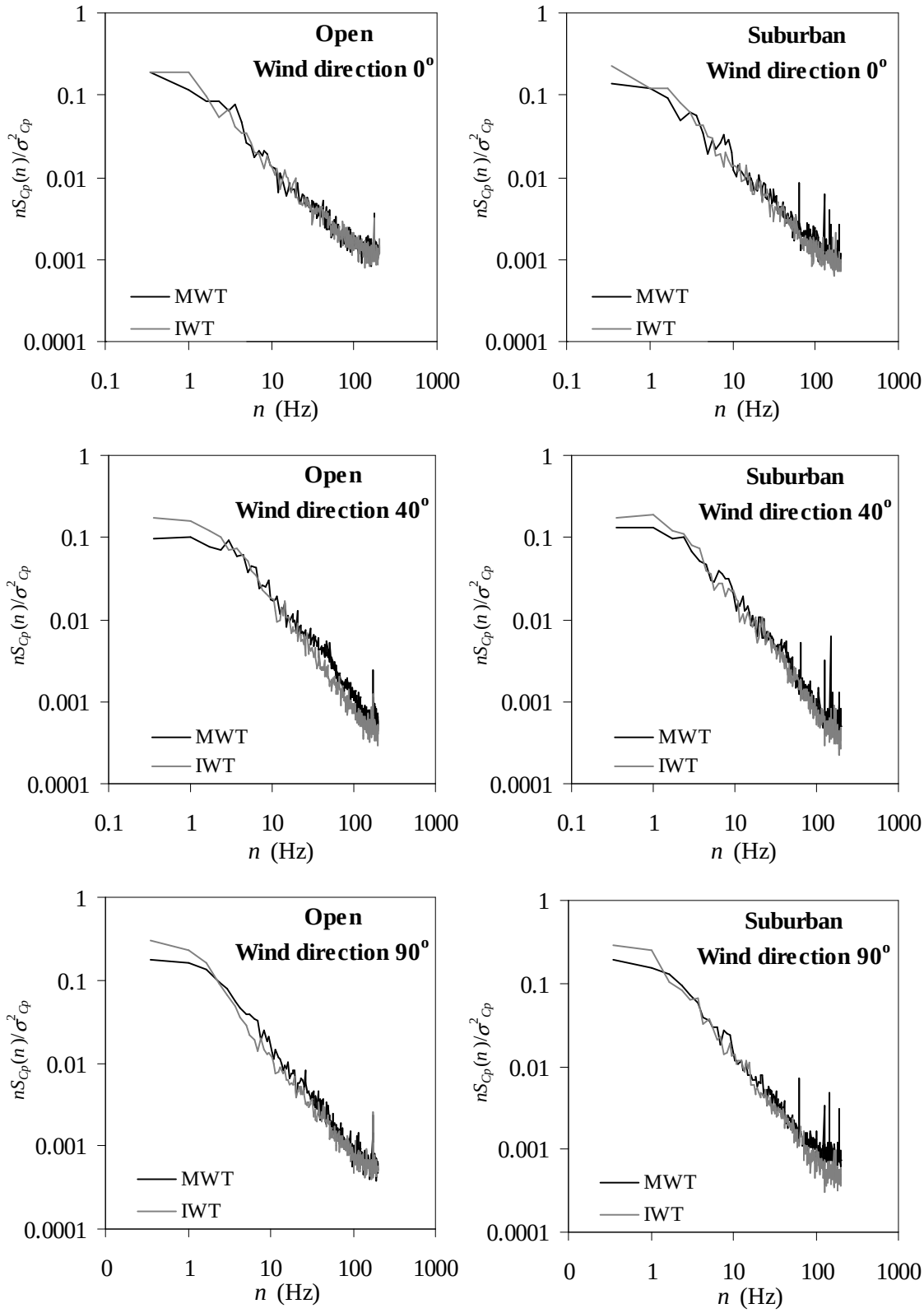

Figure 5.7 Power spectra of roof pressure for tap A, eave height = 6.1 m

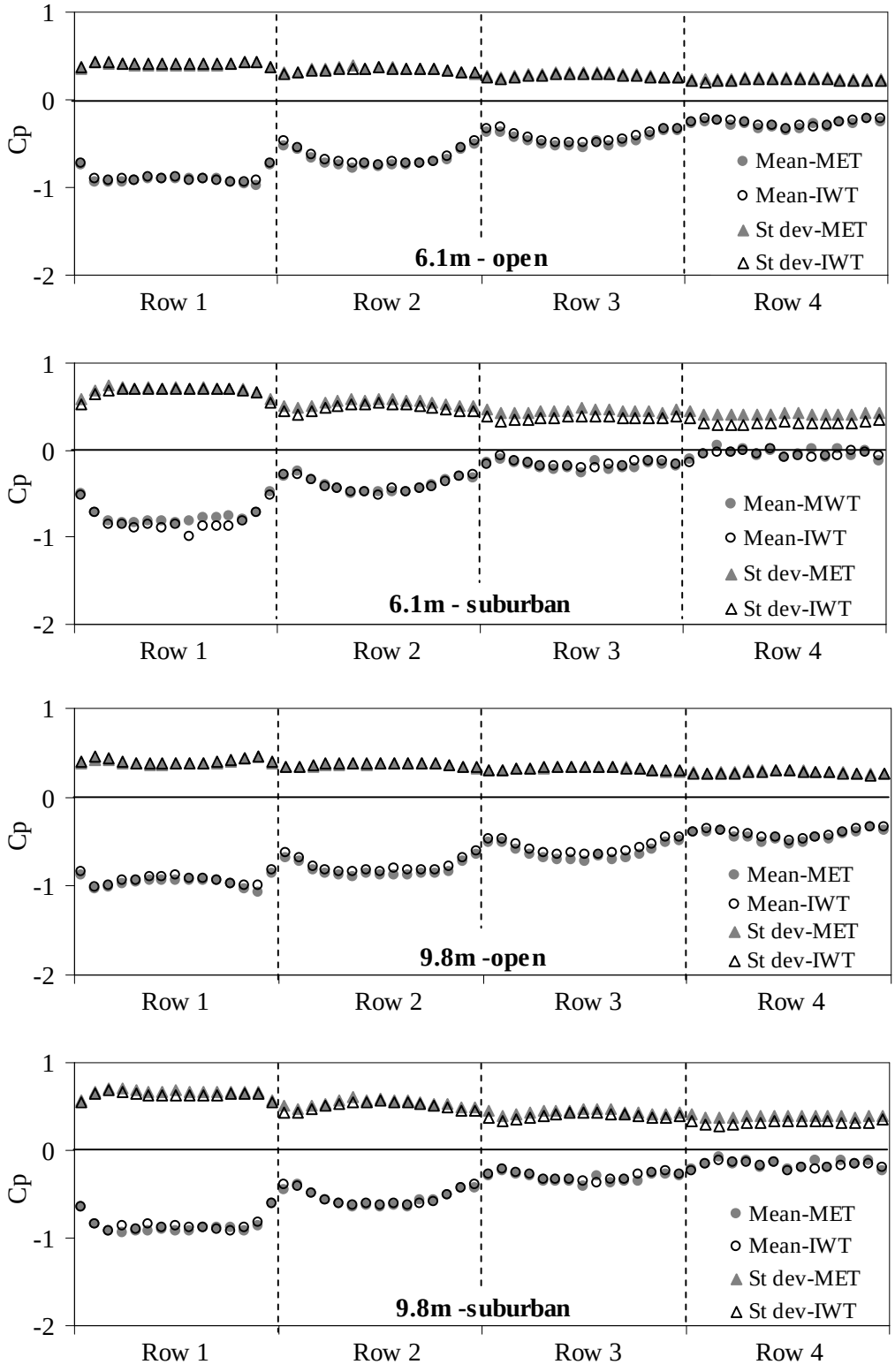

Figure 5.8 Comparison of mean and standard deviation of roof pressures, wind direction of 0^{o}

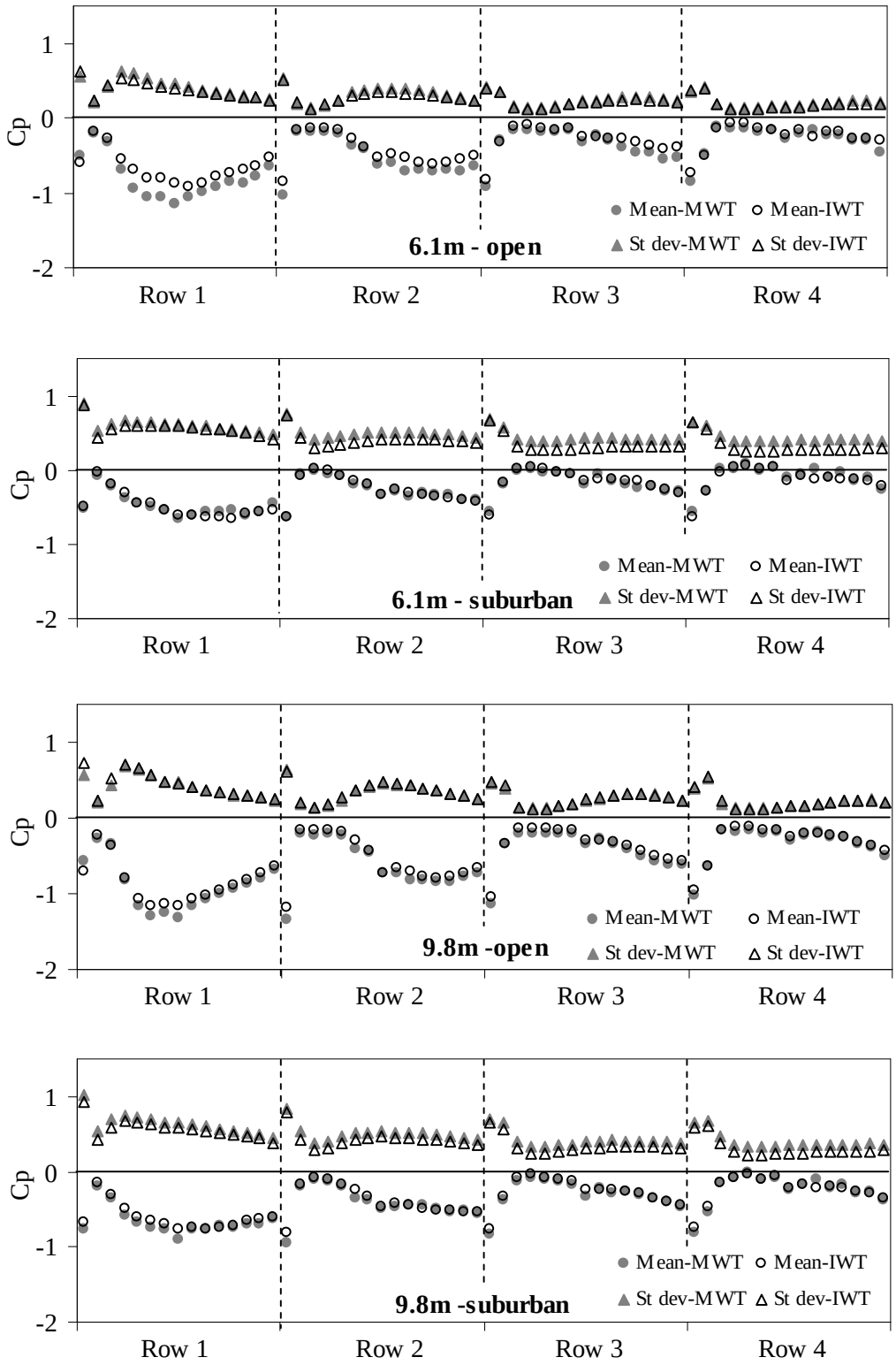

Figure 5.9 Comparison of mean and standard deviation of roof pressures, wind direction of 40^{o}

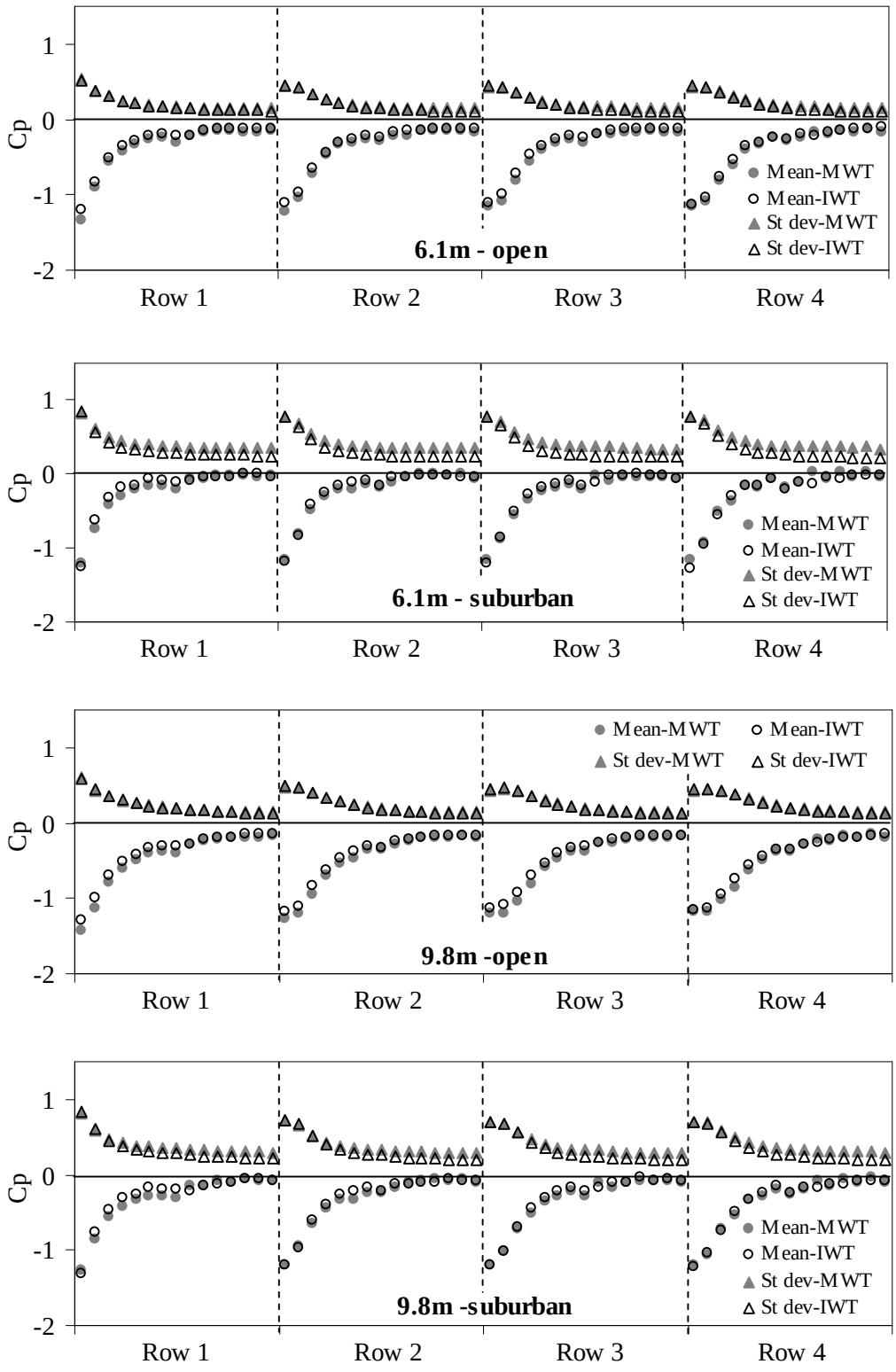

Figure 5.10 Comparison of mean and standard deviation of roof pressures, wind direction of 90^{o}

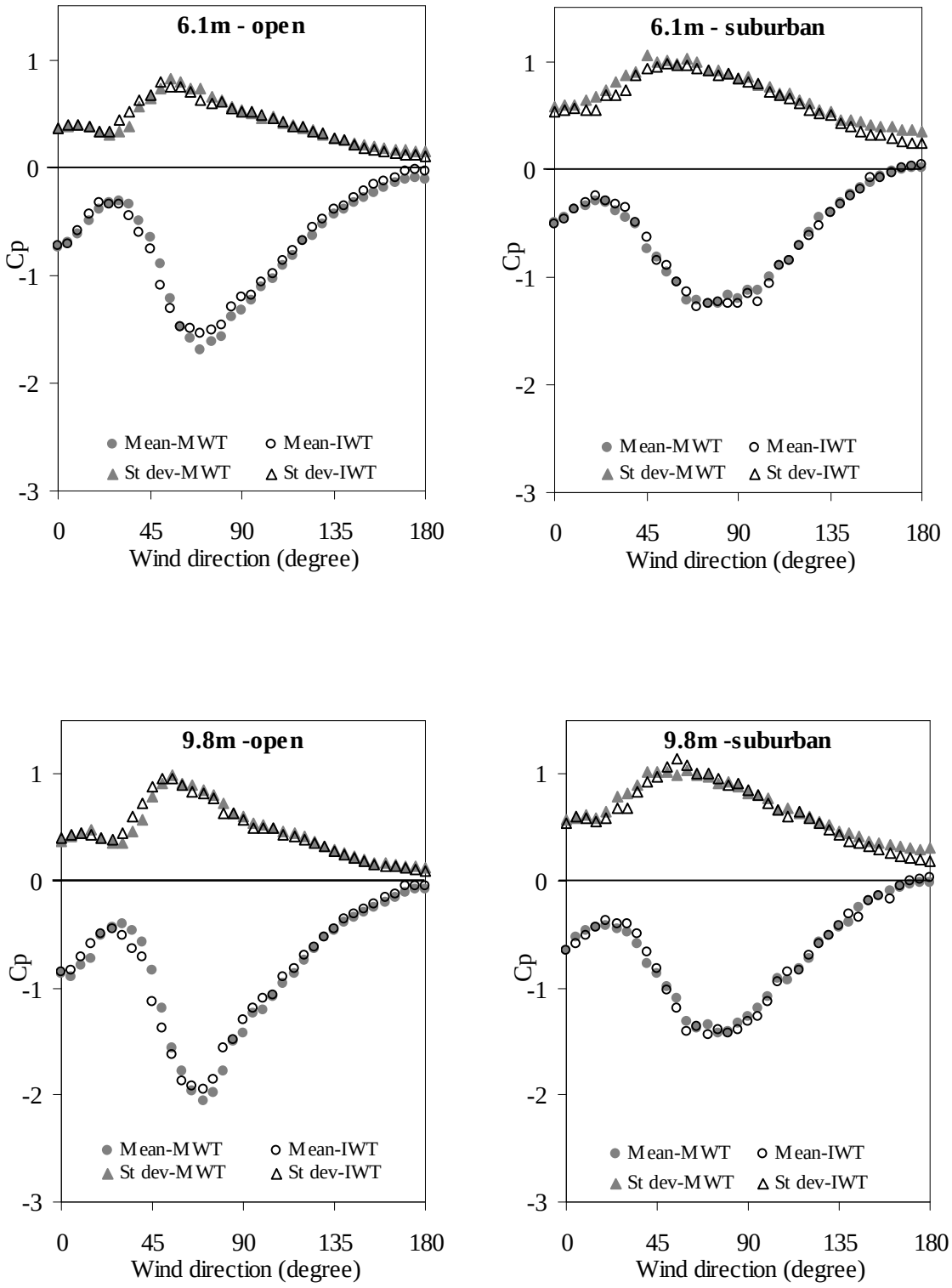

Figure 5.11 Comparison of mean and standard deviation of roof pressures, tap A

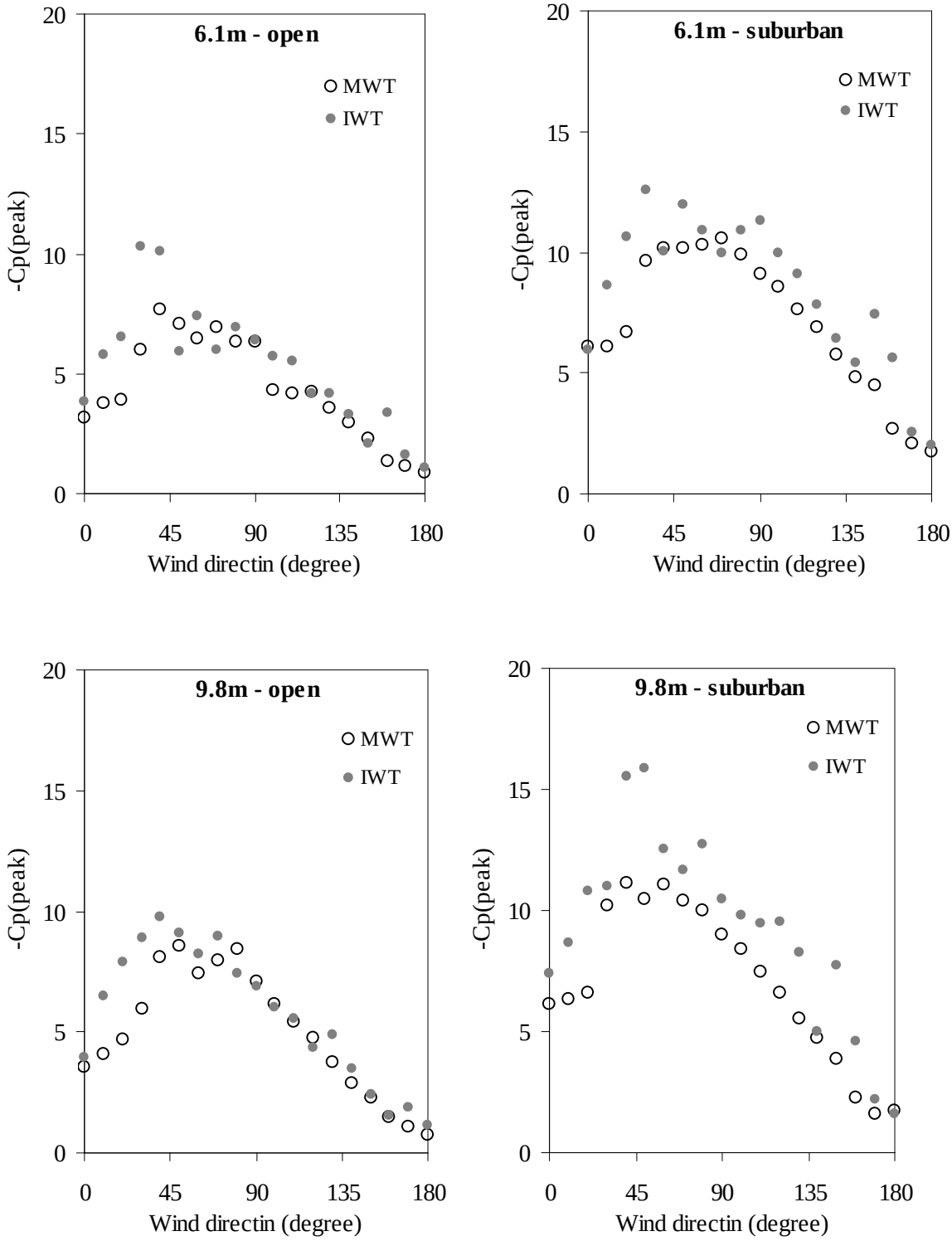

Figure 5.12 Comparison of 90th percentile peak roof pressure, tap A

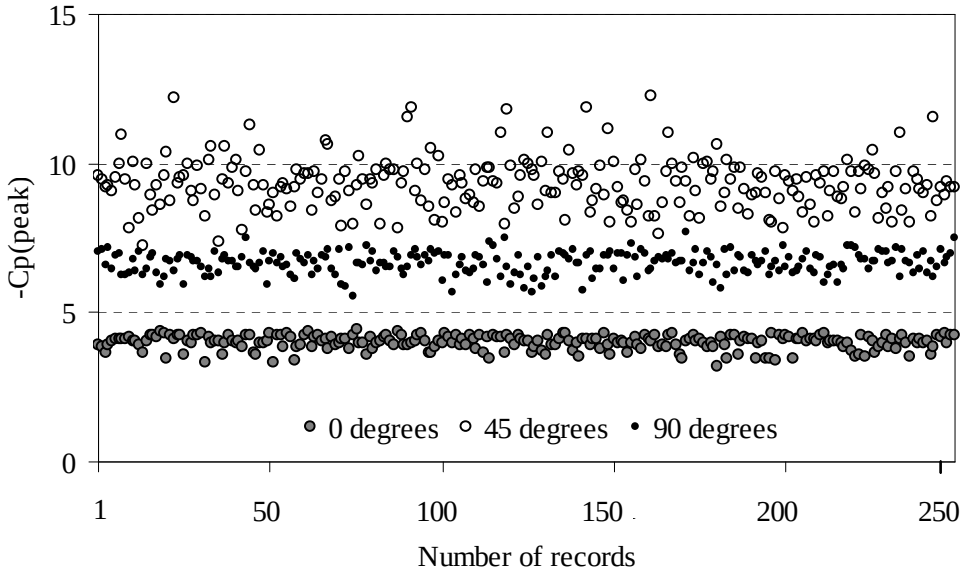

Figure 5.13 90th percentile peak pressures predicted from each record of 250 records, tap A, eave height of 9.8m, open wind exposure

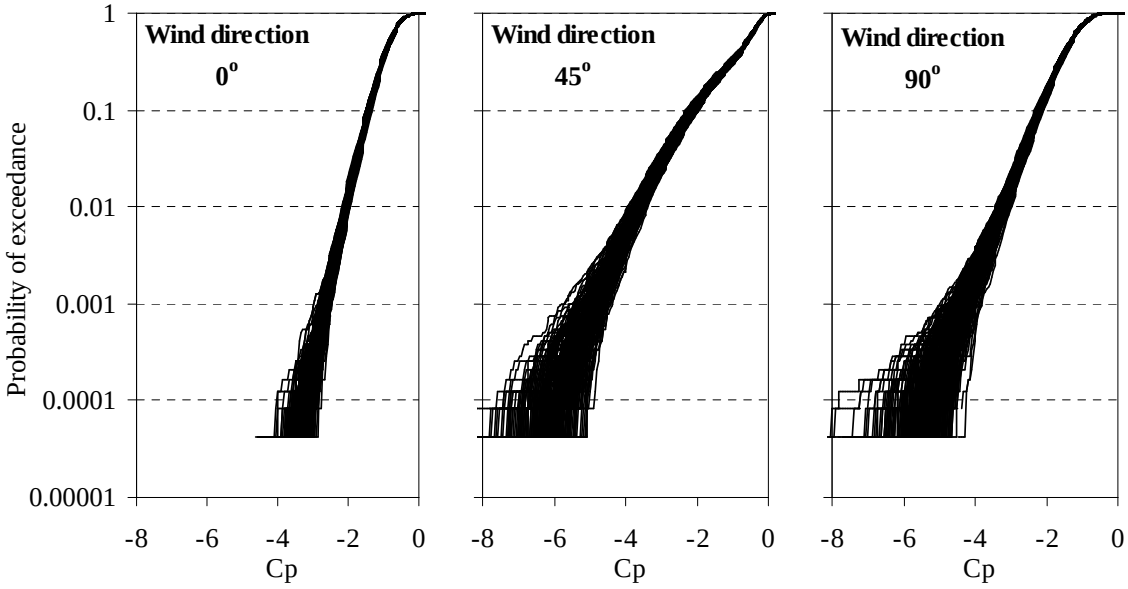

Figure 5.14 Scatter of probability of exceedance for 250 records of time series of pressure data, tap A

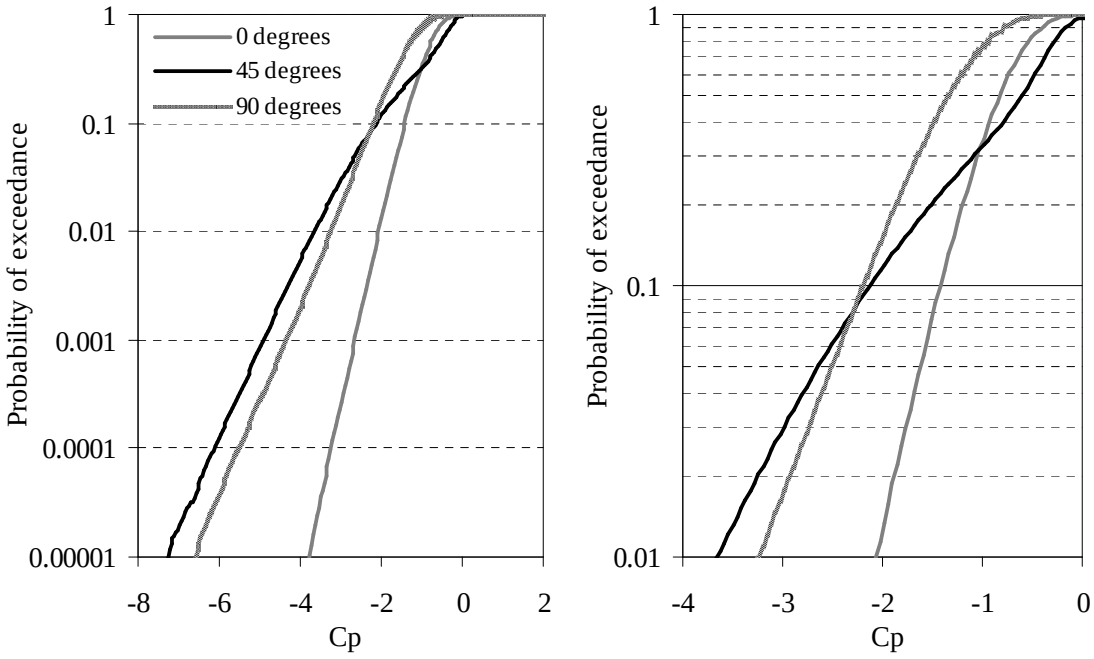

(a) Whole range of POE (b) Range of POE from 1 to 0.01

Figure 5.15 Average of probability of exceedance over 250 records of time series of pressure data, tap A

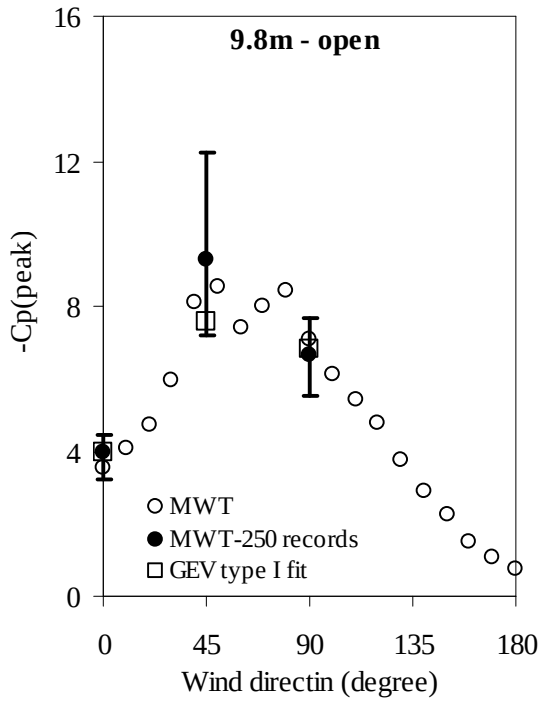

Figure 5.16 90th percentile peak pressure estimated from non-Gaussian procedure and GEV Type I, tap A

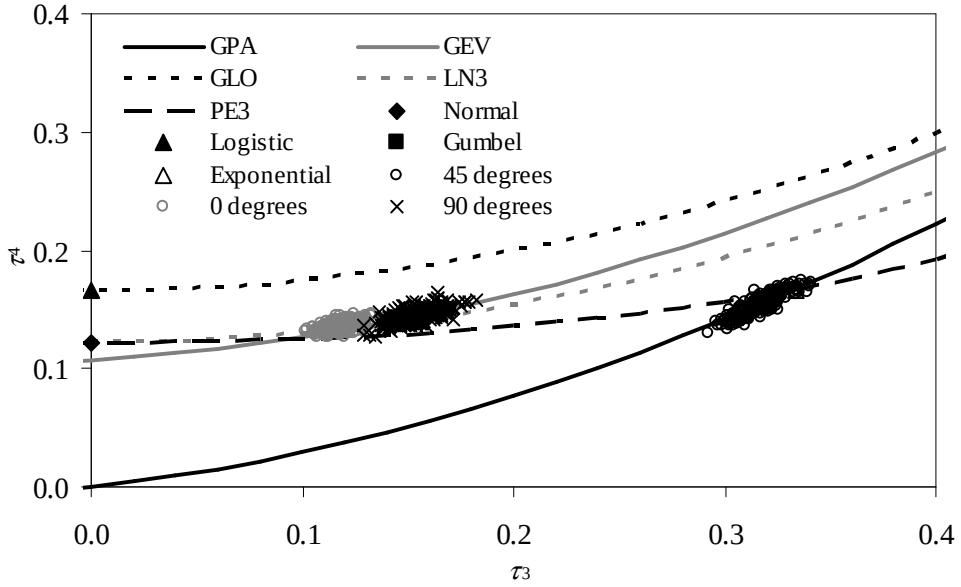

Figure 5.17 τ_3-τ_4 relationship for 250 records of Cp data, tap A

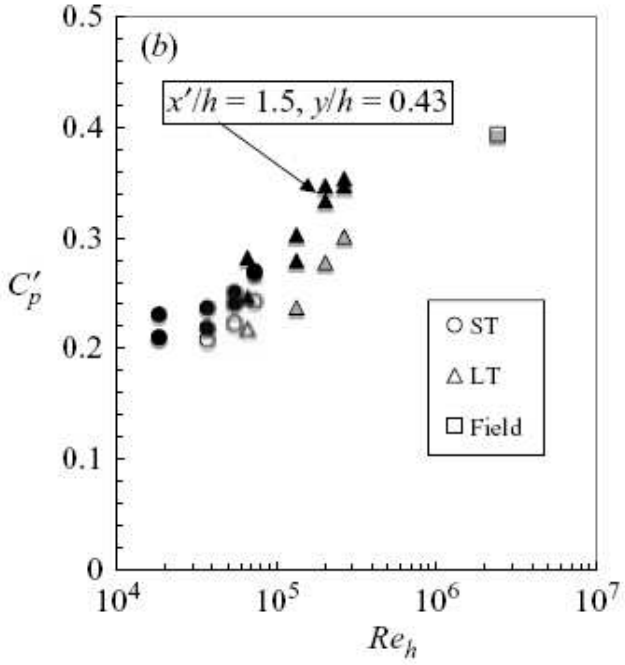

Figure 5.18 Reynolds number effect on fluctuating surface pressure on cubes (Lim *et al*, 2007)

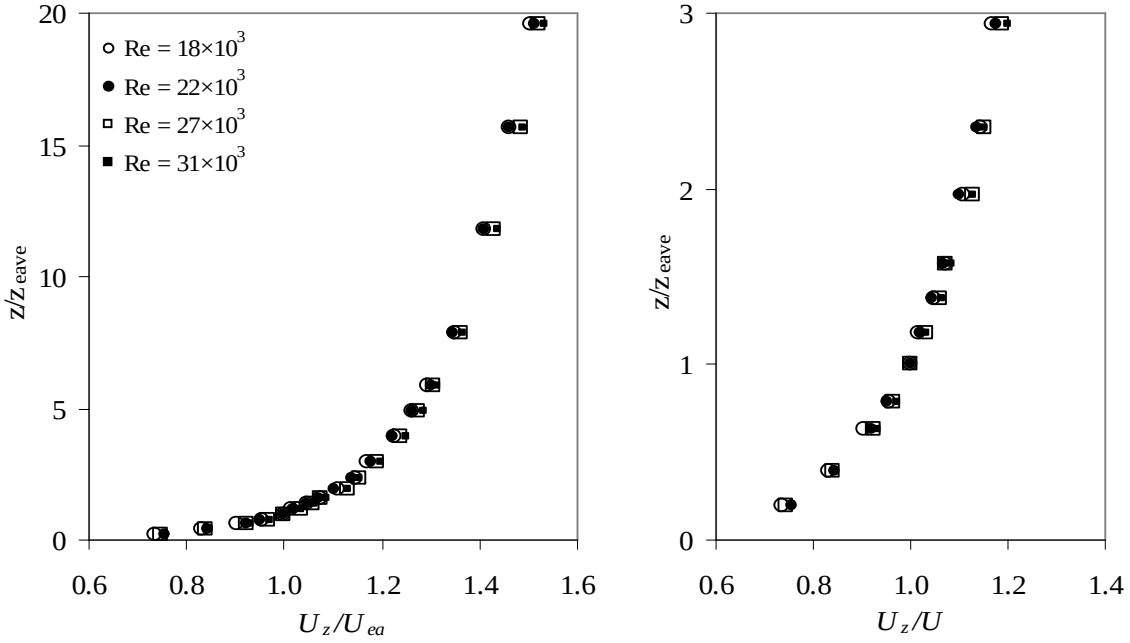

(a) Mean wind speed

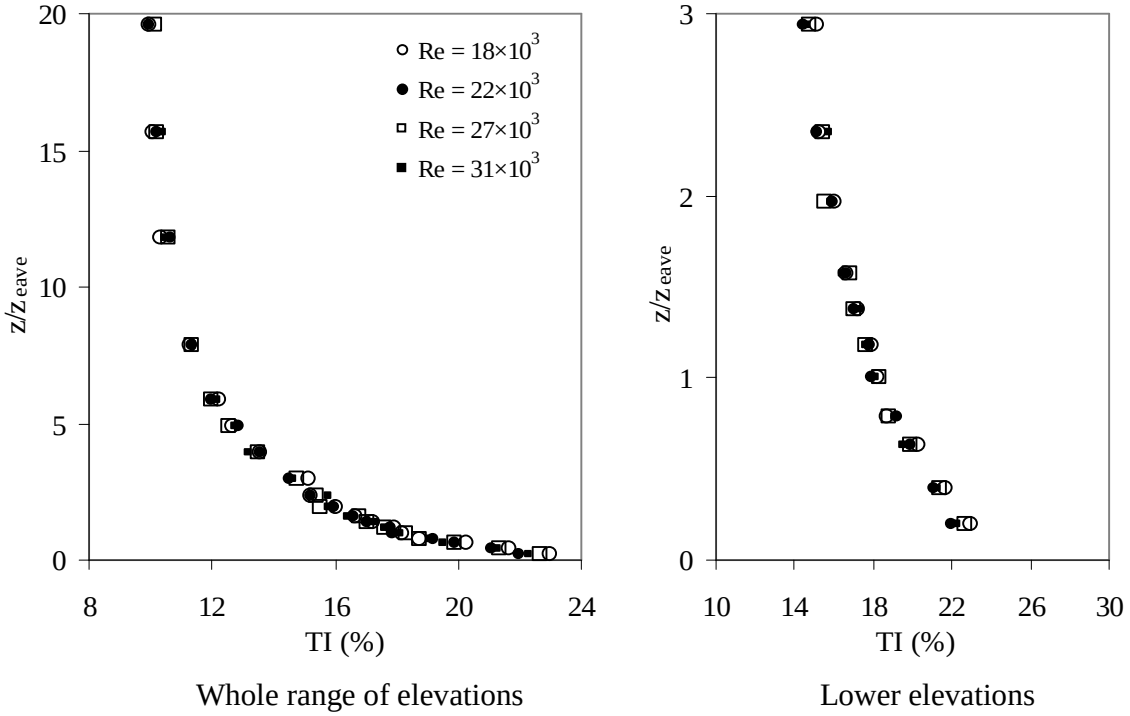

(b) Along-wind turbulence intensity

Figure 5.19 Reynolds number effects on approach flow profiles

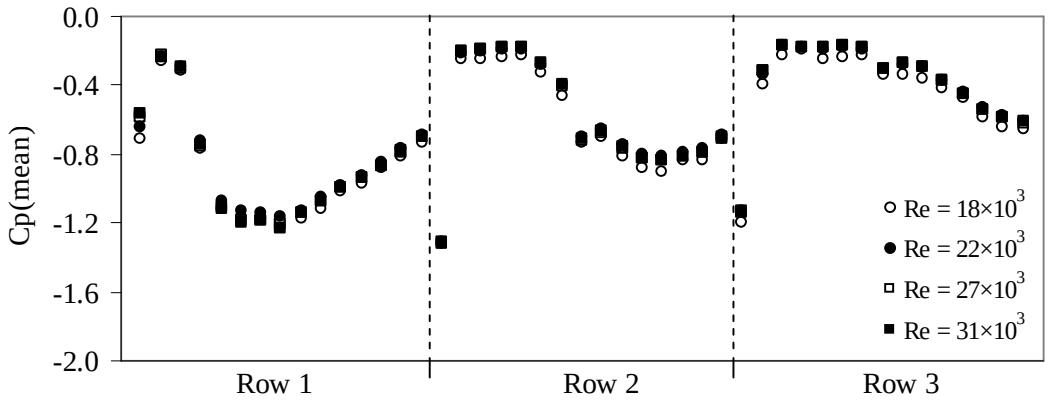

(a) Mean

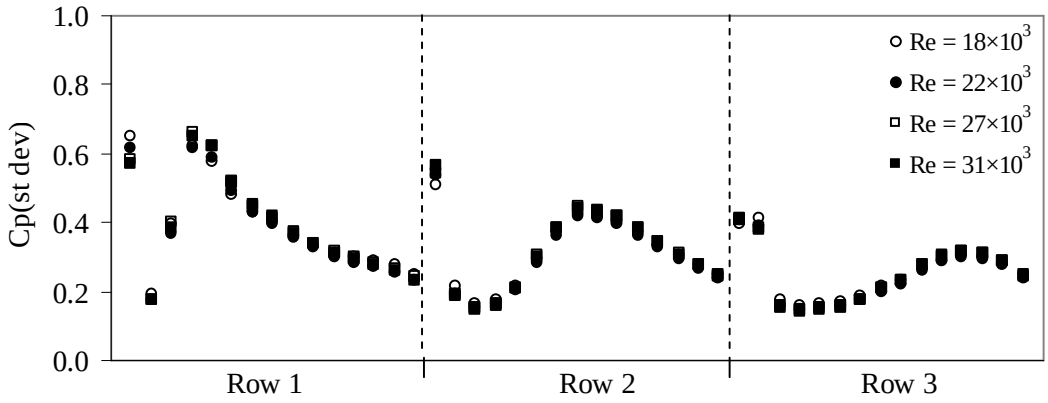

(b) Standard deviation

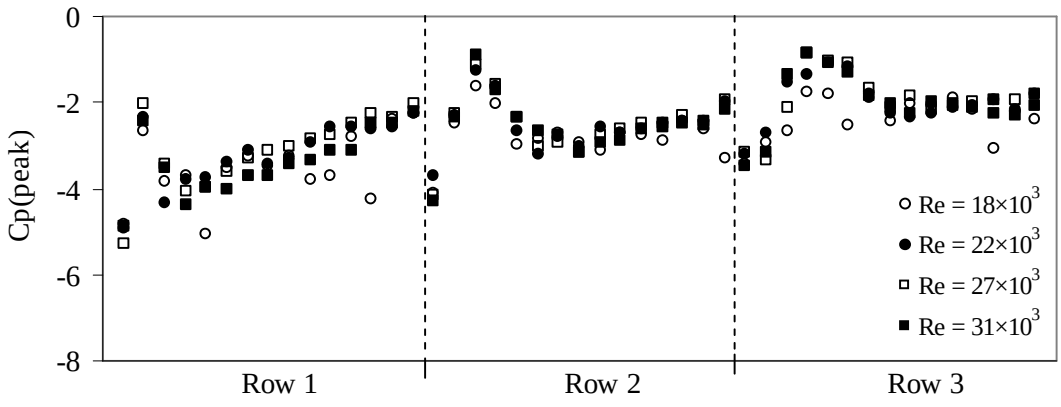

(b) Suction peak

Figure 5.20 Reynolds number effects on wind-induced roof pressures, wind direction of 45^{o}

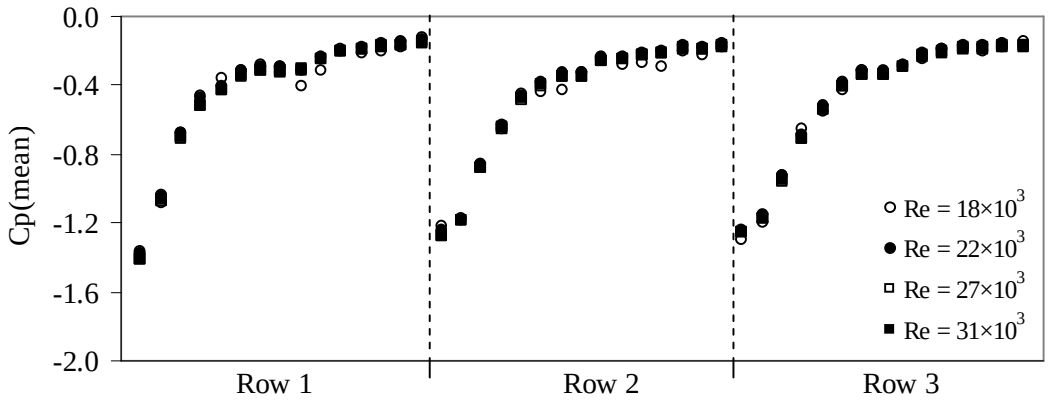

(a) Mean

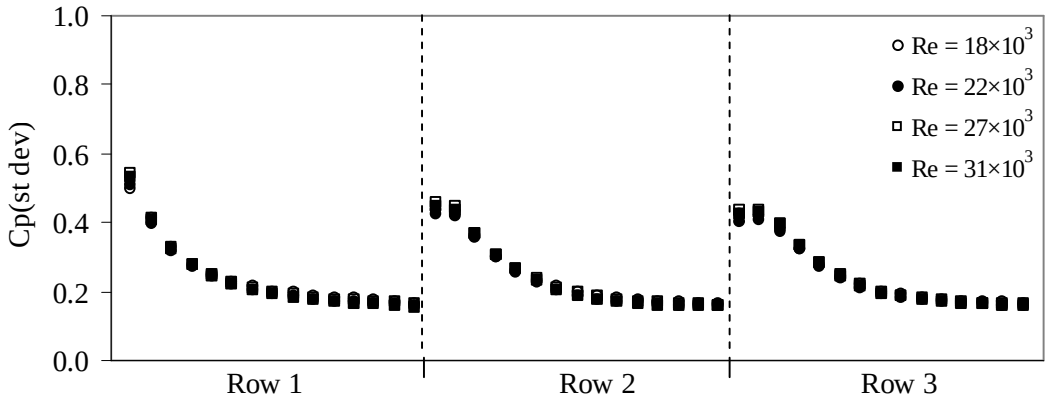

(a) Standard deviation

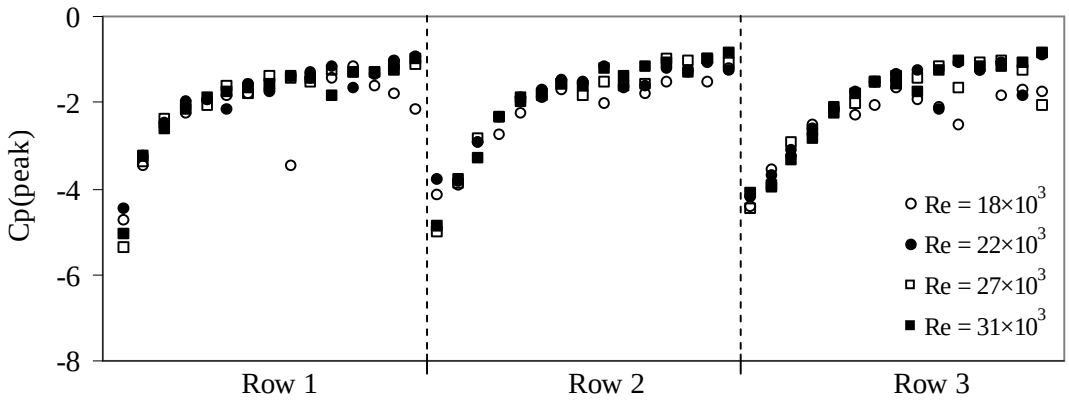

(c) Peak suction

Figure 5.21 Reynolds number effects on wind-induced roof pressures, wind direction of 90^{o}

CHAPTER 6

DEVELOPMENT AND APPLICATION OF ELECTRONICALLY SCANNED 1024-CHANNEL PRESSURE ACQUISITION SYSTEM

This chapter presents an expanded version of material contained in the following reference:

Bienkiewicz, B. and Endo, M. (2011) " Recent efforts on investigation of discrepancies in laboratory modeling of wind loading and development of standardized wind tunnel testing protocols for low buildings", Proceedings of the 2011 NSF Engineering Research and Innovation Conference, 4 – 7 January 2011, Atlanta, GA, 10 pp.

6.1 INTRODUCTION

Experimental techniques have dramatically changed with the advancement in electronic devices for measurements of physical phenomena. In a broad range of research communities, it is preferable and possible to have more precision to measure basic physical quantities through the use of new technologies. It is also desirable that any sophisticated measurement devices can be easily installed and operated during the experiments.

Recently, a unique compact instrumentation - an electronically-scanned 1024-channel pressure acquisition system (ES1024-PS, hereafter) has been developed in the Wind Engineering and Fluids Laboratory (WEFL). The ES1024-PS consists of two 512-channel subsystems operated through host computer(s). Each subsystem consists of eight

64-channel pressure scanners. The synchronized acquisition of pressure data from 1024 channels is accomplished using the two subsystems simultaneously triggered by either software from the host computer or externally by hardware. The designs for the integration and placement of the ES1024-PS have been optimized so that the system can be conveniently mounted underneath the turntables of the three large boundary-layer wind tunnels at WEFL.

The ES1024-PS was employed for the wind load modeling in the Meteorological Wind Tunnel (MWT) at WEFL. During the wind tunnel experiment, a 1:150 geometrical scale model of a generic low-rise industrial building, furnished with 990 pressure taps, was used to acquire wind pressures induced on external surfaces of the model. The study was carried out in a simulated open wind exposure. The time series of pressure data acquired from the 990 locations were next analyzed using various data processing tools.

One of the data analysis techniques employed was the Proper Orthogonal Decomposition (POD). This technique allows for characterization of large data sets – in the present case, the random pressure fields on the building surfaces.

The POD is also known as the Principal Component Analysis. The POD has become a powerful analytical tool to identify the systematic structures hidden in random phenomena. However, the application of the POD in wind-induced loading on a bluff body/building has been limited (Bienkiewicz *et al*. (1993), Holmes (1990), Tamura *et al*. (1999), Ruan et al. (2006)). The decomposition of the random surface pressures by the POD provides a set of modes representative of pressure structures containing most of the energy. Reconstruction of the pressure field using the limited modes that account for the

most dynamic variations in the pressure signal is helpful, as it makes possible reduction in the data sets to be stored for follow-up analyses.

This chapter describes first the development and integration of the ES1024-PS. Next, experimental setups employed in the wind tunnel modeling of wind-induced building pressures using ES1024-PS are described. Finally, the representative results obtained from the wind tunnel experiments employing ES1024-PS and the POD analysis of the acquired building pressures are presented.

6.2 INTEGRATION OF ES1024-PS

The integrated ES1024-PS is schematically presented in Figure 6.1. The major components of this system are arranged into four blocks indicated in the figure: electro-pneumatic subsystem, two 512-channel pressure measurement subsystems and host computer. The electro-pneumatic subsystem comprises of a pneumatic calibrator, two pressure regulators (to apply and set pressures on pressure scanners), power supplies for analog to digital (A/D) modules, and an external triggering device for the synchronized acquisition of pressure data from 1024 channels.

As seen in Figure 6.1, each 512-channel subsystem includes eight 64-channel pressure scanners (Scanivalve ZOC 33 models, denoted ZOC 33), a pneumatic control valve (Scanivalve MSCP 3200) and eight A/D modules (Scanivalve RAD 3200), as well as miscellaneous pneumatic and electronics interface connectors. Descriptions of these components are provided as follows:

ZOC33

ZOC33 is an electronic pressure scanner which has 64 pneumatic inputs. The range of measureable pressure is ±10 inch H_2O (2.5 kPa). A view of ZOC33 is displayed in Figure 6.2. Each ZOC33 comprises of 64 individual piezoresistive pressure sensors and a 500 ohm platinum RTD (resistance temperature detector) used by a RAD 3200 to determine the temperature of the ZOC33.

RAD 3200

RAD 3200 can accept up to eight A/D modules. Each A/D module serves as an interface with one ZOC33. Up to 45.7-m long cable can be used to ensure communication between the RAD 3200 and a host computer. A USB extender is used as an electronic interface. When a ZOC33 module is used with a RAD 3200, the RTD installed in a ZOC33 provides temperature information to correct for errors in the pressure data due to temperature drifts.

USB Extender

When separation between RAD 3200 and a host computer exceeds 3 m (9.8 feet), a USB Extender must be used. In such a case, an extender board must be installed in the RAD 3200 and a USB Extender must be connected between the RAD3200 and the host computer, using USB connection.

MSCP 3200

MSCP 3200 is used to control solenoids to apply control pressures to ZOC33 modules during data acquisition and calibration of the ZOC33s.

512-Channel Pressure Subsystems

All components of each of 512-Channel Pressure Subsystem are tightly packaged. Figure 6.3 shows interior of one of the systems. As can be seen, eight scanners (providing a total of 512 channels for acquisition of pressures from 512 locations) are packed in one box. Eight connectors, each capable of handling 64 pressure channels, are located on one wall of the box. The implemented packaging scheme provides the efficient removal of heat generated by the pressure measurement electronics by means of the passive thermal conduction to the exterior surface. The system is compact and rugged – designed for (usually harsh) environment of wind tunnel experiment.

The acquired data are buffered to the mass storage of the host computers, thus enabling acquisition of long data records. The host computers are used to operate the two 512-channel subsystems throughout a HyperTerminal Ethernet connection, which is typically included in the Microsoft Windows operating system. When the HyperTerminal session is open, any command listed in the Software Requirements Specification (Scanivalve Corp, 2007 (a)&(b)) may be entered to acquire data or to set control parameters.

Placement of scanners and their protection from mechanical damage and environmental effects (e.g. thermal and moisture conditions) is of concern in use of multi-channel pressure acquisition systems. In typical implementations, pressure scanners are placed inside of a tested model (if the number of pressure scanners is small – say less than 5 units) or loosely arranged outside of the wind tunnel test section. This problem is overcome by the system integration implemented via ES1024-PS. the size of each 512-channel unit has been optimized so that the system can be conveniently

mounted underneath the test sections and within turntables of the three large boundary-layer wind tunnels at WEFL. Moreover, the mounting system was developed for easy and safe installation of ES1024-PS. Figure 6.4 shows views of the mounting system and its installation under the wind tunnel turntable.

6.3 DEVELOPMENT OF PRESSURE MEASUREMENT TUBING SYSTEM

The frequency response of the tubing system for pressure measurements must optimized to ensure high quality of the acquired pressures. It magnitude (gain) has to be constant (typically set to unity) and its phase should be linear over the frequency range of interest. In general, characteristics of tubing system depend on the geometric properties of a tube (inner diameter and length of the tube) and structure/volume of pneumatic connectors. Typically, the frequency response of such system is determined experimentally.

Figure 6.5 shows the experimental configuration employed to evaluate the frequency response of the tubing system and pressure taps developed at WEFL and used in this study. A speaker driven by computer-controlled pressure generator is employed as a pressure field generator. The generated pressures are monitored using a reference pressure transducer with very short tubing. Pressure readings are acquired from a second transducer with a tested tubing. Using such an arrangement, the frequency response of the tubing system (used in measurements employing ES1024-PS) has been optimized. The resulting configuration comprised of three tubes, of inner diameter (ID) = 1.37 mm, 0.86 mm and 0.69 mm. The tubing configuration is schematically shown in Figure 6.6. The tubing system includes the pneumatic connectors for quick connection/disconnection

of 512-channel subsystem and a tested model. The views of representative pneumatic connectors are shown in Figure 6.7.

The magnitude and the phase angle of the frequency response function of the optimized tubing configuration are shown in Figure 6.8. As can be seen, the tubing system has a flat magnitude (with a discrepancy of =(+/-)10%) and a linear phase angle for a frequency range spanning up to 210 Hz.

6.4 OVERVIEW OF PROPER ORTHOGONAL DECOMPOSITION

This section briefly presents the theoretical background on the proper orthogonal decomposition (POD) analysis of random fields, such as wind-induced pressures, adapted from Bienkiewicz *et al*. (1993). The main objective of the POD is to extract the deterministic function $\Phi(x, y)$ which is highly correlated with all the elements of the ensemble of random fields, such as experimental pressure data.

By assuming a random fluctuating pressure $p(x, y, t)$ with zero mean, the maximum of the projection of $p(x, y, t)$ on the function $\Phi(x, y)$ is sought. This operation can be expressed by an integral form as follows

$$\iint p(x, y, t)\Phi(x, y)dxdy = \max. \qquad [6.1]$$

The normalized form of Equation 6.1 can be written as

$$\frac{\iint p(x, y, t)\Phi(x, y)dxdy}{\sqrt{\iint \Phi^2(x, y)dxdy}} = \max. \qquad [6.2]$$

Since $p(x, y, t)$ randomly takes both positive and negative values, the ensemble of the square of Equation [6.2] can be considered and its maximum is sought

$$\frac{\overline{\iint p(x,y,t)\Phi(x,y)dxdy \iint p(x',y',t)\Phi(x',y')dx'dy'}}{\iint \Phi^2(x,y)dxdy} = \max. \qquad [6.3]$$

This leads to an eigenvalue problem which can be written as follows

$$\iint R_p(x,y,x',y')\Phi(x',y')dx'dy' = \lambda\Phi(x,y) \qquad [6.4]$$

where $R_p(x,y,x',y')$ is the space covariance of $p(x, y, t)$. When the pressure is acquired at discrete locations that are uniformly distributed, Equation [6.4] can be expressed in a matrix form

$$R_p\Phi = \lambda\Phi \qquad [6.5]$$

where R_p is the covariance matrix, Φ is the eigenvector and λ is the eigenvalue. If the space covariance matrix R_p of $p(x, y, t)$ is known, Equation [6.5] can be solved to determine the eigenvalues λ_n and the eigenvectors $\Phi_n(x,y)$. The eigenvectors can be used to express the original fluctuating wind-induced pressure $p(x, y, t)$ as

$$p(x,y,.t) = \sum_{n=1}^{N} a_n(t)\Phi_n(x,y). \qquad [6.6]$$

where $a_n(t)$ are the principal coordinates given by

$$a_n(t) = \frac{\iint p(x,y,t)\Phi_n(x,y)dxdy}{\iint \Phi_n^2(x,y)dxdy}. \qquad [6.7]$$

6.5 WIND TUNNEL EXPERIMENT EMPLOYING ES1024-PS AND POD ANALYSIS ON BUILDING PRESSURES

6.5.1 Building Model

A generic low-rise industrial building with prototype planar dimensions of 61 m × 30.5 m and a building height of 12.2 m was selected and it was modeled at a geometrical

scale of 1:150. The model was furnished with 990 miniature pressure taps – precision tubulations (ID = 1.6 mm and length = 19.1 mm) to enable attachment of tubing connecting the taps with scanners of the pressure measurement system. The geometry of the building model and tap locations are schematically described in Figure 6.9. The pressure tap numbers are specified in Figure 6.10. It can be seen that the taps are uniformly distributed over the building surfaces. As a result, approximately equal tributary areas are associated with the taps. Such a tap arrangement simplifies spatio-temporal analysis of the time series of the acquired pressures. The fabricated model is shown in Figure 6.11.

6.5.2 Experimental Configuration and Modeled Approach Flow

The wind load modeling study was carried out in an open wind exposure modeled in the Meteorological Wind Tunnel (MWT). The approach flow was simulated at the geometrical scale of 1:150. The overall view of the developed experimental set-up and the model installed in the wind tunnel is depicted in Figure 6.12.

The mean velocity and turbulence intensity profiles of the modeled approach flow were measured using hot-film probes in conjunction with constant temperature hot-wire anemometers. The reference velocity and the static pressure were monitored using a pitot-static tube mounted at a height of 100 cm. Hot-film data were sampled at a rate of 1000 samples/second. Flow data records were 60 second in length. The analog signals were low-pass filtered with a cut-off frequency of 500 Hz.

The characteristics of the simulated approach wind exposure are shown in Figures 6.13 and 6.14. The comparison of the target (power-law exponent α = 1/7) and modeled

profiles of the mean velocity is presented in Figure 6.13a. The laboratory turbulence intensity was compared with the target ESDU turbulence model (see Equation [4.5]) in Figure 6.13b. The laboratory along-wind velocity power spectra were compared with the Kaimal spectra model (see Equation [2.2]) in Figure 6.14. Overall, very good agreement between the target and the simulated approach wind exposure was obtained.

6.5.3 Acquision of Wind-induced Pressures on Building Surfaces

As mentioned in Section 6.5.1, the building model was furnished with 990 pressures taps. Time series of building pressures were acquired at these locations using the ES1024-PS. The overall views of the ES1024-PS and the building model during and after installation in the wind tunnel test section are shown in Figure 6.15. The pressure time series were acquired at a sampling rate of 332.45 samples per second. Approximately 90-second data record (30,000 data points), per pressure tap, was acquired for wind directions of 0^o and 45^o.

The time series of building pressure data (acquired from the ES1024-PS) were stored in the host computers. Two data files containing 512 channels of pressure data/file were saved in binary format. However, such binary format data need to be converted to the ASCII (text type) format for use in the analyses of the data. A data processing tool for the conversion of the pressure data from binary to ASCII format was developed using LabView programming software. The user interface of this tool is shown in Figure 6.16.

6.5.4 Results

Time series data of wind-induced building pressures acquired at 990 locations on the building surfaces (see Figure 6.10) were employed in the data analysis. Representative results are presented in Figures 6.17 and 6.18, where the plots of the mean, average peak and standard deviation of the pressure coefficients are shown for wind directions of 0^o and 45^o, respectively. The average peaks of the building pressures were computed from ten records of the pressure data. It can be seen that, as expected, the largest wind-induced negative pressures (suctions) occur in the roof corner and edge regions, and they are larger in magnitude for the cornering wind direction (45^o).

The representative portions of the space covariance matrix for the building pressures (acquired at 990 locations) are presented in Table 6.1, for the first 15 tap locations, see Figure 6.10. The space covariance matrix was used in the POD analysis to determine eigenvalues and eigenvectors. The user interface of a computational tool developed for this analysis is shown in Figure 6.19. Figures 6.20 and 6.21 depict the first three eigenvectors of the building pressures obtained for wind directions of 0^o and 45^o, respectively. Table 6.2 lists values of eigenvalues and compares the contribution of individual and cumulative sum of the eigenvalue to the mean square (total energy of fluctuation) of the building pressures up to first 25 modes.

The percentage contribution of the eigenvalues is plotted in Figure 6.22. It can be seen in Table 6.2 that the modal contribution of the first eigenvalue is the largest, approximately 27% for both tested wind directions, 0^o and 45^o. Figure 6.22 shows a steep decay in modal contributions when the modal index n exceeds 5. These first five modes contribute more than half of the total energy, approximately 60%, for both the

wind directions. It can be also observed in the figure that the cumulative sum (contribution to the total energy of fluctuating pressures) exceeds 90% at the 92nd mode for wind direction of 0^o while the 67 modes are required for wind direction of 45^o.

Table 6.1 Space covariance matrix of building pressure for first 15 tap locations

(a) Wind direction of 0^o

Tap	1	2	3	4	5	6	7	8	9	10	11	12	13	14	15
1	1	0.899	0.815	0.726	0.646	0.566	0.484	0.407	0.335	0.270	0.206	0.140	0.075	0.025	-0.018
2		1	0.959	0.900	0.834	0.761	0.681	0.601	0.523	0.449	0.375	0.294	0.209	0.136	0.044
3			1	0.962	0.914	0.852	0.778	0.702	0.625	0.549	0.472	0.385	0.293	0.210	0.095
4				1	0.969	0.923	0.864	0.796	0.724	0.649	0.571	0.482	0.385	0.294	0.159
5					1	0.970	0.925	0.867	0.800	0.728	0.651	0.561	0.462	0.366	0.215
6						1	0.969	0.925	0.867	0.802	0.729	0.641	0.541	0.441	0.276
7							1	0.971	0.928	0.873	0.806	0.723	0.626	0.524	0.352
8								1	0.972	0.931	0.874	0.800	0.707	0.607	0.427
9									1	0.972	0.929	0.866	0.782	0.685	0.500
10										1	0.972	0.924	0.851	0.759	0.573
11											1	0.968	0.912	0.831	0.649
12				Symmetric								1	0.963	0.901	0.731
13													1	0.958	0.817
14														1	0.898
15															1

(b) Wind direction of 45^o

Tap	1	2	3	4	5	6	7	8	9	10	11	12	13	14	15
1	1	0.933	0.891	0.861	0.839	0.813	0.778	0.746	0.708	0.670	0.630	0.576	0.503	0.420	0.248
2		1	0.965	0.934	0.910	0.884	0.846	0.810	0.766	0.723	0.676	0.613	0.528	0.434	0.241
3			1	0.978	0.956	0.932	0.897	0.861	0.816	0.772	0.722	0.655	0.566	0.465	0.261
4				1	0.983	0.963	0.937	0.904	0.862	0.819	0.769	0.699	0.609	0.503	0.294
5					1	0.985	0.964	0.936	0.896	0.856	0.807	0.738	0.649	0.541	0.329
6						1	0.983	0.959	0.925	0.889	0.842	0.775	0.686	0.578	0.363
7							1	0.985	0.961	0.930	0.889	0.826	0.740	0.631	0.414
8								1	0.984	0.960	0.925	0.868	0.787	0.679	0.461
9									1	0.985	0.961	0.914	0.842	0.738	0.523
10										1	0.984	0.949	0.886	0.788	0.579
11											1	0.978	0.929	0.842	0.641
12				Symmetric								1	0.974	0.910	0.731
13													1	0.966	0.830
14														1	0.922
15															1

Table 6.2 Eigenvalues of covariance matrix for building pressures (up to first 25 modes)

Mode (n)	Eigenvalue (λ_n)		Contribution of eigenvalue (%) $\lambda_n / \sum_{n=1}^{990} \lambda_n$		Cumulative sum of eigenvalues (%) $\sum_{n=1}^{N} \lambda_n / \sum_{n=1}^{990} \lambda_n$	
	WD = 0°	WD = 45°	WD = 0°	WD = 45°	WD = 0°	WD = 45°
1	7.14	8.35	26.5	27.1	26.5	27.1
2	5.06	5.31	18.8	17.2	45.3	44.4
3	2.00	3.98	7.4	12.9	52.8	57.3
4	0.88	1.12	3.3	3.6	56.1	60.9
5	0.61	0.67	2.3	2.2	58.3	63.1
6	0.58	0.62	2.1	2.0	60.5	65.1
7	0.52	0.51	1.9	1.6	62.4	66.8
8	0.49	0.47	1.8	1.5	64.2	68.3
9	0.39	0.42	1.4	1.4	65.7	69.7
10	0.36	0.41	1.3	1.3	67.0	71.0
11	0.33	0.33	1.2	1.1	68.3	72.1
12	0.31	0.30	1.1	1.0	69.4	73.1
13	0.26	0.30	1.0	1.0	70.3	74.0
14	0.23	0.26	0.9	0.8	71.2	74.9
15	0.22	0.25	0.8	0.8	72.0	75.7
16	0.21	0.23	0.8	0.7	72.8	76.4
17	0.20	0.22	0.8	0.7	73.5	77.1
18	0.18	0.21	0.7	0.7	74.2	77.8
19	0.17	0.19	0.6	0.6	74.8	78.4
20	0.16	0.18	0.6	0.6	75.4	79.0
21	0.15	0.17	0.6	0.5	76.0	79.6
22	0.14	0.16	0.5	0.5	76.5	80.1
23	0.13	0.15	0.5	0.5	77.0	80.6
24	0.12	0.14	0.5	0.4	77.4	81.0
25	0.11	0.13	0.4	0.4	77.9	81.4

The eigenvalues and eigenvectors obtained from the POD analysis were next used to reconstruct the original time series of the building pressures, based on Equation 6.6. First, the principal coordinates $a_n(t)$ were computed using Equation 6.7. Figures 6.23 and 6.24 present the time series of first five principal coordinates for wind directions of 0^o and 45^o, respectively. They are plotted for the first 20 seconds of the data records. It can be observed that these coordinates are random and that the largest contributions (fluctuations) are exhibited by the first coordinate $a_{1,}$ for both the considered wind directions. Figure 6.25 compares the standard deviations of each principal coordinate. The modal fluctuation (standard deviation) decreases with increase in the mode index *n*.

Reconstruction of the original time series of building pressures was performed next. The time series of building pressure at tap 124 (see Figure 6.10), where the largest magnitude of suction pressure occurred, were selected for the reconstruction analysis. The original building pressure data are compared with the reconstructed time series, using first 1, 10, 100 and 990 modes, in Figures 6.27 and 6.28 for wind directions of 0^o and 45^o, respectively. The original and reconstructed time series data are plotted for the first one second of the data record. Very good agreement between the original and reconstructed data is observed when the first 100 modes of the principal coordinates (10% of all modes) are used in the reconstruction, for both wind directions. Additionally, the reconstructed data using all 990 modes fully coincide with the original time series. The convergences of peak and standard deviation of reconstructed building pressure data were also investigated, see Figure 6.28. It can be seen that the standard deviation converges faster than the maximum and minimum peaks. The convergence of peaks within $\pm$5% errors was obtained at the 170th mode. On the other hand, the 69 modes

were required for wind direction of 45^{o}. Thus, it can be concluded that significant features can be preserved when only portion of the modal eigenvalues and eigenfucntions is retained for further analysis.

6.6 CONCLUSIONS

The findings of the efforts described in this chapter can be summarized as follows:

1. Development and integration of advanced instrumentation ES1024-PS were successfully completed. This system has advantages such as simultaneous scanning of up to 1024 channels, compact and rugged design, easy setup for wind tunnel testing, thermal compensation and well-tuned tubing system.
2. Data acquired from ES1024-PS in wind tunnel experiment can provide higher resolutions of results which can be used in sophisticated data analyses, such as POD technique.
3. In the POD analysis, less than 10% of the total number of eigenvalues was required for retaining of significant portion of the pressure fluctuations.
4. Excellent reconstruction of building pressure data was achieved with 10% to 20% of the total number of the calculated modes (principal coordinates). The amount data to be required for further analyses can be dramatically reduced, by more than 80%.

6.7 REFERENCES

Bienkiewicz, B., Ham, H.J. and Sun, Y. (1993), "Proper orthogonal decomposition of roof pressure," *J. Wind Eng. Ind. Aerodyn*, Vol. 50, pp. 193-202.

Holmes, J.D. (1990), "Analysis and synthesis of pressure fluctuations on bluff bodies using eigenvectors," *J. Wind Eng. Ind. Aerodyn*, Vol. 33, pp. 219-230.

Ruan, D, He, H., Castañón, D.A. and Mehta, K.C. (2006). "Normalized proper orthogonal decomposition (NPOD) for building pressure data compression," *J. Fluids and Structures*, Vol. 94, pp. 447-461.

Tamura, Y., Suganuma, S., Kikuchi, H., and Hibi, K. (1999), "Proper orthogonal decomposition of random wind pressure field," *J. Fluids and Structures*, Vol. 13, pp. 1069-1095.

Scanivalve. (2007a), *RAD 3200 series software requirements specification – RAD2 V5.04*, Scanivalve Corp.

Scanivalve. (2007b), *RAD 3200 series software requirements specification – RAD2 V5.04 supplement – Advanced programming information*, Scanivalve Corp.

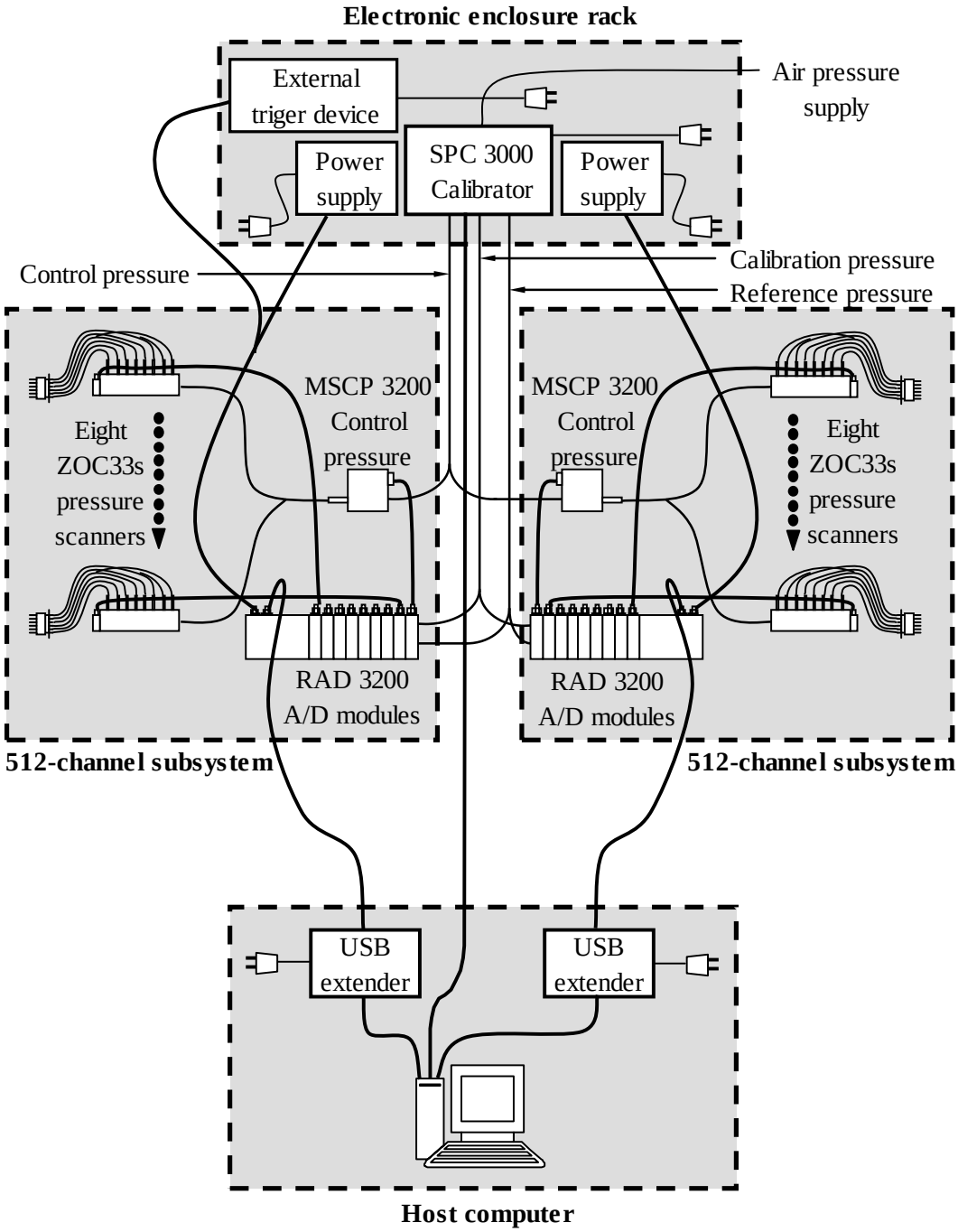

Figure 6.1 Schematic diagram of ES1024-PS

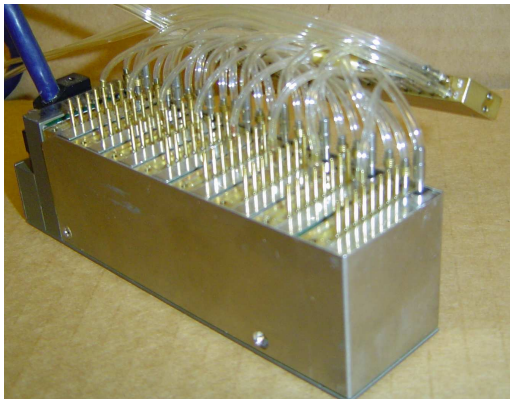

Figure 6.2 Representative 64-channel pressure scanner

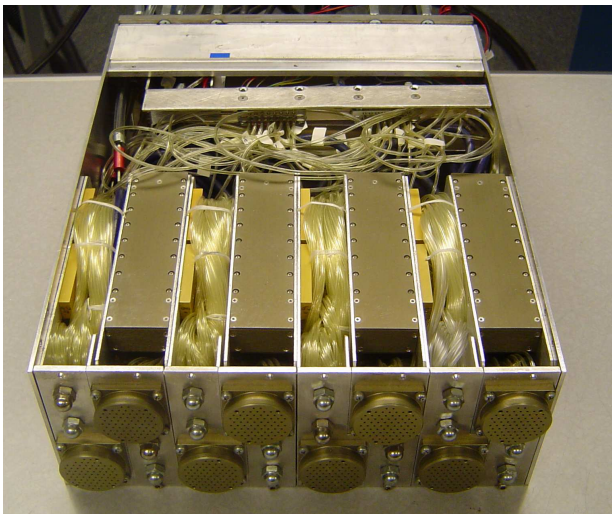

(a) Inside of 512-channel subsystem

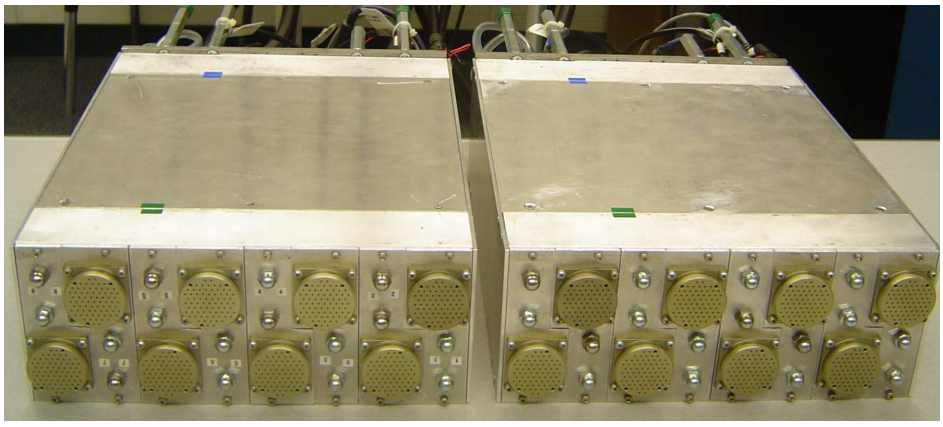

(b) Two sets of 512-channel subsystems

Figure 6.3 512-channel Subsystem

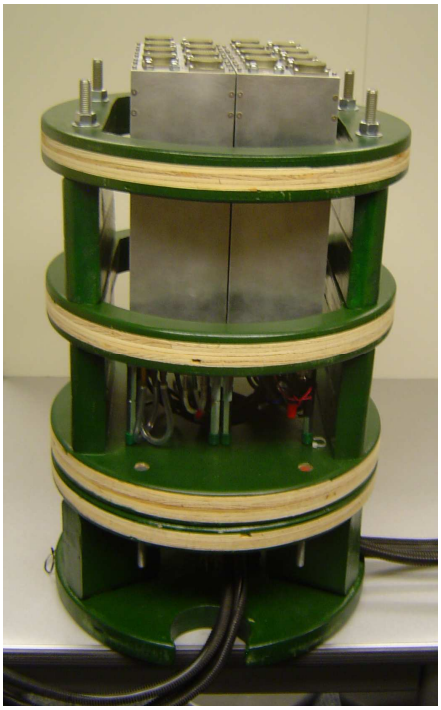

(a) Mounting system with ES1024-PS

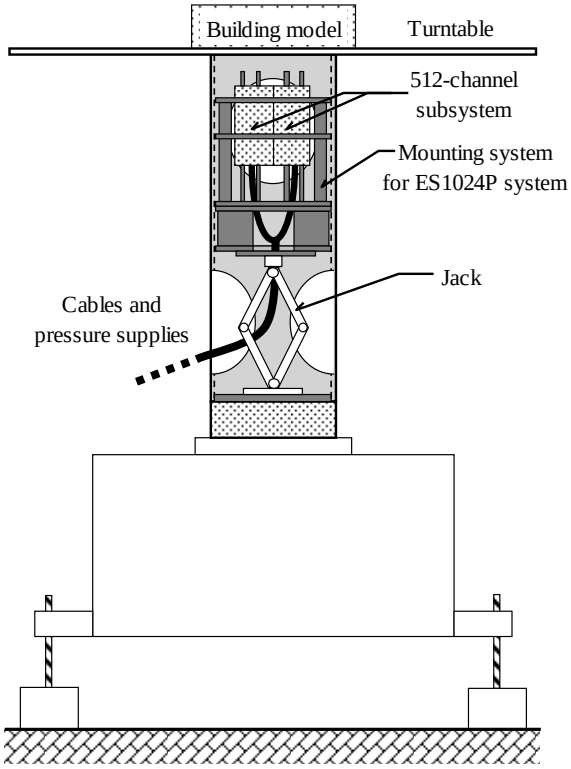

(b) Schematic view of mounting system under wind tunnel turntable

(c) Installation of ES1024-PS with mounting system in MWT

Figure 6.4 Mounting system for ES1024-PS

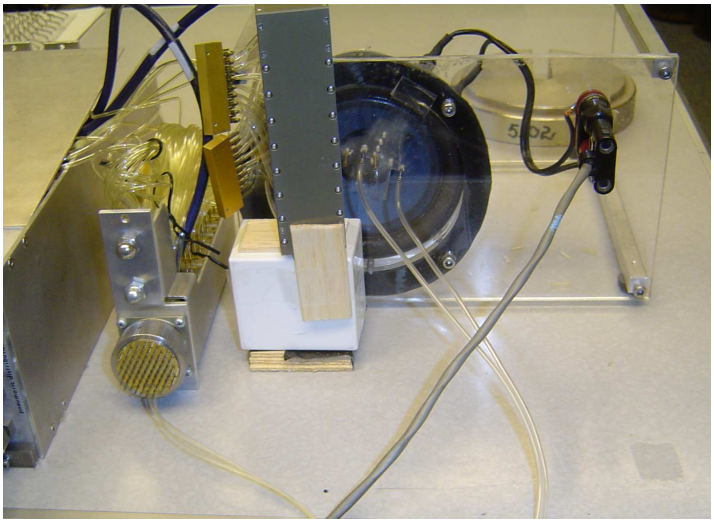

Figure 6.5 Experimental setup for evaluation of frequency response of tubing system

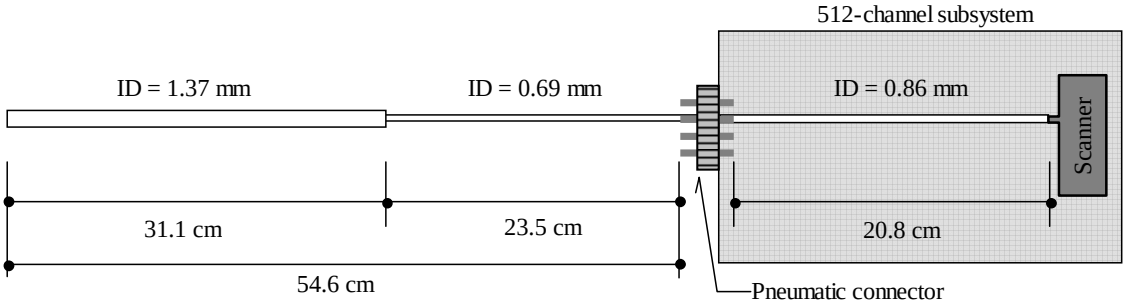

Figure 6.6 Optimized tubing system

Figure 6.7 View of pneumatic connector

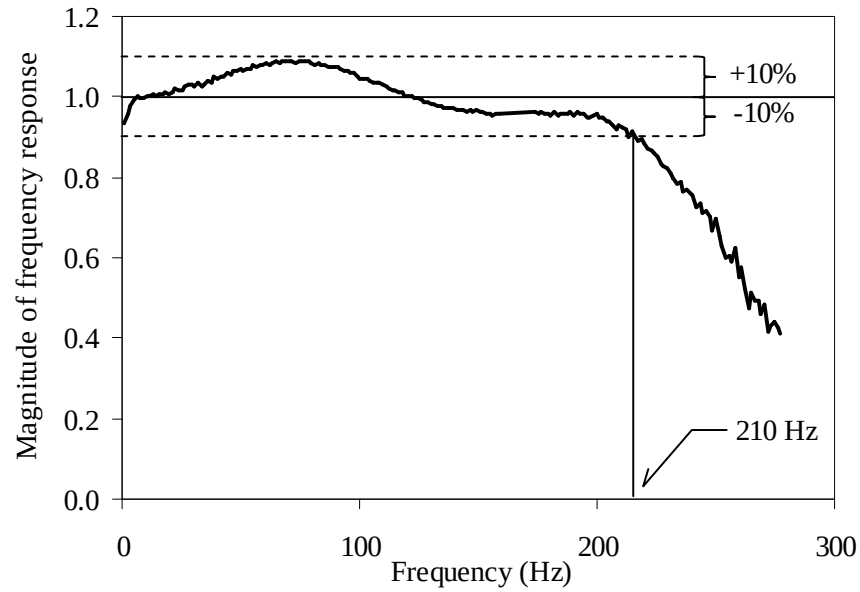

(a) Frequency response

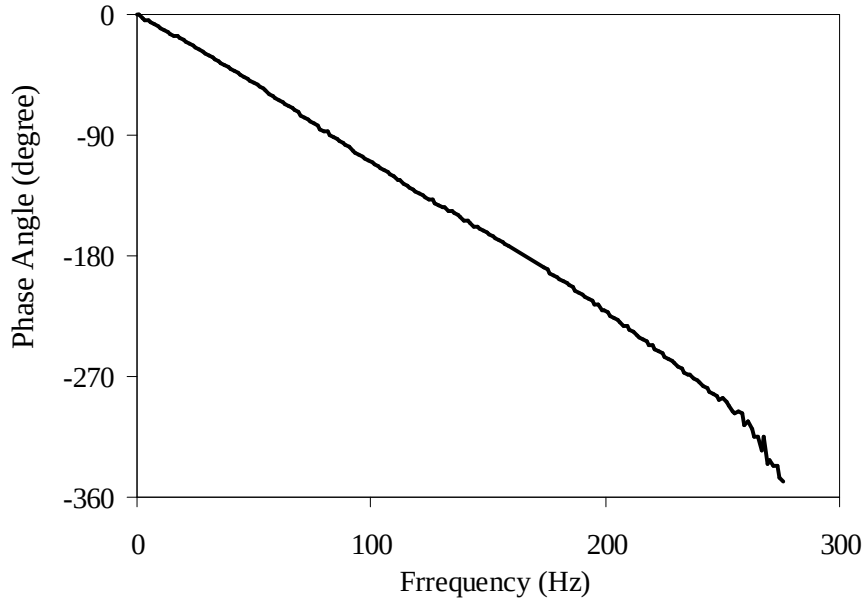

(b) Phase delay

Figure 6.8 Frequency response and phase delay of pressure measurement tubing system

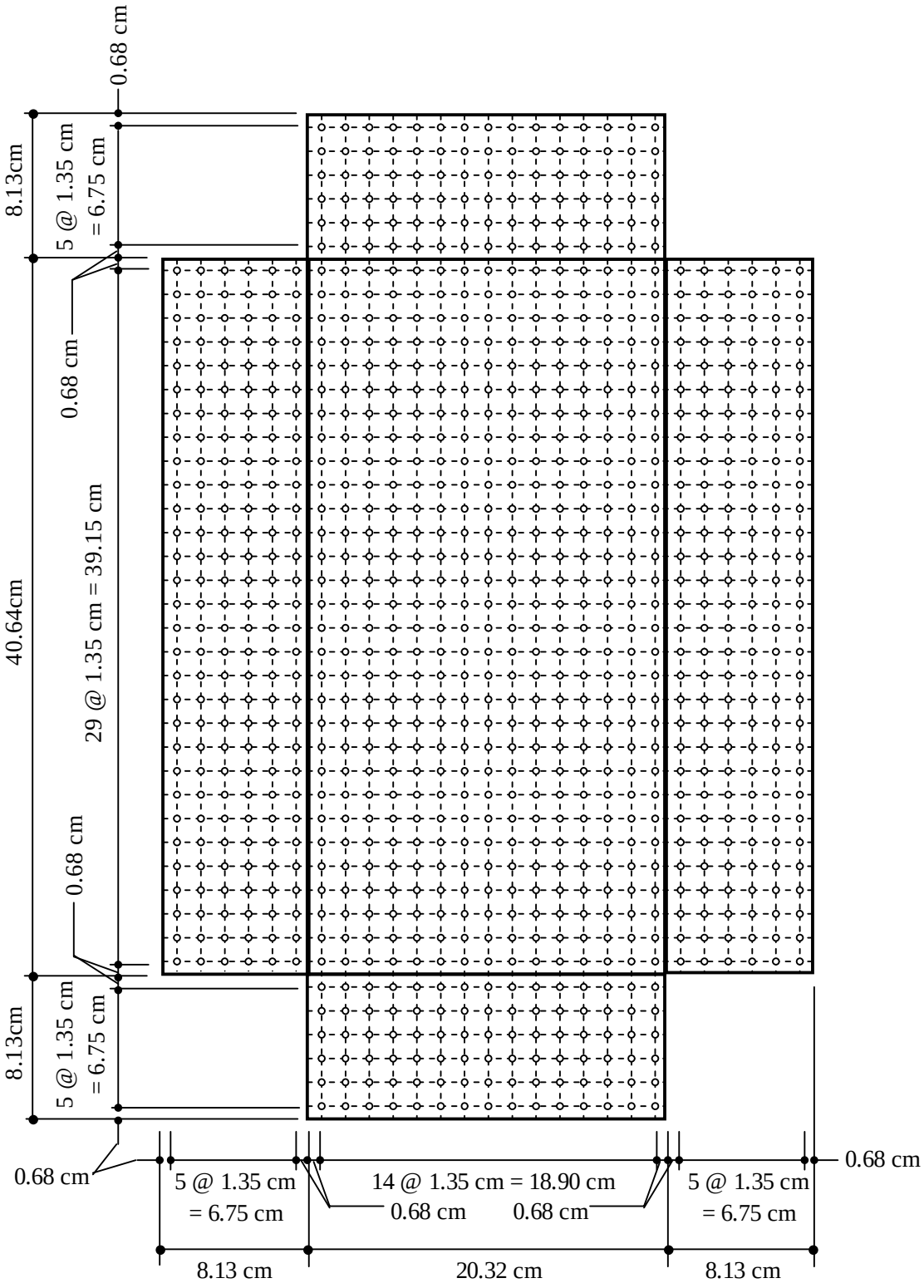

Figure 6.9 Geometry of building model and pressure tap locations

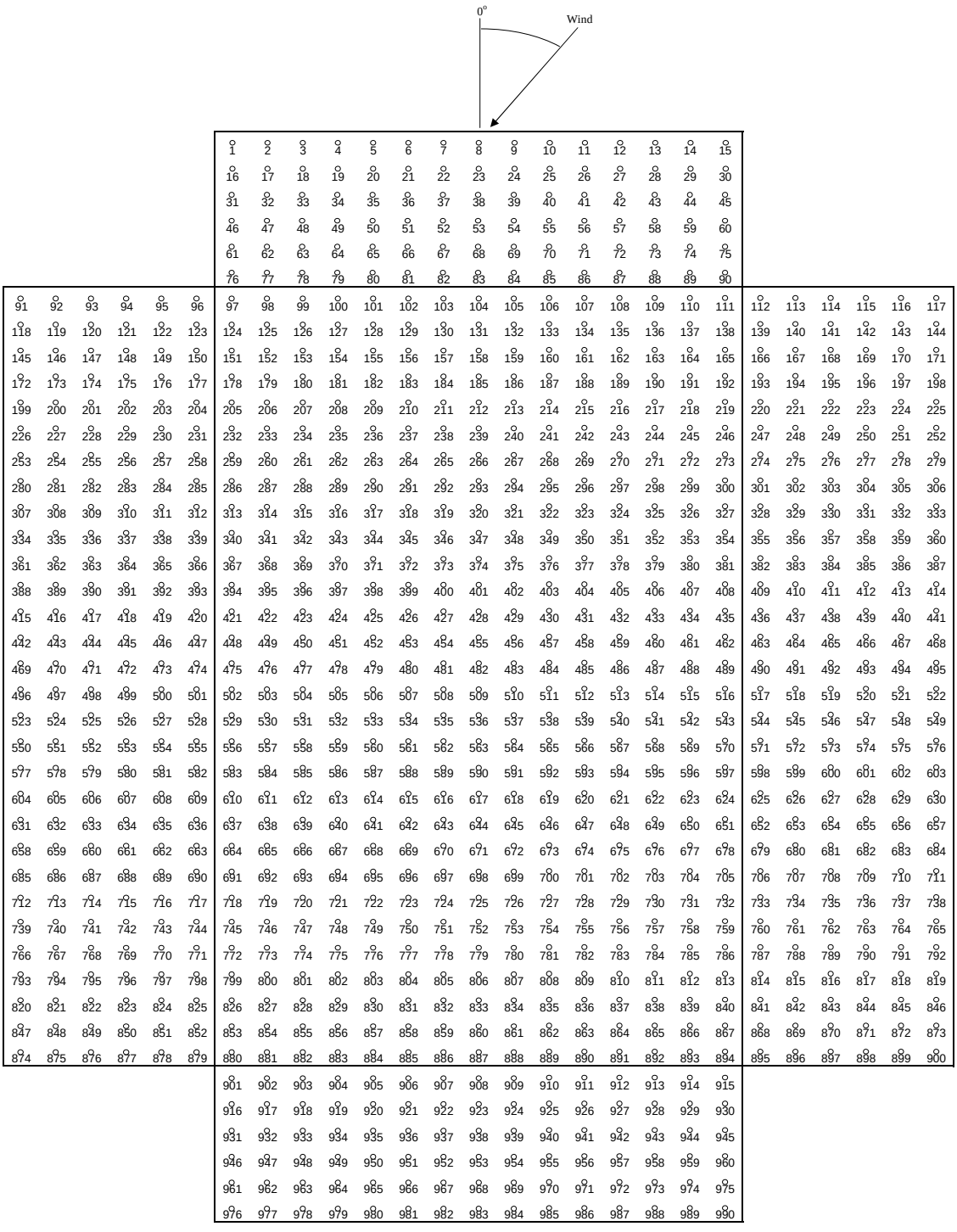

Figure 6.10 Pressure tap number

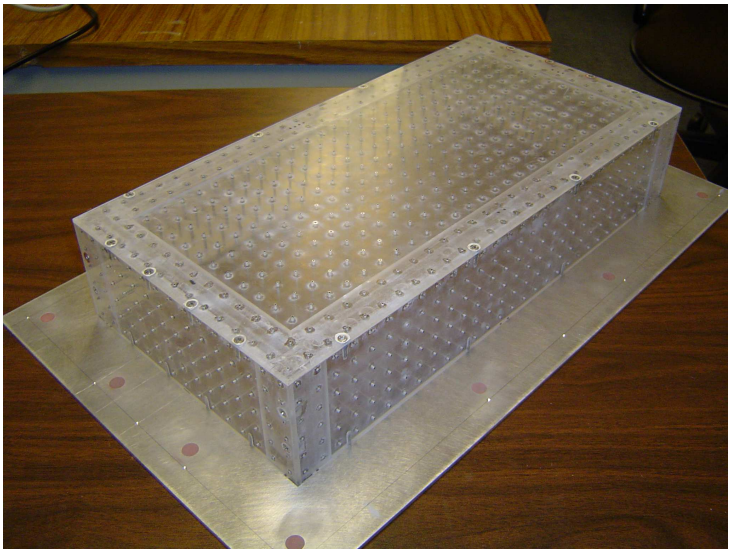

Figure 6.11 Fabricated model of building

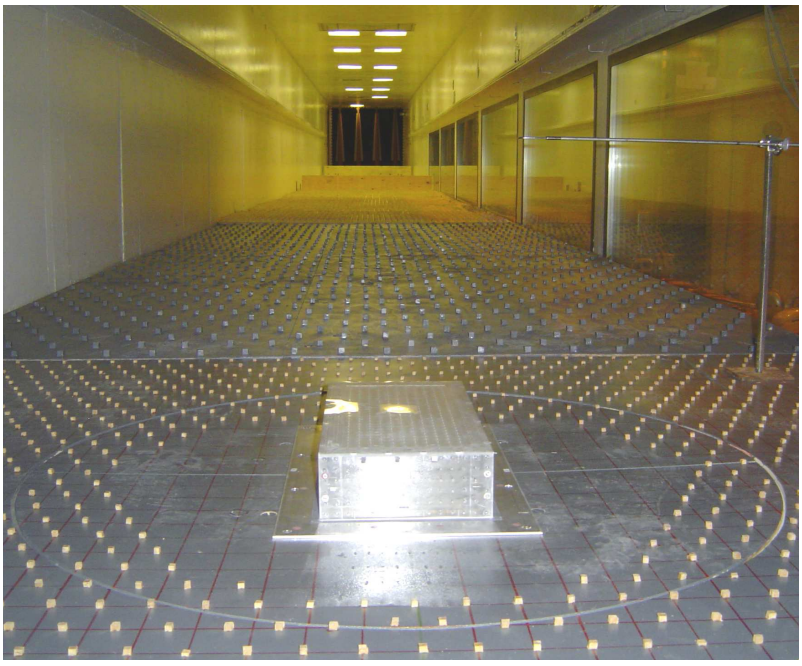

Figure 6.12 Overall view of set-up to generate open wind exposure and building model

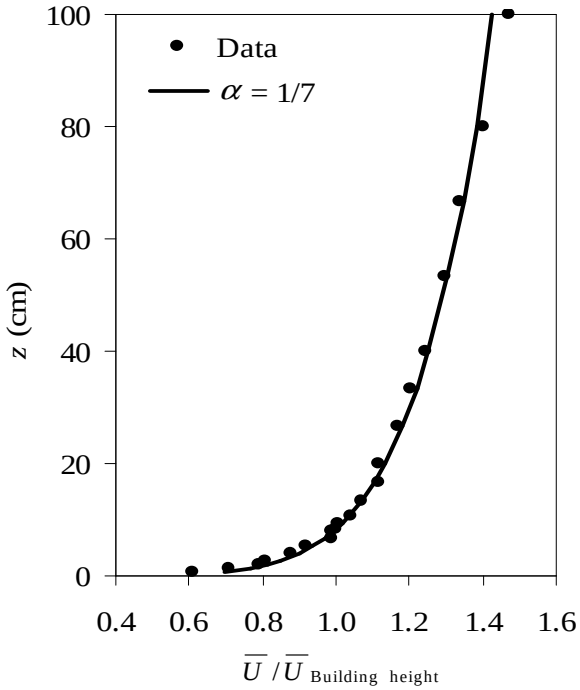

(a) Mean velocity profile

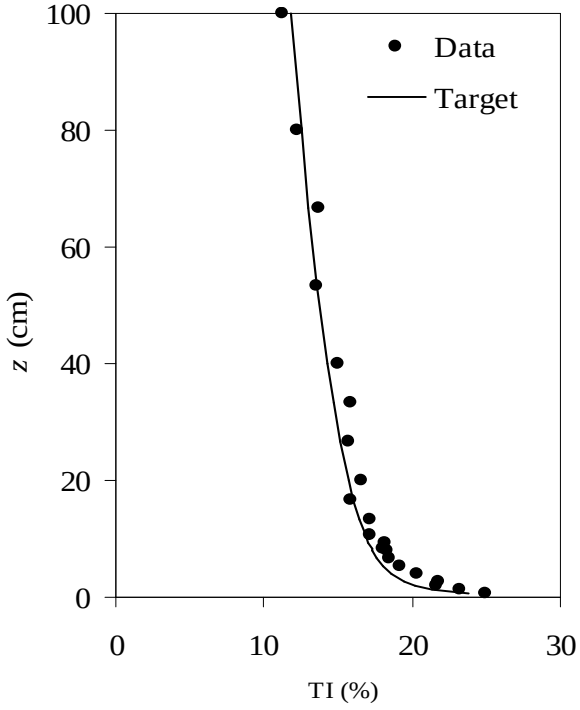

(b) Turbulence intensity profile

Figure 6.13 Target and modeled profiles of along-wind mean velocity and turbulence intensity

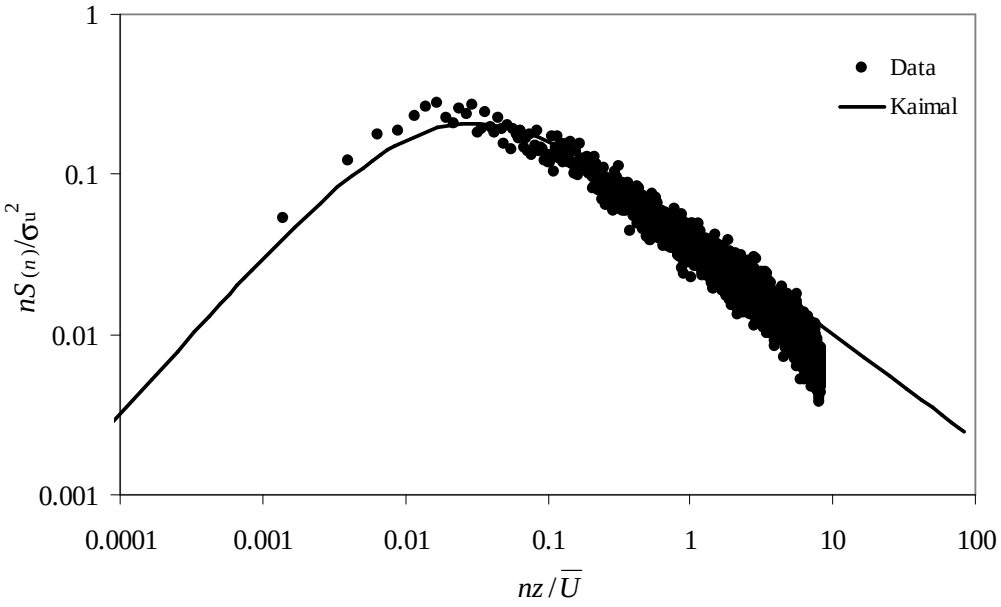

Figure 6.14 Target and modeled along-wind power spectra

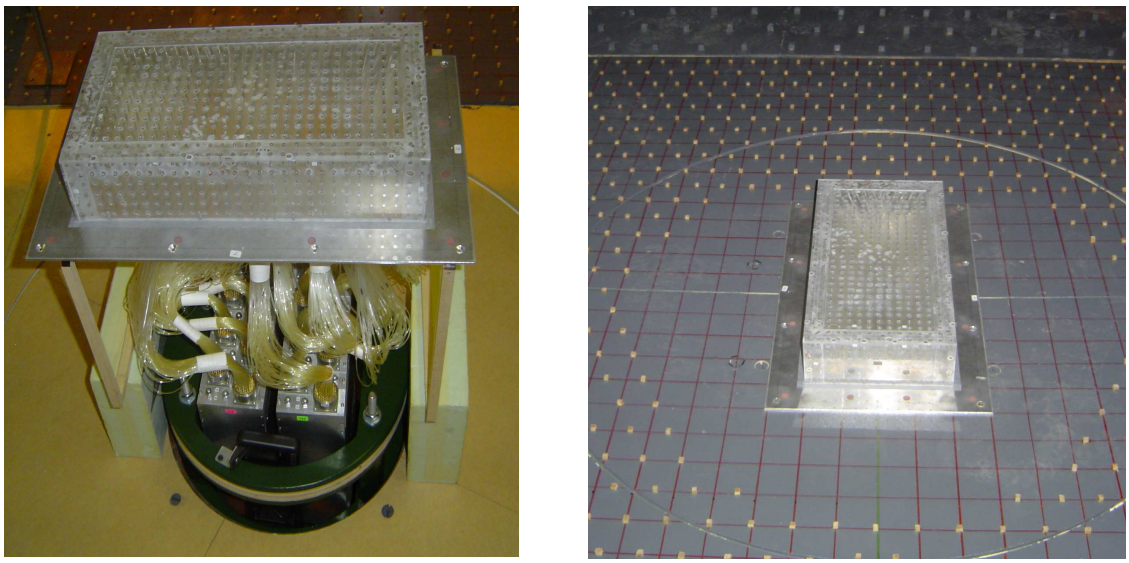

(a) During installation (b) After installation

Figure 6.15 Building model and ES1024-PS inside MWT

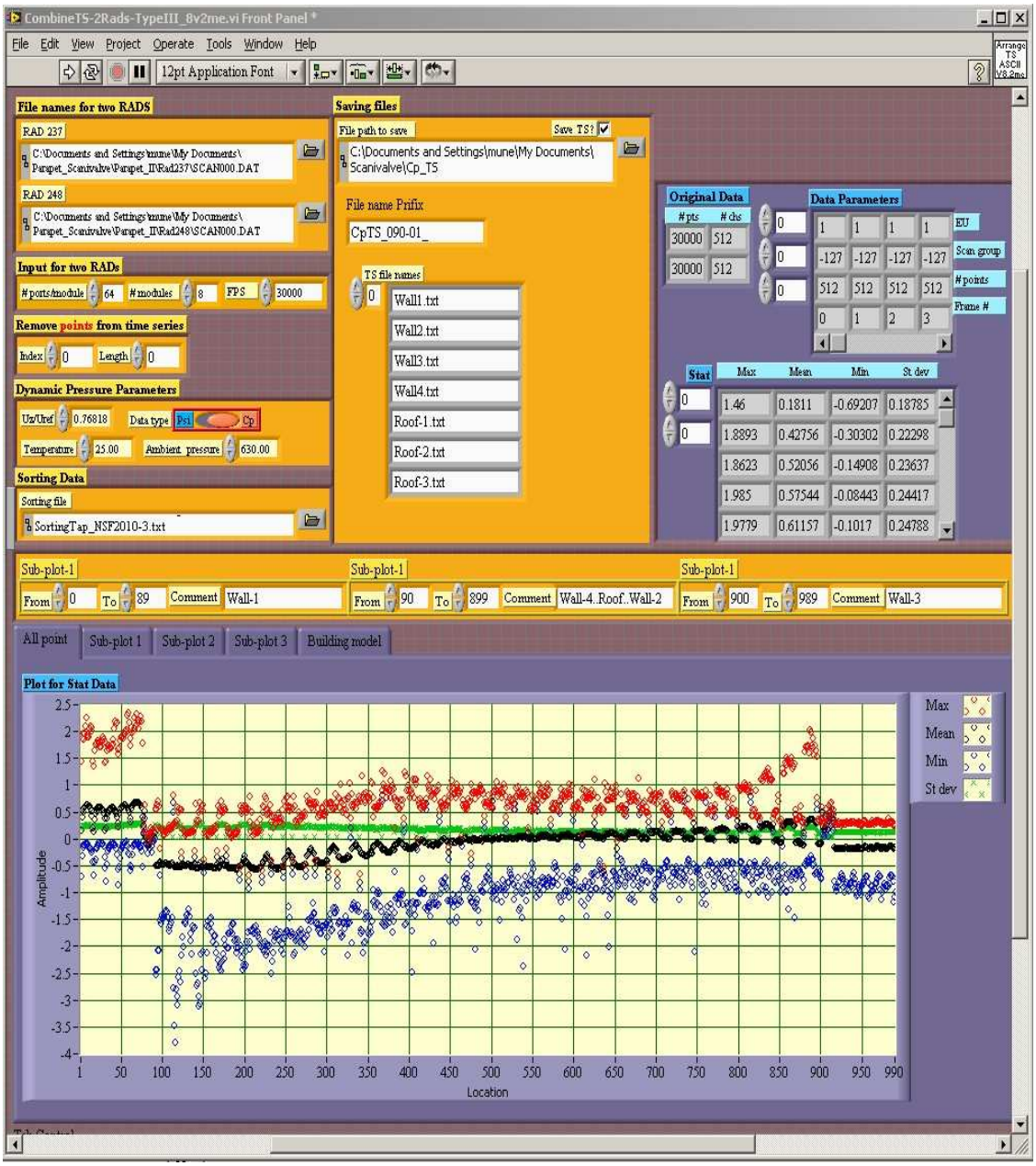

Figure 6.16 Data processing tool for conversion of data from binary to ASCII format programmed in LabView software

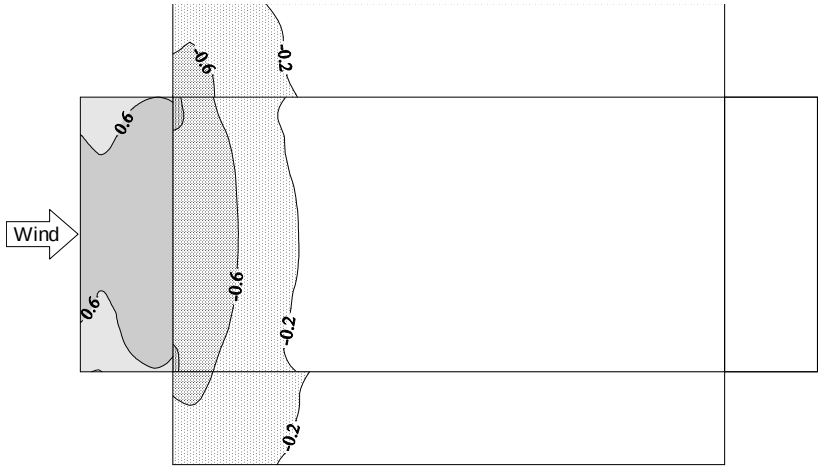

(a) Mean

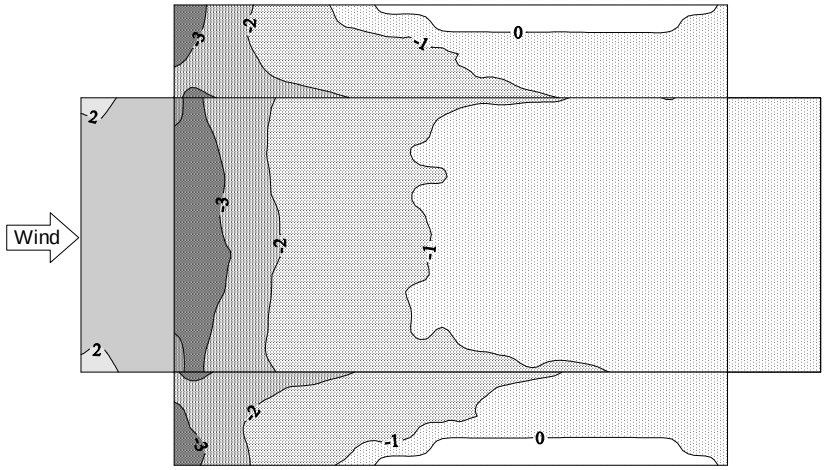

(b) Average peak

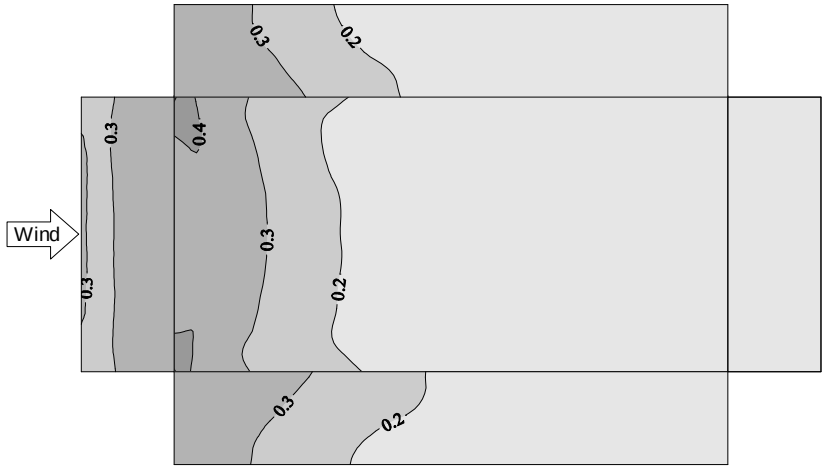

(c) Standard deviation

Figure 6.17 Distribution of building pressure coefficient, wind direction of 0^{o}

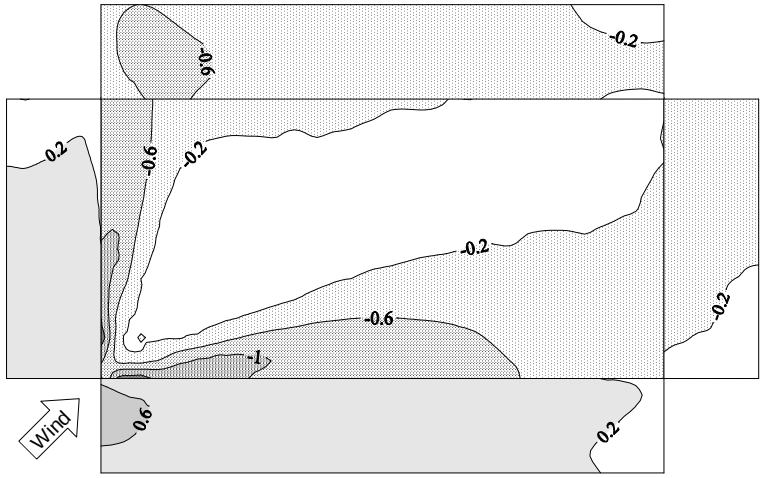

(a) Mean

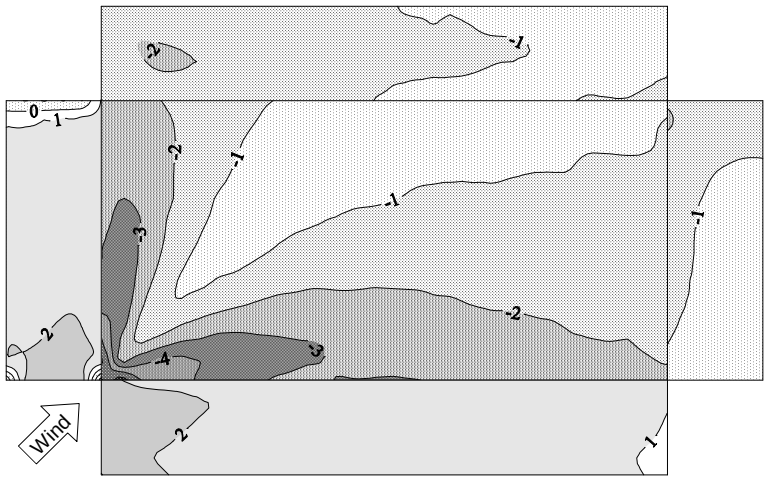

(b) Average peak

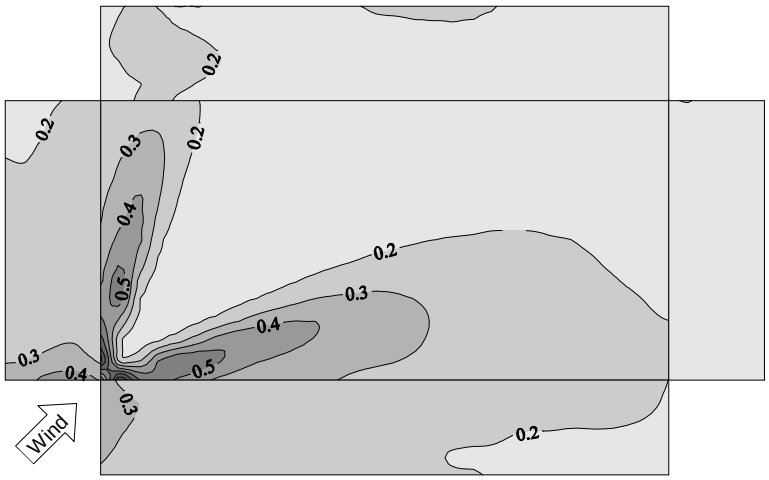

(c) Standard deviation

Figure 6.18 Distribution of building pressure coefficient, wind direction of 45^{o}

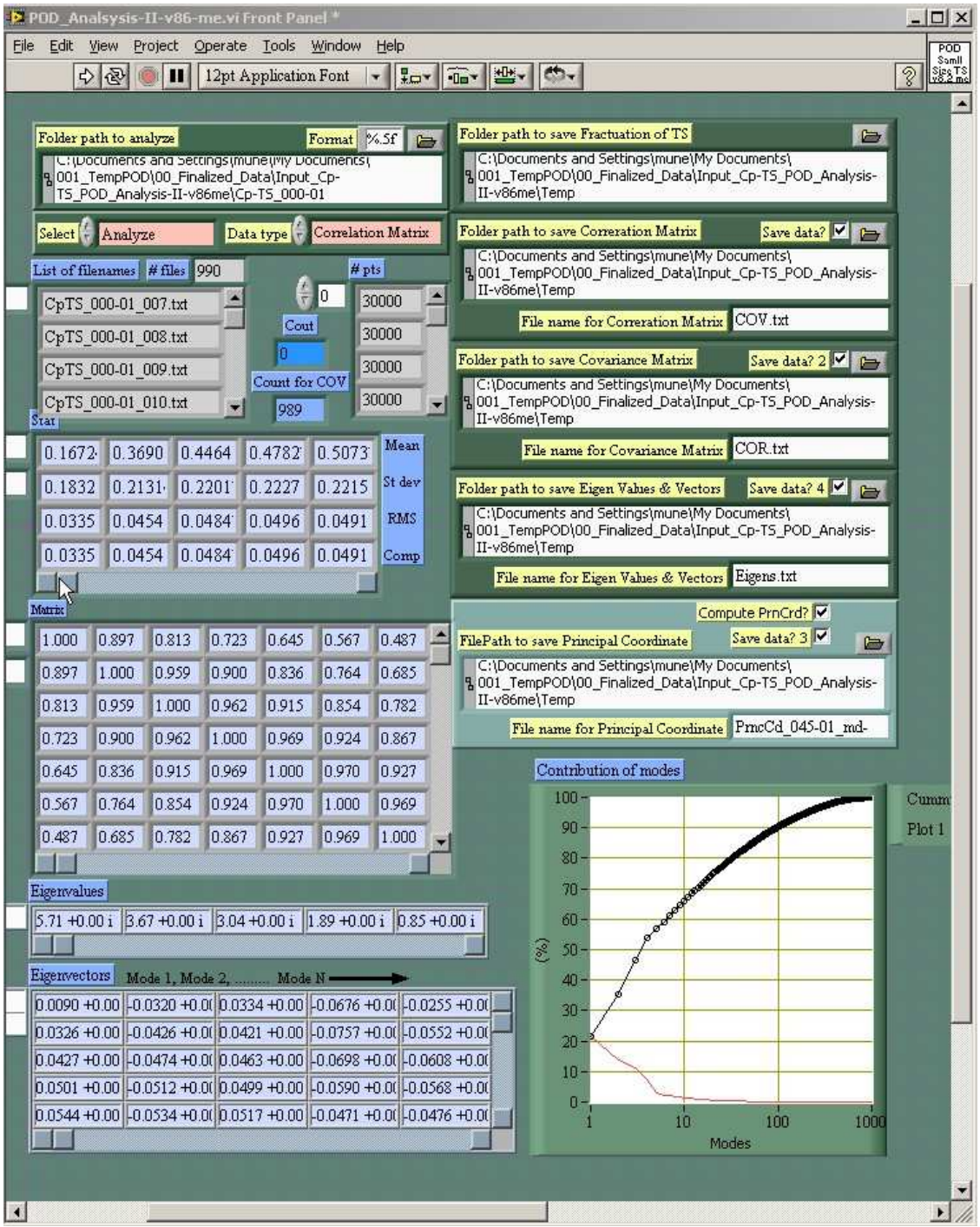

Figure 6.19 Analytical tool for proper orthogonal decomposition programmed in LabView software

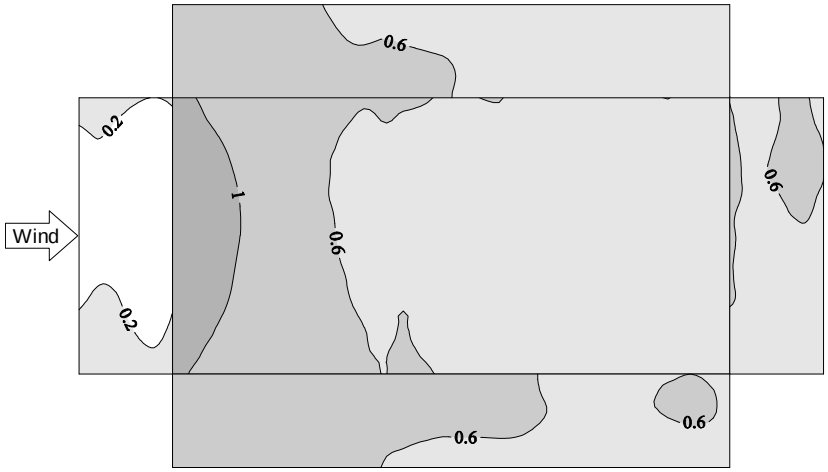

(a) 1st mode

(b) 2nd mode

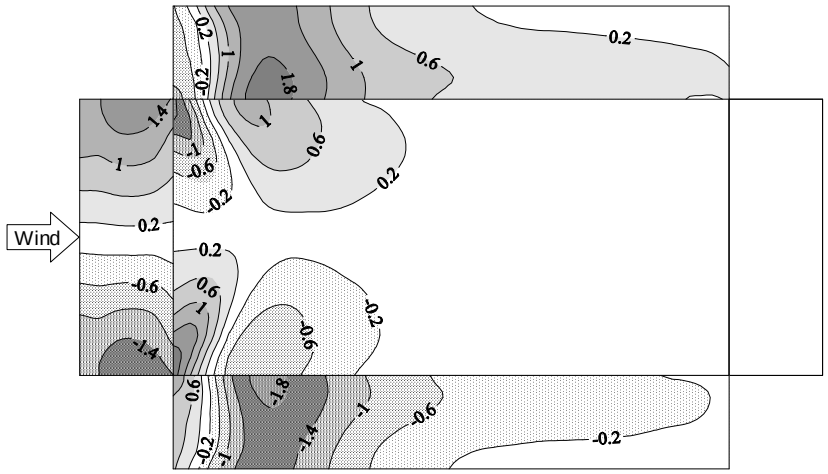

(c) 3rd mode

Figure 6.20 Eigenvectors for fluctuating pressure on building surfaces, wind direction of 0^o

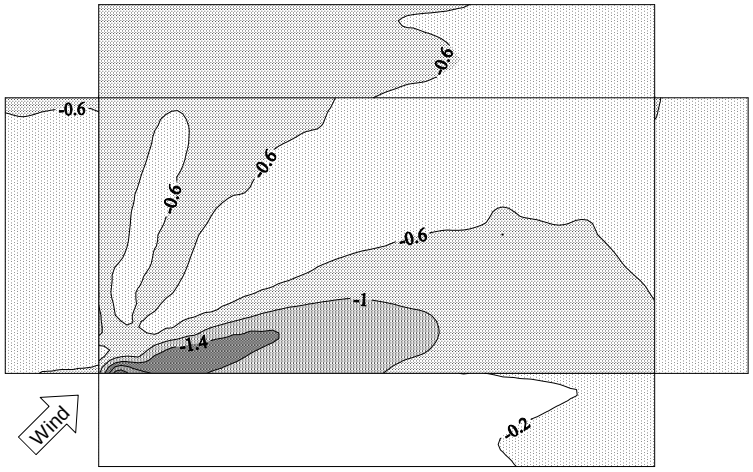

(a) 1st mode

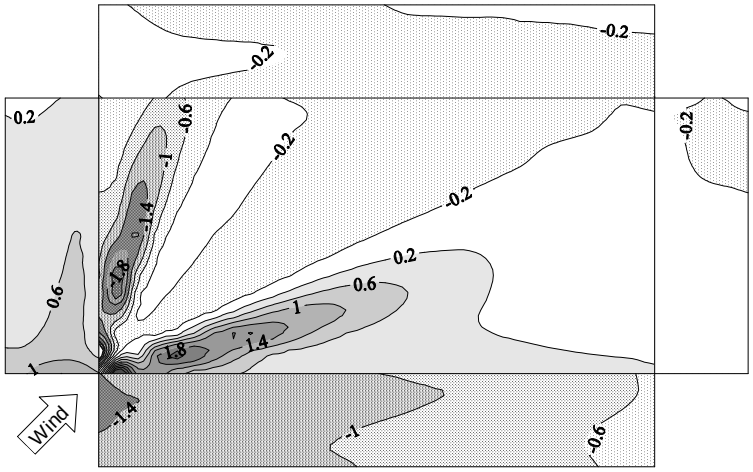

(b) 2nd mode

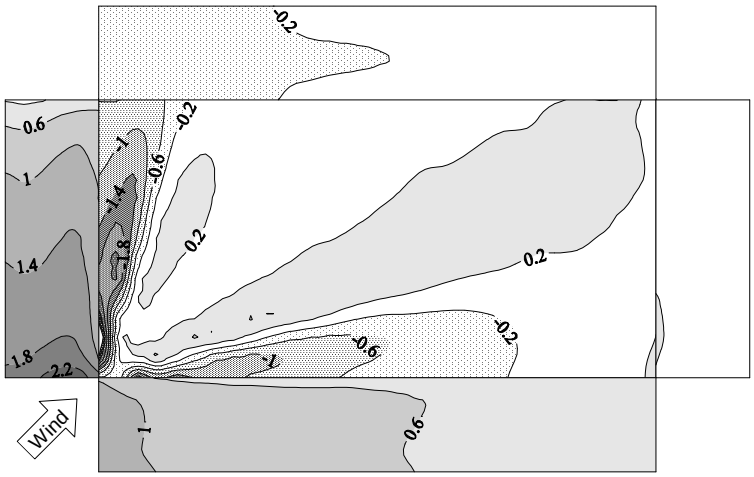

(c) 3rd mode

Figure 6.21 Eigenvectors for fluctuating pressure on building surfaces, wind direction of 45^{o}

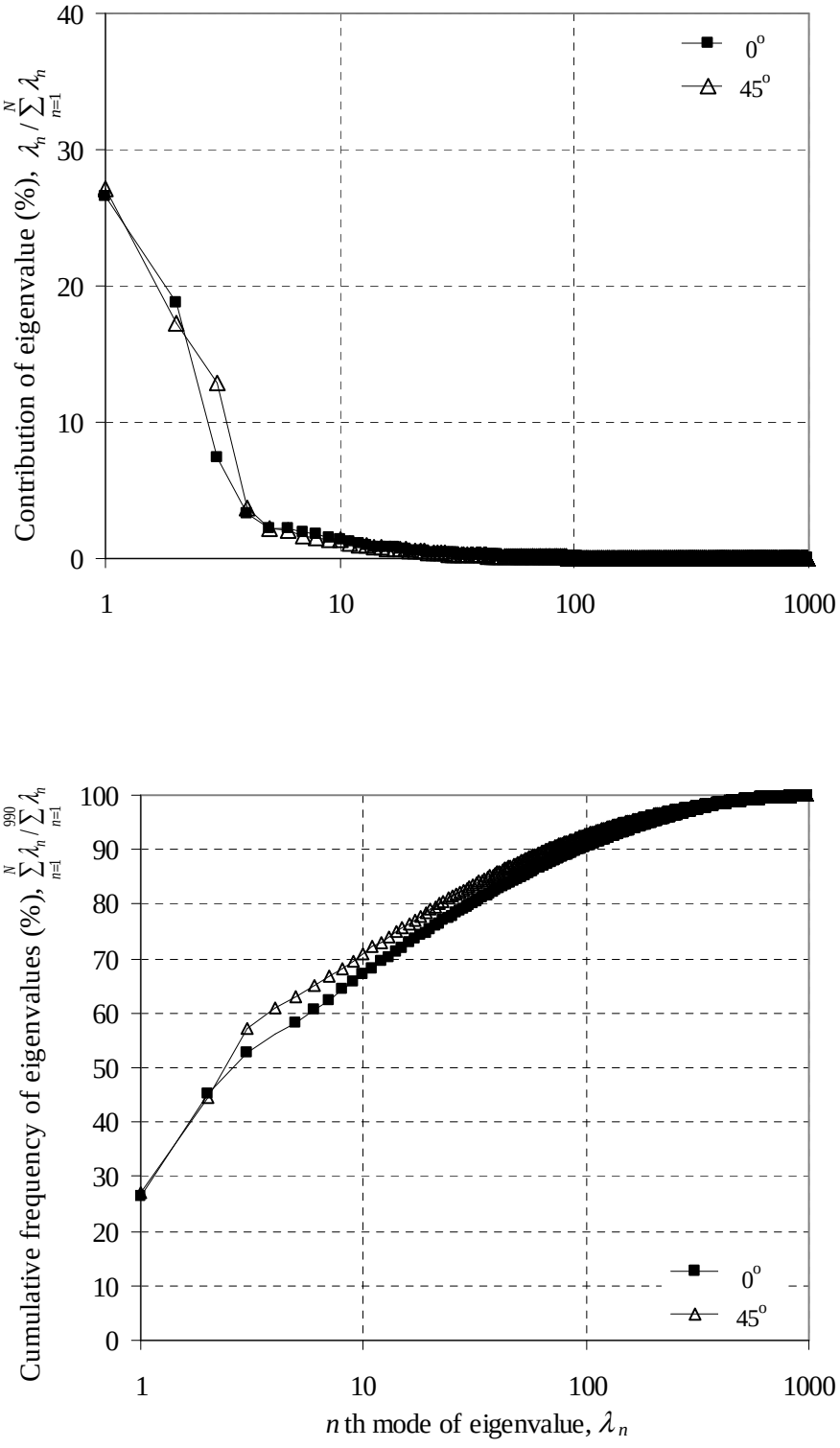

Figure 6.22 Contribution of eigenvalues for fluctuating pressure on building surfaces

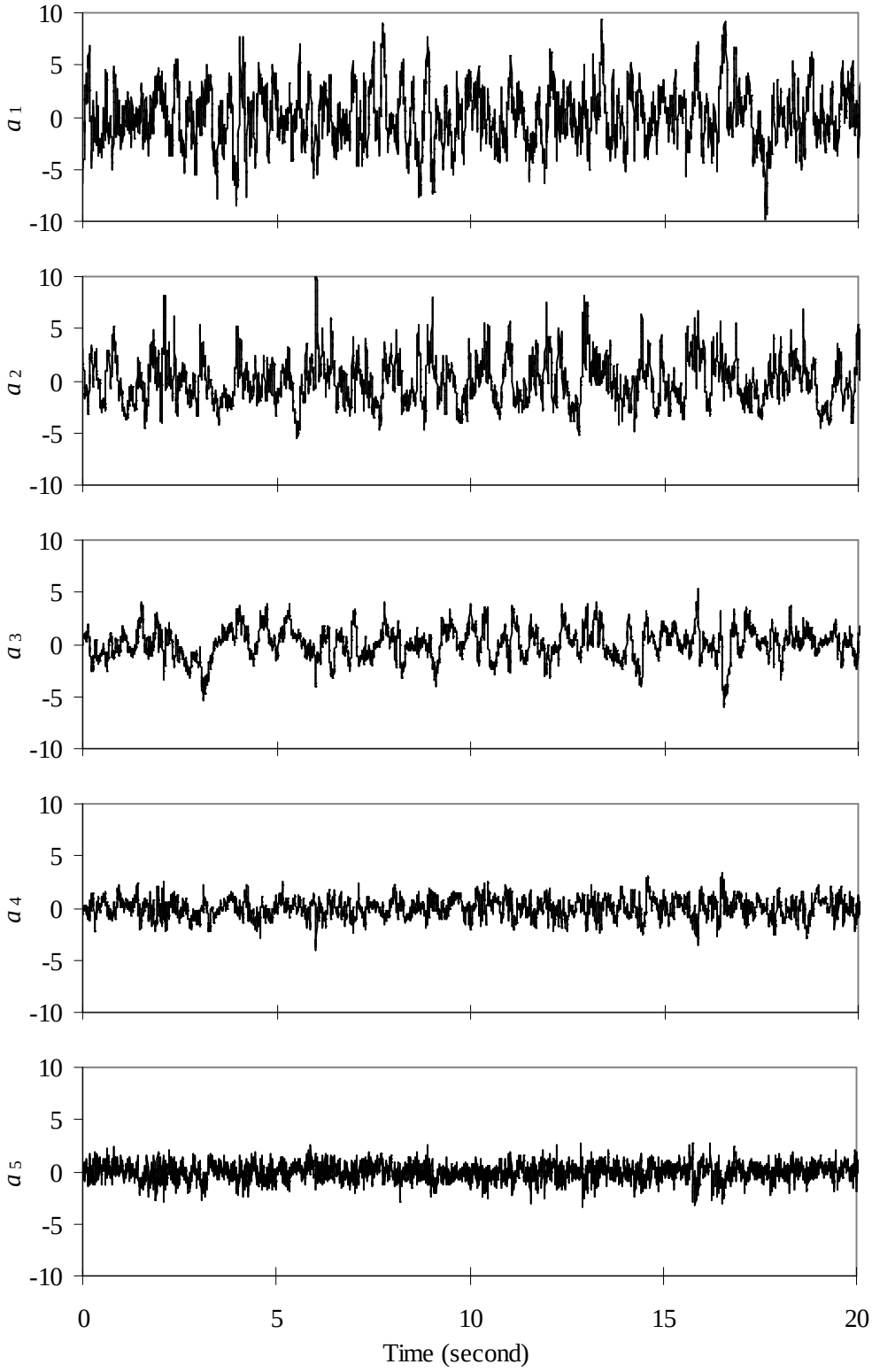

Figure 6.23 First five principal coordinates, wind direction of 0^o

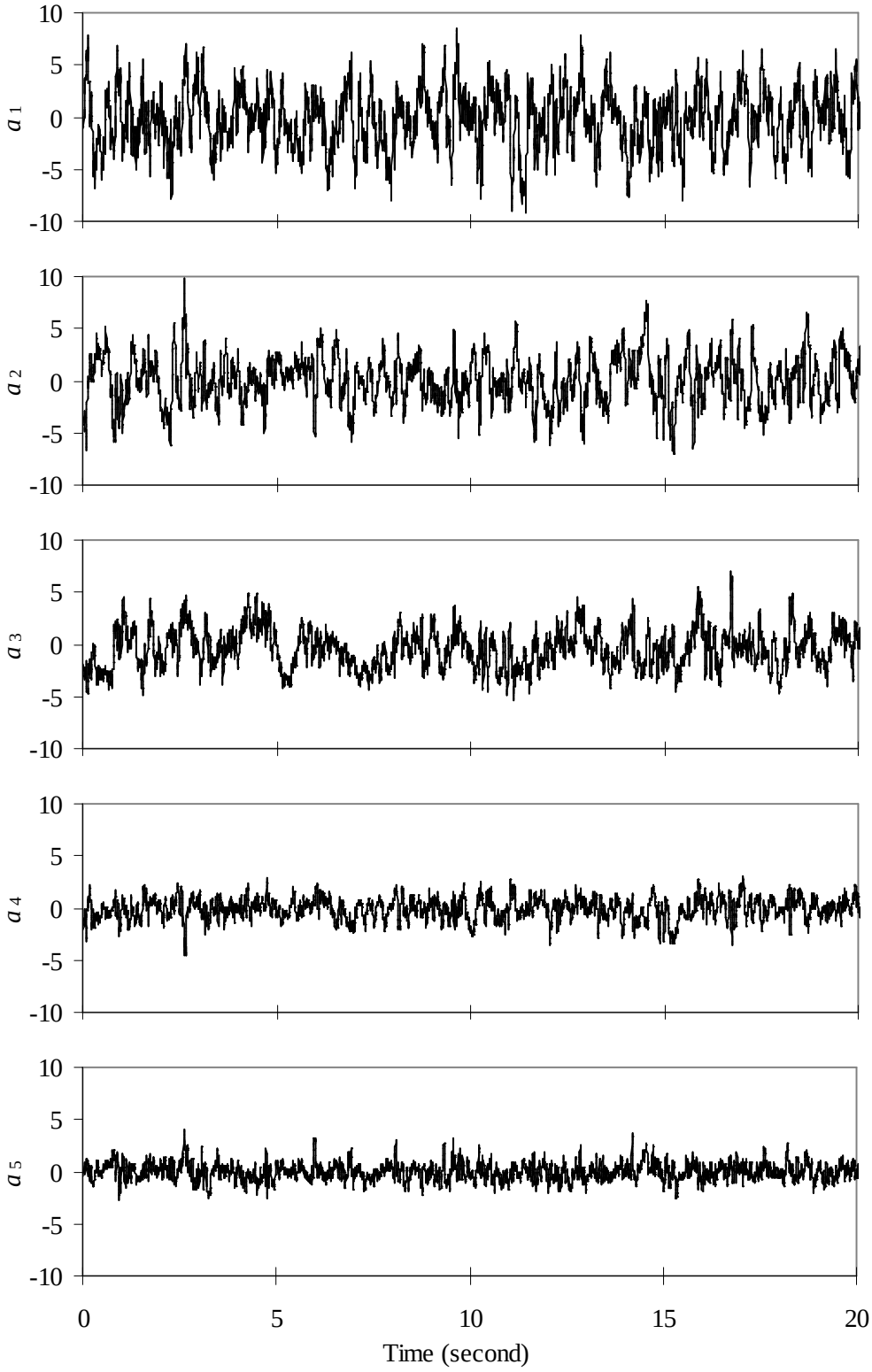

Figure 6.24 First five principal coordinates, wind direction of 45^o

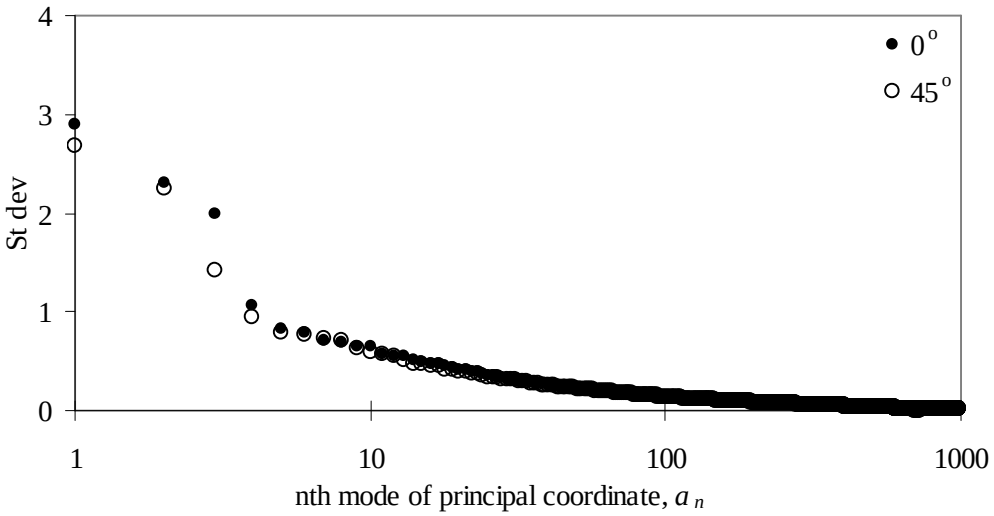

Figure 6.25 Comparison of standard deviation of principal coordinate

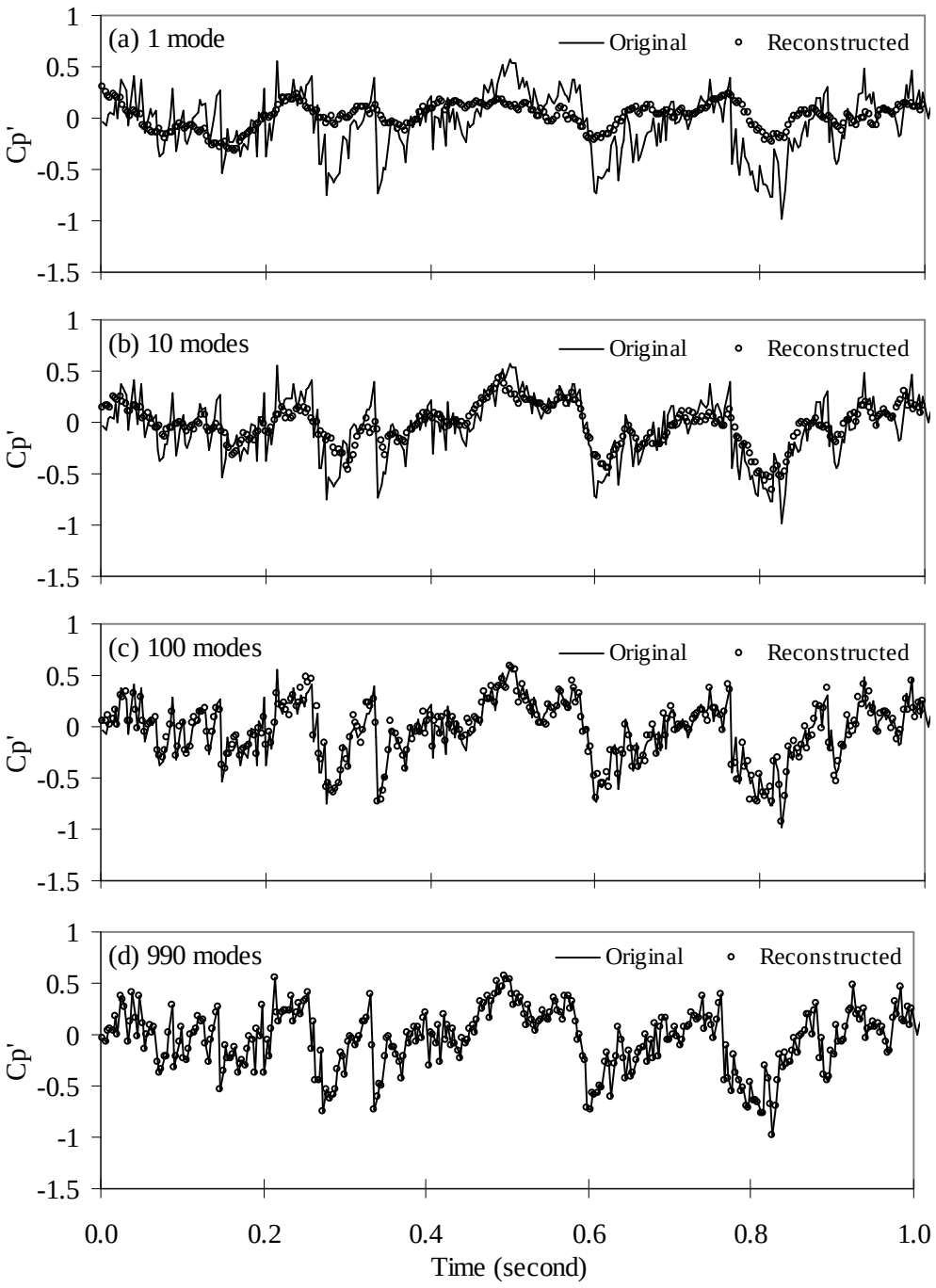

Figure 6.26 Original and reconstructed time series of fluctuating pressures, wind direction of 0^{o}, tap 124

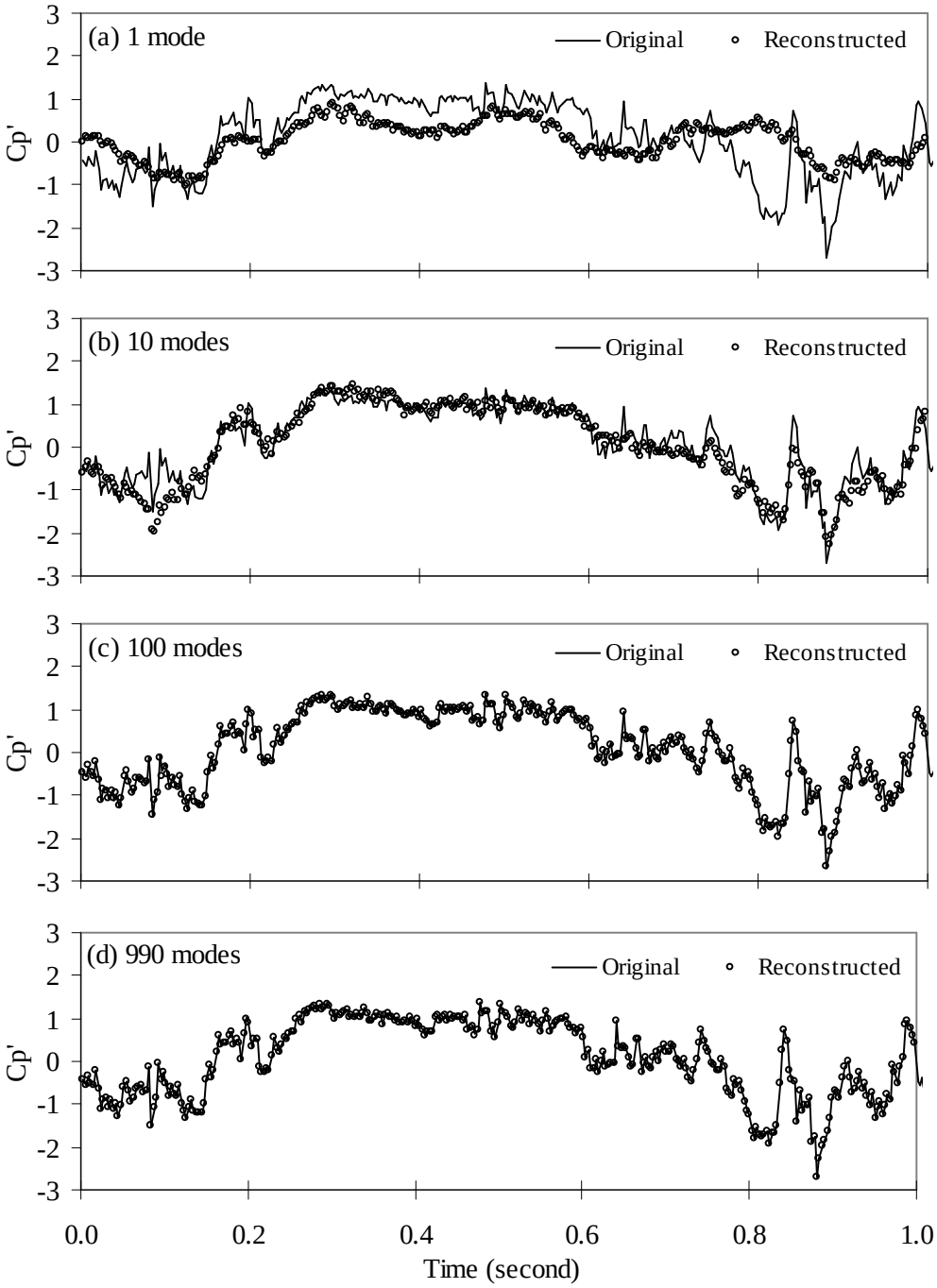

Figure 6.27 Original and reconstructed time series of fluctuating pressures, wind direction of 45^{o}, tap 124

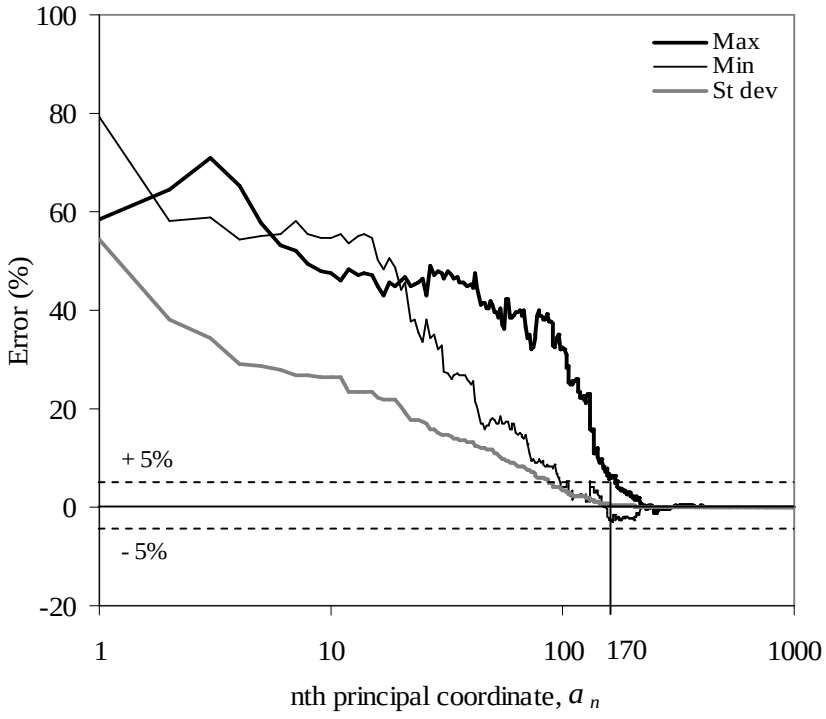

(a) Wind direction = 0^o

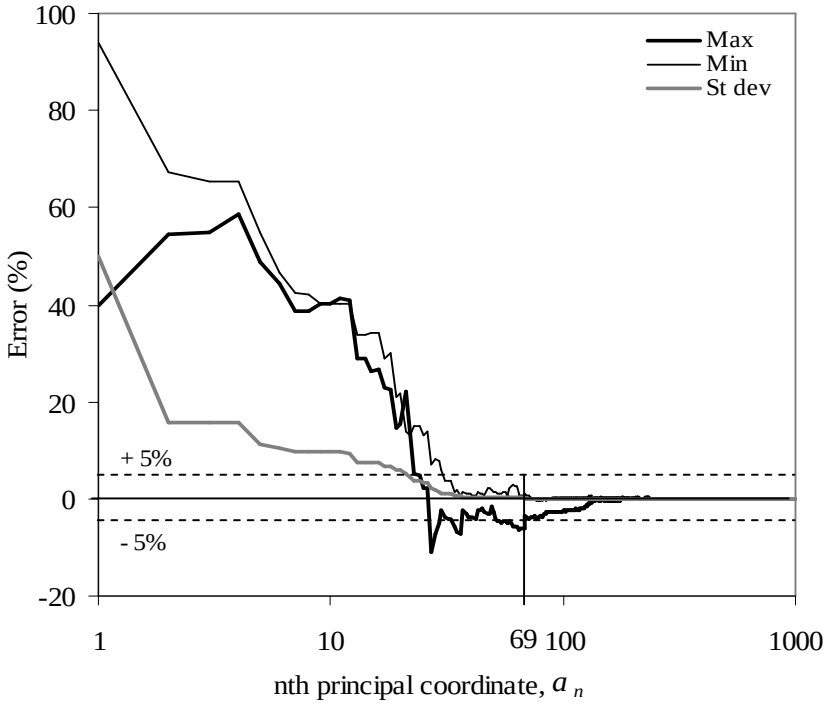

(b) Wind direction = 45^o

Figure 6.28 Comparison of maximum, minimum and standard deviation obtained from original and reconstructed time series of fluctuating pressures, tap 124

CHAPTER 7

CONCLUSIONS AND RECOMMENDATIONS

7.1 CONCLUSIONS

Although wind tunnel modeling of wind loading has been generally accepted as a viable tool, over the years a number of questions regarding accuracy and limitations of this technique have been raised and not fully answered. Questions related to wind tunnel modeling of wind loading on low-rise buildings were addressed in the presented research.

To identify the origins of discrepancies in laboratory-field and inter-laboratory comparative studies of wind loading on low-rise buildings, careful investigations of the reported wind tunnel and field experimental set-ups, modeling of field and target laboratory approach wind conditions, measurement techniques and quality of the obtained data and data analyses were carried. These efforts included verification experiments performed in boundary-layer wind tunnels. The conclusions drawn from this study can be summarized as follows:

- The reported variability in the wind-induced loading on low-rise buildings observed during comparative laboratory-field investigations and inter-laboratory comparisons can be primarily attributed by mismatching of the approach flows employed in wind tunnel modeling of wind pressures on tested building models (Chapters 2 and 5).

- Inconsistency of empirical models defining the flow characteristics - mainly the turbulence intensity profiles - of wind exposures led to modeling of different approach flows at the wind engineering laboratories participating in the comparative studies. The differences in the modeled flows resulted in the discrepancies in the measured wind loading reported by these laboratories. (Chapter 5).
- The comparison of wind-induced loading on low-rise building models measured in two boundary-layer wind tunnels at WEFL showed a good agreement in the acquired roof pressures when the characteristics of the approach flow (the mean velocity and turbulence intensity profiles, and the along-wind power spectra) generated in these tunnels were closely matched (Chapter 5).

The issue of the accuracy of predictions of the extreme field wind loading on low-rise buildings determined from wind tunnel modeling was addressed. In this investigation, the peak wind-induced pressures on models of generic low-rise buildings were analyzed using the extreme value distribution (EVD) theory and the peak-over-threshold (POT) approach. The conclusions drawn from this study can be summarized as follows (Chapter 3):

- The Type I EVD fit of the peak pressures exhibited much faster convergence than the Type III EVD fit. For the considered taps, the convergence to the Type I EVD was reached using a sample of a moderate size -20 peaks.

- In the POT analysis, restrictions placed on characteristic parameters led to the stable estimation of parameter *k* and extreme roof corner pressures predictions for specified return periods.

The advanced experimental tool, electronically scanned 1024-channel pressure measurement system (ES1024-PS) was developed and employed in wind tunnel modeling of wind loads on low-rise building. The following advances were made in wind tunnel techniques for acquisition of wind-induced pressures of high spatial and temporal resolution (Chapter 6):

- The unique features of the ES1024-PS unique features include: simultaneous scanning of up to 1024 pressure channels, compact and rugged design, convenient arrangement/configuration for installation/setup for wind tunnel testing, thermal compensation and well-tuned pneumatic (tubing) system.
- Wind pressure data were simultaneously acquired (at high sampling rates) at 990 locations on the generic low-rise building model. The resulting time series allowed for detailed investigations of spatio-temporal features of the wind loading exerted on the tested building models. One of the techniques used in these investigations was the Proper Orthogonal Decomposition (POD) analysis. Based on the POD results, it was concluded that that the obtained data sets can be significantly reduced (e.g. during archiving in a database) without significantly degrading the spatio-temporal information on the loading properties.

7.2 RECOMMENDATIONS FOR FUTURE RESEARCH

On the basis of the research presented in this dissertation, the following topics are recommended for further study:

- Investigations of the effects of the Reynolds number on wind load modeling in wind tunnel experiments. This topic could not be fully addressed during the present study due to the size of the test section and limited wind speed range of the wind tunnels available during the course of the described research.

- A further exploration of application of POD analysis and application of other advanced techniques for spatio-temporal analysis of the large sets of pressure time series generated using the ES1024-PS developed during the described efforts focused on advanced wind tunnel techniques for wind loading investigations.

APPENDIX A

WIND ENGINEERING AND FLUIDS LABORATORY

A.1 INTRODUCTION

Wind Engineering and Fluids Laboratory (WEFL) consists of three large boundary-layer wind tunnels and a number of smaller wind-tunnel facilities. It is housed at the Engineering Research Center, which provides support services for the laboratory. The layout of WEFL is depicted in Figure A.1. Determination and mitigation of wind effects on buildings and structures as well as dispersion of pollutants, using boundary-layer wind tunnels, are the main thrust areas of research and service activities at this laboratory. The WEFL has been the center of excellence for fundamental and applied research in wind engineering and fluid dynamics for over 50 years. It is one of the international laboratories where the foundations of wind engineering were established. The core of the WEFL is three large boundary-layer wind tunnels: Meteorological Wind Tunnel (MWT), Industrial Aerodynamics Wind Tunnel (IWT), and Environmental Wind Tunnel (EWT).

A.2 METEOROLOGICAL WIND TUNNEL (MWT)

This is the most unique facility of the WEFL. It permits the air and 12.2 m of the test-section floor to be independently heated or cooled and 21.3 m of the floor to be cooled for generation of thermally stratified flows. The wind speed can be continuously

adjusted in the range from 0 through 37 m/sec. Other characteristics of MWT are listed in Table A.1. The schematic view of the MWT is shown in Figure A.2. The tunnel surface roughness, pressure gradient, and humidity can also be varied. It is designed for basic research on flow characteristics of the atmospheric surface layer and applied investigations of atmospheric dispersion and wind effects on buildings and structures.

A.3 INDUSTRIAL AERODYNAMICS WIND TUNNEL (IWT)

This recirculating facility has a test section 1.83 m wide by 18.29 m long with a ceiling height adjustable from 1.52 m through 2.13 m. The wind speed can be continuously varied up to approximately 24 m/sec, depending on blockage inside the tunnel. Further characteristics are listed in Table A.1. The schematic view of the IWT is shown in Figure A.3. This tunnel has been primarily employed in studies of wind effects on buildings and structures, and their components.

A.4 ENVIRONMENTAL WIND TUNNEL (EWT)

This is an open-circuit wind tunnel of a test section 3.66 m wide by 18.29 m long, with a flexible ceiling which can be adjusted from 2.13 m to 2.74 m. The flow velocity can be adjusted in the range from 0 through 12 m/sec. Other characteristics of the EWT are listed in Table A.1. The schematic view of the IWT is shown in Figure A.4. The EWT is well suited for model studies of flow over cities, tall structures, and topographic features, as well as environmental studies of dispersion of pollutants.

Table A.1 Characteristic of three boundary-layer wind tunnels

Characteristic	**MWT**	**IWT**	**EWT**
Section Length	26.8 m	18.3 m	18.3 m
Test-section Area	1.8 m x 1.8 m	1.8 m x 1.8 m	3.6 m x 2.4 m
Contraction Ratio	9:1	9:1	4:1
Drive Power	400 hp	75 hp	50 hp
Mean Velocity	0 to 36 m/sec	0 to 24 m/sec	0 to 12 m/sec
Boundary-layer thickness	up to 1.5 m	up to 1.5 m	up to 1.5 m
Background Turbulence intensity	about 0.1 %	about 0.5 %	about 1%

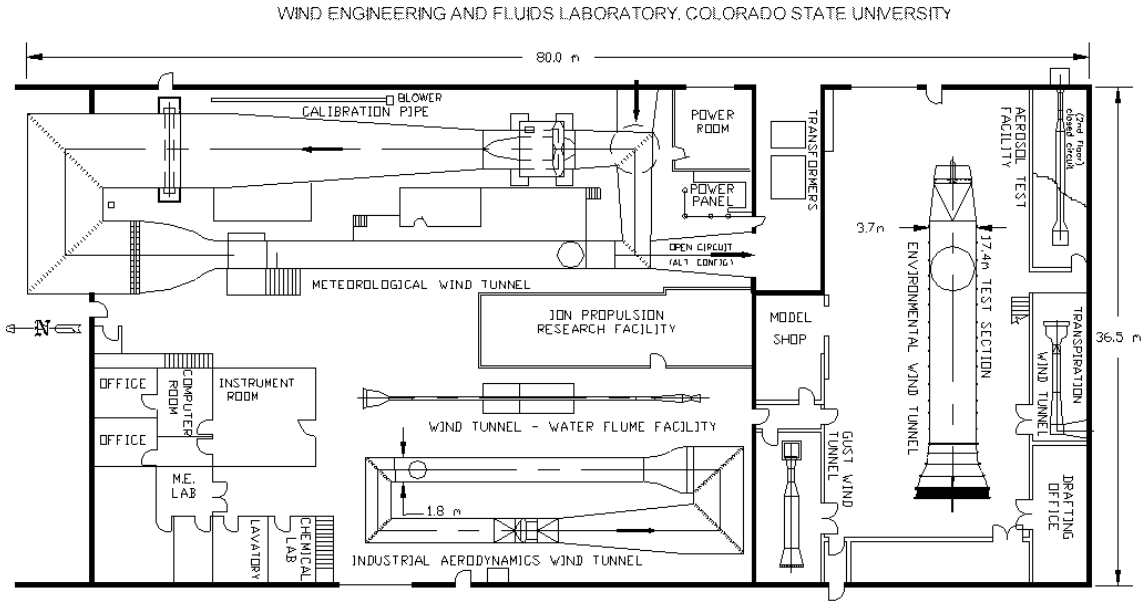

Figure A.1 Layout of the Wind Engineering and Fluids Laboratory at Colorado State University

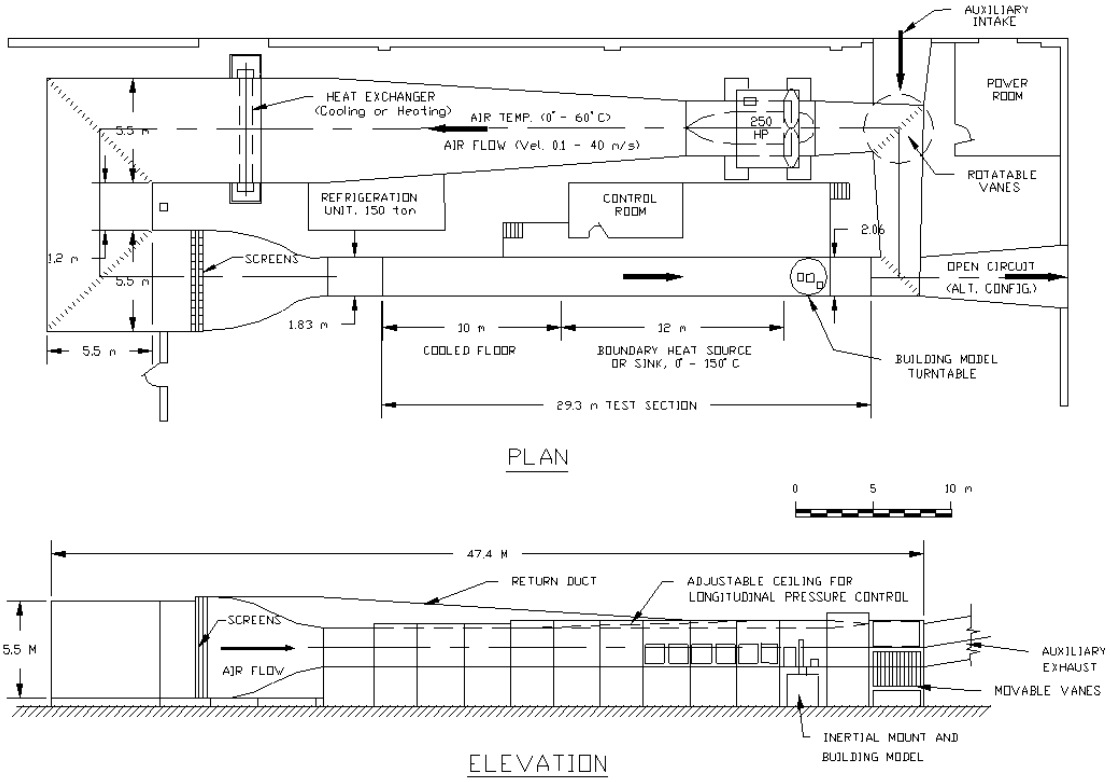

Figure A.2 Schematic view of the Meteorological Wind Tunnel

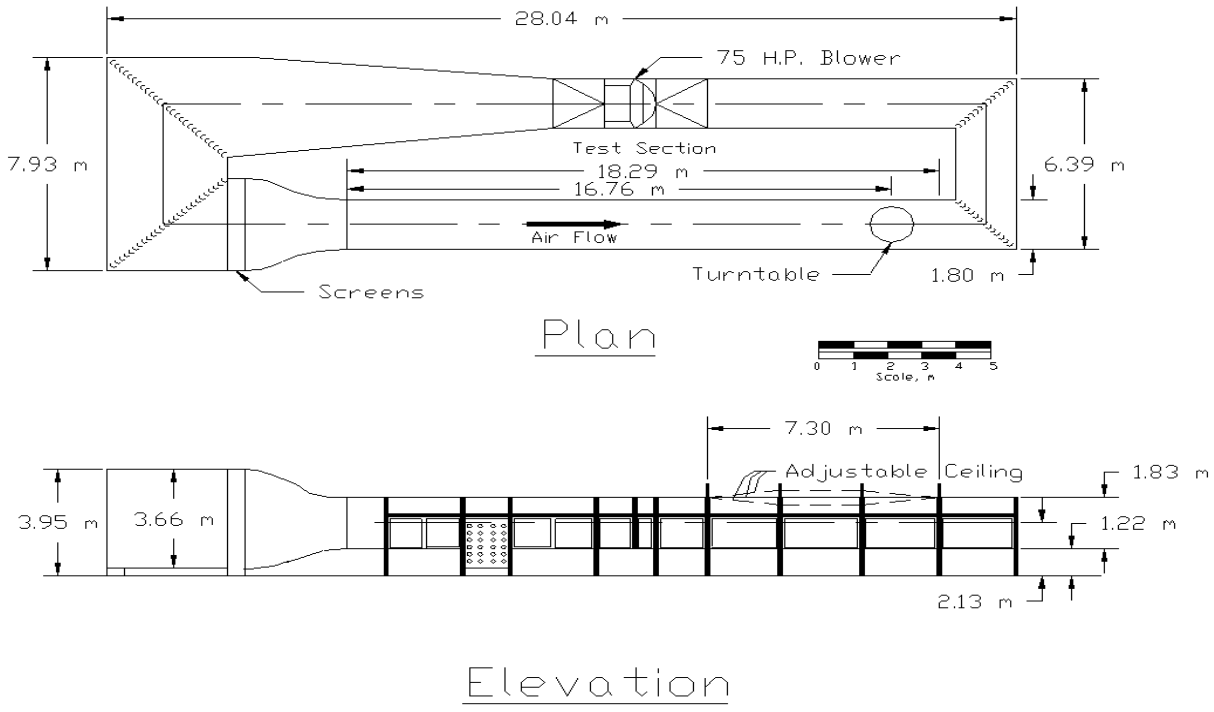

Figure A.3 Schematic view of the Industrial Wind Tunnel

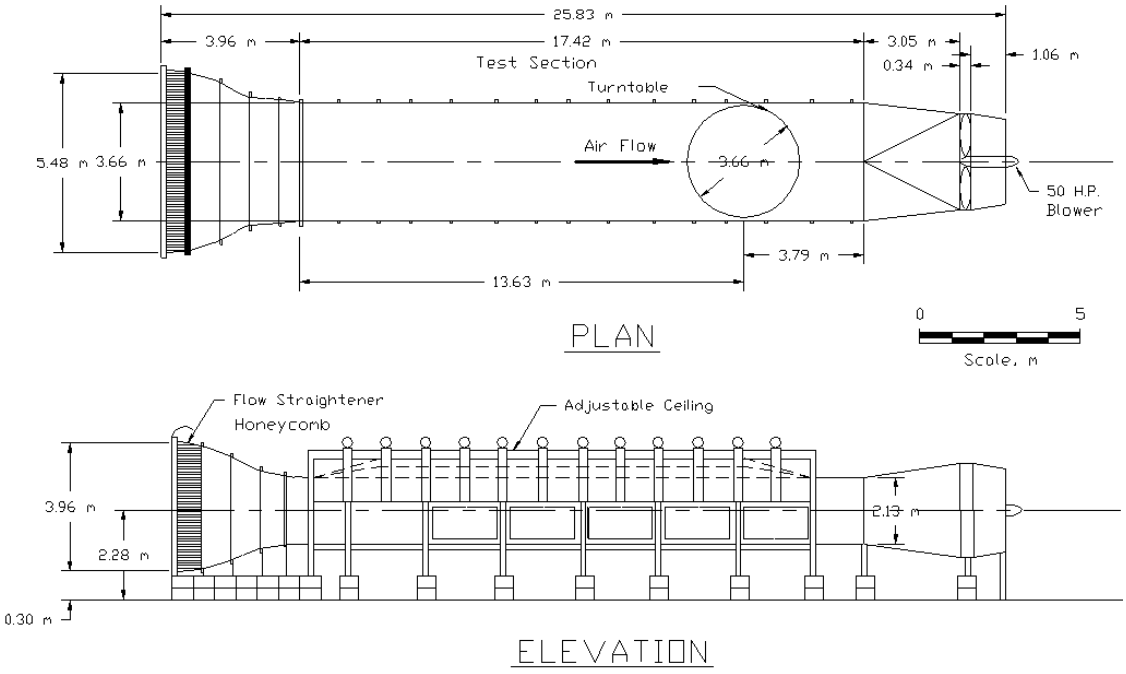

Figure A.4 Schematic view of the Environmental Wind Tunnel

APPENDIX B

DETERMINATION OF INFLUENCE LINES

FOR SIMPLIFIED FRAME

The simplified geometry of a frame structure shown in Figure B.1 was employed to determine influence lines for vertical and horizontal reactions at supports A and B (denoted V_A, V_E, H_A, H_E). Parameters α and β indicated in the figure were introduced to allow for evaluation of the frame flexural rigidity and geometry on the calculated reactions. The coefficient α is the ratio of the flexural rigidity (EI) of the frame roof part to the rigidity of the column. The frame span-to-height ratio can be controlled by the parameter β.

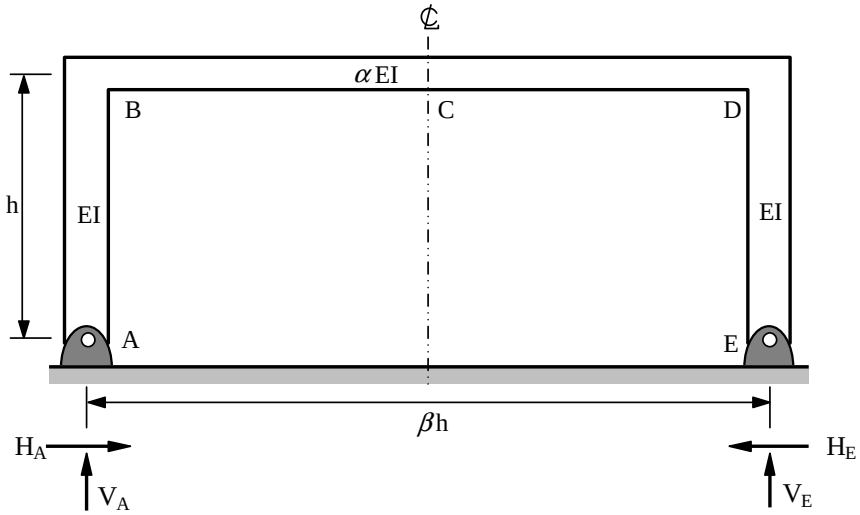

Figure B.1 Simplified geometry of structural frame and support reactions

Taking account for these parameters, the influence lines for the reactions were first determined. For the derivation of the influence line for vertical and horizontal reactions at supports A and E (see Figure B.1), three load cases acting on the structural frame were considered as follows:

Case 1: A load acts on the left column,

Case 2: A load acts on the roof beam, and

Case 3: A load acts on the right column.

Using these load cases, the influence lines for those reactions are derived with the virtual work principle.

First of all, the frame structure with load case 1 shown in Figure B.2a is statically indeterminate to the first degree. Removal of a horizontal reaction H_E at the right support (denoted E) would leave a statically determinate structural frame as shown in Figure B.2b, i.e. H_E is used as the redundant reaction. To calculate the reactions, the three equations of static equilibrium are established as follows:

$$\overset{+}{\rightarrow} \sum F_H = H_A + P = 0 \qquad \therefore H_A = -P \qquad [B.1]$$

$$\uparrow + \sum F_V = V_A + V_E = 0 \qquad \therefore V_E = -V_A \qquad [B.2]$$

$$\circlearrowleft + \sum M_E = V_A \beta h + P x_1 = 0 \qquad \therefore V_A = -\frac{P x_1}{\beta h} \qquad [B.3]$$

Substitution of Eq. [B.3] into Eq. [B.2] leads to $\therefore V_E = \frac{P x_1}{\beta h}$ [B.4]

The resulting bending moment equations at a point with distance X_1 from the left support, X_2 from the left corner of the frame, or X_3 from the right support are

$$\circlearrowleft + M_X = -H_A X_1 = P X_1 \qquad \text{for } 0 \leq X_1 < x_1 \text{ in left column} \qquad [B.5]$$

$$\circlearrowright \; M_X = -H_A X_1 - P(X_1 - x_1) = P x_1 \quad \text{for } a_1 \le X_1 \le h \text{ in left column} \qquad [B.6]$$

$$\begin{aligned} \circlearrowright \; M_X &= -H_A h + V_A X_2 - P(h - x_1) \\ &= -\frac{P x_1}{\beta h} X_2 + P x_1 \end{aligned} \quad \text{for } 0 \le X_2 \le \beta h \text{ in roof beam} \qquad [B.7]$$

$$\circlearrowright \; M_X = 0 \quad \text{for } 0 \le X_3 \le h \text{ in right column} \qquad [B.8]$$

Next a unit virtual force, H = 1, is applied to the right column as shown in Figure B.2c. The bending moment equations for the virtual force are written as follows:

Since $V_A = V_E = 0$ and $H_A = 1$,

$$\circlearrowright \; m_X = -H_A X_1 = -X_1 \quad \text{for } 0 \le X_1 < h \text{ in left column} \qquad [B.9]$$

$$\circlearrowright \; m_X = -H_A h + V_A X_2 = -h \quad \text{for } 0 \le X_2 \le \beta h \text{ in roof beam} \qquad [B.10]$$

$$\circlearrowright \; m_X = -H_A X_3 = -X_3 \quad \text{for } 0 \le X_3 \le h \text{ in right column} \qquad [B.11]$$

Using Eqs. [B.5] through [B.11], the primary deflection δ_0 and virtual deflection δ_V are obtained as follows

$$\begin{aligned} \delta_0 &= \frac{1}{EI}\int_0^L M_X m_X dX = \frac{1}{EI}\int_0^{x_1} (P X_1)(-X_1) dX_1 + \frac{1}{EI}\int_{x_1}^{h} (P x_1)(-X_1) dX_1 \\ &\quad + \frac{1}{\alpha EI}\int_0^{\beta h} \left(-\frac{P x_1}{\beta h} X_2 + P x_1\right)(-h) dX_2 + \frac{1}{EI}\int_0^{h} 0(-X_3) dX_3 \\ &= \frac{P}{EI}\left\{\frac{1}{6} x_1^{\,3} - \frac{1}{2} x_1 h^2 \left(1 + \frac{\beta}{\alpha}\right)\right\} \end{aligned} \qquad [B.12]$$

$$\begin{aligned} \delta_V &= \frac{1}{EI}\int_0^L m_X m_X dX \\ &= \frac{1}{EI}\int_0^h (-X_1)^2 dX_1 + \frac{1}{\alpha EI}\int_0^{\beta h} (-h)^2 dX_2 + \frac{1}{EI}\int_0^h (-X_3)^2 dX_3 \\ &= \frac{2}{3}\frac{h^3}{EI}\left[1 + \frac{3}{2}\frac{\beta}{\alpha}\right] \end{aligned} \qquad [B.13]$$

The solution of the horizontal reaction at the right support H_E is obtained as follows:

$$H_E = -\frac{\delta_0}{\delta_V} = -\frac{\frac{P}{EI}\left\{\frac{1}{6}x_1^3 - \frac{1}{2}h^2 x_1\left(1+\frac{\beta}{\alpha}\right)\right\}}{\frac{2}{3}\frac{h^3}{EI}\left[1+\frac{3}{2}\frac{\beta}{\alpha}\right]}$$

$$= \frac{3}{2}P\left(\frac{\alpha}{2\alpha+3\beta}\right)\left\{\left(1+\frac{\beta}{\alpha}\right)\left(\frac{x_1}{h}\right) - \frac{1}{3}\left(\frac{x_1}{h}\right)^3\right\} \qquad [B.14]$$

From Figure B.2 for load case 1, the horizontal reaction at the left support H_A is

$$\sum F_H = H_A + P - H_E = 0 \qquad \therefore H_A = H_E - P \qquad [B.15]$$

Therefore, $$H_A = P\left[\frac{3}{2}\left(\frac{\alpha}{2\alpha+3\beta}\right)\left\{\left(\frac{x_1}{h}\right)\left(1+\frac{\beta}{\alpha}\right) - \frac{1}{3}\left(\frac{x_1}{h}\right)^3\right\} - 1\right] \qquad [B.16]$$

For the vertical components of reactions V_A and V_E are

$$V_A = -\frac{P}{\beta}\left(\frac{x_1}{h}\right) \quad \text{and} \quad V_E = \frac{P}{\beta}\left(\frac{x_1}{h}\right) \qquad [B.17]$$

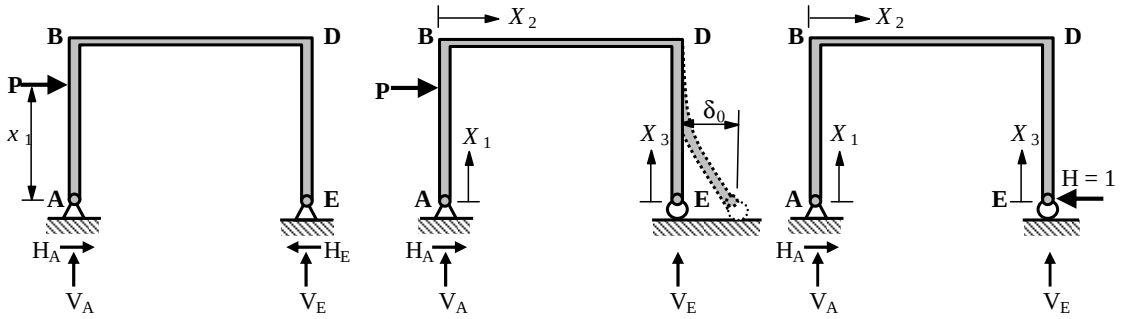

(a) Frame subjected to load P (b) Primary force system (c) Virtual force system

Figure B.2 Frame system for load case 1

Similarly, consider the frame structure with load case 2 shown in Figure B.3a. The horizontal reaction H_E is selected as redundant reaction (see Figure B.3b). To calculate the reactions, three equations of static equilibrium are established as follows:

$$\overset{+}{\rightarrow} \sum F_H = H_A = 0 \qquad \therefore H_A = 0 \qquad \text{[B.18]}$$

$$\uparrow + \sum F_V = V_A + V_E - P = 0 \qquad \therefore V_E = P - V_A \qquad \text{[B.19]}$$

$$\circlearrowleft \sum M_E = V_A \beta h - P(\beta h - x_2) = 0 \qquad \therefore V_A = P\left(1 - \frac{x_2}{\beta h}\right) \qquad \text{[B.20]}$$

Substitution of Eq. [B.3] into Eq. [B.2] leads to $\therefore V_E = \frac{P x_2}{\beta h}$ [B.21]

The resulting bending moment equations at a point with distance x_1 from the left support, x_2 from the left corner of the frame, or x_3 from the right support are

$$\circlearrowleft M_X = -H_A X_1 = 0 \qquad \text{for } 0 \le X_1 < h \text{ in left column} \qquad \text{[B.22]}$$

$$\circlearrowleft M_X = -H_A h + V_A X_2 = P\left(1 - \frac{x_2}{\beta h}\right) X_2 \quad \text{for } 0 \le X_2 \le x_2 \text{ in roof beam} \quad \text{[B.23]}$$

$$\circlearrowleft M_X = -H_A h + V_A X_2 - P(X_2 - x_2)$$
$$= P\left(x_2 - \frac{x_2}{\beta h} X_2\right) \qquad \text{for } x_2 \le X_2 \le \beta h \text{ in roof beam} \quad \text{[B.24]}$$

$$\circlearrowleft M_X = 0 \qquad \text{for } 0 \le X_3 \le h \text{ in right column} \quad \text{[B.25]}$$

Using bending moment equations for the virtual force defined in Eqs. [B.9] through [B.11] and Eqs. [B.22] through [B.25] for M_X, the primary deflection δ_0 and virtual deflection δ_V are obtained as follows

$$\delta_0 = \frac{1}{EI}\int_0^L Mm\,dX = \frac{1}{EI}\int_0^h 0(-X_1)dX_1 + \frac{1}{\alpha EI}\int_0^{x_2} P\left\{1 - \frac{x_2}{\beta h}\right\} X_2(-h)dX_2$$
$$+ \frac{1}{\alpha EI}\int_{x_2}^{\beta h} P\left(x_2 - \frac{x_2}{\beta h} X_2\right)(-h)dX_2 + \frac{1}{EI}\int_0^h 0(-X_3)dX_3$$
$$= \frac{1}{2\alpha}\frac{P}{EI}\left\{\beta h^2 x_2 - h x_2^2\right\} \qquad \text{[B.26]}$$

$$\delta_V = \frac{2}{3}\frac{h^3}{EI}\left[1 + \frac{3}{2}\frac{\beta}{\alpha}\right] \qquad \text{[B.27]}$$

The solution of the horizontal reaction at the right support H_E is obtained as follows:

$$H_E = \frac{\delta_0}{\delta_V} = \frac{\frac{1}{2\alpha}\frac{P}{EI}\left\{\beta h^2 x_2 - h x_2^2\right\}}{\frac{2}{3}\frac{h^3}{EI}\left[1+\frac{3}{2}\frac{\beta}{\alpha}\right]}$$

$$= \frac{3}{2}P\left(\frac{1}{2\alpha+3\beta}\right)\beta^2\left\{\left(\frac{x_2}{\beta h}\right)^2 - \left(\frac{x_2}{\beta h}\right)\right\} \qquad [B.28]$$

From Figure B.7 for load case 2, the horizontal reaction at the left support H_A is

$$\stackrel{+}{\rightarrow}\sum F_H = H_A - H_E = 0 \qquad \therefore H_A = H_E \qquad [B.29]$$

Therefore, $$H_A = \frac{3}{2}P\left(\frac{1}{2\alpha+3\beta}\right)\beta^2\left\{\left(\frac{x_2}{\beta h}\right)^2 - \left(\frac{x_2}{\beta h}\right)\right\} \qquad [B.30]$$

For the vertical components of reactions V_A and V_D are

$$V_A = P\left\{1-\left(\frac{x_2}{\beta h}\right)\right\} \quad \text{and} \quad V_E = P\left(\frac{x_2}{\beta h}\right) \qquad [B.31]$$

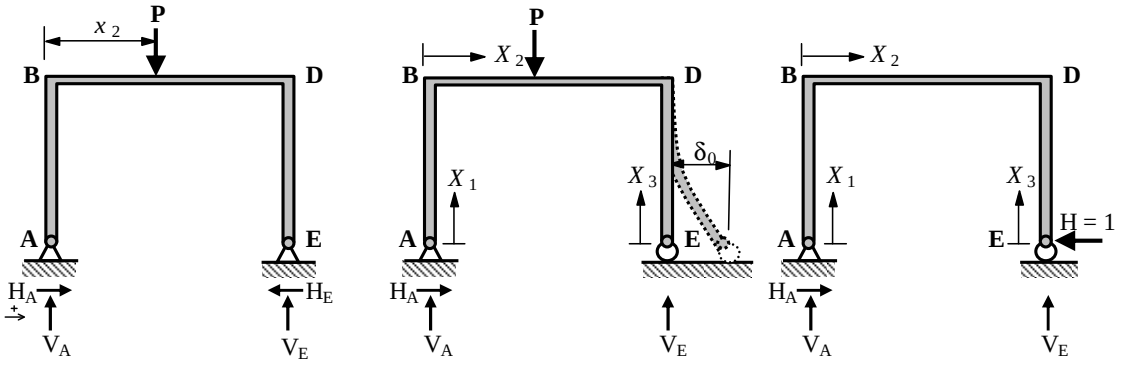

(a) Frame subjected to load P (b) Primary force system (c) Virtual force system

Figure B.3 Frame system for load case 2

Now, consider the frame structure with load case 3 shown in Figure B.4a. The horizontal reaction H_E will be selected as redundant reaction (see Figure B.4b). To calculate the reactions, three equations of static equilibrium are established as follows:

$$\overset{+}{\rightarrow} \sum F_H = H_A - P = 0 \qquad \therefore H_A = P \qquad \text{[B.32]}$$

$$\uparrow + \sum F_V = V_A + V_E = 0 \qquad \therefore V_E = -V_A \qquad \text{[B.33]}$$

$$\circlearrowleft \sum M_E = V_A \beta h - P x_3 = 0 \qquad \therefore V_A = \frac{P x_3}{\beta h} \qquad \text{[B.34]}$$

Substitution of Eq. [B.34] into Eq. [B.33] leads to $\therefore V_E = -\dfrac{P x_3}{\beta h}$ [B.35]

The resulting bending moment equations at a point with distance x_1 from the left support, x_2 from the left corner of the frame, or x_3 from the right support are

$$\circlearrowleft M_X = -H_A X_1 = -P X_1 \qquad \text{for } 0 \le X_1 < h \text{ in left column} \qquad \text{[B.36]}$$

$$\circlearrowleft M_x = -H_A h + V_A X_2 = P\left(\frac{x_3}{\beta h} X_2 - h\right) \qquad \text{for } 0 \le X_2 \le \beta h \text{ in roof beam} \qquad \text{[B.37]}$$

$$\circlearrowleft M_x = 0 \qquad \text{for } 0 \le X_3 \le x_3 \text{ in right column} \qquad \text{[B.38]}$$

$$\circlearrowleft M_x = -P(X_3 - x_3) \qquad \text{for } x_3 \le X_3 \le h \text{ in right column} \qquad \text{[B.39]}$$

Using bending moment equations for the virtual force defined in Eqs. [B.9] through [B.11] and Eqs. [B.36] through [B.39] for M_X, the primary deflection δ_0 and virtual deflection δ_V are obtained as follows

$$\delta_0 = \frac{1}{EI}\int_0^L Mm dX = \frac{P}{EI} h^3 \left\{\left(\frac{2}{3} + \frac{\beta}{\alpha}\right) - \left(\frac{x_3}{h}\right)\left\{\frac{\beta}{2\alpha} + \frac{1}{2}\right\} + \frac{1}{6}\left(\frac{x_3}{h}\right)^3\right\} \qquad \text{[B.40]}$$

$$\delta_V = \frac{2}{3}\frac{h^3}{EI}\left[1 + \frac{3}{2}\frac{\beta}{\alpha}\right] \qquad \text{[B.41]}$$

The solution of the horizontal reaction at the right support H_D is obtained as follows:

$$H_E = \frac{\delta_0}{\delta_V} = P\left[\frac{3}{2}\left(\frac{\alpha}{2\alpha + 3\beta}\right)\left\{\left(\frac{x_3}{h}\right)\left(1 + \frac{\beta}{\alpha}\right) - \frac{1}{3}\left(\frac{x_3}{h}\right)^3\right\} - 1\right] \qquad \text{[B.42]}$$

From Figure B.4a for load case 3, the horizontal reaction at the left support H_A is

$$\xrightarrow{+} \sum F_H = H_A - H_E - P = 0 \multimap \qquad \therefore H_A = H_E + P \qquad \text{[B.43]}$$

Therefore, $$H_A = \frac{3}{2} P \left(\frac{\alpha}{2\alpha + 3\beta} \right) \left\{ \left(1 + \frac{\beta}{\alpha} \right) \left(\frac{x_3}{h} \right) - \frac{1}{3} \left(\frac{x_3}{h} \right)^3 \right\} \qquad \text{[B.44]}$$

For the vertical components of reactions V_A and V_E are

$$V_A = \frac{P}{\beta} \left(\frac{x_3}{h} \right) \quad \text{and} \quad V_E = -\frac{P}{\beta} \left(\frac{x_3}{h} \right) \qquad \text{[B.45]}$$

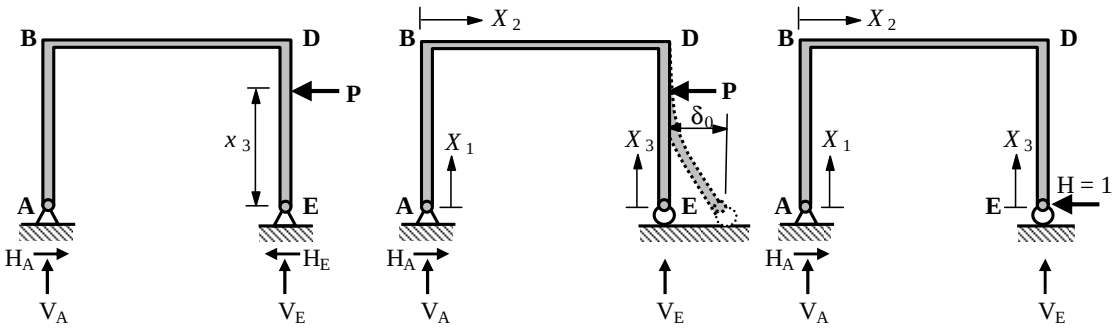

(a) Frame subjected to load P (b) Primary force system (c) Virtual force system

Figure B.4 Frame system for load case 3

Lists of Influence Lines for Reactions

$$H_A = P\left[\frac{3}{2}\left(\frac{\alpha}{2\alpha+3\beta}\right)\left\{\left(\frac{x_1}{h}\right)\left(1+\frac{\beta}{\alpha}\right)-\frac{1}{3}\left(\frac{x_1}{h}\right)^3\right\}-1\right] \qquad \text{for } 0 \le x_1 < h \text{ in left column}$$

$$H_A = \frac{3}{2}P\left(\frac{1}{2\alpha+3\beta}\right)\beta^2\left\{\left(\frac{x_2}{\beta h}\right)^2-\left(\frac{x_2}{\beta h}\right)\right\} \qquad \text{for } 0 \le x_2 \le \beta h \text{ in roof beam}$$

$$H_A = \frac{3}{2}P\left(\frac{\alpha}{2\alpha+3\beta}\right)\left\{\left(1+\frac{\beta}{\alpha}\right)\left(\frac{x_3}{h}\right)-\frac{1}{3}\left(\frac{x_3}{h}\right)^3\right\} \qquad \text{for } 0 \le x_3 \le h \text{ in right column}$$

$$H_E = \frac{3}{2}P\left(\frac{\alpha}{2\alpha+3\beta}\right)\left\{\left(1+\frac{\beta}{\alpha}\right)\left(\frac{x_1}{h}\right)-\frac{1}{3}\left(\frac{x_1}{h}\right)^3\right\} \qquad \text{for } 0 \le x_1 < h \text{ in left column}$$

$$H_E = \frac{3}{2}P\left(\frac{1}{2\alpha+3\beta}\right)\beta^2\left\{\left(\frac{x_2}{\beta h}\right)^2-\left(\frac{x_2}{\beta h}\right)\right\} \qquad \text{for } 0 \le x_2 \le \beta h \text{ in roof beam}$$

$$H_E = P\left[\frac{3}{2}\left(\frac{\alpha}{2\alpha+3\beta}\right)\left\{\left(\frac{x_3}{h}\right)\left(1+\frac{\beta}{\alpha}\right)-\frac{1}{3}\left(\frac{x_3}{h}\right)^3\right\}-1\right] \qquad \text{for } 0 \le x_3 \le h \text{ in right column}$$

$$V_A = -\frac{P}{\beta}\left(\frac{x_1}{h}\right) \qquad V_E = \frac{P}{\beta}\left(\frac{x_1}{h}\right) \qquad \text{for } 0 \le x_1 < h \text{ in left column}$$

$$V_A = P\left\{1-\left(\frac{x_2}{\beta h}\right)\right\} \qquad V_E = P\left(\frac{x_2}{\beta h}\right) \qquad \text{for } 0 \le x_2 \le \beta h \text{ in roof beam}$$

$$V_A = \frac{P}{\beta}\left(\frac{x_3}{h}\right) \qquad V_E = -\frac{P}{\beta}\left(\frac{x_3}{h}\right) \qquad \text{for } 0 \le x_3 \le h \text{ in right column}$$